P 2mit

Interdisciplinary Studies
of Samples from

Boulder 1, Station 2
Apollo 17

CR 134215

VOLUME (NASA-CR-134215) INTERDISCIPLINARY STUDIES OF SAMPLES FROM BOULDER 1, STATION 2, APOLLO 17, VOLUME 1 (Smithsonian Astrophysical Observatory) CSCL 03B G3/30 34264

N74-20508 THRU N74-20515 Unclas

NGL 09-~~194~~ 191 p HC $12.75

JB Adams
SO Agrell
E Anders
SK Banerjee
W Compston
LA Haskin
WM Muehlberger
PB Price
GW Reed
JH Reynolds
HH Schmitt
M Tatsumoto
HG Wilshire
JA Wood

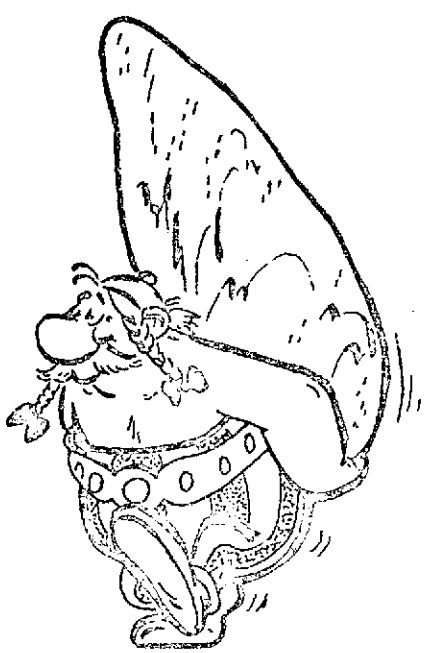

Consortium Indomitabile

INTERDISCIPLINARY STUDIES OF SAMPLES FROM BOULDER 1, STATION 2, APOLLO 17

Consortium Indomitabile

J. B. Adams
S. O. Agrell
E. Anders
S. K. Banerjee
W. Compston
L. A. Haskin
W. M. Muehlberger
P. B. Price
G. W. Reed
J. H. Reynolds
H. H. Schmitt
M. Tatsumoto
H. G. Wilshire
J. A. Wood, Leader

Volume 1

March 15, 1974

403-003

This publication was assembled and produced by the Editorial and Publications Department, Smithsonian Astrophysical Observatory. Its production was supported by NASA Lunar Sample Analysis Grant NGL 09-015-150, as was the research reported in Sections II, III, and IV. The figure of Obelix on the cover was created by Goscinny and Uderzo (Copyright, Dargaud S. A.).

Copies can be obtained by writing Ms. Karen Motylewski, Smithsonian Astrophysical Observatory, 60 Garden Street, Cambridge, Massachusetts 02138, USA.

TABLE OF CONTENTS

I. THE GEOLOGIC SETTING OF BOULDER 1, STATION 2

R. W. Wolfe*

Center for Astrophysics
Harvard College Observatory and Smithsonian Astrophysical Observatory
Cambridge, Massachusetts 02138

H. H. Schmitt

Office of the Administrator
National Aeronautics and Space Administration
Washington, D.C. 20546

and

W. M. Muehlberger

Department of Geology
University of Texas
Austin, Texas 78712

Apollo 17 landed on the flat floor of a deep, narrow valley embayed in the mountainous highlands that comprise the southeastern rim of Mare Serenitatis (Figure I-1). Serenitatis is one of the youngest multiringed basins on the lunar nearside and is underlain by a mascon. The valley of Taurus-Littrow, which is radial to the basin, is generally interpreted as a graben formed as a result of structural adjustments of the lunar crust in response to the Serenitatis event (Apollo Lunar Geology Investigation Team, 1973a).

The highlands surrounding the valley can be divided on the basis of their morphologies into 1) high, steep, smooth massifs, 2) lower domical hills (the Sculptured Hills), and 3) other low hills adjacent to both the massifs and the Sculptured Hills (Figure I-1) (Apollo Lunar Geology Investigation Team, 1973a). According to Schmitt (1973),

> Although certainly internally complex, the dominant fabric of the North Massif is apparently that of roughly horizontal structural units that may be depositional or intrusive layers. In the South Massif these units appear to be tilted westward or southwestward. High angle normal faulting and tan-gray breccia intrusions apparently break the continuity of the structural fabrics in both massifs. The tilting and faulting of massif units may relate to their uplift during the Serenitatis impact event or subsequent major basin events.

*Acting as editor, I have drawn freely on the references cited and materials submitted by the other authors. The credit for the information presented here is theirs; errors in the presentation are mine.

Figure I-1. High-oblique view toward the southeast of the Apollo 17 landing site (NASA photograph AS15-9290).

The materials of North Massif and South Massif were sampled from boulders that rolled down their slopes or were, perhaps, ejected by small impacts higher on the massifs.

South Massif materials were collected from Station 2, EVA-II. This station is located about 50 m above the break in slope at the foot of the massif at the southeastern edge of Nansen crater and is on the bright deposit extending northward across the valley floor from the base of the massif (Figures I-2A and I-3). This deposit consists of breccias similar to those of the massif and is interpreted as material shed from the slopes of the massif as a landslide or avalanche. In the area of Station 2, subdued craters 3 to 5 m in diameter are common. There are no blocky craters visible, nor do any of the fresher craters appear to penetrate to bedrock (Apollo Lunar Geology Investigation Team, 1973a, b).

A concentration of boulders occurs at and near the break in slope at the foot of South Massif. Those with visible tracks on the massif slopes were emplaced after the avalanche that formed the light mantle, and probably emplacement of all the boulders postdates the light mantle. If they were a part of the avalanche itself, the boulders would be more uniformly distributed across the surface of the light mantle, rather than concentrated near the base of the massif (Apollo Lunar Geology Investigation Team, 1973a).

The most obvious sources for the boulders near Station 2 are on the upper one-quarter of the massif slope (Figure I-2B). Visual inspection from a distance indicated that linear source-crops on this part of the massif and the subtle contact between blue-gray and tan-gray units have an apparent dip of 10° to 15° to the west. Offsets of the color changes, downward to the east, suggest that normal faults dipping steeply eastward cut this apparent massif structure (Figure I-4A, B) (Schmitt, 1973).

In the area of color variation, blocky patches are common, especially in the blue-gray unit (Figure I-4A, B). There is no apparent source for the Station 2 boulders on the lower three-quarters of the massif (Figure I-2B). Although none of the sampled boulders has visible tracks on the slope, the boulders lie directly below the blocky area above the contact between the tan-gray and blue-gray units near the top of South

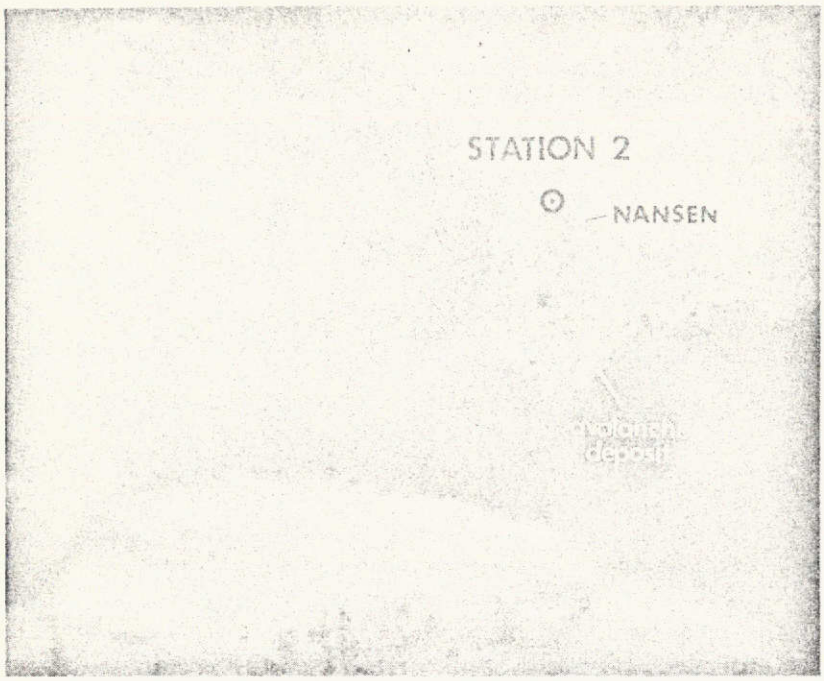

Figure I-2A. Environs of Station 2 (circled) (NASA photograph AS15-9290).

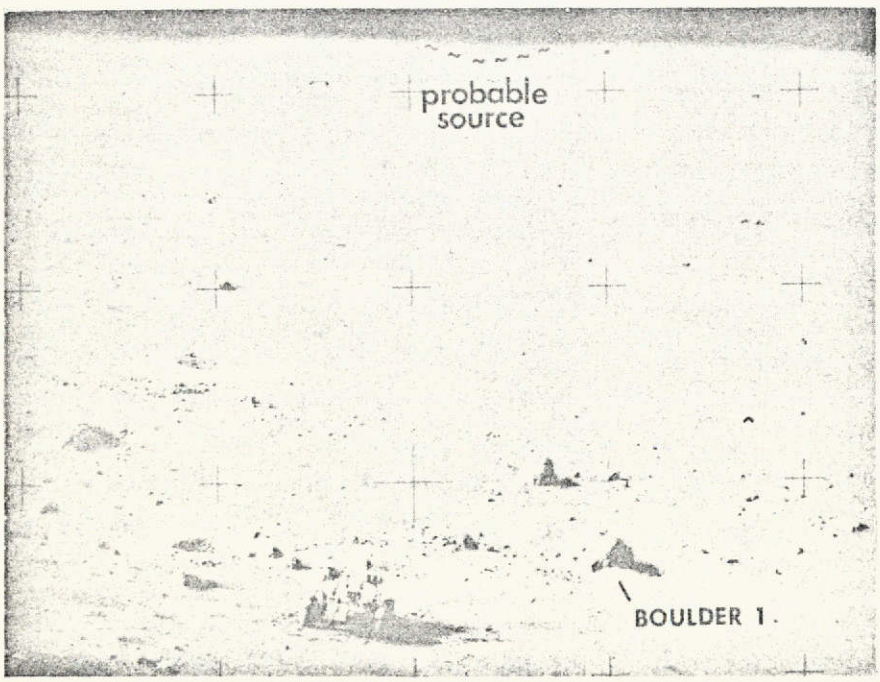

Figure I-2B. Station 2 looking toward South Massif (NASA photograph AS17-21072).

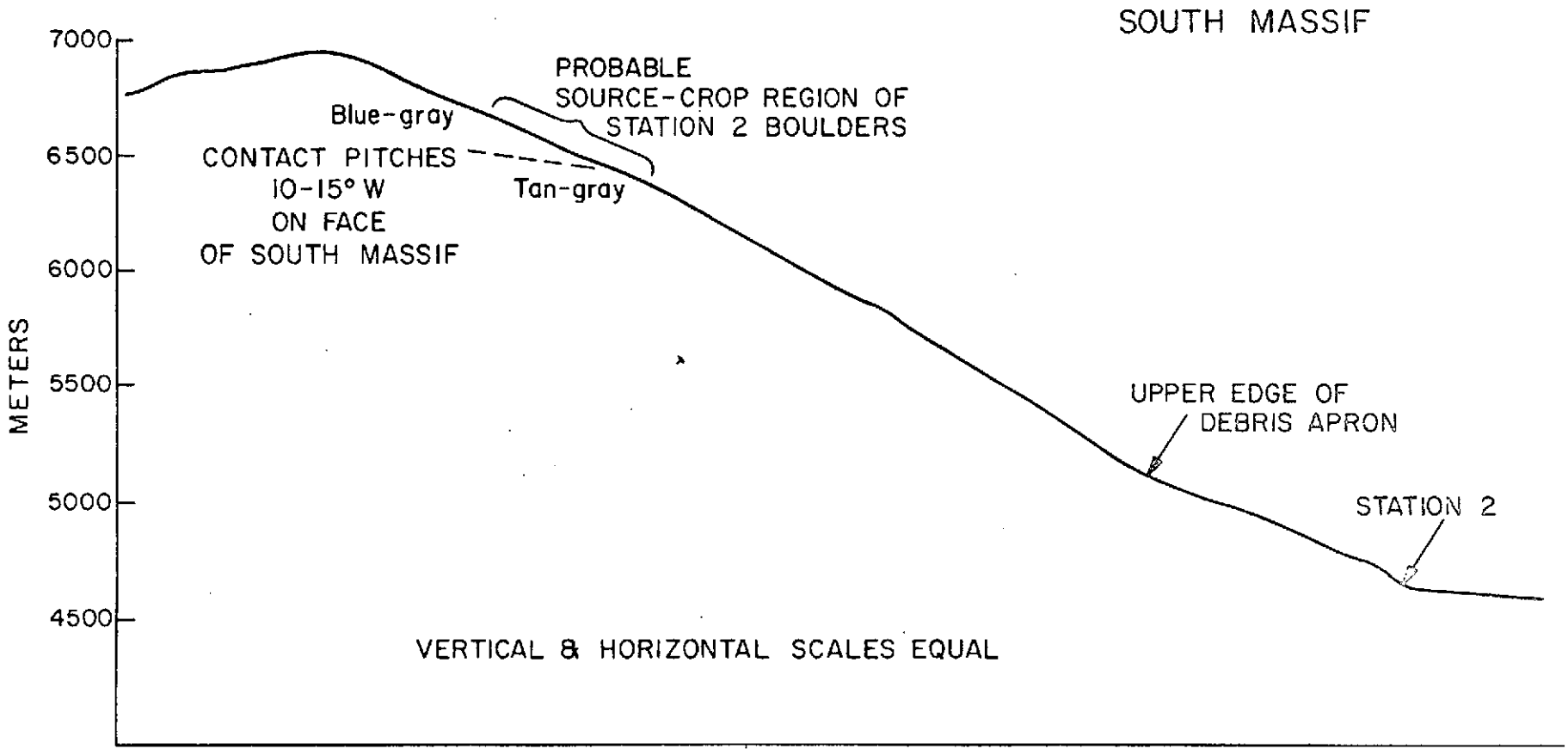

Figure I-3. Topographic profile of South Massif drawn through Station 2.

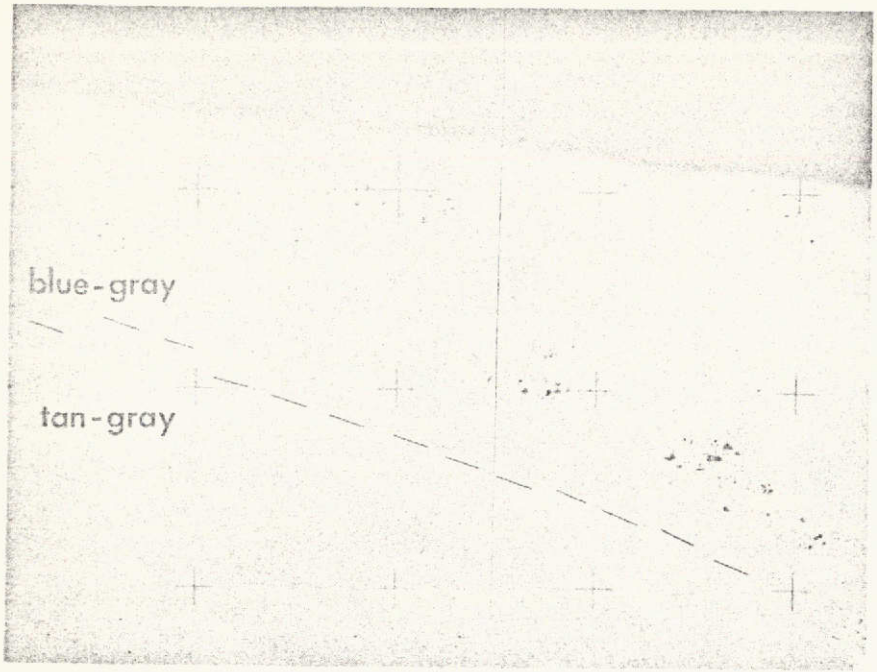

Figure I-4A. Telephoto view of the blocky area near the top of South Massif (NASA photograph AS17-22089).

Figure I-4B. More southeasterly view of a portion of the area in A (NASA photograph AS17-22057).

Massif (Figure 1-2B). Boulder tracks from the blue-gray source-crops on the upper portion of the massif led to the large boulders in Nansen. This supports the conclusions based on visual correlation of colors viewed from a distance that boulders from the blue-gray source-crops reached the base of the massif and that Boulder 1 is probably one of these.

In summarizing the activities at Station 2, Schmitt (1972) commented on the significance of Boulder 1 in the following transmission upon leaving the station:

> Those two major kinds of blocks that we sampled there were about the two varieties we saw in the area. It's a long extrapolation I realize, but they do resemble in color, and I believe in texture, the blue-gray rocks and the tan-gray rocks up on the massif. So I feel fairly confident that we sampled at least the two major units visible from a distance in the South Massif.

The regional stratigraphic relations of the foliated and layered fragment-rich breccias as represented by Boulder 1 were summarized by Schmitt (1973):

> The oldest through youngest stratigraphic units which are present as bedrock in the North and South Massifs are as follows: (i) Light gray breccia and crystalline rock as distinctive clasts in the blue-gray breccias. (These clasts may be closely related to the differentiates of an early melted lunar crust.) (ii) Crystalline blue-gray fragment-rich breccias and their metamorphic equivalents. (These breccias are possibly quenched and brecciated impact melts produced during the formation of the large lunar basins or even older events.) (iii) Crystalline, vesicular, tan-gray matrix-rich breccia and any metamorphic effects associated with its intrusion into the blue-gray breccias. (These instrusions may be partially molten impact breccias, possibly of Serenitatis age, or polygenetic tuff-breccia eruptives of undetermined origin.) (iv) Foliated layered breccia of low metamorphic grade which is rich in a variety of breccia clasts and which appears to correlate with units near the crest of the South Massif. (These rocks may be representative of the youngest ejecta blankets from large basins.)

REFERENCES

Apollo Lunar Geology Investigation Team (1973a). Preliminary geologic analysis of the Apollo 17 site. USGS Astrogeology 72.

Apollo Lunar Geology Investigation Team (1973b). Documentation and environment of the Apollo 17 samples: A preliminary report. USGS Astrogeology 71.

Schmitt, H. H. (1972). Apollo 17 air-to-ground communication. Tape 95A.

Schmitt, H. H. (1973). Apollo 17 report on the valley of Taurus-Littrow. Science, vol. 182, pp. 681-690.

II. MORPHOLOGY AND SURFACE MAPPING

Ursula B. Marvin

Center for Astrophysics
Harvard College Observatory and Smithsonian Astrophysical Observatory
Cambridge, Massachusetts 02138

Of the many boulders photographed at the Apollo 17 site, Boulder 1 from Station 2 is unique in having a strongly developed foliation. Resistant layers form four steeply inclined ridges separated by joint planes or by deeply eroded beds of softer materials. A prominent cleavage, or set of cross joints, is oriented almost normal to the foliation (Figure II-1). The cleavage is expressed as subparallel cracks, some of which are open fissures. The entire surface of the boulder is rough and studded by dark-colored knobs ranging in diameter from 1 to 15 cm.

The unusual morphology of this boulder, which is about 2 m long by 1 m wide and stands about 1 m above the surface of the regolith, attracted the attention of Astronauts Schmitt and Cernan, who collected four specimens from the locations shown in Figure II-1. Two of these specimens, 72275 and 72255, were subdivided and distributed to consortium members in the autumn of 1973. The other two, 72215 and 72235, will be distributed by summer 1974. The results assembled in this report show that Boulder 1 from Station 2 is unique in several other respects besides its morphology. It is a polymict breccia containing at least one type of rock that has not been recognized in any other lunar sample, and it records an unusual minor-element distribution and magnetic history. These early findings on two of the specimens greatly enhance our interest in the remaining two.

All four specimens were prominent features on the boulder: 72275 stood up in bold relief at the top of the boulder; 72235 was a black knob from a lower portion of the same layer; and the other two specimens were gently rounded bulges on two different layers (Figure II-1B).

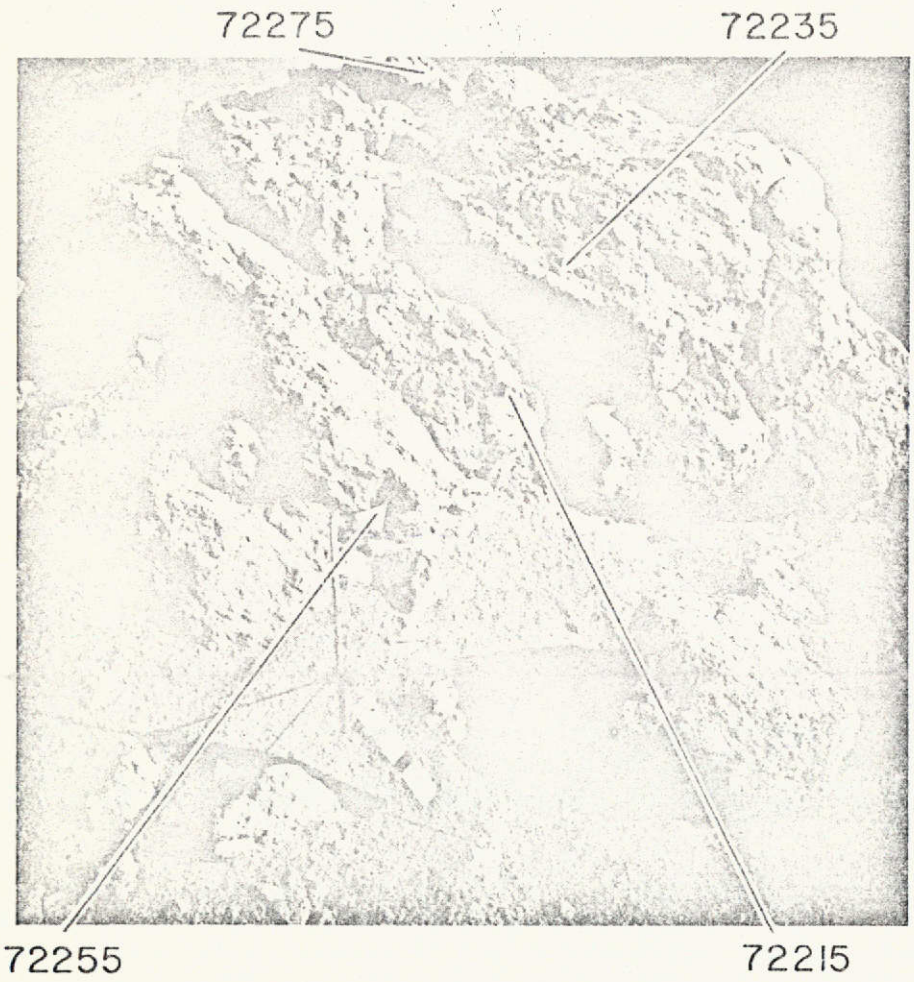

Figure II-1A. NASA photograph (AS17-137-20901) of the southeast face of Boulder 1 in situ at Station 2. Arrows indicate the sampling sites.

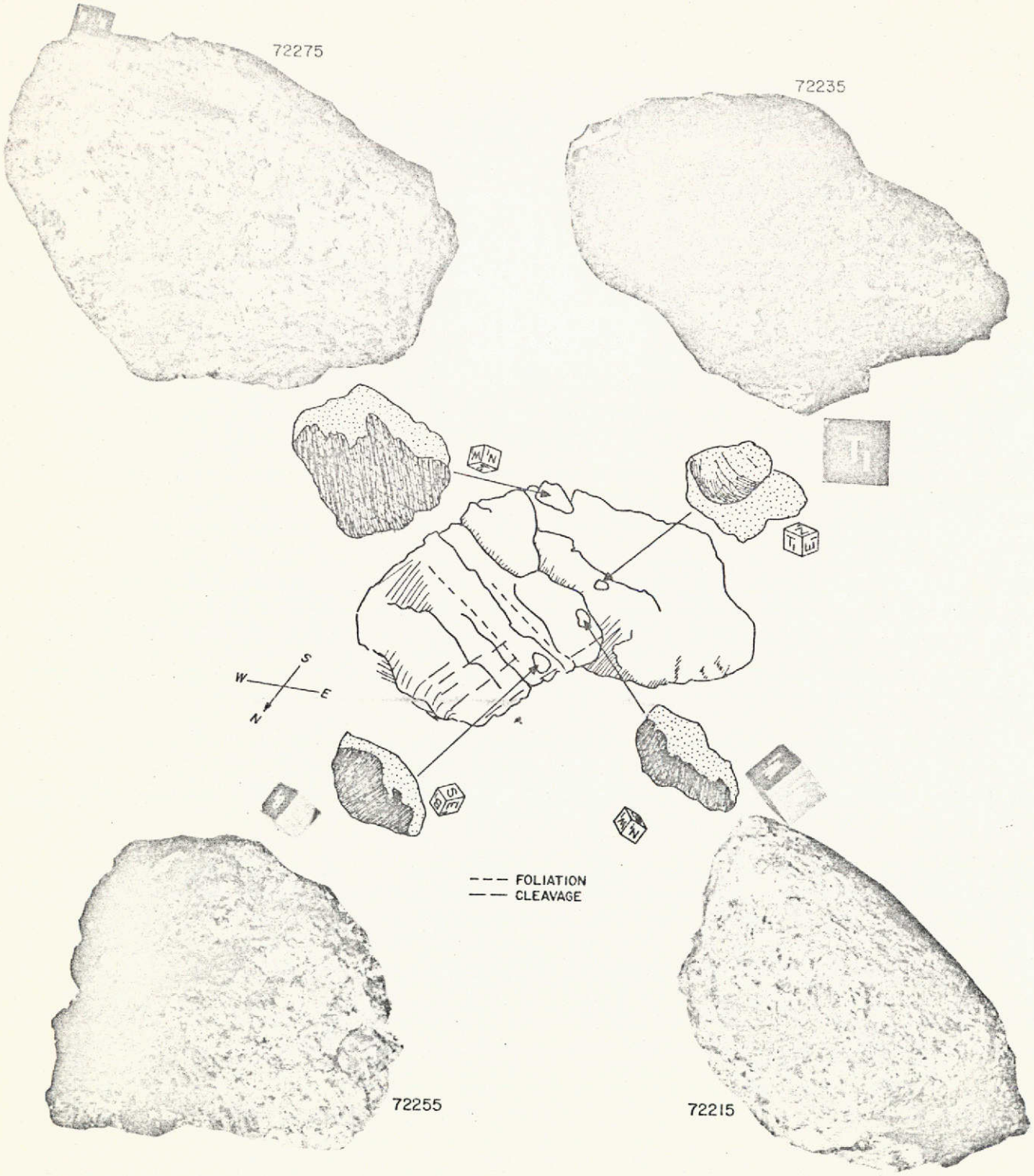

Figure II-1B. Sketch of Boulder 1 in situ at Station 2, showing the foliation, cleavage, and sampling sites. The photographs show the four specimens as they were positioned on the boulder. The lunar orientation of the boulder, and hence of the specimens, is indicated by the compass directions. The cubes give the conventional orientations assigned to the specimens after they arrived at the Lunar Receiving Laboratory. The lunar and the laboratory orientations are not the same.

Despite its exposed position, 72275 is the most friable of the four specimens. By the time it was transported from the Moon to the Lunar Receiving Laboratory in Houston, it had broken into four main fragments plus numerous chips and fines. A reassembly of the four identifiable fragments of this specimen is shown in Appendix A (see Figure A-1), where all the subdivisions of 72275 are documented. Four views of the main mass, 72275, 0 – the only portion of the original specimen that has been subdivided and distributed for study – are shown in Figure II-2.

Specimen 72255 is more resistant than 72275; nevertheless, it also broke into fragments en route from the Moon. The reconstructed specimen is shown in Appendix B (Figure B-1), along with complete documentation of its subdivisions. Figure II-3 shows three views of the main mass, 72255, 0, from which samples have been taken for distribution to consortium members.

The most coherent of the four specimens is 72215. It is competent enough to maintain one rather large open crack and several subparallel cracks aligned with the main foliation direction of the parent boulder (see Figure II-4). This specimen includes two features of special interest: an apparent layering within the matrix itself, and a small knob consisting partially of chalky white anorthosite, including several holocrystalline lithic clasts.

Specimen 72235 is a resistant black knob embedded in a gray friable matrix resembling that of 72275. The knob consists of gray and white fluidized cataclastic breccia enclosed in a strongly annealed aphanitic gray-black rind (Figure II-5).

SPECIMEN 72275: SURFACE CHARACTERISTICS

The surface features of 72275, 0 visible through the cabinet windows of the nitrogen lines at the Lunar Receiving Laboratory are outlined in the maps of Figure II-6. The portions that were exposed on the lunar surface have a brown patina and abundant zap pits, represented on the maps by stippling. A number of dark, resistant knobs covered with patina are shown in view B_1. The most prominent feature on any surface of the specimen is a light-colored clast with a black rim, seen in view N_1. This clast (designated hereafter as clast #1) appears to be the remnant of a knob that broke away

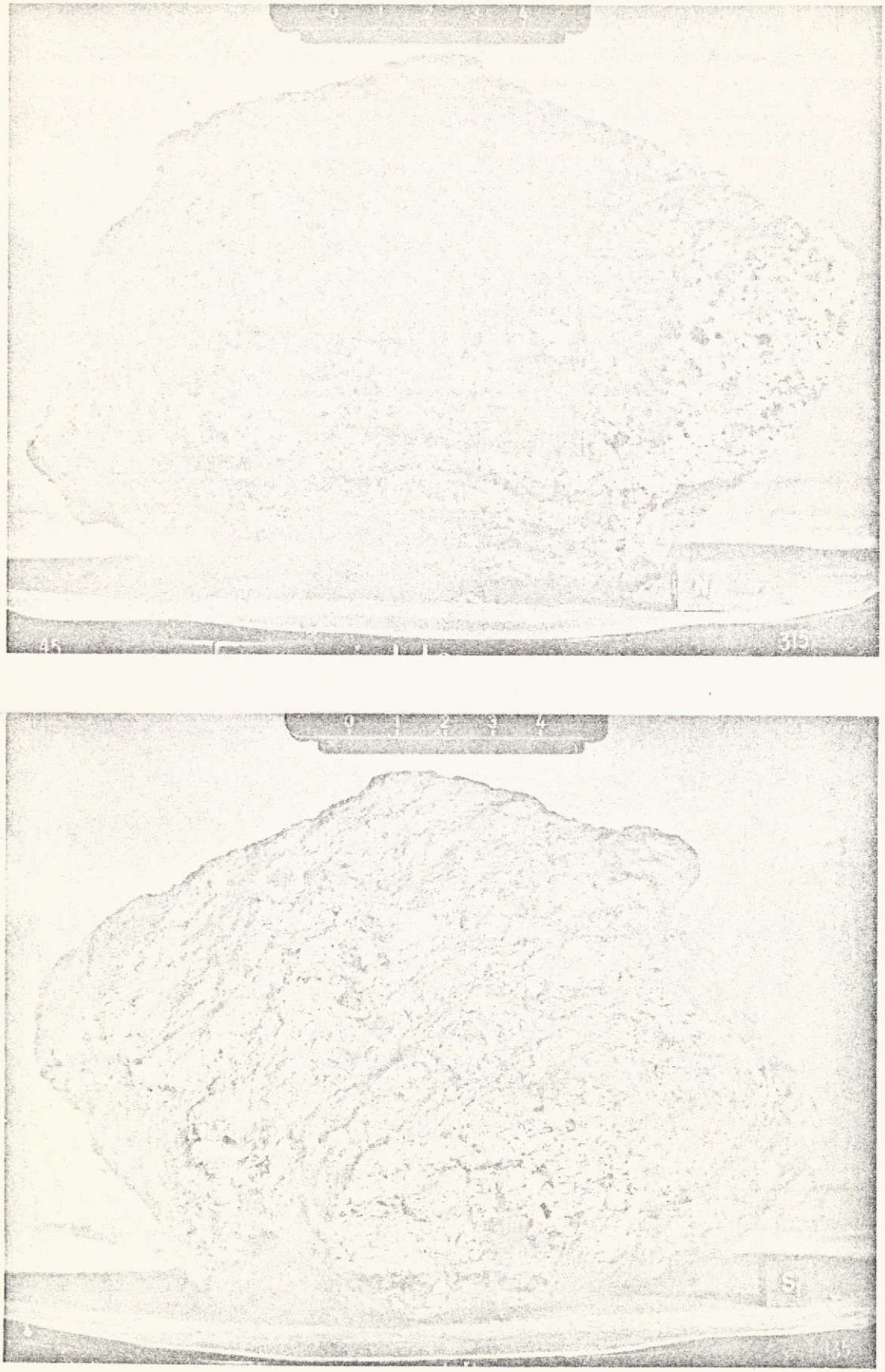

Figure II-2A. The north and south surfaces of specimen 72275. Maps of these surfaces are shown in Figure II-6.

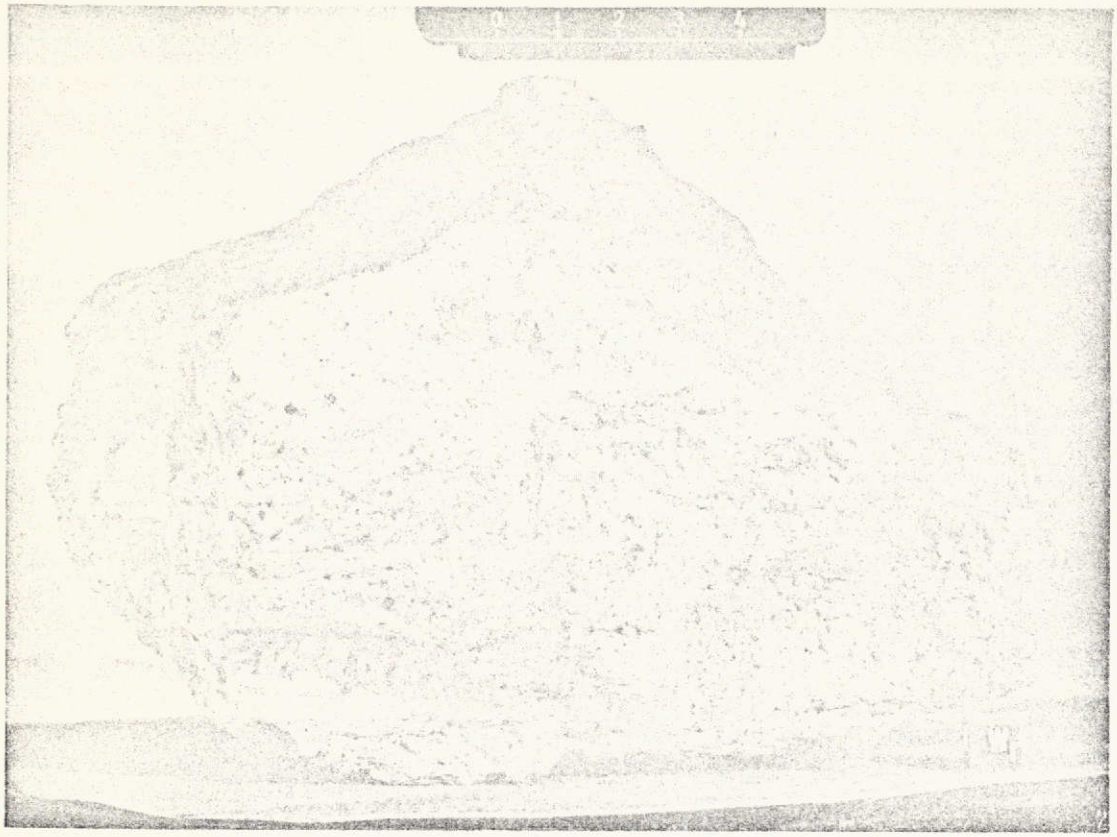

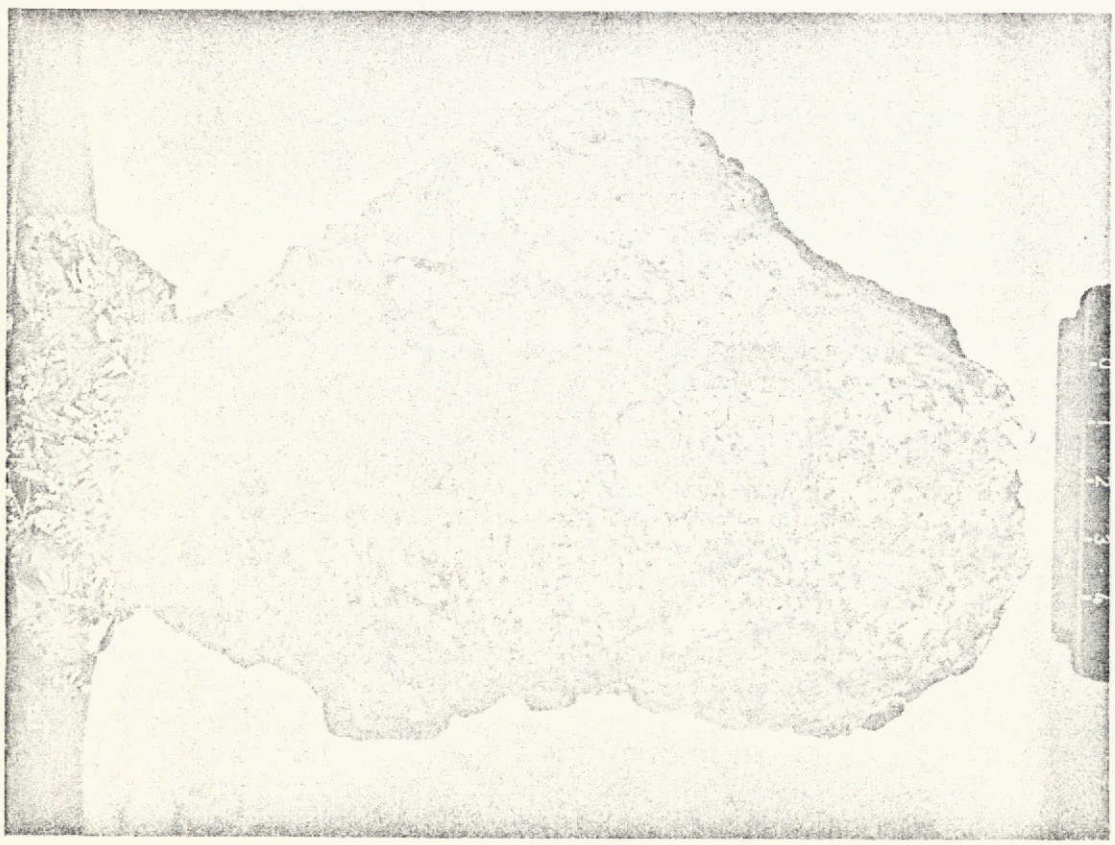

Figure II-2B. East and west surfaces of specimen 72275. Maps of these surfaces are shown in Figure II-6.

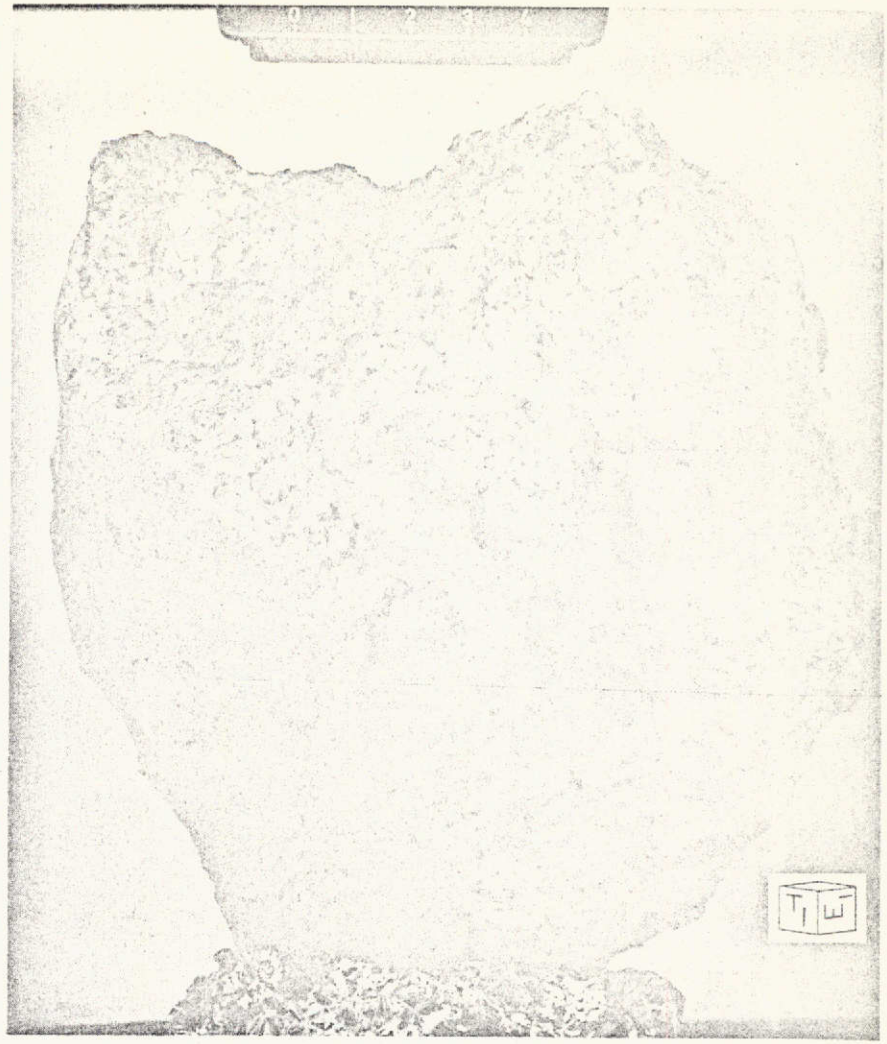

Figure II-2C. Left photograph: Some of the dark knobs that occur on the exterior of the boulder. Right photograph: The top surface (T_1), where the specimen was attached to the parent boulder, and the east surface, which is markedly irregular and partially covered with fine-grained delicately layered and ripple-marked material (see also Figures II-7 and A-2).

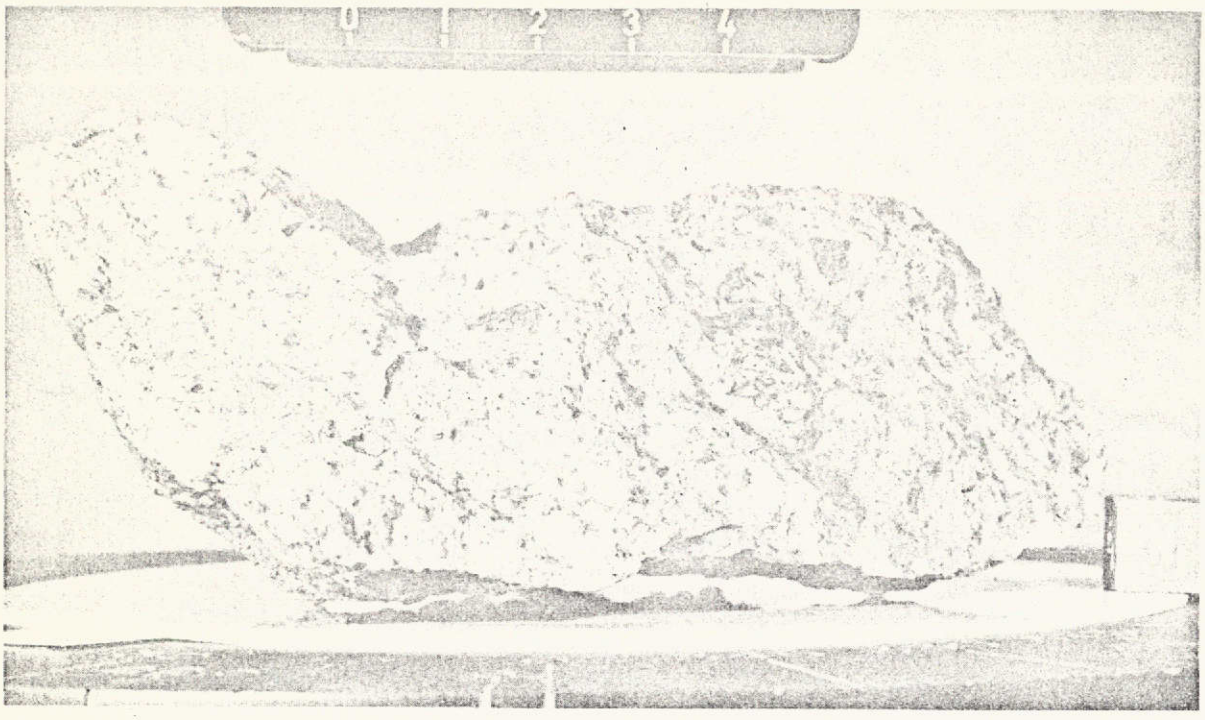

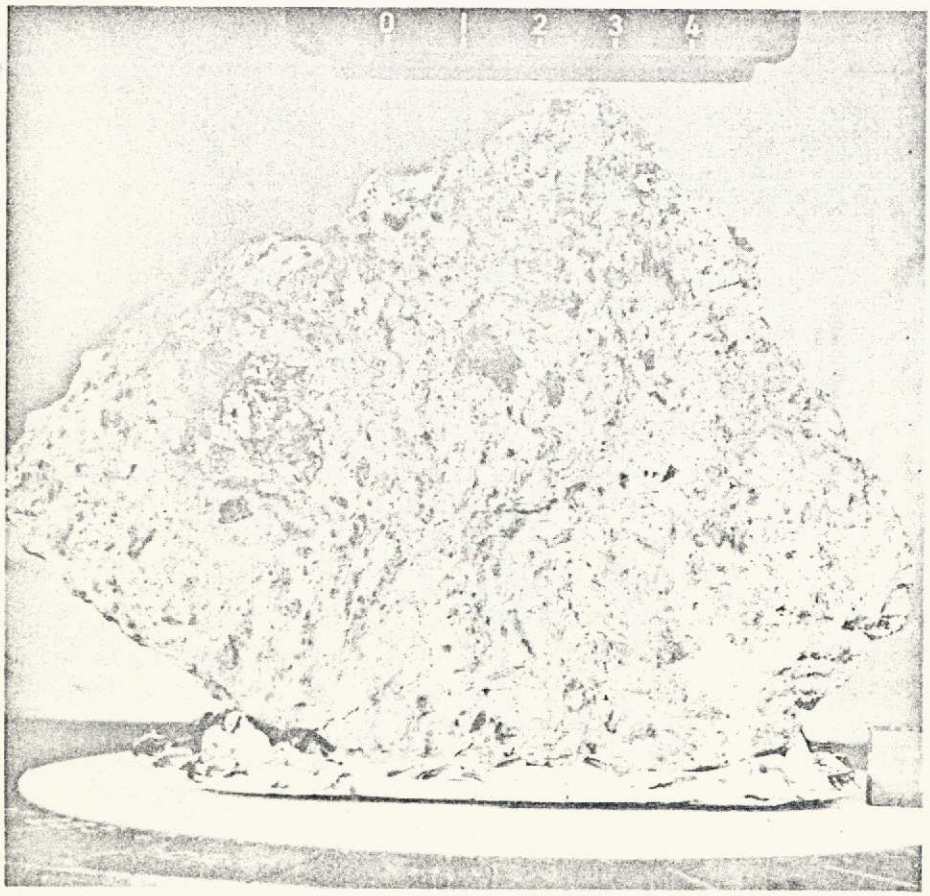

Figure II-3. Two views of specimen 72255. The unique Civet Cat clast, a dark wedge-shaped fragment with lenticular white inclusions, is visible in both photographs. Surface maps of 72255 are shown in Figures II-10 and II-12.

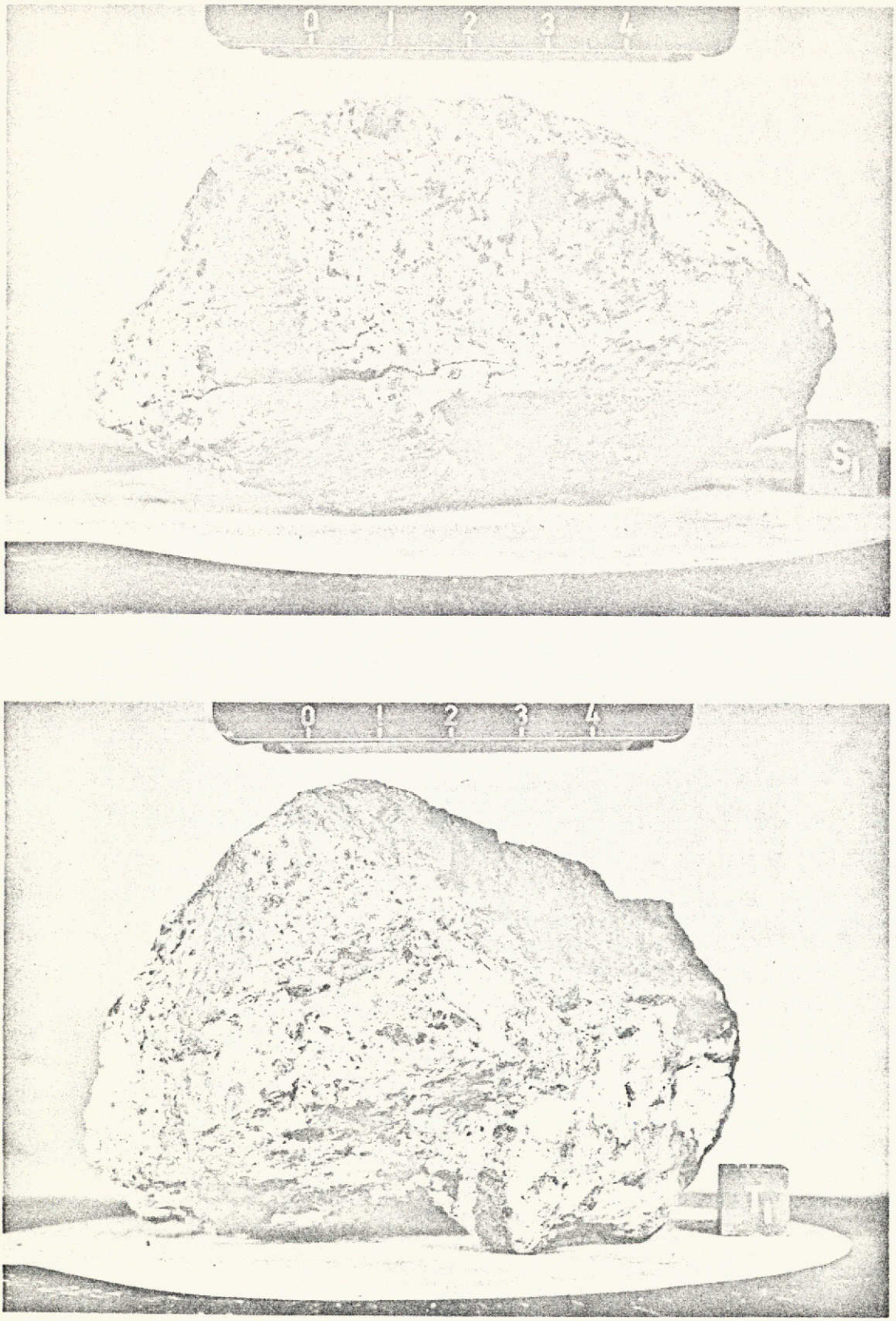

Figure II-4. Two views of specimen 72215. The subparallel cracks across the south face are aligned with the dominant foliation of the parent boulder. The upper photograph gives a clear view of an irregular medium-gray layer or streak through the matrix; and the lower photograph, a small knob at the lower right that encloses layers of gray and white breccia.

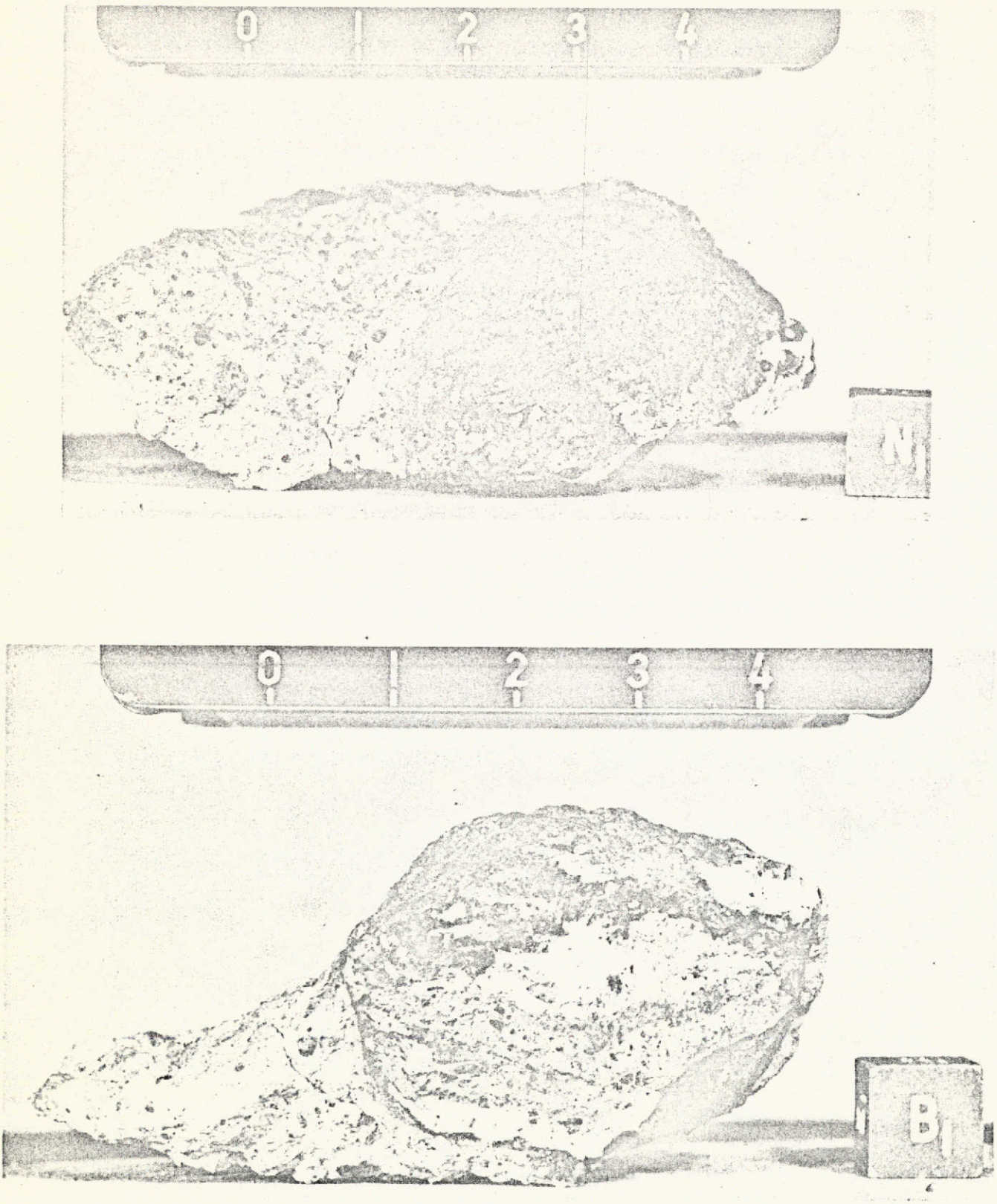

Figure II-5. Two views of specimen 72235, a black knob embedded in a friable gray matrix. The lower photograph shows the interior of the knob, which consists of layers of gray and white fluidized cataclastic breccia enclosed within a rim of aphanitic black breccia.

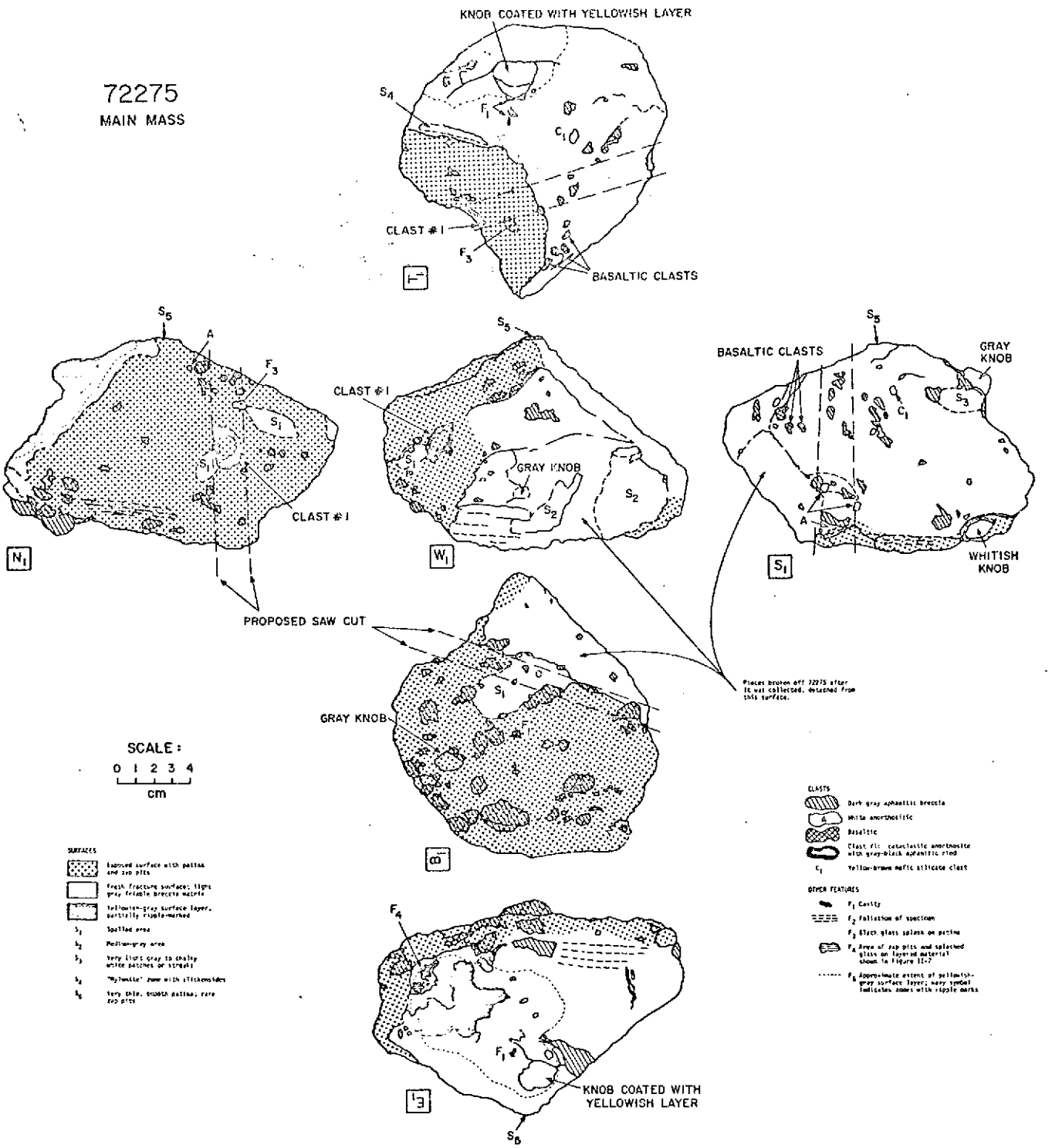

Figure II-6. Surface maps of specimen 72275. See Figures II-2A and B for photographs.

from the boulder, leaving a fresh interior surface that subsequently acquired a patina. The cutting plan for 72275, 0 was designed to slice open clast #1 and include most of it within a large slab. The cutting lines are represented by the dashed lines in views N_1 and S_1 of Figure II-6.

Most of the freshly fractured surfaces of 72275, 0 consist mainly of fine-grained matrix and small gray or white clasts. The matrix tends to shed dust each time the specimen is handled, and the dust obscures the fine structure of the interior. However, a most unusual surficial feature is exposed on the E_1 face. Here, the surface is partially coated with a very fine-grained yellowish-gray clay-like material that is delicately layered and, in places, ripple-marked. The location of the rippled surface is indicated by an appropriately rippled symbol in views N_1 and E_1 of Figure II-6, and photographs of this lunar minitopography are shown in Figure II-7. The origin of the ripples has not been satisfactorily explained, but the following observations may be relevant.

The material of the rippled surface layer appears to have much the same composition as does the parent boulder. Optical determinations by the immersion method show that the grain size ranges from about 1 to 12 μ and averages 1.5 μ. Most of the particles have an index of refraction of approximately 1.580, which matches anorthite; a few range above 1.650, and these could be any mafic silicate. X-ray-diffraction films of the bulk material yield a dominant anorthite pattern plus a weaker bronzite pattern. An average of 16 defocused-beam electron-microprobe analyses is listed in Table II-1, where it is compared with analyses of the friable gray matrix and of dark matrix breccias, which are an abundant component of the boulder (see Section III). All these lines of evidence suggest that the layered and rippled material is derived from the boulder itself, rather than being dust of an alien composition that was wedged into a boulder crack or plastered onto the surface.

While it was attached to the parent boulder, the E_1 surface faced down toward the lunar surface. However, it was neither a fully exposed surface, as is shown by its fine state of preservation and its lack of a patina, nor a freshly fractured surface. When 72275 was collected by the astronauts, the specimen broke away from the parent boulder along face T_1, and during transport from the Moon, fragments broke away from faces W_1 and S_1 (see Figure II-6). Therefore, either the rippled face, E_1, was

Table II-1. Electron-microprobe analyses of the ripple-marked surface layer and light and dark matrix materials.

	72275, 17* Ripple-marked surface layer	72275, 128† Light gray matrix	72275, 128† Dark matrix
SiO_2	51.0	47.3	49.7
TiO_2	0.9	0.6	1.1
Cr_2O_3	0.2	0.1	0.2
Al_2O_3	20.2	21.3	18.8
FeO	7.6	8.8	10.0
MnO	0.1	0.1	0.1
MgO	6.7	8.3	9.0
CaO	12.0	12.4	11.4
Na_2O	0.4	0.4	0.5
K_2O	0.2	0.1	0.3
P_2O_5	0.2	0.5	0.5
Total	99.5	99.9	101.6
Fo	0.0	0.0	0.0
Fa	0.0	0.0	0.0
En	16.6	20.7	22.0
Fs	12.5	15.2	16.3
Wo	1.3	1.0	2.1
Or	1.2	0.8	2.0
Ab	3.4	3.7	3.9
An	54.5	55.8	47.5
Ilm	1.7	1.2	2.1
Chr	0.3	0.1	0.3
Qtz	8.0	0.2	2.7
Cor	0.0	0.0	0.0
Ap	0.6	1.1	1.1

*Recalculated average of 16 defocused-beam analyses. The rippled material is very porous and took a poor polish. The sums clustered at 86.5%. The result is therefore to be taken as only an approximation.

†For further explanation, see Table III-6.

an interior surface bounding a preexisting crack along which rock powder was pulverized and rippled by grinding between the walls, or it was protected by an overhang. Perhaps the best explanation invokes two stages of formation: The powdery surface layer was produced by grinding motion within a crack, and the opposite wall of the crack later fell to the lunar surface leaving the E_1 surface facing down toward the regolith. Such a sequence of events is suggested by the presence of a very few zap pits in the surficial layered material. Although none of these occurs within the rippled area, they are present near its margins, where, at one site, they are accompanied by delicate splashes of black glass (feature F_4 in Figure II-7).

If the production of ripple marks requires the distribution of material by a moving medium, then Boulder 1 at Station 2 records the passage of a cloud of gas (?) or fine particles, generated in a landslide or base surge, either through a crack or across a surface. Alternatively, a fine powdery layer within a crack may have been rippled by vibrations accompanying an event such as the one that emplaced the boulder on top of the landslide at South Massif.

The sawing of a slab from 72275, 0 was done on July 26 and 27, 1973. The process was made difficult by the friability of the matrix, and dust and small fragments were produced in abundance along the saw cut. Several times the saw blade bit into hard, resistant clasts that stopped the motion altogether or twisted the specimen out of line. To obtain a single, coherent slab proved impossible. When the sawing was complete, the specimen consisted of the four main subdivisions shown in Figure II-8.

As sawing proceeded, each freshly exposed surface was examined and mapped by Ursula Marvin and Stewart Agrell, who used transparent overlays on Polaroid photographs. The Polaroids were taken through the cabinet windows at different magnifications, so the maps are drafted to different scales, as is readily apparent in Figure II-9.

The materials mapped are of four main lithologic types:

A. Light gray matrix with minor darker gray zones.
B. Anorthositic clasts.

Figure II-7. Two views of the fine-grained layer on the east surface of 72275. Upper photograph: A ripple-marked area, where a piece has broken away, and exposed deeper layers, where ripples are oriented in a direction different from that on the surface. Lower photograph: A site near the lower edge of the layered material, where the surface is marked by zap pits and splashes of black glass. The location of this area is indicated by the symbol F_4 on the E_1 map of Figure II-6. For additional views of the rippled surface, see Appendix A, Figure A-2.

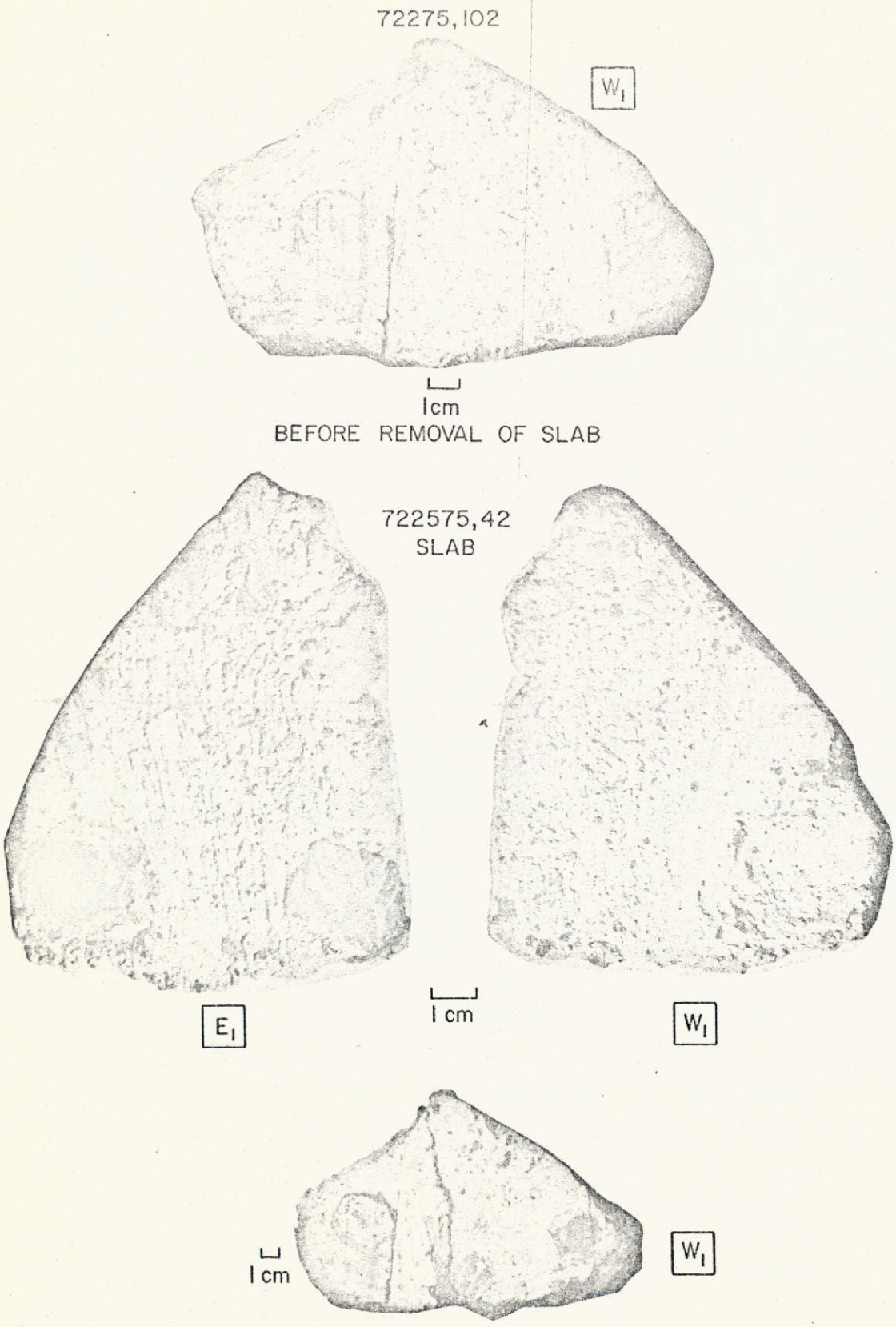

Figure II-8A. Photographs of the main mass, 72275, 102, and the slab, 72275, 42, after sawing was completed. Maps of these surfaces are shown in Figure II-9A.

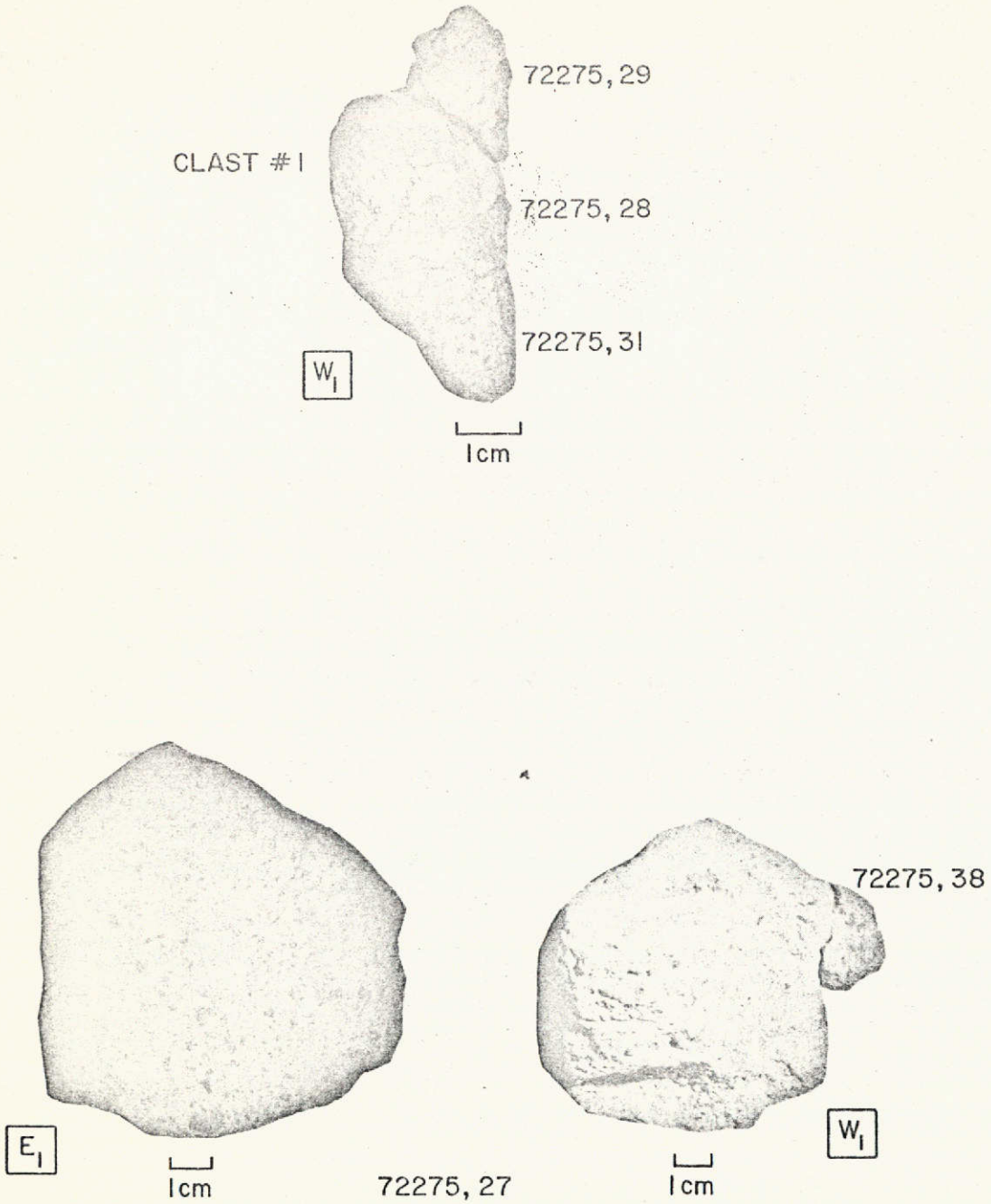

Figure II-8B. Photographs of clast #1, 72275, 28, and the east-end piece, 72275, 27, after sawing was completed. Maps of these surfaces are shown in Figure II-9B.

KEY TO SAMPLE LOCATIONS

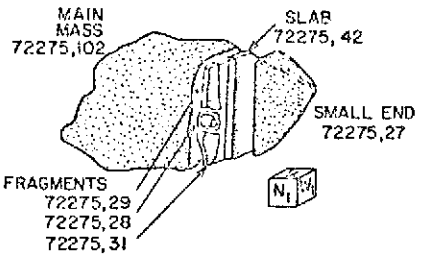

MAIN MASS 72275,102

BEFORE REMOVAL OF SLAB 72275, 42

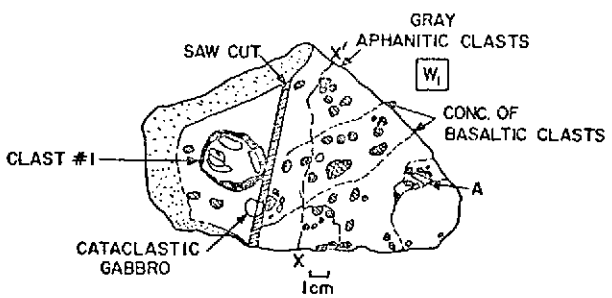

SLAB 72275, 42

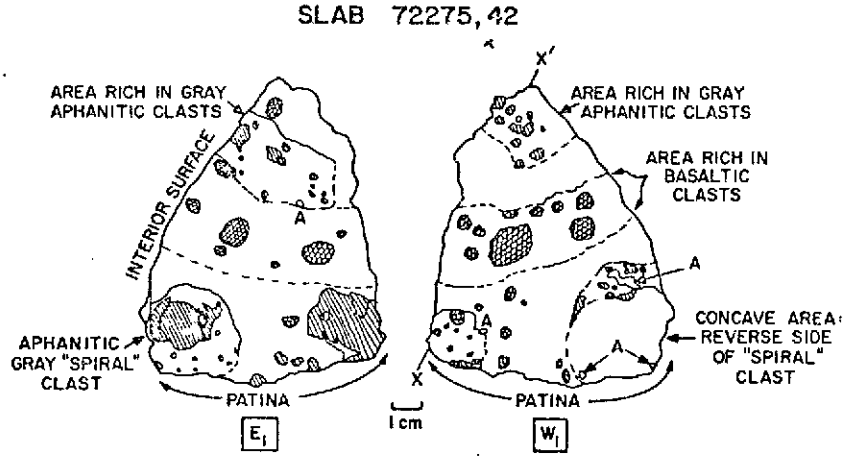

MAIN MASS 72275, 102

AFTER REMOVAL OF SLAB 72275, 42

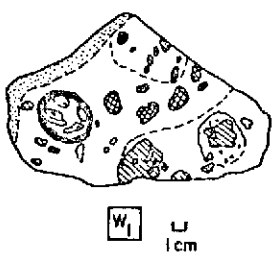

Figure II-9A. Maps of the sawed surfaces of the main mass, 72275, 102, and the slab, 72275, 42. See Figure II-8A for photographs of these surfaces.

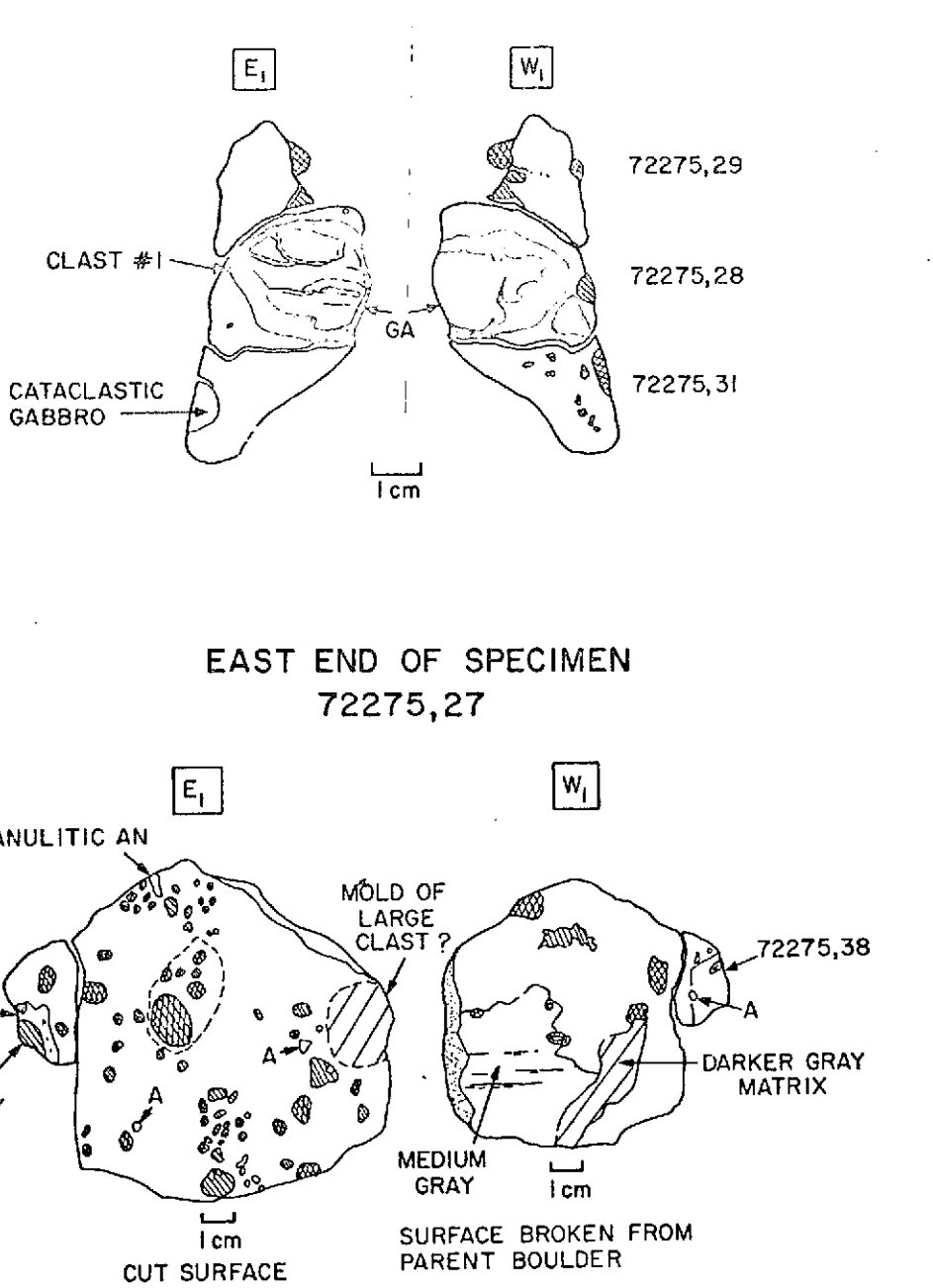

Figure II-9B. Surface maps of clast #1 and the east-end piece (see photographs in Figure II-8B).

C. Dark gray aphanitic clasts.

D. Basaltic clasts and zones.

The petrologic character of these materials, based on thin-section studies, will be described in Section III of this report. Their broad distribution through the specimen, as observed with the unaided eye and through a binocular microscope, is indicated in the maps of Figure II-9. The following observations were made during examination of the hand specimens.

A. Light gray matrix (areas unmarked by map symbol). The matrix appears to be a friable aggregate of mineral and lithic clasts ranging in size from a few microns to about 0.5 mm. The identifiable components are predominantly fragments of plagioclase admixed with a few percent of brown or yellow mafic silicates plus sparse grains of pink or amber spinel and metallic iron.

Some darker gray areas with indistinct boundaries occur within the matrix. These areas are somewhat finer grained and more strongly annealed than is the typical light gray matrix.

B. Anorthositic clasts. The most striking of these is clast #1, the conspicuous white clast with a black rim. Smaller white clasts, with and without thin rims, occur throughout the specimen. Those of mappable size are outlined and marked with an "A" on the figures. Clast #1 is not pure white; it contains 10 to 20% of yellow mafic silicates. Texturally, it appears to be a fluidized cataclastic breccia crudely interlayered with gray breccia and black rim material. The rim itself is a breccia of black aphanitic material containing distinct angular xenoliths of feldspar. The subdivisions of clast #1 are documented in Appendix A.

Some of the smaller white clasts appear to be sugary anorthosite with a granulitic texture.

C. Dark gray aphanitic clasts (oblique hatching on maps). Clasts #2 and #3 on the east face of the slab are of hard, resistant dark gray material, which we have described as aphanitic. The term simply means that the material is too structureless for an observer to tell macroscopically whether it is crystalline, glassy, or both.

However, clasts #2 and #3 do contain some small angular fragments and thin white streaks, indicating that they are annealed breccias. Smaller fragments of the same material are common throughout the specimen. Clast #2 (see Figures II-8 and II-9) has a swirled form and is embedded in an area rich in small angular fragments that appear to be broken from the main clast. This clast looks as though it has been crushed and rotated in situ.

D. Basaltic clasts and zones (cross hatching on maps). Numerous rounded basaltic clasts occur in this specimen. These clasts typically consist of white feldspar laths and yellow pyroxene. Among the more conspicuous of these are clast #4 on the west face and clast #5 on the east face of the slab. Clast #5 was removed in toto and subdivided as shown in Appendix A, Figure A-9. On close examination under the binocular microscope, the clasts appeared to be embedded within zones rich in fine-grained basaltic detritus. Thin-section studies have since confirmed that the basaltic clasts, which are rich in pigeonite, do indeed exist within a matrix of crushed basalt having only minor amounts of admixed gray matrix or gray clast material. The basaltic zones are difficult to delineate with any assurance on the hand specimens. The most visible ones are sketched on the maps of Figure II-9, but the actual amount of crushed basalt may be greater than is indicated.

A unique clast of coarse, chalky-white plagioclase and brown pyroxene occurs in fragment 72275, 31. On the maps of Figure II-9, it is labeled "cataclastic gabbro." That clast has not been distributed for study.

SPECIMEN 72255: SURFACE CHARACTERISTICS

This specimen was taken from a resistant bulge in the parent boulder at the site indicated in Figure II-1. Three views of the specimen are shown in Figure II-3.

Specimen 72255 differs from 72275 in three important respects:

A. 72255 is markedly less porous and more coherent than 72275.

B. Neither the freshly fractured surfaces of 72255 nor its sawed surfaces reveal any of the clasts or zones of crushed pigeonite basalt that were so conspicuous in 72275. However, two or three small brownish holocrystalline clasts, rich in mafic silicates, were observed on the T_1 surface (see C_1 in Figure II-10).

C. 72255 includes a unique, wedge-shaped clast with white-tabular-to-lenticular inclusions in a very dark brownish-gray matrix. It was dubbed the Civet Cat clast by Astronaut Schmitt. Detailed study has shown that the Civet Cat clast consists almost exclusively of anorthite and orthopyroxene, and although it has been shocked, it preserves the outlines of a coarse igneous texture. It is unlike any other lithic fragment described to date in the lunar samples. The petrology and Rb/Sr age of the clast are discussed in Sections III and VII.

Maps of the surface characteristics of 72255 are shown in Figure II-10. The cutting plans called for a single slab that would include part of the Civet Cat clast. The sawing, performed on July 26, 1973, was accomplished with comparative ease. Unlike 72275, this specimen is coherent enough for a slab to be cut without significant breakage or shedding of fines. The sawed surfaces of the boulder and the slab are illustrated in Figure II-11 and mapped in Figure II-12.

The maps in Figures II-10 and II-12 display four main lithologies:

A. The light gray matrix is similar in color to the matrix of 72275 but much more strongly annealed.

B. The anorthositic clasts are relatively small and rare. The largest, in the E_1 face of the slab, is about 9 mm across. Most of the clasts are pure white, sugary, granulitic anorthosite.

C. The dark gray aphanitic clasts are abundant, irregular in shape, and very coherent and appear to be similar in all respects to the material of clasts #2 and #3 in 72275. In addition to the clearly defined clasts, some regions of the matrix are intermediate in color and coherence compared to the dark aphanitic clast material and the light gray matrix (see Figure II-12).

D. The Civet Cat clast consists of a unique variety of lunar norite.

The composition and textures of these materials, as well as of the less common components of 72275 and 72255, are discussed in detail in Section III.

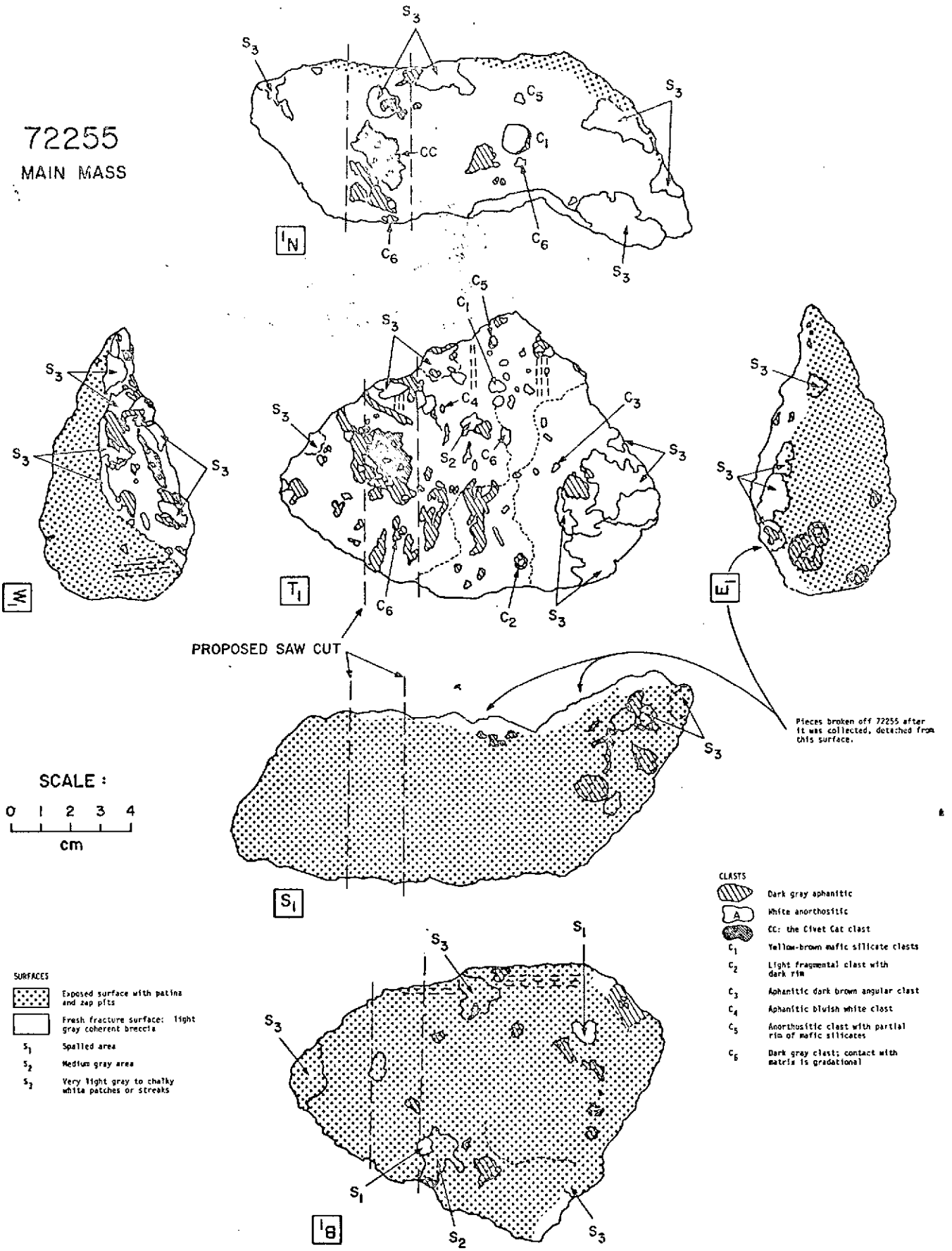

Figure II-10. Surface maps of specimen 72255. Two views of this specimen appear in Figure II-3.

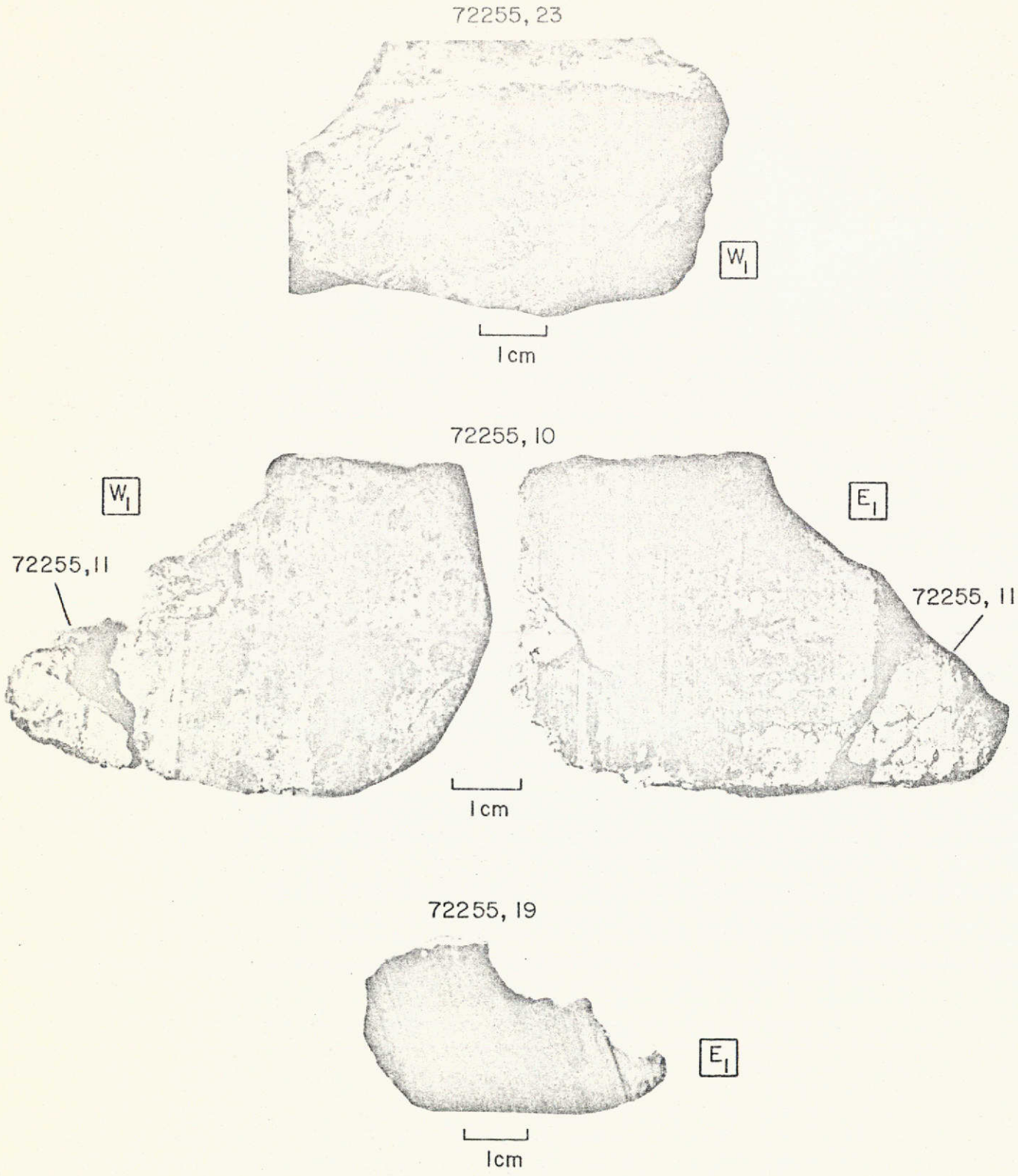

Figure II-11. Photographs of the sawed surfaces of specimen 72255, after removal of the slab. Maps of these surfaces are given in Figure II-12.

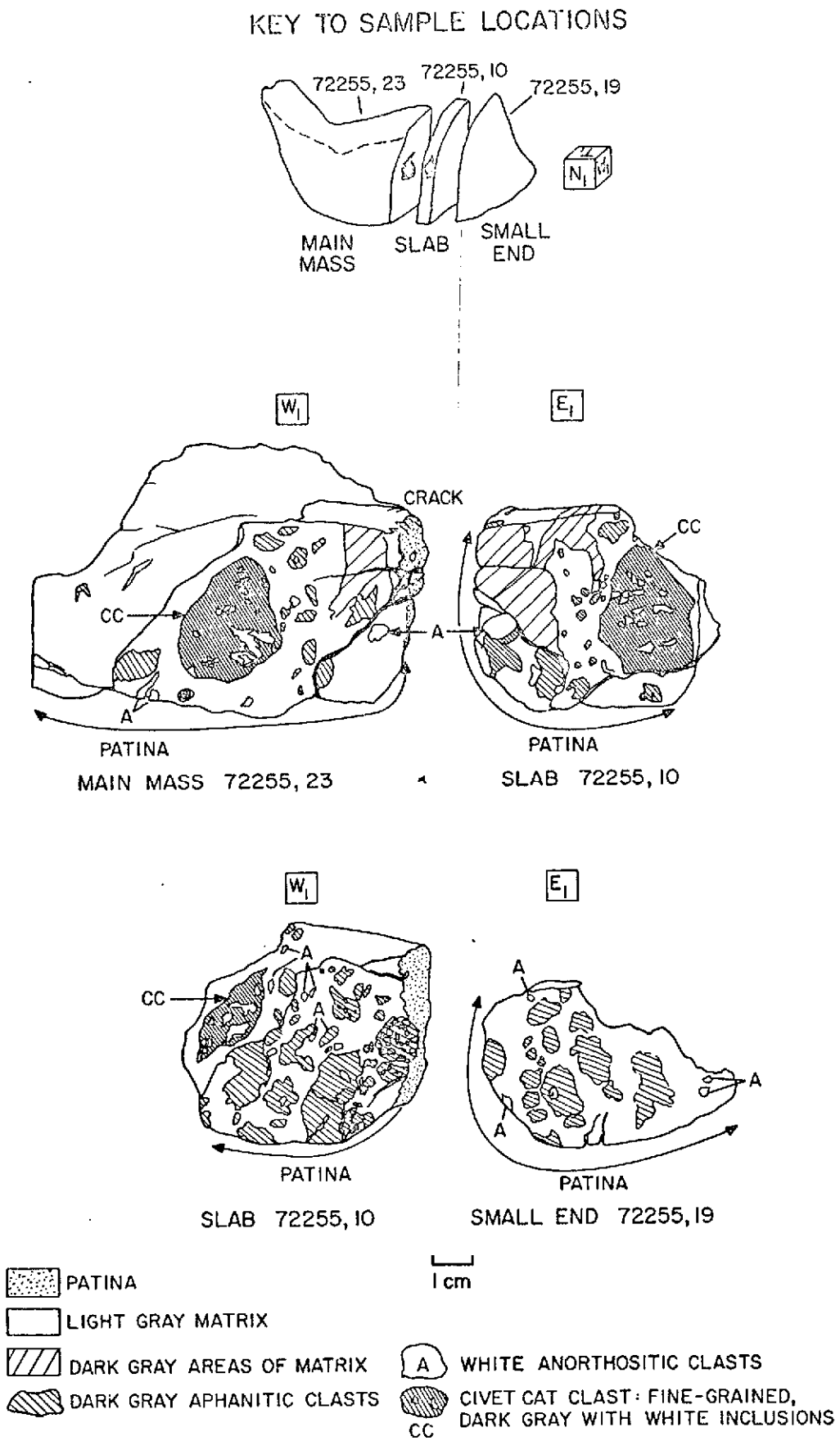

Figure II-12. Maps of the sawed surfaces of 72255. See Figure II-11 for photographs of these same surfaces.

III. PETROLOGY

D. B. Stoeser, R. W. Wolfe, J. A. Wood, and J. F. Bower

Center for Astrophysics
Harvard College Observatory and Smithsonian Astrophysical Observatory
Cambridge, Massachusetts 02138

INTRODUCTION

Boulder 1, Station 2 as a whole can be considered a complex polymict breccia consisting of lithic and breccia clasts seated in a matrix that ranges from friable and poorly sintered to densely welded. Only two of the four samples collected from Boulder 1, Station 2 have been examined in detail: 72255 and 72275. Of the remaining two, only two undocumented thin sections from 72235 have been studied, while none from 72215 has been examined. Sample 72275 was collected as representative of the boulder matrix, whereas the other three samples were thought to be large clasts.

SAMPLE DESCRIPTIONS

A. 72275

Sample 72275 contains two major, distinct types of lithologic domains: gray polymict breccia, and pigeonite basalt breccia (Figure III-1). The former is composed of a porous, poorly sintered light gray matrix, which contains lithic clasts of dark matrix breccia, granulitic ANT (anorthosite-norite-troctolite), anorthosite, troctolite, pigeonite basalt, and fine-grained granitic particles (in order of abundance). The clasts of dark matrix breccia are themselves polymict, containing lithic clasts of the granulitic ANT, anorthosite, and microgranite.

A point count of the 72275, 128 gray polymict breccia (Figure III-1B) produced the following mode:

Figure III-1. 72275 thin-section photographs.

A. 72275, 12: Typical gray polymict breccia. The lithic clasts consist largely of dark matrix breccias and ANT. Note the large anorthositic clast with the dark envelope at the right. Clasts of rimmed anorthosite are one of the distinctive features of Boulder 1.

B. 72275, 128: The 72275 breccia here consists of two very contrasting domains, a pigeonite basalt breccia above the arrows and a typical gray polymict breccia below. The contact between the two domains is relatively sharp, with a gradational transition zone a few millimeters wide. The white streak left of center in the gray polymict breccia is a disaggregated gabbroic anorthosite.

C. 72275, 135: Here, in contrast to 72275, 128, the relationship between the gray polymict breccia and the pigeonite basalt breccia is not distinct; rather, the two are intercalated in diffuse bands and stringers. The areas of the gray polymict breccia are marked by the dark matrix breccia and white ANT clasts. Note the large clast of pigeonite basalt at the bottom, just above the scale.

D. 72275, 122: Pigeonite basalt breccia. This rock, which is similar to the pigeonite basalt breccia domain of 72275, 128, is essentially a pure pigeonite basalt breccia, consisting of clasts of pigeonite basalt in a matrix of crushed pigeonite basalt. Two foreign clasts of granulitic ANT are present in the lower left corner.

72275

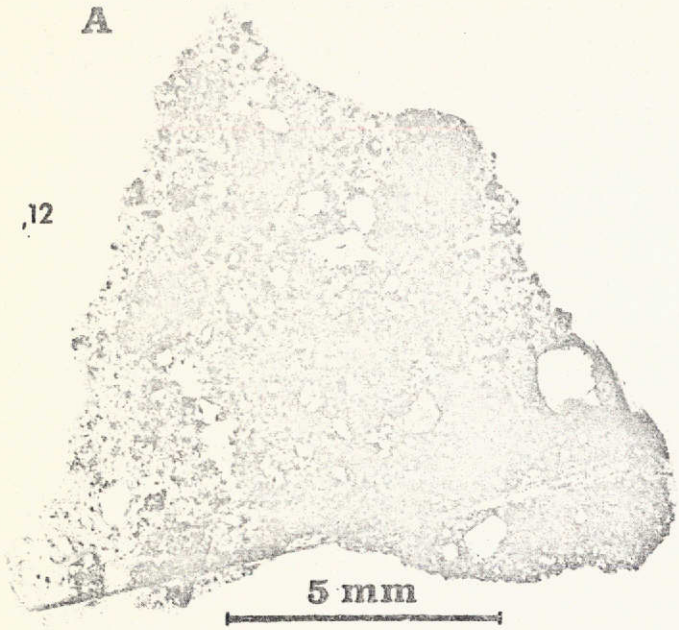

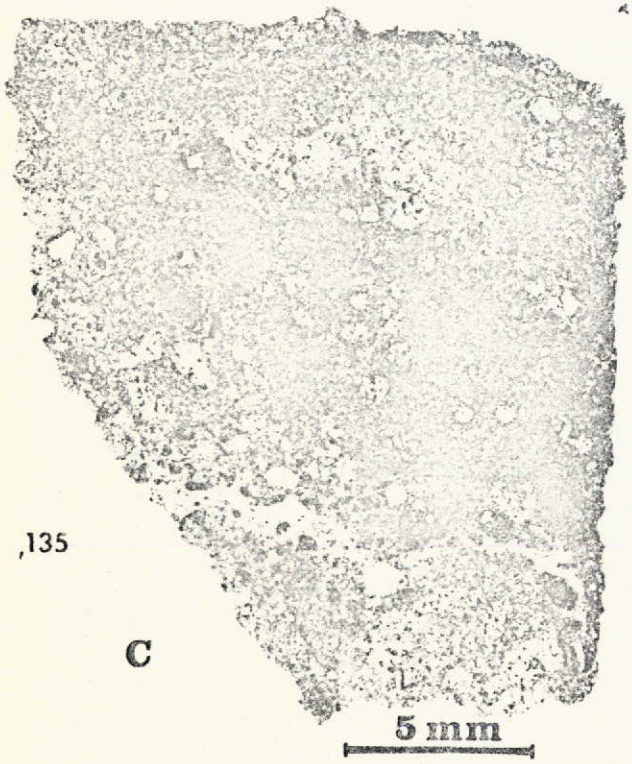

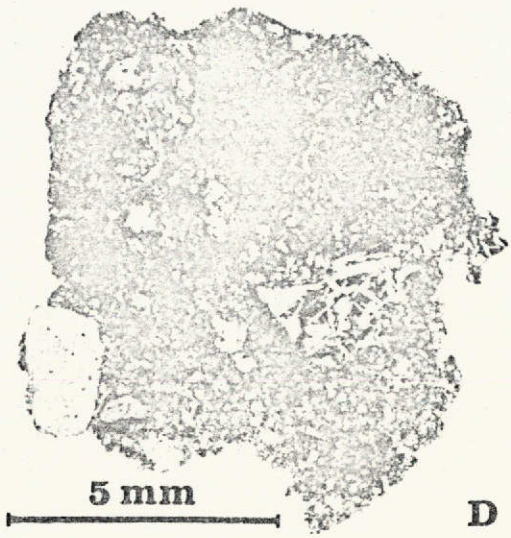

,122

Figure III-2. 72255 thin-section photographs.

A. 72255, 91:
72255, 93:
72255, 95:
Orthogonal thin-section set of typical 72255 breccia. Note the contrast in clast sizes and the dark color of the matrix compared to 72275. Whereas the 72275 matrix is porous and friable, that of 72255 is very welded with low porosity. The bulk of the large clasts visible are monomineralic plagioclase, mafic silicates, granulitic ANT, and anorthosites.

B. 72255, 97:
C. 72255, 99:
D. 72255, 107:
It can be seen from these photographs that 72255 is quite uniform throughout. One notable difference between 72255 and 72275 is the apparent lack of dark matrix breccia clasts, but this may be largely a function of contrast. 72255, 107 appears to have such clasts. The large white clasts in 72255, 99 and 107 are granulitic ANT clasts.

A

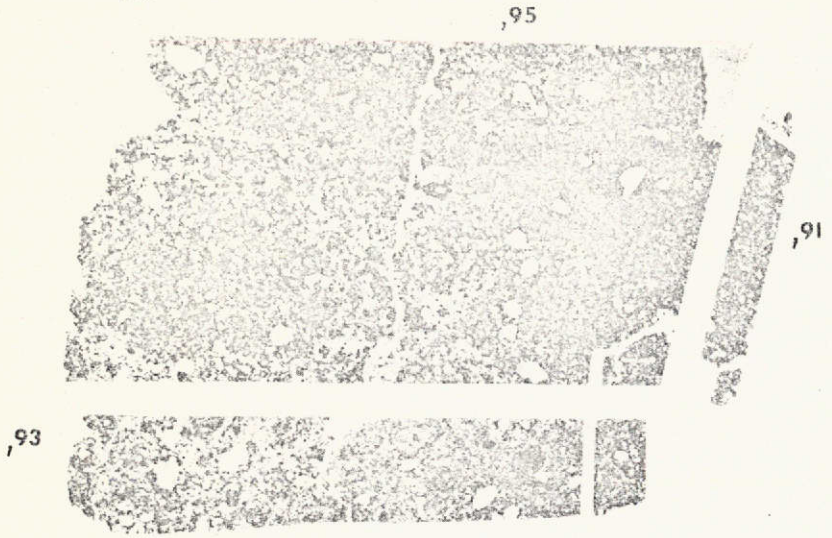

5 mm

B

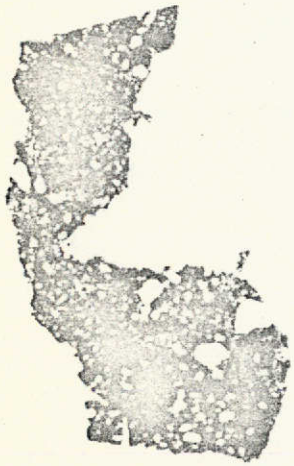

C

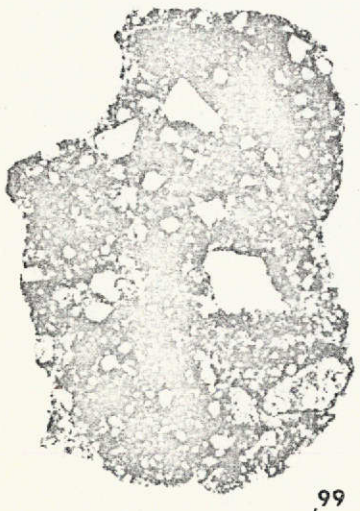

D

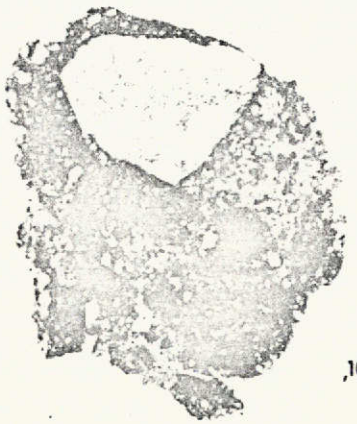

2 mm

III-2

Material	%
Matrix	65.0
Monomineralic clasts >100 μ	2.2
Dark matrix breccia clasts	27.7
Granulitic ANT and anorthosite clasts	4.1
Troctolite clasts	0.6
Pigeonite basalt clasts	0.4
Glass shards	trace
Granitic clasts	trace

The pigeonite basalt breccias consist of clasts of pigeonite basalts seated in a matrix of finely granulated pigeonite basalt (Figure III-1B, C, and D). A small amount of granulitic ANT, anorthosite, and dark matrix breccia clasts are generally present. The pigeonite basalt breccias occur as clots and bands up to 2 cm thick within the gray polymict breccia (Figure II-9). The contact between the two types of breccias may be sharp (Figure III-1B), or the two breccias may be intermixed as stringers, one within the other (Figure III-1C).

B. 72255

Sample 72255 differs markedly from 72275 in having a dark dense matrix with little porosity and in lacking domains of pigeonite basalt breccia (Figure III-2). The lithic clast population of 72255, however, is similar to that of 72275 except for the absence of the pigeonite basalt. Dark matrix breccia clasts appear to be present, but they have low contrast against the dense dark matrix of 72255 (Figure III-2). A survey of lithic clasts greater than 200 μ in diameter in thin section 72255, 95 (Figure III-2A) produced the following:

Material	%
Granulitic ANT	48.7
Anorthosite	19.2
Devitrified glass	20.0
Troctolite	4.3
"Basalt"	0.9
Granitic clasts	4.3
Ultramafic particles	1.7
Plutonic norite	0.9
	100.0
Number of clasts surveyed	118

C. 72235

Sample 72235 consists mainly of a single, large complex clast with an aphanitic rind, which appears at least superficially to be similar to that of the gabbroic anorthosite clast #1, 72275 (Figures II-8 and II-9). At present, we have only two undocumented thin sections from 72235; these came not from the large clast, but from the small amount of light gray breccia matrix material adhering to it. There does not appear to be any significant difference between the 72235 breccia and the gray polymict breccia domains of 72275, although no pigeonite basalt clasts were observed.

LITHIC CLASTS

The lithic clasts of the two samples 72275 and 72255 are essentially the same, except for the pigeonite basalts (which occur only in 72275). In general, the lithic clasts fit within the following classification scheme:

A. ANT.
B. Devitrified glasses.
C. Troctolites.
D. Pigeonite basalt clasts and breccias.
E. Granitic clasts.
F. Ultramafic particles.
G. Plutonic norite (Civet Cat clast).
H. Dark matrix breccias.

Descriptions of each follow.

A. ANT

The acronym ANT is used here to describe generally plagioclase-rich, potash, and phosphorus-poor rocks whose mineralogy varies over the range anorthosite-norite-troctolite. These rocks have a variety of metamorphic textures, including recrystallized (granulitic) breccias and cataclasites. Similar rocks have been found in soils and breccias from Apollo 11, 15, and 16, as well as from Luna 16 and 20 (Keil et al., 1972; Delano et al., 1973; Prinz et al., 1973a; Taylor et al., 1973).

The ANT suite of clasts forms the dominant crystalline lithic clast group in the boulder samples. In this section, the suite will be discussed under the following subheadings: granulitic ANT, poikiloblastic norites, other anorthosites, and a special dark-rimmed gabbroic anorthosite (clast #1, 72275). In a study of the lithic clast population of thin section 72255, 95, the relative proportions of the first three categories were 68:4:28 (78 clasts counted, >200 μ in diameter).

Granulitic ANT

This abundant group of clasts is composed primarily of monomict breccias with recrystallization textures. They exhibit a range of textures, from obvious breccias with finely recrystallized matrices (Figures III-3A and B) to rocks that are much coarser and approach equigranular (Figure III-3C). In these coarser varieties, the olivines tend to occur as rounded, small inclusions in the plagioclase, whereas the pyroxenes tend to be interstitial and some border on poikiloblastic. Spinel, ilmenite, phosphates, and zircon occur as minor phases.

Preliminary whole-rock analytical work indicates that more of the granulitic ANT rocks are troctolitic than are noritic. This conclusion is also supported by microprobe mafic-mineral surveys, which indicate a greater abundance of olivine than pyroxene. The compositional range of olivine is Fo_{64-85} (Figure III-4). The pyroxenes generally fall in the compositional fields established for ANT from other lunar samples (Figure III-5A) (Taylor et al., 1973). Most of the ANT plagioclases have compositions in the range An_{92-98} (Figure III-6). Whole-rock analyses of typical granulitic ANT clasts are presented in Table III-1, analyses 1 to 3, and granulitic ANT analytical data are presented in Figures III-22 and III-23 (pp. 96 and 97).

A distinctive type of granulitic ANT is a "vesicular" mafic-rich granulitic troctolite (Figure III-3D). These rocks, which are also recrystallized breccias, have euhedral mafic silicates in a matrix of subpoikiloblastic plagioclase. An analysis of one of these vesicular troctolites is presented in Table III-1, analysis 5.

Poikiloblastic norites

This relatively rare, but distinctive, lithology consists of small plagioclase crystals enclosed by poikiloblastic orthopyroxene (Figure III-3E). The largest clast

Table III-1. Lithic ANT clasts.

	1 763C20	2 770C7	3 770C12	4 770C24	5 770C27	6 770C26	7 770C37	8 72275, 12
SiO_2	44.2	43.9	46.2	51.1	44.3	44.9	42.8	42.7
TiO_2	0.1	0.1	0.1	0.3	0.2	0.1	0.1	tr.
Cr_2O_3	0.1	0.0	0.0	tr.	tr.	0.1	tr.	tr.
Al_2O_3	29.4	25.8	32.2	20.6	23.8	33.9	35.3	34.9
FeO	3.7	4.1	2.4	6.3	6.4	0.8	0.2	0.2
MnO	tr.	0.1	tr.	0.1	0.1	tr.	tr.	–
MgO	7.8	5.7	1.0	7.9	11.6	0.8	tr.	0.1
CaO	15.9	15.8	17.5	12.2	13.6	19.3	19.4	19.1
Na_2O	0.2	0.4	0.6	0.4	0.3	0.4	0.3	0.7
K_2O	0.1	0.1	0.1	0.2	0.1	0.1	0.1	0.1
P_2O_5	tr.	tr.	tr.	tr.	tr.	tr.	tr.	0.2
BaO	–	tr.	tr.	0.1	0.1	0.1	0.1	–
Total	101.5	96.0	100.1	99.2	100.5	100.5	98.3	98.0
Fo	11.2	4.0	0.0	0.0	15.1	0.0	0.0	0.2
Fa	4.3	2.3	0.0	0.0	6.7	0.0	0.1	0.2
En	3.1	9.1	2.5	19.8	7.2	2.0	0.0	0.0
Fs	1.1	4.8	4.4	11.3	2.9	1.3	0.0	0.0
Wo	0.0	4.3	0.9	2.7	1.6	2.0	1.4	4.4
Or	0.6	0.7	0.3	0.9	0.6	0.8	0.4	0.7
Ab	1.9	3.3	5.2	3.3	2.2	3.0	2.6	5.6
An	77.5	71.3	84.6	54.5	63.3	90.3	94.3	85.2
Ilm	0.1	0.1	0.1	0.7	0.3	0.2	0.2	0.1
Chr	0.1	0.0	0.0	0.0	0.0	0.1	0.0	0.0
Qtz	0.0	0.0	1.8	6.8	0.0	0.3	0.0	0.0
Cor	0.1	0.0	0.0	0.0	0.0	0.0	0.8	3.2
Ap	0.0	0.0	0.0	0.1	0.1	0.0	0.1	0.4

Key:

1. 72275, 128: clast #763C20, granulitic ANT (average of 2 600 μ × 100 μ DBA traverses; Figure III-3A).
2. 72255, 95: clast #770C7, granulitic ANT (average of 6 100 μ diam. DBAs).
3. 72255, 95: clast #770C12, granulitic ANT (average of 13 100 μ diam. DBAs).
4. 72255, 95: clast #770C24 poikilitic norite (average of 7 100 μ diam. DBAs; Figure III-3E).
5. 72255, 95: clast #770C27, "vesicular" mafic-rich ANT troctolite (average of 27 100 μ diam. DBAs; Figure III-3D).
6. 72255, 95: clast #770C26, anorthosite breccia (average of 16 100 μ diam. DBAs; Figure III-7A).
7. 72255, 95: clast #770C37, fine-grained polygonal anorthosite (average of 16 100 μ diam. DBAs; Figure III-7B).
8. 72275, 12: shocked anorthosite (average of 23 100 μ diam. DBAs; Figure III-16A, B).

Figure III-3. Granulitic ANT.

A. 72255, 95:
B. 72255, 95:
C. 72275, 12:

Granulitic ANT clasts. The granulitic ANT suite appears to show a complete transition from fine breccias, which have only a minor amount of recrystallization (Figure A), to relatively coarse, completely recrystallized varieties with large equigranular plagioclase, which include small olivines and pyroxenes (Figure C). (Figure C is with crossed nicols.)

D. 72255, 95:

"Vesicular" mafic-rich ANT (troctolite). This rock type is clearly part of the granulitic ANT suite, being a recrystallized breccia of troctolitic composition. It is distinct in having moderately abundant pores, or "vesicles," and a matrix that consists of small euhedral olivines in a groundmass of plagioclase. An analysis of this particular sample is presented in Table III-1, analysis 4.

E. 72255, 95:

Poikiloblastic ANT. Clasts of granulitic ANT, which consist of individual plagioclase crystals set in poikiloblastic orthopyroxene, are rare. The bulk of the mafic mineral present in this clast (the largest observed) is a single pyroxene. An analysis of this particular sample is presented in Table III-1, analysis 5.

A

B

C

D

E

45

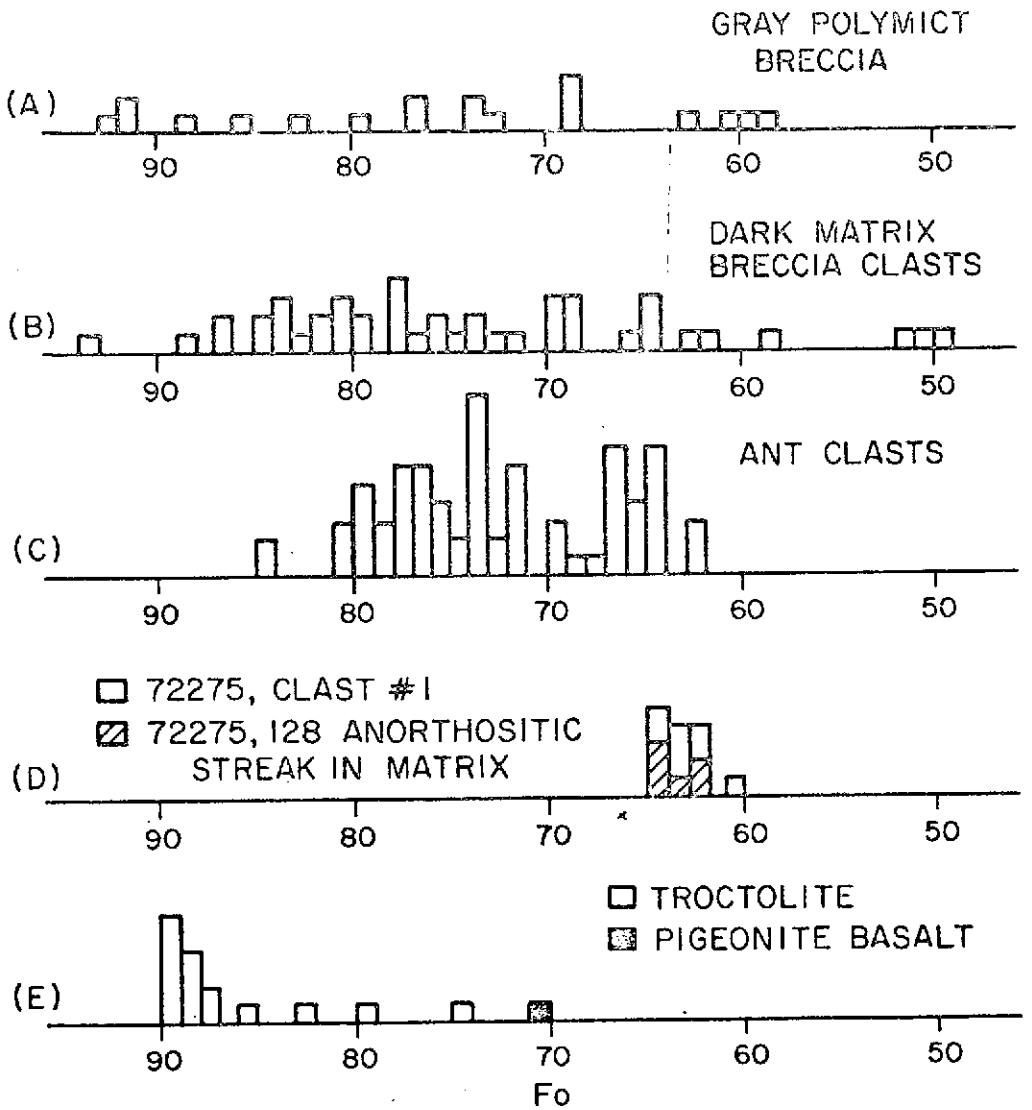

Figure III-4. Olivine histograms. A: Monomineralic olivine clasts in the polymict gray breccia matrix of 72275, 12. B: Monomineralic olivine clasts in dark matrix breccia clasts of 72275, 128, 134, and 135. C: Olivines from granulitic ANT clasts from 72275, 122 and 128 and 72235, 7 and 9. D: Monomineralic olivines from the anorthositic portions of clast #1, 72275, 140 and a similar white anorthositic streak in the gray polymict breccia matrix of 72275, 128. E: Olivines from clasts of troctolite and a pigeonite basalt from 72275, 128. Only one olivine grain has been observed in the pigeonite basalts.

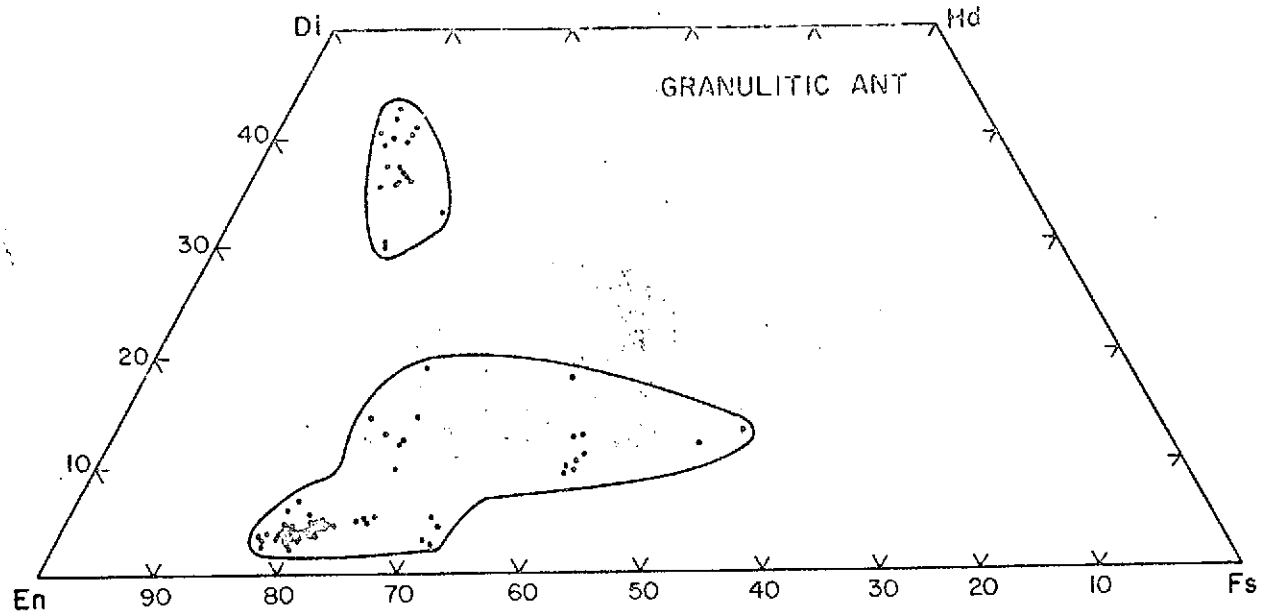

Figure III-5A. Three-element (Mg/Fe/Ca) electron-microprobe survey of pyroxenes in 10 granulitic ANT clasts (recrystallized ANT breccias) in thin section 72275, 128. Note the strong convergence of orthopyroxene at approximately En_{76-81}. Fourteen more analytical points fall in that cluster but were not plotted, because of the density of points already on the diagram.

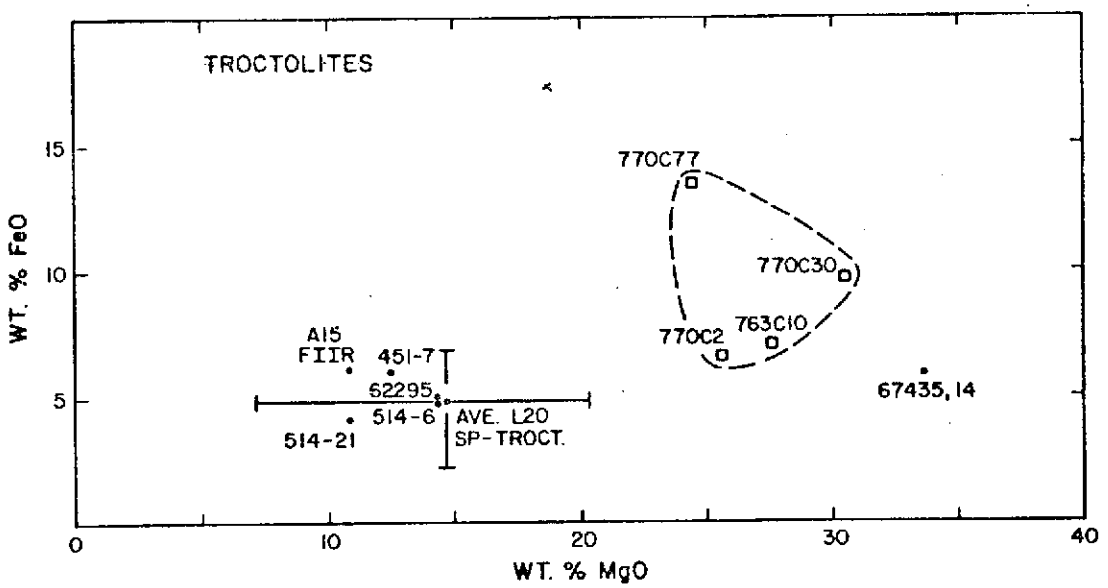

Figure III-5B. FeO versus MgO diagram for the Boulder 1 troctolites (open squares). Sources for other data (solid circles with sample numbers): 451-7, 514-6, and 514-21: Apollo 15 spinel troctolites (Reid, 1972); A15 FIIR: average Apollo 15 feldspathic intersertal igneous rocks (Delano et al., 1973); Ave. L20 sp-troct.: average Luna 20 spinel troctolite (Prinz et al., 1973a); and 67435, 14: Apollo 16 spinel troctolite (spinel-olivine cumulate) (Prinz et al., 1973b); 62295: spinel troctolite (Hodges and Kushiro, 1973). The bars on the Luna 20 plot give the range for individual samples.

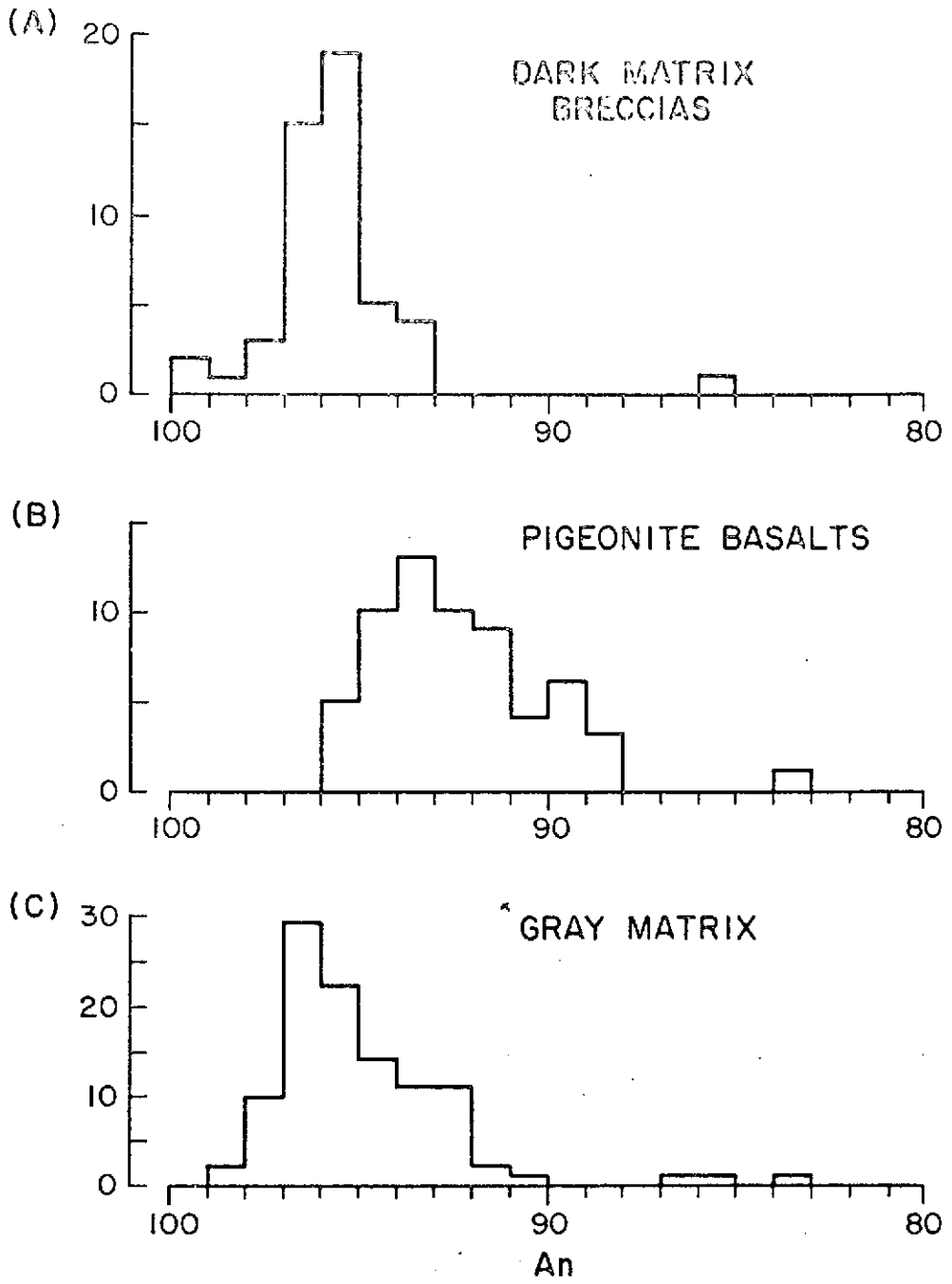

Figure III-6. Plagioclase histograms. A: Plagioclases from monomineralic and lithic clasts in the dark matrix breccia clasts of 72275, 134 and 135. B: Plagioclases from pigeonite basalt clasts and monomineralic clasts of the pigeonite basalt breccia matrix of 72275, 122 and 147. C: Plagioclase monomineralic clasts in the gray polymict breccia matrix of 72275, 12.

of this rock type is only about 200 μ in diameter, and its analysis is not felt to be necessarily representative (Table III-1, analysis 4). Mineralogic studies of these clasts remain to be done.

Other anorthosites

Besides plagioclase-rich members of the granulitic ANT group, three other types of lithic clasts have anorthosite compositions: 1) anorthosite breccias (Figure III-7A), 2) fine-grained polygonal anorthosite (Figure III-7B), and 3) devitrified maskylenite and anorthositic glasses (Figure III-7C and D). The third group will be discussed in Section B.

The first type forms a distinct group of clasts in both 72275 and 72255. They consist of abundant angular plagioclase set in an annealed matrix and appear to be a coarse-grained anorthosite that has been crushed, but with little or no recrystallization. Mafic minerals are rare and are confined to the matrix. This group comprises 7% of the total lithic clast population (>200 μ) of thin section 72255, 95. An analysis of a typical anorthosite breccia of this type is presented in Table III-1 (analysis 6).

The fine-grained polygonal anorthosite particles appear to be recrystallization products of larger plagioclases. They constitute 12% of the lithic clast suite of thin section 72255, 95. They are essentially pure feldspar and have an average composition of $An_{96.2}Or_{0.6}Ab_{3.2}$ and an unusual MgO/(MgO + FeO) ratio of about 0.1.

Clast #1, 72275; gabbroic anorthosite

This clast is set apart both because of its wide distribution among the consortium and because of its distinctive structures and composition. The designation, clast #1, is derived from the sawed slab mapping of Marvin (Section II).

This large clast, with a diameter of 3 cm, consists of a light-colored core with a dense envelope of dark matrix breccia material (Figures II-8, II-9, and III-8A, B). A similar (?) clast also appears to constitute the bulk of the 72235 sample (Figure II-5). Currently, we have only two serial sections, taken from the margin of the clast, and have nothing from either the core or the pure rind. The two sections are essentially

Figure III-7. Anorthosites and devitrified maskylenites.

A. 72255, 95: Anorthosite breccia. This distinct type of clast, though sparse, is widely distributed throughout the 72275 and 72255 samples. The texture is that of a coarse-grained anorthosite that has been crushed and annealed without significant recrystallization. (Plain light.)

B. 72255, 95: Polygonal fine-grained anorthosite. These clasts apparently are the result of recrystallization of large plagioclases; usually no mafic phase is present. (Slightly crossed nicols.)

C. 72275, 146: Devitrified maskylenite glass. (Both crossed nicols.)
D. 72255, 95:

A

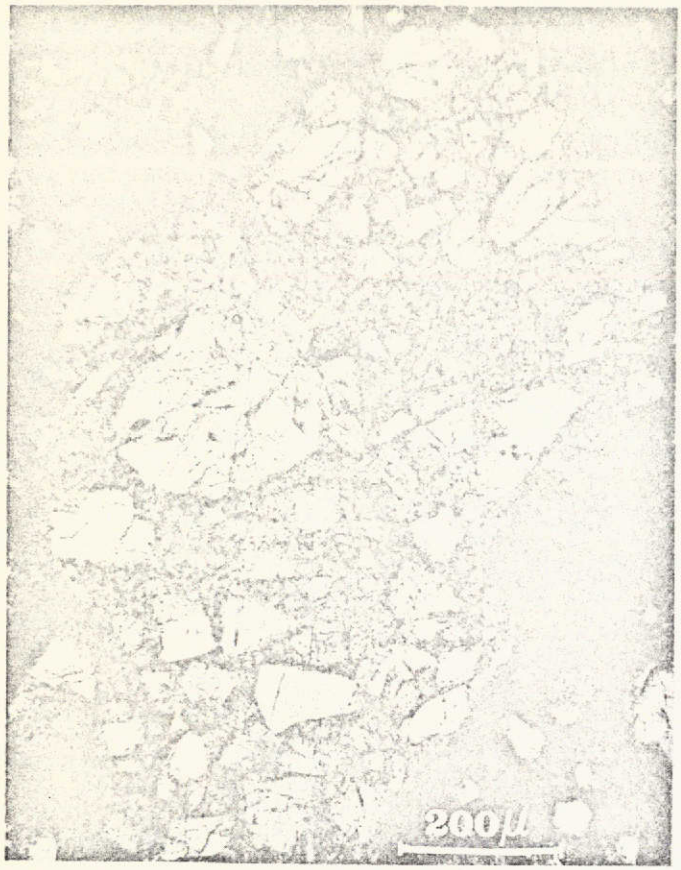

B

C

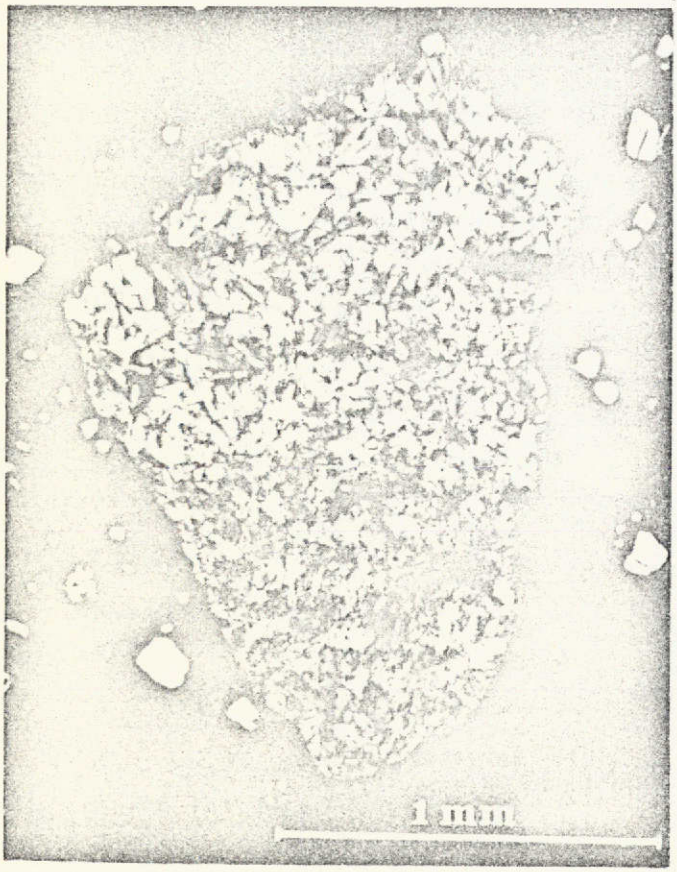

D

Figure III-8. 72275, clasts #1 and #2, ultramafic particle.

A. 72275, 140: Clast #1, 72275 (Figures II-8 and II-9). Thin section of a marginal portion of clast #1, a large dark-rimmed gabbroic anorthosite. The material seen here consists of intercalated crushed gabbroic anorthosite and a dark matrix breccia. It seems probable that the two must have been mixed before ejection at the impact site. Analyses of both types of rock are given in Tables III-2 (analysis 4) and III-6 (analysis 9).

B. 72275, 140: Enlargement of center region of A.

C. 72275, 146: Clast #2 (Figures II-8 and II-9), dark matrix breccia. The large white clast is devitrified maskylenite (Figure III-7C). An analysis of this clast is given in Table III-6, analysis 8.

D. 72255, 95: Ultramafic particle (microdunite). The source rock of these granular olivine particles is not known.

A

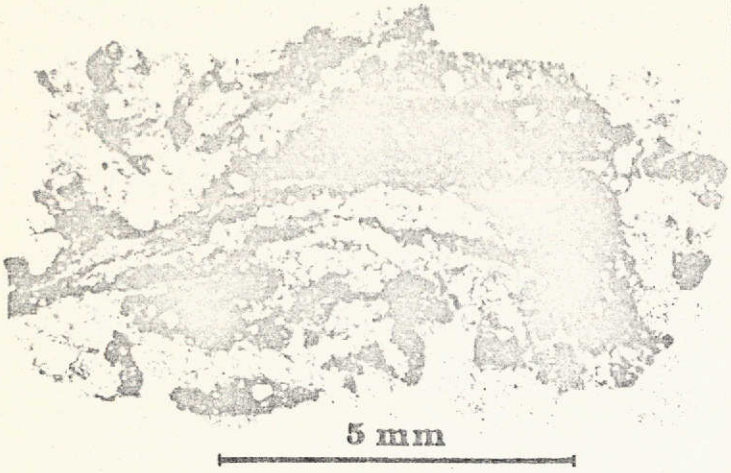

72275, 140

B

C

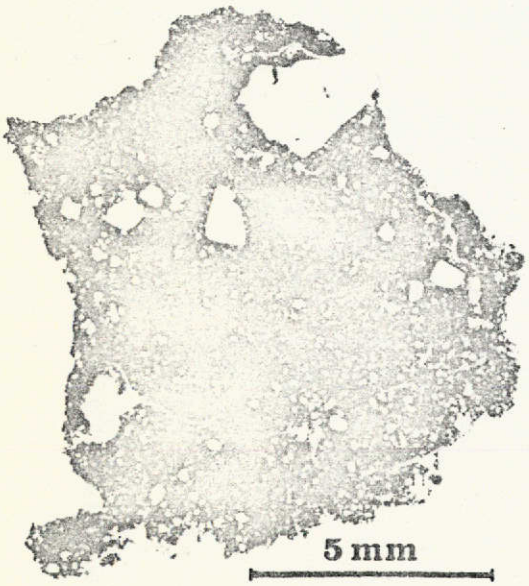

,146

D

identical, consisting of intimately intercalated bands and lenses of a porous, crushed gabbroic anorthosite breccia and a dense dark matrix breccia; the latter breccia will be described in Section H. It is clear that the anorthosite constitutes the core material of the clast, and the dark matrix breccia, the rind. The intermixing of these two materials is essentially like the one that would be produced if two essentially immiscible fluids were mixed together by a moderate amount of stirring.

The anorthositic bands have the appearance of a single rock type that has been crushed to a relatively fine breccia. This rock appears to have been a gabbroic olivine-pyroxene anorthosite composed of 85% moderately shocked plagioclase and 15% mafic silicates (olivine, Fo_{60-64}; orthopyroxene, $En_{60.5}Wo_3Fs_{36.5}$; and augite, $En_{40}Wo_{45}Fs_{15}$). The relative proportions of the mafic silicates are not known, but olivine appears to be the most abundant. The minimum measured diameters for each silicate mineral are plagioclase 1 mm, olivine 150 μ, orthopyroxene 250 μ, and augite not known. Deep red-brown spinels up to 80 μ in diameter are also present, but they constitute less than 1% of the anorthositic gabbro. Traces of fine ilmenite and sulfide have also been observed.

Residual lithic fragments in the anorthositic bands suggest that the parent rock had a texture consisting of polygonal interlocking plagioclase in which many of the mafic silicates occur as smaller inclusions. This texture, as well as the composition of the orthopyroxene, suggests a metamorphic rock, since pigeonite would be expected if it were an igneous rock. The composition of the whole rock (Table III-2, analysis 4), as well as of the mafic silicate minerals, indicates a distinctly higher Fe/Mg ratio than those of the granulitic ANT rocks (Figure III-22).

B. Devitrified Glasses

All the glasses in the boulder samples are devitrified, with the possible exception of a few small brown glass shards in the 72275 gray polymict breccia. The glasses are of two types, maskylenite and thermal melts. The survey of thin section 72255,95 showed that 20% of the lithic clasts (>200 μ) were devitrified glasses, of which three-quarters were maskylenite (Figure III-7C and D). At least some of the maskylenites were fluid at the time of deposition because a few are tear-drop or dumbbell shaped. The glasses that appear to be thermal melts are distinguishable from the colorless-to-pale-brown maskylenites in having a distinct, often deep, red-brown color (Figure III-9B and C).

Table III-2. Devitrified glasses and clast #1, gabbroic anorthosite.

	1 770C10 devitrified glass	2 770C39 devitrified glass	3 770C83 devitrified maskylenite	4 72275, 140 anorthosite domains	5 72275, 140 KREEP-rich area
SiO_2	44.0	42.4	44.8	43.5	46.4
TiO_2	0.2	0.3	0.1	0.1	1.3
Cr_2O_3	0.1	tr.	tr.	tr.	0.2
Al_2O_3	25.3	31.6	32.8	34.6	20.8
FeO	5.0	3.7	0.7	1.8	8.0
MnO	0.1	0.1	0.1	tr.	0.1
MgO	12.0	0.7	0.4	1.0	4.3
CaO	13.9	17.1	18.4	18.4	14.9
Na_2O	0.4	0.3	0.5	0.3	0.4
K_2O	0.1	tr.	0.1	0.1	1.0
P_2O_5	0.1	tr.	0.2	0.1	3.1
BaO	0.1	0.1	—	tr.	0.1
Total	101.3	96.3	98.1	99.9	100.1
Fo	19.2	0.1	0.0	0.9	0.0
Fa	6.3	0.5	0.0	1.3	0.0
En	2.1	1.6	1.0	1.2	10.7
Fs	0.6	1.1	1.2	1.5	12.6
Wo	0.7	0.0	1.7	0.0	0.0
Or	0.8	0.2	0.5	0.6	5.9
Ab	3.5	2.8	4.0	2.5	3.4
An	66.0	88.0	89.2	90.8	51.3
Ilm	0.6	0.2	0.2	0.2	2.5
Chr	0.2	0.1	0.0	0.0	0.3
Qtz	0.0	0.0	2.1	0.0	6.0
Cor	0.0	0.0	0.0	0.8	0.3
Ap	0.2	0.1	0.0	0.2	7.1

Key:

1. 72255, 95: clast #770C10, devitrified brown glass (Figure III-9B) (average of 11 100 μ diam. DBAs).
2. 72255, 95: clast #770C39, devitrified brown glass (Figure III-9C) (average of 3 100 μ diam. DBAs).
3. 72255, 95: clast #770C83, devitrified maskylenite (average of 4 100 μ diam. DBAs).
4. 72275, 140: clast #1, gabbroic anorthosite domains (Figure III-8A, B) (average of 18 100 μ diam. DBAs).
5. 72275, 140: clast #1, KREEP-rich domain (see text, Section H) (average of 3 100 μ diam. DBAs).

Figure III-9. Troctolites and devitrified glasses.

A. 72255, 95: Civet Cat-type plagioclase. Monomineralic clasts of plagioclase that have been heavily shocked and closely resemble those found in the Civet Cat clast (Figure III-15) are common throughout the 72275 and 72255 samples. They typically have distinct re-equilibration rims, even though nearby unshocked plagioclase clasts have none. (Crossed nicols.)

B. 72255, 95: Devitrified glass (DG). Both clasts are deep red-brown in color.
C. 72255, 95: In C, the white clasts are maskylenites (M). Analyses of the two devitrified glasses of B and C are given in Table III-2 (analyses 1 and 2). (Both plain light.)

D. 72255, 95: Troctolite. This clast is essentially bimineralic with euhedral to anhedral olivines (OL) set in a groundmass of subpoikilitic plagioclase (PL) (Table III-3, analysis 2). (Plain light.)

E. 72275, 128: Cataclastic troctolite. E is very similar to the troctolite shown in
F. 72275, 95: D except that it has been cataclasized. The olivine grain marked OL in E can be seen to be euhedral in crossed nicols (Table III-3, analyses 1 and 3). (Both plain light.)

A
B
C
M
D
OL
PL
E
OL
F
OL

Table III-3. Troctolite group.

	1	2	3	4	5	6	7	8
	763C10	770C2	770C30	770C77	A15 FIIR	62295, 48	67435, 14	Average Luna 20 sp-troct.
SiO_2	42.2	42.3	42.5	41.2	45.2	45.3	37.5	43.7
TiO_2	0.2	0.3	0.2	0.4	0.8	0.8	0.05	0.17
Cr_2O_3	0.1	0.3	0.1	0.0	0.2	0.2	0.49	0.11
Al_2O_3	14.6	16.3	9.8	12.5	24.4	20.8	15.9	22.7
FeO	7.0	6.5	9.7	13.3	6.1	5.99	5.8	4.9
MnO	0.1	0.1	0.1	0.2	0.1	–	0.16	0.07
MgO	27.6	25.6	30.5	24.4	10.8	14.4	33.7	14.7
CaO	7.4	8.7	6.3	7.1	12.7	11.5	6.2	13.1
Na_2O	0.2	0.3	0.3	0.2	0.5	0.4	0.14	0.39
K_2O	0.1	0.1	0.1	0.1	0.2	0.14	0.04	0.05
P_2O_5	0.01	0.2	0.1	0.1	–	–	0.02	0.04
BaO	–	0.1	0.1	0.0	–	–	–	
Total	99.5	100.8	99.8	99.5	101.0	99.5	100.0	99.93
Fo	44.7	44.1	50.0	40.5	11.5	14.8	58.9	23.2
Fa	9.1	8.8	12.8	17.7	4.7	4.3	8.1	6.1
En	5.4	0.5	4.9	3.5	10.2	15.0	0.0	3.6
Fs	1.0	0.1	1.2	1.4	3.7	4.0	0.0	0.9
Wo	0.0	0.0	2.2	0.6	0.0	1.0	8.2	2.0
Or	0.3	0.5	0.4	0.3	1.2	0.8	0.2	0.3
Ab	1.4	2.7	2.4	1.8	4.2	3.4	1.2	3.3
An	36.8	41.9	25.4	33.3	62.4	54.9	10.9	60.2
Ilm	0.3	0.5	0.4	0.7	1.5	1.5	0.1	0.3
Chr	0.1	0.4	0.1	0.0	0.3	0.0	0.7	0.2
Qtz	0.0	0.0	0.0	0.0	0.0	0.0	0.0	0.0
Cor	0.9	0.3	0.0	0.0	0.3	0.0	11.7	0.0
Ap	0.0	0.3	0.2	0.2	0.0	0.0	0.0	0.1

Key:

1. 72275, 128: clast #763C10, troctolite (average of 4 600 μ × 100 μ DBA traverses, Figure III-9E).
2. 72255, 95: clast #770C2, troctolite (average of 16 100 μ diam. DBAs, Figure III-9D).
3. 72255, 95: clast #770C30, cataclastic troctolite (average of 10 100 μ diam. DBAs, Figure III-9F.
4. 72255, 95: clast #770C77, cataclastic troctolite (average of 7 100 μ diam. DBAs).
5. Apollo 15: feldspathic intersertal igneous rocks (FIIR) (average of 18 samples, Delano et al., 1973).
6. 62295, 48: spinel micro-troctolite (Walker et al., 1973).
7. 67435, 14: spinel troctolite (spinel-olivine cumulate; Prinz et al., 1973b).
8. Average Luna 20 spinel troctolite (Prinz et al., 1973a).

Analyses of both types are presented in Table III-2 (analyses 1 to 3). From the analyses available, it appears that the glasses as a whole span the entire composition range from granulitic ANT to anorthosite, although very anorthositic compositions dominate.

C. Troctolites

Though not common, troctolites appear to be widely disseminated throughout the boulder. They superficially resemble troctolitic ANT rocks but can often be distinguished by their euhedral olivine and distinctive textures. Unaltered examples have a basaltic texture with olivine crystals (Fo_{89-75}) about 200 μ in diameter, set in a groundmass of plagioclase and Ca-poor pyroxene(?) (Figures III-4 and III-9). Most of them have the appearance of annealed cataclasites, in which fractured olivines sit in a granulated groundmass (Figures III-9E and F). A few, however, have escaped this process and show no signs of cataclasis (Figure III-9D). Most are very poor in opaque minerals, with rare spinel and ilmenite.

The troctolites chemically resemble the Apollo 15 and 16 and Luna 20 troctolites and spinel troctolites, except that those of the boulder are much more mafic and less feldspathic than most (Table III-3, Figure III-22). Several of them approach the composition of the Apollo 16 olivine-spinel cumulate (spinel troctolite) sample 67435, 14 (Prinz et al., 1973b) (Figure III-5B).

D. Pigeonite Basalt Clasts and Breccias

The bulk of the pigeonite basalt is restricted to the basalt breccia domains of 72275, but disseminated clasts of pigeonite basalt are also found in some portions of the gray polymict breccia. No pigeonite basalt has been observed in 72255, with the possible exception of one very small subophitic basalt clast 200 μ in diameter (in 72255, 95). The pigeonite basalt breccias are primarily composed of pigeonite basalt clasts seated in a matrix that appears to consist almost entirely of crushed pigeonite basalt (Figure III-1). A small amount of ANT and dark matrix breccia clasts, however, are usually also present.

Most of the pigeonite basalt clasts have a mesostasis-rich subophitic texture, in which the majority of the pyroxene is pigeonite (Figure III-10). The grain size of the subophitic varieties tends to be uniform within any particular clast. A few clasts, however, are much finer grained, and some exhibit a variolitic texture. This range of textures, and the relative proportions of fine-grained basalts, suggest that the fine-grained varieties are derived from the chilled margins of flows, and the subophitic varieties, from the flow interiors.

One unusual basaltic clast is included here (72255, 95; #770C29), although it does not properly belong to the pigeonite basalts. Its texture is essentially intersertal, but the groundmass appears granulated and may be recrystallized (see Figure III-14A, Section E). The composition is similar to the pigeonite basalts, but it is more mafic and has a distinctly higher FeO/MgO ratio (Table III-3, Figures III-11 and 22).

The earliest pyroxene to crystallize has a composition of $En_{75}Wo_5Fs_{20}$. The bulk of the early pyroxene is pigeonite, but a few grains may have orthopyroxene cores (Table III-4, analyses 1 to 6). Calcium-poor augite and ferroaugite appear late as rims on the pigeonite or as small interstitial grains. The major-element compositions of the pigeonite basalt pyroxenes are shown in Figures III-12A and B. Figure III-12B is a plot of pyroxene compositions for mineral clasts in the pigeonite basalt breccia matrix of 72275, 128. This plot is interesting because it probably indicates the full compositional range of pigeonite basalt pyroxenes and because it demonstrates that there is very little contamination of the breccia by foreign material. The general paragenetic sequence of the pigeonite basalts is plagioclase-pigeonite-subcalcic augite-ferroaugite. Olivine (Fo_{70}) has been observed in only one clast of pigeonite basalt (Figure III-10A).

The overall compositional range of the plagioclase is An_{94-86}, with most analyses falling in the range An_{93-90} (Figure III-6 and 13). Large opaque mineral grains are rare; those present appear to be chrome-spinel and ilmenite. The mesostasis is complex, and the detailed mineralogy remains to be worked out. Minerals known to be present are iron-metal, troilite, ilmenite, rare spinel, a phosphate mineral, and at least one zirconium mineral.

The mineralogy and whole-rock major-element chemistry of the pigeonite basalts are similar to those of the Apollo 14 Fra Mauro basalts (such as 14310) and the Apollo 15

Table III-4. Pyroxene analyses.

	1 763C18 ortho- pyroxene	2 763C18 Mg- pigeonite	3 763C18 intersertal pigeonite	4 763C18 subcalcic augite	5 761C1 augite	6 761C1 ferro- augite	7 Civet Cat ortho- pyroxene
SiO_2	54.06	53.58	52.06	50.46	48.15	46.85	54.11
TiO_2	0.17	0.37	0.33	0.85	0.83	1.02	0.52
Cr_2O_3	0.60	0.99	0.89	0.75	0.74	0.56	0.70
Al_2O_3	0.88	2.25	2.34	2.05	2.37	2.10	0.80
FeO	15.47	17.01	20.87	22.02	17.90	20.49	16.07
MgO	26.82	23.48	20.34	14.60	13.99	10.65	27.03
CaO	2.31	3.25	3.28	9.52	14.92	15.78	1.82
Total	100.31	100.93	100.11	100.25	98.90	97.45	101.65
Fe	23.36	26.99	34.05	36.56	28.90	34.34	23.76
Ca	4.46	6.62	6.85	20.26	30.87	33.88	3.45
Mg	72.18	66.39	59.11	43.18	40.23	31.78	72.79

Key:

1 to 4. 72275, 128: typical pyroxenes from a subophitic pigeonite basalt clast (single focused-beam electron-microprobe analyses).

5 and 6. 72275, 136: typical iron-rich pyroxenes from a subophitic pigeonite basalt clast (Table III-5, analysis 1) (single 100 μ diam. DBAs).

7. 72255, 105: orthopyroxene from the Civet Cat norite (1 100 μ diam. DBA).

Figure III-10. Pigeonite basalts.

A. 72275, 128: Subophitic pigeonite basalt. The subophitic texture of this clast is typical of most of these basalts (P – pigeonite, PL – plagioclase, OL – olivine, and M – mesostasis). This clast is unusual in that it contains the only grain of olivine (Fo_{70}) observed in any of the pigeonite basalts.

B. 72275, 136: Subophitic pigeonite basalt. This is a relatively fine-grained clast that borders on intersertal.

C. 72275, 128: Variolitic pigeonite basalt. The variolitic bundles are a mixture of plagioclase and pigeonite (M – mesostasis). (Plain light.)

D. 72275, 122: Typical pigeonite basalt mesostasis. The bright grains are sulfide and iron metal; the darker areas consist of ilmenite, a mafic silicate, phosphate and zirconium minerals, and glass (?). The surrounding mineral is plagioclase. (Reflected light.)

A

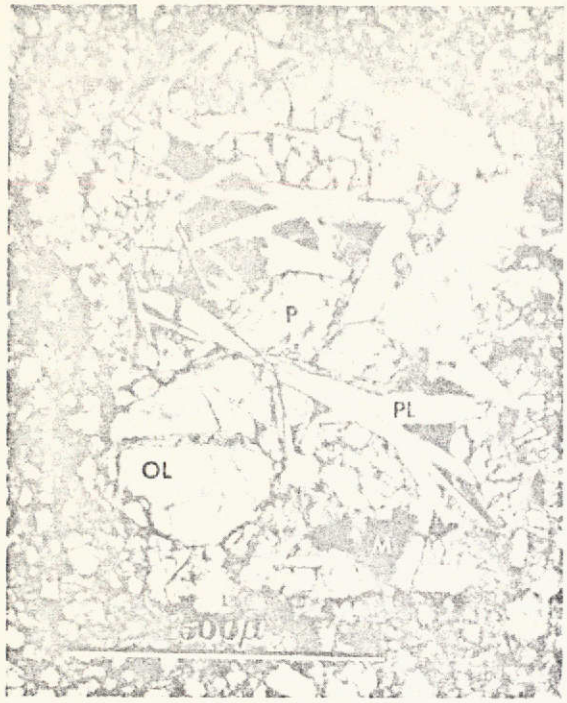

B

C

D

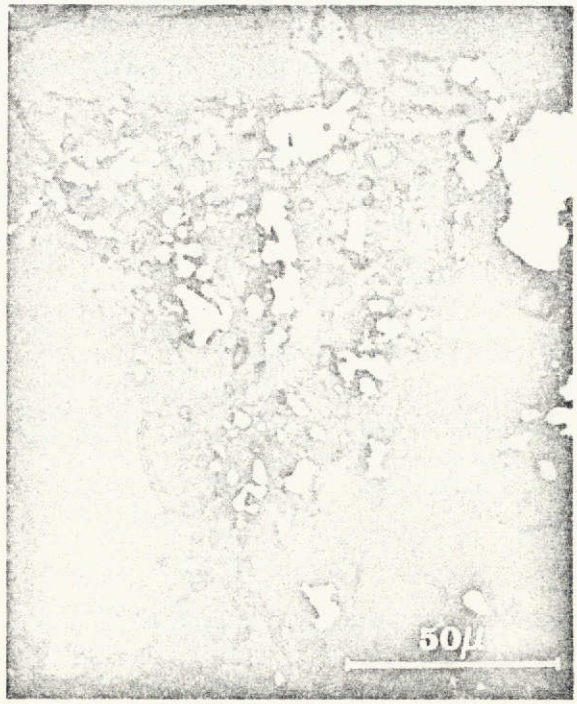

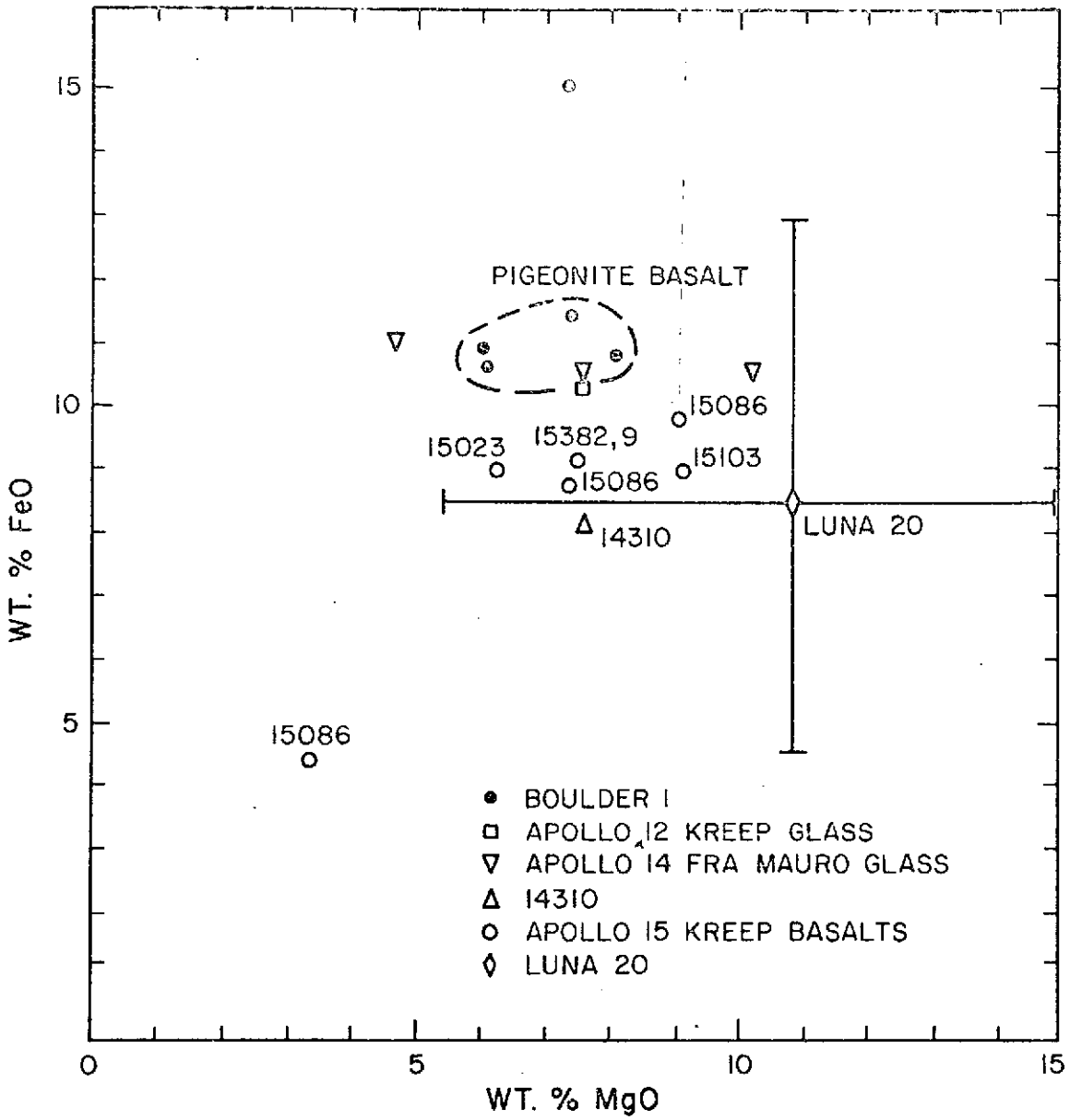

Figure III-11. MgO and FeO contents of Boulder 1 pigeonite basalts compared to compositionally similar rocks from Apollo 12, 14, and 15. The Boulder 1 pigeonites are enclosed by the dashed line. The lone Boulder 1 plot at the top of the figure is 72255, 95, clast #770C29, which is not included with the pigeonite basalts. Sources of other data are as follows: average Apollo 12 KREEP glass, Meyer et al. (1971); average Apollo 14 Fra Mauro glasses, Reid et al. (1972); 14310, 30, Longhi et al. (1972); Apollo 15 KREEP basalts, Phinney et al. (1972), Drake and Klein (1973), and Cameron et al. (1973); and average Luna 20 alkali-rich (KREEP) basalt, Prinz et al. (1973a). The bars on the Luna 20 plots give the range for each oxide of individual samples.

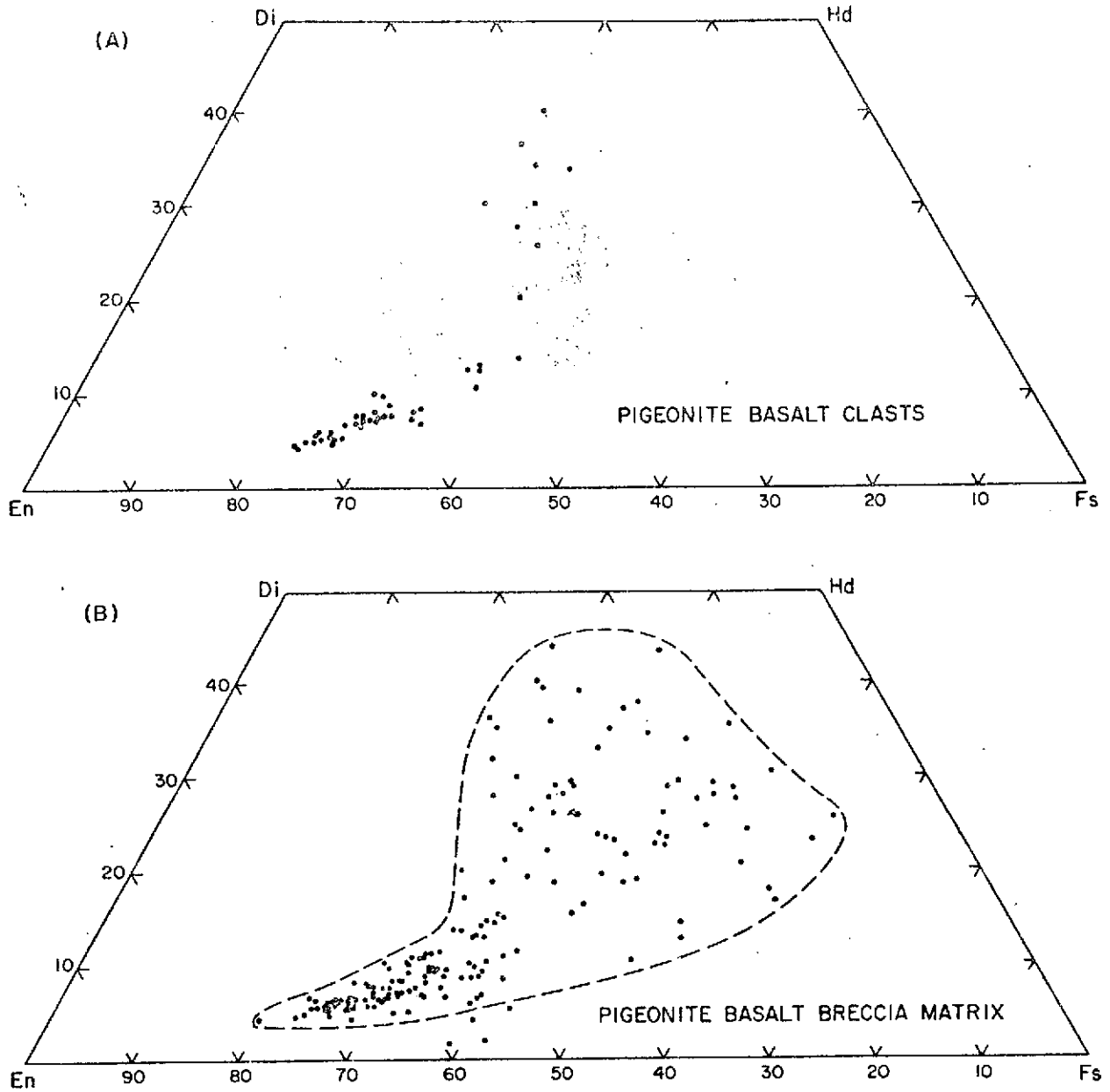

Figure III-12. Pyroxene quadrilaterals. A: For pyroxenes from pigeonite basalt clasts from 72275, 122, 128, and 136 (from complete major- and minor-element microprobe analyses). B: For a three-element (Mg/Fe/Ca) electron-microprobe survey of monomineralic pyroxene clasts in the pigeonite basalt breccia matrix of 72275, 128 (see Figure III-1B).

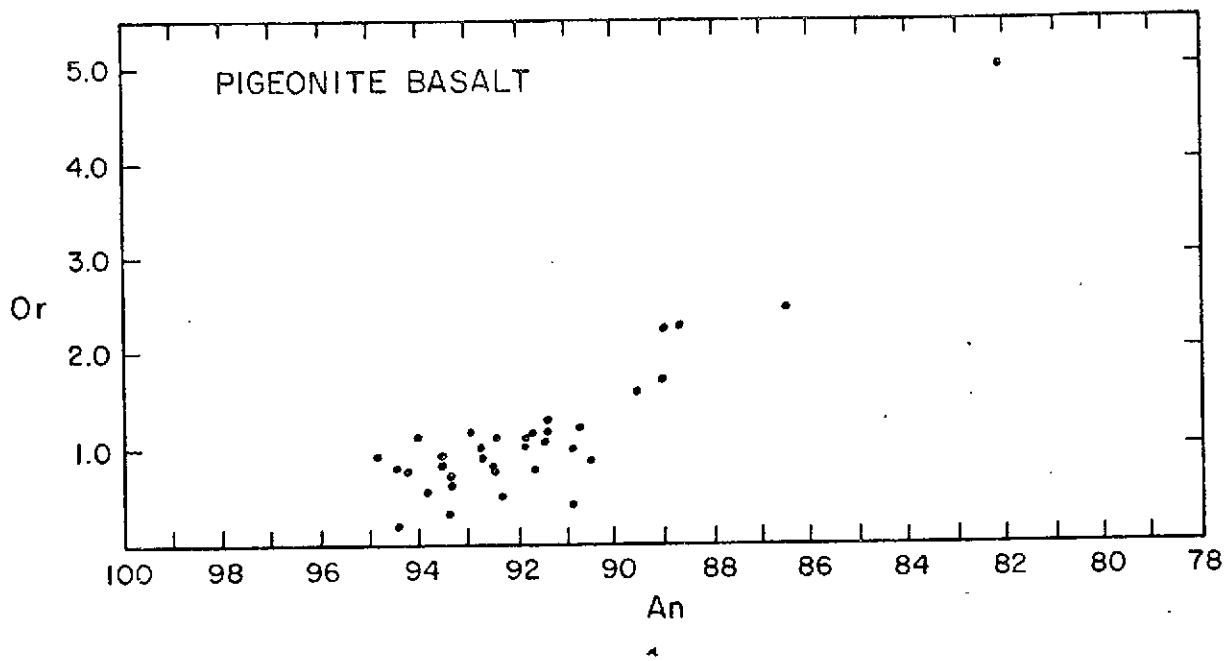

Figure III-13. Anorthite (An) versus orthoclase (Or) contents of plagioclases from pigeonite basalt clasts and monomineralic clasts in the pigeonite basalt breccia matrix of 72275, 147.

Table III-5. Pigeonite basalts, granitic clasts, and the Civet Cat norite.

	1	2	3	4	5	6	7	8	9	10	11
	763C19	761C1	761C2	761C3	770C29	14310	Ave. A15 KREEP basalt	761C1 meso-stasis	770C3 granitic clast	72275, 140 average granite	72275, 105 Civet Cat
SiO_2	48.3	48.0	48.2	47.9	47.0	48.27	51.3	49.0	71.2	65.6	50.3
TiO_2	0.6	0.6	0.8	1.0	0.4	1.27	1.7	1.1	0.1	0.1	1.8
Cr_2O_3	0.3	0.2	0.2	0.2	0.2	0.20	–	–	tr.	tr.	0.3
Al_2O_3	16.2	15.5	14.0	14.2	14.7	20.26	17.8	3.8	12.7	17.6	14.4
FeO	11.6	10.6	10.7	11.3	15.1	8.11	8.3	18.7	0.6	0.7	9.6
MnO	0.2	0.1	0.2	0.2	0.3	–	–	0.1	tr.	tr.	0.3
MgO	8.0	6.4	6.6	7.8	7.2	7.76	6.9	0.9	0.1	0.2	15.7
CaO	11.4	12.1	11.4	10.1	13.9	12.25	10.0	13.6	1.1	3.5	7.9
Na_2O	0.4	0.3	0.4	0.3	0.2	0.81	0.9	0.1	0.2	0.4	0.3
K_2O	0.4	0.3	0.4	0.3	0.1	0.55	0.8	0.8	8.5	8.2	0.1
P_2O_5	0.3	0.5	0.2	0.5	0.0	–	–	5.7	tr.	0.2	0.0
BaO	–	0.1	0.1	0.1	0.1	–	–	0.1	0.6	0.7	–
S	0.3	0.7	0.1	0.7	–	–	–	4.5	–	–	–
Total	98.0	95.4	93.3	94.6	99.2	99.48	97.7	99.4	95.1	97.2	100.7
Fo	–	–	–	–	1.2	–	–	–	0.0	0.0	0.0
Fa	–	–	–	–	2.1	–	–	–	0.0	0.0	0.0
En	20.5	16.7	17.7	20.7	16.5	19.5	17.6	2.4	0.2	0.5	39.0
Fs	19.4	16.6	19.6	17.5	25.0	12.7	12.7	14.9	1.0	1.2	15.1
Wo	5.9	7.6	8.8	4.6	12.7	4.5	3.2	9.8	0.0	0.0	0.6
Or	2.3	2.0	2.5	1.6	0.6	3.3	4.8	4.7	53.3	50.2	0.6
Ab	3.9	3.0	3.6	3.0	1.6	6.9	7.8	0.9	1.4	3.5	2.5
An	41.8	41.8	37.8	38.8	39.3	50.3	43.2	7.8	5.8	16.7	37.5
Ilm	1.3	1.2	1.5	2.0	0.7	2.4	3.3	2.3	0.2	0.2	3.4
Chr	0.5	0.3	0.4	0.4	0.3	0.3	0.0	0.1	0.0	0.0	0.0
Qtz	3.0	7.6	7.2	8.3	–	0.1	7.3	30.6	36.8	25.0	1.2
Cor	–	–	–	–	–	–	–	–	1.3	2.3	0.0
Ap	0.6	1.1	0.6	1.2	–	–	–	13.6	0.0	0.5	0.0
Troi	0.9	2.0	0.3	2.0	–	–	–	12.8	–	–	–

Key:

1. 72275, 128: clast #763C10, intersertal pigeonite basalt (average of 4 600 μ × 100 μ DBA traverses).
2. 72275, 135: clast #761C1, subophitic pigeonite basalt (average of 28 100 μ diam. DBAs).
3. 72275, 135: clast #761C2, fine-grained feathery (quench textured?) pigeonite basalt (average of 6 100 μ diam. DBAs).
4. 72275, 135: clast #761C3, subophitic pigeonite basalt (average of 18 100 μ diam. DBAs).
5. 72255, 95: clast #770C29, "intersertal basalt" (Figure III-14A; average of 13 100 μ diam. DBAs).
6. 14310, 138 (Longhi et al., 1972).
7. Average of 6 Apollo 15 KREEP basalts (Phinney et al., 1972; Drake and Klein, 1973; Cameron et al., 1973).
8. Mesostasis of the pigeonite basalt (clast #761C1) given in column 2 (average of 32 25 μ diam. DBAs).
9. 72255, 95: clast #770C3, glassy granitic clast (average of 9 100 μ diam. DBAs). (Very similar to clast shown in Figure III-14D.)
10. 72275, 140: clast #1, average of two glassy granitic clasts in the dark matrix breccia domains (average of 5 100 μ diam. DBAs).
11. Estimated bulk composition of the Civet Cat norite, from an estimated mode of 60% ± 10% orthopyroxene and 40% ± 10% plagioclase. Estimate made from two defocused-beam traverses 2 mm long and 100 μ wide in orthopyroxene-rich and plagioclase-rich areas whose modes were determined (thin section 72255, 105, Figure III-15A).

and Luna 20 KREEP basalts (Table III-5, analyses 1 to 7). The outstanding differences between the Boulder 1 pigeonite basalts and these others are lower K_2O, P_2O_5, Al_2O_3, TiO_2, and SiO_2 abundances and lower MgO/(MgO + FeO) ratios (Figures III-11 and III-22). Although they are similar to KREEP basalts and glasses, their content of K_2O (<0.4 wt. %) and phosphorus disqualifies them from being labeled as KREEP basalts (Cameron et al., 1973). Some of the pigeonite basalt clasts appear to be more mesostasis-rich than any analyzed so far, and later work may detect some clasts that fall into the compositional range of KREEP basalt.

E. Granitic Clasts

Lithic clasts of granitic composition are sparse in the 72275 gray polymict breccia, where they apparently are confined largely to the dark matrix breccia clasts, but relatively common in 72255. They are also present in both our thin sections from sample 72235. In thin section 72255, 95 (our one large thin section of typical 72255), we have observed 30 granitic clasts in the size range 25 to 250 μ. Although they are usually small (<300 μ), one granitic clast in thin section 72255, 103 has a length of 2 mm (Figure III-2A). Overall, however, the granitic clasts constitute less than 1% of the boulder.

The main phase assemblage of the granitic clasts is silica (cristobalite?) ± barian K-feldspar ± plagioclase (rare) ± glass. Rare, very small opaques and mafic silicates may also be present. Texturally, the granitic clasts fall into two groups of about equal abundance – holocrystalline and glassy. The holocrystalline variety consists primarily of silica plus barian K-feldspar (usually with K-feldspar > silica) (Figures III-14B and C). The glassy variety tends to consist of parallel or subparallel sets of crystalline silica grains in a groundmass of clear brown glass (Figure III-14D), which often contains fine, feathery, quench crystallites. The glasses analyzed are similar to whole-rock compositions. Table III-5 presents whole-rock analyses of two typical granitic clasts.

The potash feldspar of the granitic clasts is rich in barium and very poor in soda. An average of 13 feldspar analyses from 3 clasts gave the following:

		Range
SiO_2	62.10	58.64–63.73
Al_2O_3	20.06	19.32–21.06
CaO	0.44	0.04– 1.18
Na_2O	0.03	0.00– 0.16
K_2O	15.25	14.01–16.00
BaO	2.01	1.12– 3.11
Sum	99.89	

A few potash feldspars are perthitic (Figure III-14E), but considering the very low soda content, it seems unlikely that the lamellae are an alkali feldspar. Those K-feldspars with greater than 0.3 wt. % CaO are generally perthitic, and therefore these lamellae may be anorthitic.

The granitic clasts have reacted with the 72255 matrix and have dark reaction rims approximately 10 μ thick. The composition of these rims has not yet been determined. The 72255 matrix was also hot enough to partially melt the holocrystalline granitic clasts such that a film of glass surrounds every grain within a clast. In some clasts, the degree of melting is the greatest around the margins, indicating that the heating was probably related to the matrix (Figure III-14F). The degree of partial melting is slight, and therefore it seems unlikely that the initial temperature of the matrix was much above the orthoclase plus silica eutectic temperature of 990 ± 20°C (Levin et al., 1964).

There appears to be a complete textural transition from the holocrystalline to the glassy varieties. Three possibilities arise to explain the observed textures: 1) They are primary igneous textures; 2) they are the result of varing degrees of thermal partial melting of originally holocrystalline granitic rock; or 3) they have resulted from varing degrees of shock melting of the parent rocks and are diaplectic. The similarity in the glass composition compared to the bulk chemistry of the granitic clast makes the third possibility the least likely, since the diaplectic glass should have the composition of a K-feldspar.

Figure III-14. Granitic clasts.

A. 72255, 95: Unusual basalt clast. This clast has an intersertal texture, but the groundmass appears granulated and the rock may have undergone some recrystallization. The groundmass is largely pyroxene, but mineral analyses have not yet been performed (whole-rock analysis, Table III-5, analysis 5). (Plain light.)

B. 72255, 95: Holocrystalline granitic clast. The texture consists of crystalline silica grains (S) in poikilitic barian potash-feldspar (F). The clast has reacted with the matrix, resulting in a dark matrix halo about 15 μ thick. (Plain light.)

C. 72255, 95: Holocrystalline granitic clast. The texture is similar to that of the clast in B, with crystalline silica (S) and plagioclase(?) (P) in poikilitic barian potash-feldspar. (Crossed nicols.)

D. 72275, 146: Glassy granitic clast. The texture consists of a framework of crystalline silica (S) in a clear brown glass (G). The "eye" is a hole in the section.

E. 72235, 9: "Perthitic" barian potash-feldspar (PF). The feldspar (F) at top center is without the perthitic lamellae. These feldspars are part of a brecciated granitic clast. (See Section E of the text for a discussion of these feldspars.)

F. 72255, 95: Partially melted granitic clast. Each grain is isolated from the others by a thin film of glass. Note that the greatest concentration of glass (G) is at the margin of the clast. (Reflected light.)

A
200μ
C
S
F
PL
100μ
E
F
PF
50μ
B
F
S
200μ
D
S
200μ
F
50μ

The granitic clasts always occur as isolated particles and have never been observed to be directly related to any other lithology. In distribution, they tend to be most closely associated with the dark matrix breccias and the ANT suite. Whatever their origin, the occurrence of these ubiquitous granitic clasts throughout the boulder suggests a derivation from larger widespread bodies of granitic composition at the impact site.

F. Ultramafic Particles

No large clasts of ultramafic rock have been observed in thin sections of the boulder, but sparse, small polycrystalline ultramafic clasts usually less than 200 μ in diameter are present (Figure III-8D). Only three of these clasts have been analyzed. Two are similar in composition to pyroxenes from the ANT group, while the third consists of magnesian olivine (Fo_{87}). Many of these small ultramafic particles do not resemble any of the olivines or pyroxenes found in the crystalline clasts; they may be derived from other unseen lithologies. The presence of debris from rocks with a very high Mg/Fe ratio is also hinted at by the occurrence of a few very magnesian olivines in the dark matrix breccias and the 72275 gray polymict breccia (Figure III-4A and B).

G. Plutonic Norite (Civet Cat Clast)

Civet Cat is a shocked, relatively coarse, orthopyroxene-rich norite. In Figure II-11, it can be seen that Civet Cat has a mottled texture with diffuse light streaks set in a dark matrix. Thin-section examination indicates that the light areas are almost pure plagioclase, and the dark areas are chiefly orthopyroxene (Figure III-15). In spite of its porous appearance by transmitted light, reflected-light illumination reveals that Civet Cat has almost no porosity.

Modal analysis of our thin section of Civet Cat (72255, 105) showed it to contain 53.8% plagioclase, 45.9% orthopyroxene, and 0.3% opaque minerals. From an examination of the macroscopic documentation photographs, however, it appears that our thin sections are from a plagioclase-rich portion of the clast and are not representative. Assuming that the dark and light portions of Civet Cat as seen in thin section

are analogous to those seen in the macroscopic photographs, we estimate that the clast consists, very approximately, of 40% plagioclase and 60% orthopyroxene. Revision of this estimate awaits the arrival of new thin sections.

Texturally, the plagioclase ranges from occasional unshocked rectangular grains to whole areas of plagioclase that have been nearly isotropized or recrystallized to a very fine-grained crystalline material like the rim material shown in Figure III-9C. The plagioclase has a narrow compositional range, An_{92-95} (average, An_{94}) and $Or_{1-0.5}$ (seven analyses). The largest single crystal of plagioclase observed had a maximum dimension of 1.6 mm.

The orthopyroxene has a compositional range of $En_{75}Wo_2Fs_{23}$ to $En_{70}Wo_4Fs_{26}$, with an average composition of $En_{73}Wo_3Fs_{24}$ (Table III-4, analysis 7). The Civet Cat orthopyroxenes are distinctive in having abundant platey brown inclusions (ilmenite?) that appear to be exsolution lamellae and rare Ca-rich clinopyroxene(?) exsolution lamellae. The orthopyroxene commonly shows substantial shock effects, but a few grains are subhedral. The largest orthopyroxene grain measured was 1.4 mm in diameter.

We have observed distinctive large clasts of orthopyroxene and plagioclase (the latter with fine-grained rims) in most of our 72275, 72255, and 72235 thin sections, for which Civet Cat appears to provide the required type of source rock. The fine-grained rims around the shocked monomineralic plagioclase clasts apparently result from re-equilibration with the matrix (Figure III-9A). One clast analyzed has a core of An_{95} and a rim of almost pure fine-grained plagioclase of An_{90}. The average composition of normative plagioclase in the surrounding matrix was also An_{90}. Unshocked homogeneous plagioclase clasts in the matrix near these shocked ones do not exhibit obvious re-equilibration rims.

It seems clear that Civet Cat is a shocked igneous rock of norite composition (Table III-5, analysis 11), which originally had an average grain size in the range 1 to 4 mm. The overall texture is suggestive of a plutonic rock. This rock has been dated at 4.18 b.y. (see Section VII of this report).

Figure III-15. Civet Cat clast.

A. 72255, 101: Orthogonal set of thin sections of the Civet Cat clast, a shocked
72255, 103: plutonic norite, and surrounding matrix. The clast marked G is an
72255, 105: unusually large granitic clast.

B. 72255, 105: Heavily shocked portion of Civet Cat. The orthopyroxene (OPX) has been crushed and the plagioclase (PL) maskylenized. (Plain light.)

C. 72255, 105: Matrix rind around a portion of Civet Cat. An analysis of the dark rind is given in Table III-6, analysis 4. (Plain light.)

A

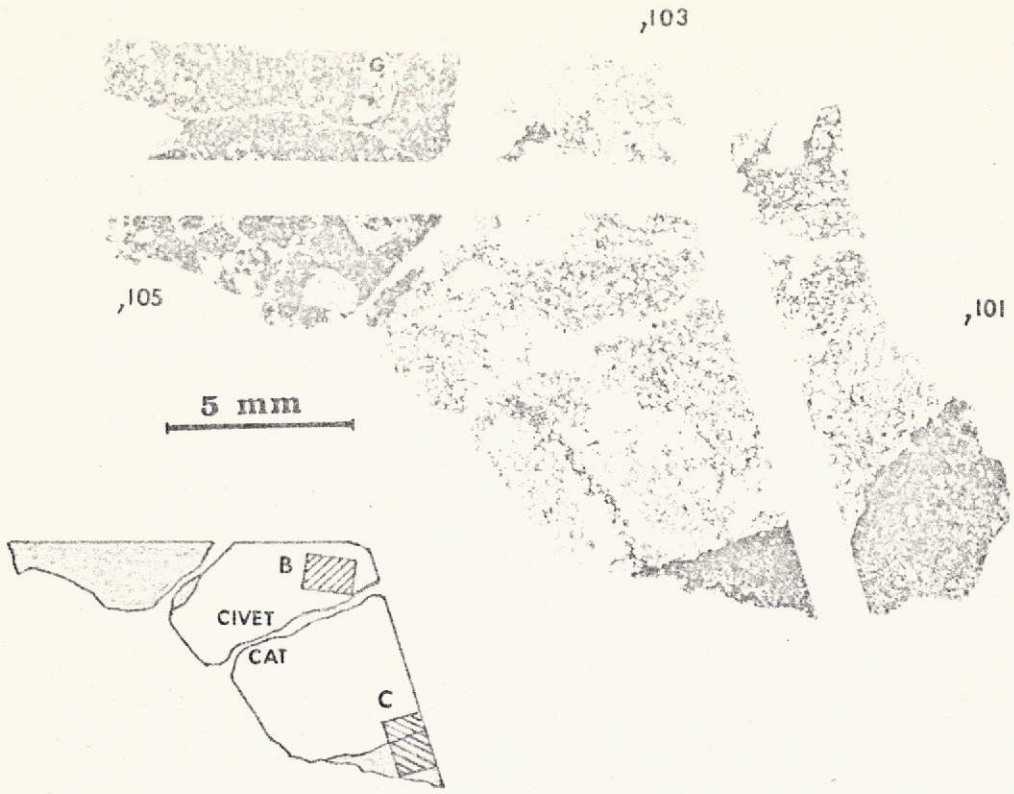

B

C

H. Dark Matrix Breccias

Besides the layering of the boulder, one of its most distinctive features is the occurrence of large, dark-rimmed anorthositic clasts (Figures II-2, II-4, and II-8). At least two large samples of these clasts were returned, 72235 and 72275 (clast #1) (see Section II of this compilation). The rind material of clast #1, 72275, which will be discussed separately, as well as a number of smaller rimmed ANT clasts, consists of dark matrix breccias (Figure III-16).

In addition to these rimmed clasts, similar dark matrix breccias are found as uncored clasts (Figure III-17A, B, and C). In the 72275 gray polymict breccia domains, dark matrix breccias form the largest group of lithic clasts. The uncored varieties range in shape from angular to rounded and bomb-like types that were clearly plastic. The bulk of the angular dark matrix breccia clasts is probably derived from the disintegration of larger rounded clasts. In 72275, the number of uncored dark matrix breccia clasts greatly exceeds that of the cored variety, although both are common. The question of whether or not dark matrix breccias occur in sample 72255 will be discussed below. In Section II of this compilation, the uncored dark matrix breccia clasts are referred to by Marvin as gray or dark gray aphanitic clasts (e.g., clasts #2 and #3, 72275).

Clasts similar to the dark matrix breccia clasts found in the boulder have been observed in Apollo 14 breccia 14082, which is classified as a glass-poor breccia with a fragmental matrix (Engelhardt et al., 1972). This breccia, which consists primarily of ANT debris in a fragmental matrix, also contains irregular clasts of dark matrix breccias whose style of occurrence and matrix are very similar to those observed in Boulder 1, Station 2 (Figures III-17D, E, and F). An analysis of the dark clasts, which are considerably more feldspathic than those of 72275, is presented in Table III-6, analysis 6.

In thin section, the dark matrix breccias are easily recognized by their very dark, usually opaque, very fine-grained matrix with little porosity (Figure III-17E). They contain sparse ANT clasts, large monomineralic clasts, and rare granitic clasts. The monomineralic clasts are primarily plagioclase, pyroxene, and olivine and sparse spinel, ilmenite, sulfide, and iron-metal. No pigeonite basalt clasts have been observed in the dark matrix breccias.

Table III-6. 72275 and 72255 matrices and dark matrix breccias (DMB).

	1	2	3	4	5	6	7	8	9	10
	72275 PET	72275, 128 gray matrix	72255, 95 matrix	72255, 105 Civet Cat rind	72275, 128 DMB matrix	72275, 134 DMB matrix	72275, 12 vesicular rim	72275, 146 clast #2 matrix	72275, 140 DMB	14082, 9 DMB
SiO_2	47.5	47.3	45.1	46.5	49.7	47.7	43.9	47.0	46.6	45.8
TiO_2	0.9	0.6	0.6	0.9	1.1	1.1	0.9	1.0	1.3	2.6
Cr_2O_3	0.4	0.1	0.2	0.2	0.2	0.2	0.2	0.2	0.2	0.1
Al_2O_3	17.0	21.3	20.0	21.4	18.8	20.3	22.9	22.8	19.6	25.8
FeO	11.6	8.8	7.7	8.5	10.0	10.6	8.7	8.9	11.0	5.1
MnO	0.2	0.1	0.1	0.1	0.1	0.2	0.1	0.1	0.2	0.1
MgO	9.4	8.3	9.1	9.4	9.0	10.0	12.1	8.7	8.2	3.3
CaO	11.7	12.4	12.7	12.3	11.4	11.5	11.6	12.9	11.4	14.7
Na_2O	0.4	0.4	0.5	0.3	0.5	0.5	0.7	0.6	0.6	1.5
K_2O	0.3	0.1	0.2	0.2	0.3	0.2	0.3	0.2	0.5	0.2
P_2O_5	0.4	0.5	0.2	0.4	0.5	0.4	0.3	0.5	0.8	0.3
Total	99.8	99.9	96.4	100.2	101.6	102.7	101.7	102.9	100.4	99.5
Fo	0.4	0.0	4.3	1.9	0.0	3.4	16.5	4.5	1.6	0.2
Fa	0.4	0.0	2.8	1.2	0.0	2.7	8.8	3.3	1.5	0.1
En	22.8	20.7	17.3	20.8	22.0	19.5	6.1	14.8	18.2	7.9
Fs	19.3	15.2	10.2	12.1	16.3	13.9	3.0	9.9	15.5	4.9
Wo	5.0	1.0	4.3	0.8	2.1	0.7	0.0	0.8	1.1	3.3
Or	1.7	0.8	1.3	1.3	2.0	1.3	1.6	1.3	2.9	1.4
Ab	3.2	3.7	4.1	2.3	3.9	4.2	5.4	4.9	5.5	13.0
An	44.1	55.8	53.9	56.5	47.5	51.1	55.1	57.4	48.7	63.3
Ilm	1.7	1.2	1.1	1.7	2.1	2.0	1.6	1.8	2.5	5.0
Chr	0.5	0.1	0.2	0.3	0.3	0.3	0.3	0.3	0.3	0.1
Qtz	0.0	0.2	0.0	0.0	2.7	0.0	0.0	0.0	0.0	0.0
Cor	0.0	0.0	0.0	0.0	0.0	0.0	1.0	0.0	0.0	0.0
Ap	0.8	1.1	0.5	0.8	1.1	1.0	0.6	1.0	1.8	0.7

Key:

1. 72275: whole-rock analysis (PET, 1973a).
2. 72275, 128: gray polymict breccia matrix (average of 26 100 μ diam. DBAs of the < 50 μ portion of the matrix).
3. 72255, 95: dark matrix (average of 40 100 μ diam. DBAs of the < 50 μ portion of the matrix).
4. Dark rind of the Civet Cat norite clast. The material analyzed can be seen in Figure III-15C as the very dark, dense, approximately 1/2-mm-thick rind immediately adjacent to the norite. (Average of 5 100 μ diam. DBAs of the < 50 μ portion.)
5. 72275, 128: average matrix of two dark matrix breccia clasts (average of 10 100 μ diam. DBAs of the < 50 μ portion).
6. 72275, 134: dark matrix breccia clast matrix (average of 21 100 μ diam. DBAs).
7. Dark vesicular rind material around the anorthosite of 72275, 12 (Figure III-16A, B, and C) (average of 5 100 μ diam. DBAs).
8. Clast #2, 72275: matrix (a dark matrix breccia, Figure III-8C) (average of 15 100 μ diam. DBAs).
9. Analysis of the dark matrix breccia portion of clast #1 (Figure III-8A and B) (average of 10 100 μ diam. DBAs).
10. Dark matrix breccia clasts of Apollo 14 breccia 14082, 9 (Figure III-17D) (average of 19 25 μ diam. DBAs).

Figure III-16. Cored dark matrix breccia clasts.

A. 72275, 12: Clast with shocked anorthosite core and dark matrix breccia rim (plain light). The dark blur at the left is due to a crack in the section.

B. 72275, 12: Same clast as A in reflected light. Vesicles are clearly visible in the dark matrix breccia rind, showing that it once had fluid properties. This is a very rare example of vesicles in dark matrix breccia material, however; they are absent in most clasts.

C. 72275, 12: Enlargement of a portion of B. Note vesicles, but also the high abundance of monomineralic fragments in the dark rind.

D. 72275, 12: Typical clasts of ANT-cored dark matrix breccia. Note the smooth, streamlined envelope of the left-hand clast, as compared to the more angular and fragmented appearance of the right-hand clast.

A
B
C
D
200μ
200μ

Figure III-17. Dark matrix breccias.

A. 72275, 128:
B. 72275, 135: Streamlined bomb-shaped clasts of dark matrix breccia. Note that the clast in A has been broken in half.

C. 72275, 128: Typical rounded-to-angular clasts of dark matrix breccia in the 72275 gray polymict breccia. The white portion of the matrix is a crushed disaggregated gabbroic anorthosite. The darker matrix at the lower left is more typical of the 72275 gray polymict breccia.

D. 14082, 9: Cored and uncored clasts of dark matrix breccia in an Apollo 14 breccia. The core of the clast at the bottom is a shocked anorthosite.

A

B

C

D

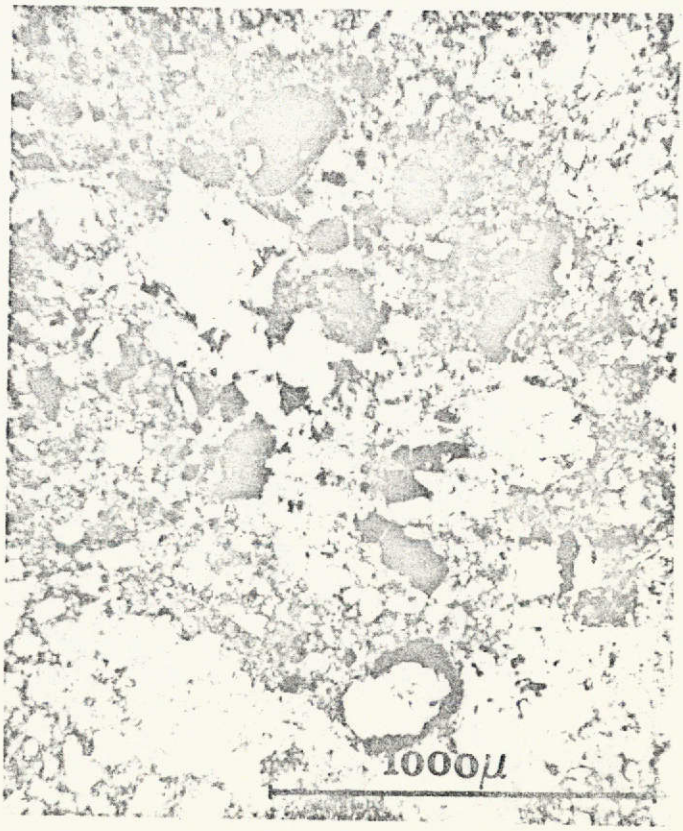

Figure III-17 (Cont.).

E. 72275, 129:
F. 14082, 8:

Closeup of the matrix of a typical 72275 dark matrix breccia clast compared to one from 14082 (Figure D). Note the lack of vesiculation, the fine grain size, and the abundant small monomineralic fragments. (Reflected light.)

E

72275, 129

F

14082, 8

The matrix consists of abundant fine monomineralic and lithic particles seated in a very fine (<1 μ), more or less opaque groundmass (Figures III-17E and III-18D). The opaque quality of the matrix is due to a myriad of disseminated opaque minerals almost too fine to be resolved optically. Excluding the larger sparse lithic and monomineralic clasts (>200 μ), the matrix of two large dark matrix breccia clasts in 72275, 128 consisted of 7% lithic particles (10 to 200 μ), 13% monomineralic particles (10 to 200 μ), and 70% fine matrix (<10 μ diameter particles). Electron-microprobe analyses have shown that the monomineralic olivines in the matrix have re-equilibration rims 10 to 15 μ thick. The lack of such rims around olivine and pyroxene clasts in the surrounding gray polymict breccia indicates that these rims are directly related to the dark matrix breccia. Superficially, the dark matrix breccias resemble soil breccias, but they lack the ropy glasses and glass spherules associated with soil breccias and are much better sorted.

Some workers have suggested that the dark matrix material contained significant glass. In thin section, however, no glass is discernible. With one exception – a vesicular rind around an anorthosite clast (Figure III-16A, B, and C) – no vesicles, flow structures, nor devitrification textures that would indicate large amounts of glass have been observed. If glass is or was present, it must represent a very small percentage of the matrix and must be finely dispersed. We prefer an origin of essentially complete sintering of very finely granulated crystalline material without significant recrystallization.

Although most of the lithic clasts in the dark matrix breccias are granulitic ANT and other anorthosites, the composition of the matrix is more mafic and has a lower MgO/(MgO + FeO) ratio than does granulitic ANT (Table III-6, Figure III-22). The matrix also has a distinctly higher KREEP content, as determined from potassium and phosphorus abundances, than do the ANT rocks (Figure III-23). The presence of the potash-rich granitic clasts might explain the higher KREEP content of the dark matrix breccias, but it cannot explain their more mafic chemistry. Therefore, at least one other major component must be present. In terms of their major-element chemistry and their MgO/(MgO + FeO) ratios, the dark matrix breccias are compositionally intermediate between granulitic ANT and the pigeonite basalts (Figures III-22 and III-23).

The compositions of the monomineralic clasts also suggest that the dark matrix breccia contains other than ANT and granitic materials. In Figure III-4, it can be seen that the range of olivine compositions is more extensive than that of the ANT suite. Similarly, for the pyroxenes, it appears that basaltic pyroxenes are present (Figure III-19). Since it seems improbable that these pyroxenes are derived from mare basalts, the most likely source is from basalts similar to the pigeonite basalts described earlier (compare Figures III-19 and III-12). It is interesting, however, that no lithic clasts of the hypothetical basaltic component have been observed in the dark matrix breccia clasts.

Clast #1, 72275; dark matrix breccia rind

The gabbroic anorthosite core of clast #1 was discussed in Section A. Petrographically, the dark matrix breccia rind is similar to other dark matrix breccias found in 72275, although it is even darker. Its clast population consists of sparse ANT, rare granitic clasts (Table III-5, analysis 10), and monomineralic particles. The major-element chemistry of clast #1 is also similar to that of the other dark matrix breccias in 72275, although it has the highest $K_2O + P_2O_5$ content of any dark matrix breccias analyzed (Table III-6, analysis 9).

In addition to the dark matrix breccia and the white gabbroic anorthosite portions, clast #1 contains some breccia domains intermediate in color between the two major lithologies. One of these areas can be seen in Figure III-14A, at the top edge, just right of center. An analysis of this area (Table III-2, analysis 5) had the highest P_2O_5 content of any boulder material yet analyzed by us (P_2O_5, 3.1 wt. %; K_2O, 1.0 wt. %). It is not yet known whether this analysis is characteristic of these areas or whether it is a fluke. Nevertheless, the KREEPy nature of this material, as well as that of the dark matrix breccia portions, suggests the possibility that clast #1 as a whole may be KREEPier than most other boulder materials.

Clast #2, 72275; dark matrix breccia

Clast #2, which was mapped by Marvin (see Section II), is a large clast of dark matrix breccia, approximately 3 1/2 cm in diameter (Figures II-8 and II-9). It

Figure III-18. 72275 and 72255 matrices.

A. 72275, 12: Typical 72275 gray polymict breccia with clasts of dark matrix breccia (cored and uncored), ANT, and abundant monomineralic fragments.

B. 72255, 8: Typical 72255 breccia with a dark, highly welded matrix and clasts of ANT and monomineralic fragments.

Figure III-18 (Cont.).

C. 72275, 128: Closeup of the poorly sintered, very porous, 72275 gray polymict breccia matrix (reflected light).

D. 72275, 129: Closeup of dark matrix breccia matrix at the same scale as C. The opaqueness of this material in transmitted light is due to abundant, dispersed, very fine opaque minerals.

E. 72255, 95: Closeup of 72255 matrix. The 72255 matrix is distinct from those of 72275 in that it has been partially recrystallized. The main mineral assemblage of the recrystallized portion is plagioclase, pyroxene, and dispersed tabular ilmenite. Porosity is low, but the shapes of the pores suggest a small amount of vesicularity.

A

72275

B

72255

Figure III-18 (Cont.).

C. 72275, 128: Closeup of the poorly sintered, very porous, 72275 gray polymict breccia matrix (reflected light).

D. 72275, 129: Closeup of dark matrix breccia matrix at the same scale as C. The opaqueness of this material in transmitted light is due to abundant, dispersed, very fine opaque minerals.

E. 72255, 95: Closeup of 72255 matrix. The 72255 matrix is distinct from those of 72275 in that it has been partially recrystallized. The main mineral assemblage of the recrystallized portion is plagioclase, pyroxene, and dispersed tabular ilmenite. Porosity is low, but the shapes of the pores suggest a small amount of vesicularity.

C

D

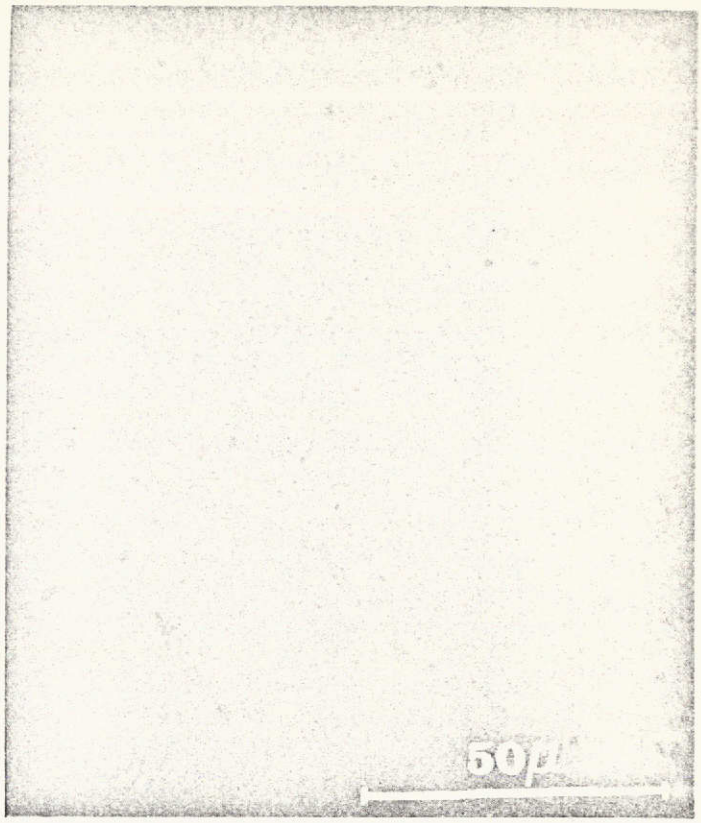

E

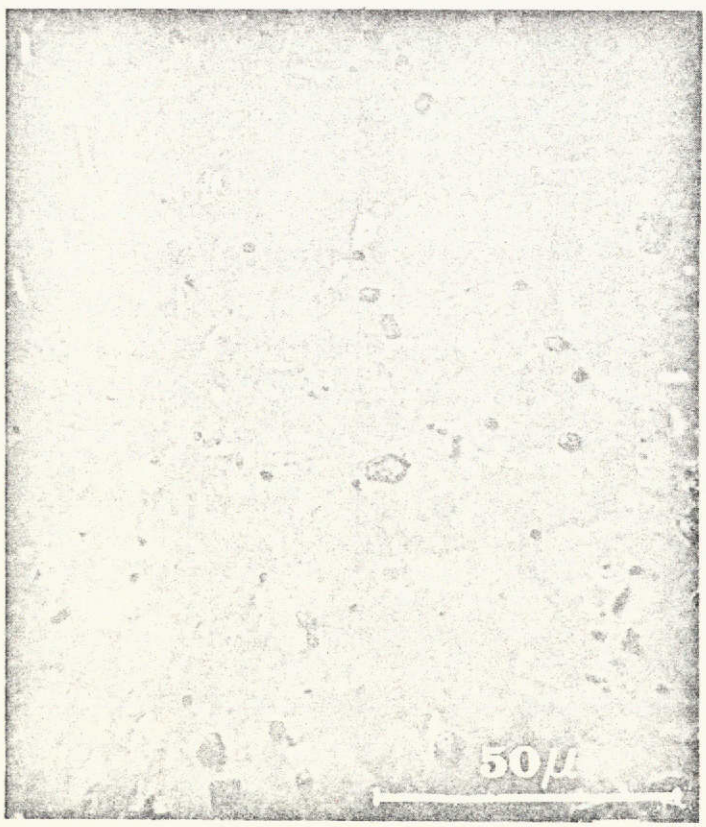

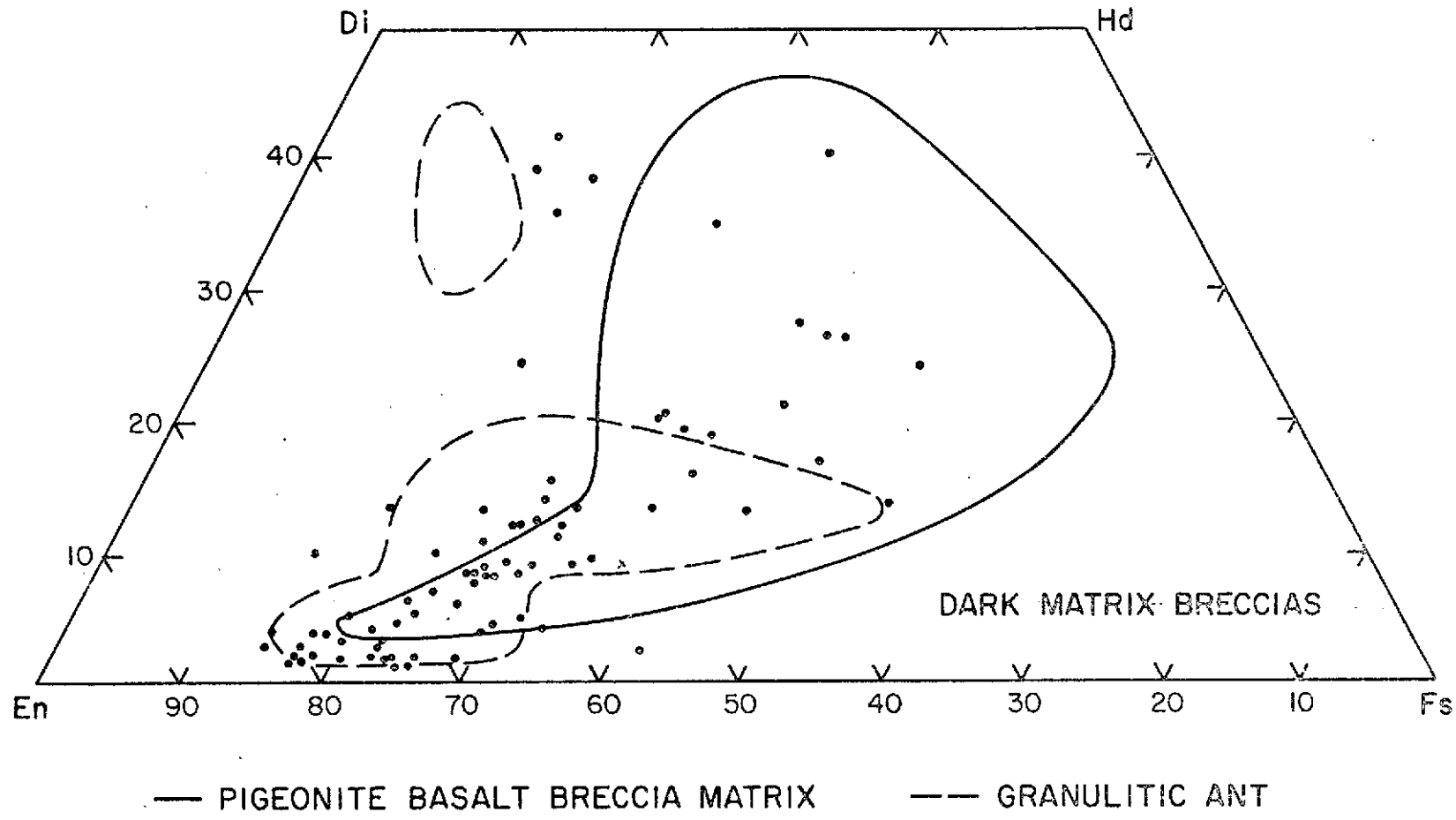

Figure III-19. Three-element (Mg/Fe/Ca) microprobe survey of monomineralic pyroxenes in dark matrix breccia clasts of 72275, 128. The pyroxene fields indicated by dashed lines are those of the Boulder 1 granulitic ANT rocks (see Figure III-5A), and the solid lines indicate the fields of the pigeonite basalt breccia matrix (Figure III-11B).

contains lithic clasts of ANT, devitrified maskylenite, and granitic particles (Figures III-7C and III-8C). Its composition is the same as that of smaller typical 72275 dark matrix breccia clasts (Table III-6, analysis 8).

72275 GRAY POLYMICT BRECCIA MATRIX

The gray polymict breccia domains of 72275 consist of approximately 60% matrix and 40% clastic material (PET, 1973a). The matrix is very porous (10 to 40%) and poorly sintered (Figure III-18C). It is a feldspathic microbreccia that consists largely of sintered mineral and lithic fragments. The matrix is heterogeneous, ranging in color from whitish to medium gray (Figures III-1B and III-17C).

The whitish areas are plagioclase-rich and appear to be disaggregated gabbroic anorthosite. A survey of pyroxenes in one of these anorthositic areas (Figure III-17C) indicated pyroxenes similar to those of clast #1 (gabbroic anorthosite) (Figure III-20A). The darker gray material constitutes the bulk of the matrix (Figure III-1A, B). An analysis of the finest grained portion of typical 72275 gray matrix and the PET (1973b) whole-rock analysis of 72275 are presented in Table III-6, analyses 1 and 2.

The monomineralic clast population consists of plagioclase, olivine, orthopyroxene, pigeonite, Ca-rich clinopyroxene, ilmenite, spinel, troilite, Fe-metal, and trace amounts of K-feldspar, silica, zircon, and armalcolite. The plagioclases show a somewhat diffuse range of compositions, most values being in the range An_{92-98}, with a distinct peak at An_{96} (Figure III-6). It appears that the plagioclases can be explained as being derived mainly from ANT, with a lesser contribution from the pigeonite basalts. Olivine shows a wide range of compositions (Fo_{58-94}) without any marked concentration of values (Figure III-4). Neither the olivines with Fo > 90 nor those with Fo < 62 can be explained by derivation from known crystalline lithic clast rock types of the boulder samples. Most of the pyroxene compositions fall within the fields of the ANT pyroxenes, but a few are distinctly different and are probably from the pigeonite basalts (Figure III-20B). Two main groups of spinels are present. The most common variety is deep red-brown-to-opaque chromite. A few, very aluminous clear-pink-to-orange spinels, up to 300 μ in diameter, also occur. Typical analyses of both types are presented in the following:

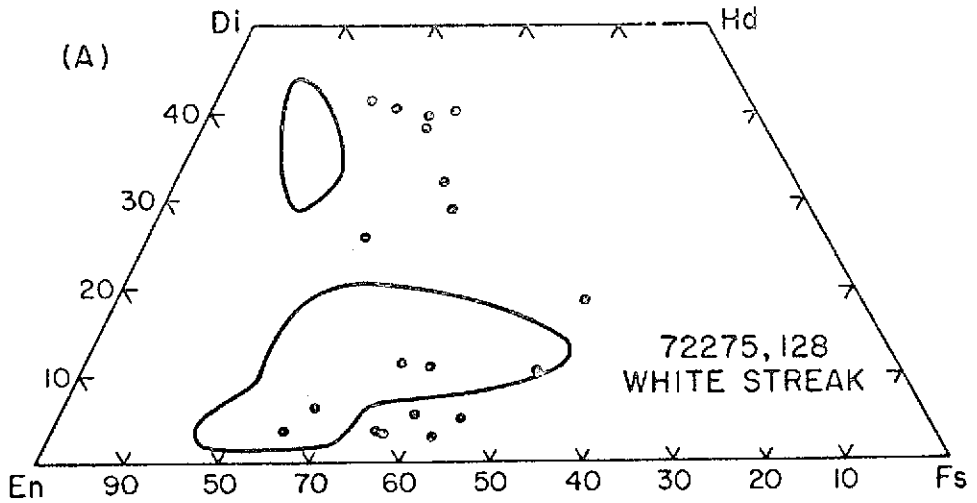

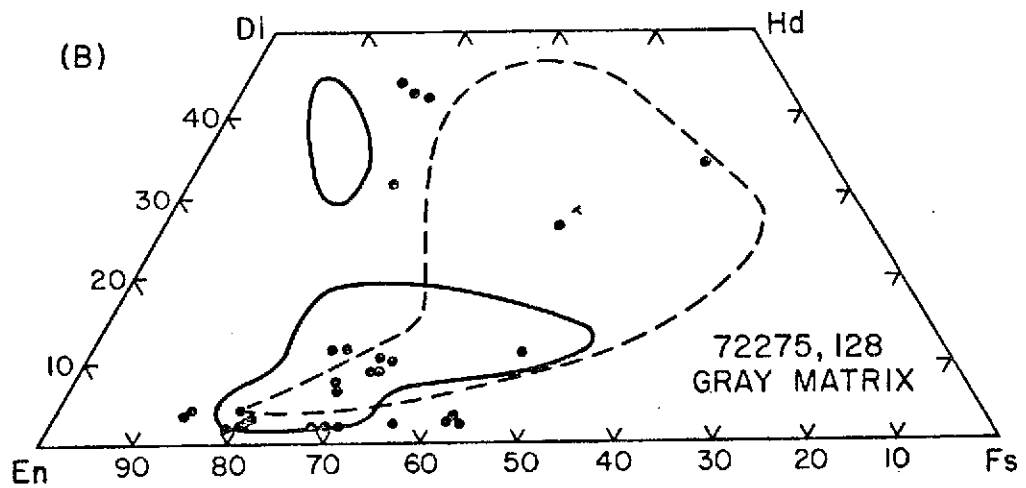

Figure III-20. A: Three-element (Mg/Fe/Ca) electron-microprobe survey of pyroxenes in a white streak in the gray polymict breccia of thin section 72275, 128. This streak can be seen as an elongated, very white area near the left arrow of Figure III-1B. The material appears to be similar to the anorthositic portions of clast #1, 72275 (see Figure III-8A). B: Monomineralic pyroxene clasts in the gray polymict breccia matrix of 72275, 12. The fields outlined by the solid lines indicate compositional range of Boulder 1 granulitic ANT pyroxenes (Figure III-5A), and that by the dashed line, pyroxenes from the pigeonite basalt breccia matrix (Figure III-11B).

	72275, 12 chromite	72275, 128 pink spinel
MgO	3.3	19.2
FeO	33.0	12.0
Al_2O_3	18.0	60.4
Cr_2O_3	44.0	8.8
TiO_2	1.3	0.1
Sum	99.6	100.5
Atomic Cr/(Cr + Al)	0.62	0.09
Atomic Mg/(Mg + Fe)	0.15	0.74

It does not seem that the gray polymict breccia matrix was subjected to high temperatures for any great length of time, as indicated by the lack of extensive sintering and the presence of small (< 100 μ), apparently undevitrified, rare glass shards of anorthositic composition. Electron-microprobe analyses of a few monomineralic olivines and pyroxenes failed to detect any re-equilibration rims against the matrix. Small silica (cristobalite?) fragments, however, had narrow reaction rims of Ca-poor pyroxene.

72255 MATRIX

The 72255 matrix, in contrast to the 72275 gray polymict breccia matrix, is dense, with a generally low porosity (0 to 10%). From megascopic examination of sample 72255, Marvin and Jackson (PET, 1973a) estimated that 72255 was 60% matrix, or about the same as 72275. The 72255 matrix consists of abundant small monomineralic and lithic clasts seated in a finely crystalline submatrix, which has an average grain size of about 5 μ (Figure III-18E). The main mineral assemblage of this submatrix is plagioclase, pyroxene, and sparsely disseminated small tabular ilmenites. The larger matrix monomineralic clasts consist of plagioclase, olivine, orthopyroxene, clinopyroxene, and sparse-to-trace amounts of pink-to-red spinel, chromite, and ilmenite.

The bulk of the 72255 matrix is dense and very dark, but a few light, more feldspathic streaks are also present (Figures III-2D and III-21) (PET, 1973a). None of

Figure III-21. Whole thin-section photograph of 72255, 8 showing the two types of matrix domains in 72255. The dark matrix domain is typical of the bulk of 72255, whereas the light-colored feldspathic area resembles the matrix of 72255. Note the occurrence of dark matrix breccia clasts.

our thin sections contains a good example of these areas, but they resemble – at least superficially – the 72275 gray polymict breccia domains. In these light-colored areas, dark matrix breccia clasts are visible (Figures III-2D and III-21). Large dark clasts can also be seen megascopically on the sample surface and in sawed slabs (Figures II-3 and II-11). In most of our thin sections of 72255, they are either absent or difficult to distinguish from the dense dark 72255 matrix itself (Figure III-2A, B, and C). Where these dark matrix breccia clasts can be distinguished, they are similar to those in 72275, except that their matrices are texturally identical to the dense portions of the 72255 matrix. It would appear that the dark matrix breccia clasts have been recrystallized to the same degree as has the rest of 72255.

Partial matrix recrystallization (Figure III-18E), the presence of re-equilibration rims up to 15 μ thick around olivines and pyroxenes (detected by electron-microprobe analysis), narrow reaction rims around spinel clasts, devitrification of all glasses, reaction rims around granitic clasts, and the partial melting of at least some of the holocrystalline granitic clasts (Figure III-14F) indicate that the 72255 matrix was initially at high temperatures. The complete devitrification of all maskylenite indicates annealing temperatures of 800°C or more for at least a few hours (Anderson et al., 1972). The partial melting of the granitic clasts indicates a minimum temperature equal to that of the orthoclase-quartz eutectic of 990° ± 20°C (Levin et al., 1964).

The texture of the 72255 matrix may be the result of high-temperature sintering with high temperatures sustained long enough to result in partial recrystallization of the matrix, or it might indicate devitrification of an initial interstitial glass. The sparsity of identifiable clasts of thermal-melt glass (now devitrified) and the great abundance of fine clastic material in the matrix would seem to make a sintering-recrystallization origin preferable. The similarity in compositions among the 72275 gray polymict breccia, the dark matrix breccias, and the 72255 matrix (Table III-6) suggests that they may be essentially the same material and that the differences in their textures may be mainly a function of their thermal histories.

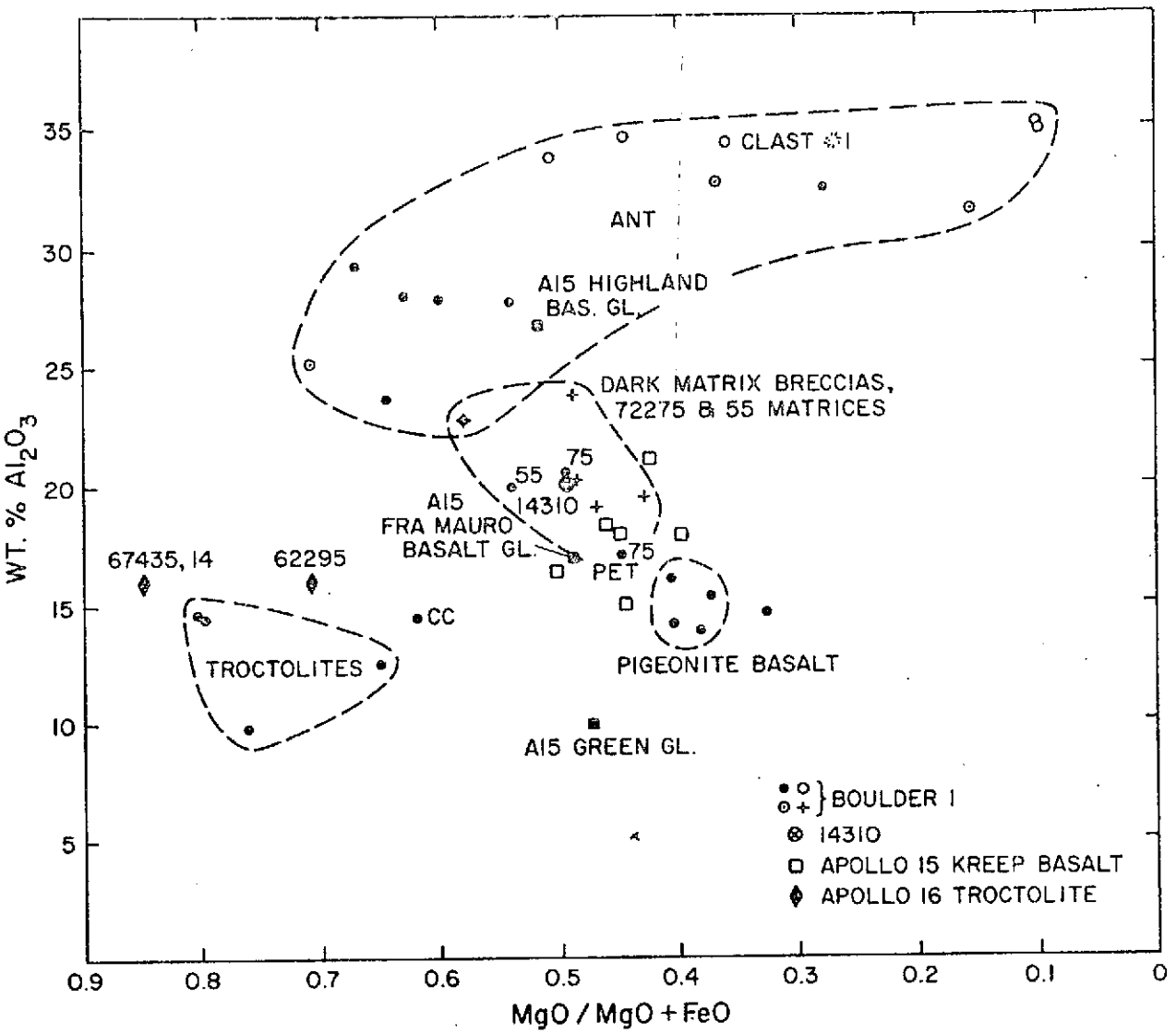

Figure III-22. Al_2O_3 versus MgO/(MgO + FeO) plot for Boulder 1 materials. In the ANT field, filled circles are used for granulitic ANT, open circles for other anorthosites, and partially filled circles for devitrified glasses. Elsewhere, filled circles are used for Boulder 1 plots, except for the dark matrix breccias, which are indicated by a plus (+). The Civet Cat norite is indicated by CC. The single point just right of the pigeonite basalt field is the "intersertal basalt" of 72255, 95 (clast #770C29, Table III-5, analysis 5, Figure III-14A). The points marked with filled squares are taken from Drake and Klein (1973). For references to the other nonboulder plots, see the captions for Figures III-5B and III-13.

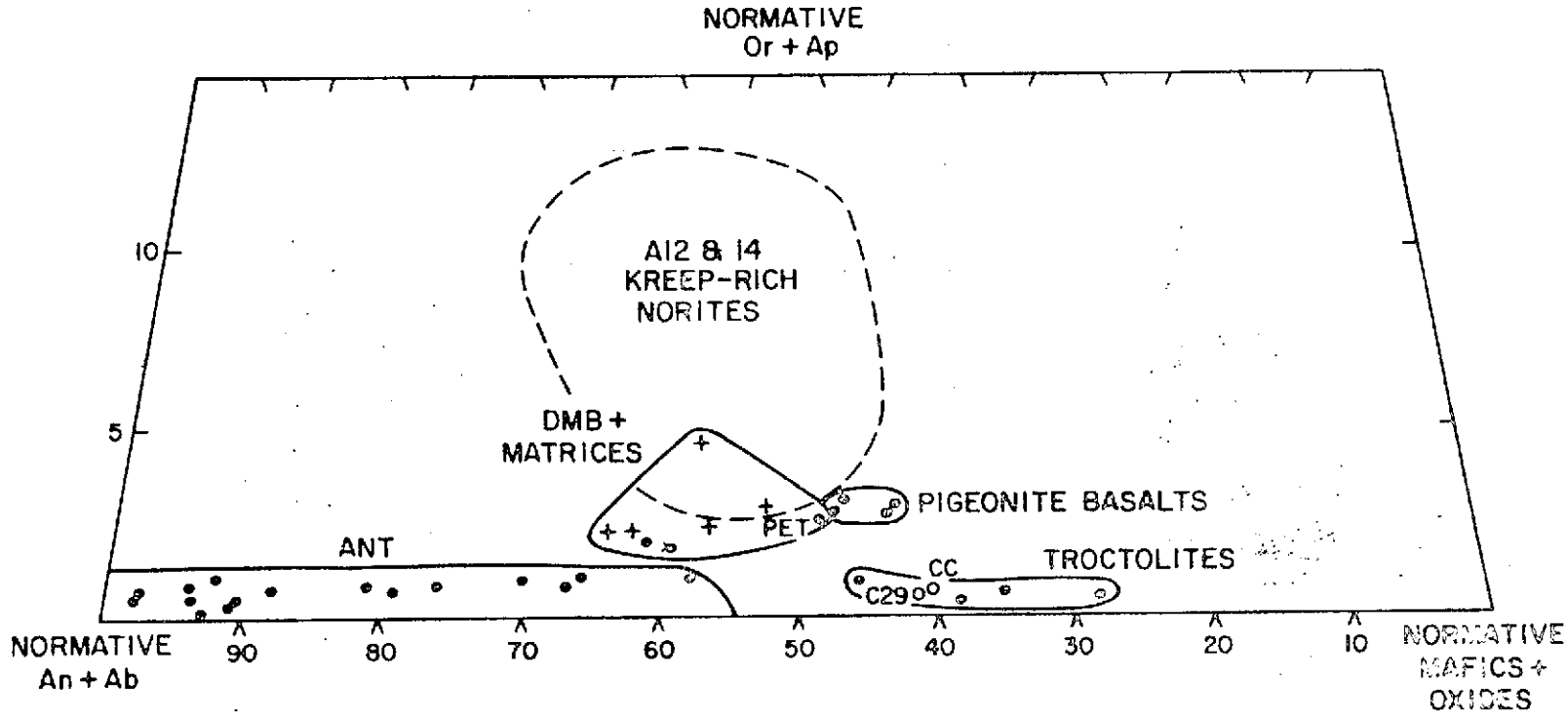

Figure III-23. Truncated triangular plot of Boulder 1 materials, in which KREEPiness is indicated by the sum of the normative wt. % of orthoclase (Or) and apatite (Ap). The normative mafics + oxides is the sum of wt. % norms of olivine, pyroxene, ilmenite, chromite, and troilite. The ANT field includes all analyses of crystalline and glassy lithic clasts of ANT composition. The field marked DMB + Matrices includes the dark matrix breccias (indicated by a +), the PET (1973b) whole-rock analysis of 72275, and the average analyses of the fine portions of the 72275 and 72255 matrices (unmarked solid circles). The two open circles that happen to plot in the troctolite field are the Civet Cat norite (CC) and the intersertal basalt clast #770C29 (Table III-5, analysis 5). The KREEP-rich norite field is taken from Taylor et al. (1972).

DISCUSSION

In their overall chemistry, the samples from Boulder 1, Station 2 fall within the range of materials collected from terra regions elsewhere on the Moon. Figures III-24 through III-28 show the relationship of several categories of boulder material to the recognized range of lunar terra rock types.

A. Nature of the Boulder Breccias

The boulder breccias examined contain no glassy spherules of the type that characterizes unconsolidated regolith samples or regolith breccias elsewhere on the Moon, nor do they contain devitrified relics of spherules. For this reason, we do not believe them to be soil breccias. (This possibility will be tested more conclusively when the noble-gas content of the boulder samples has been measured; soils – i.e., unconsolidated rock debris that has resided for a long time near the lunar surface and has been cycled through various depths by the stirring effect of meteoroid bombardment – are characterized by their high content of noble gases implanted by solar wind.)

On the other hand, we feel that the overall compositions and clast populations of samples from two different strata in the boulder are sufficiently similar to preclude the possibility that the various layers represent the ejecta deposits of many different cratering events, widely separated in space and time. It also seems unlikely that modest-sized cratering events would heat their debris to a high-enough temperature to effect the metamorphism of the debris deposits noted below. At this point, we think it most probable that Boulder 1, Station 2 is a sampling of the stratigraphic sequence of debris deposits laid down by a single, very large, very energetic cratering event. Intuitively, it seems likely that the scale of the cratering event was that of a mare-basin-forming impact. The boulder was undoubtedly once part of a much more extensive debris deposit, presumably at the crest of the South Massif (Section I); we assume that one or more minor cratering events exhumed it from these beds and rolled it down to the vicinity of Station 2.

Figures III-24 through III-28.

These five figures compare the compositions of five prominent materials from Boulder 1, Station 2 with the broad range of other rocky materials encountered on the Moon. The "pins" that comprise the plotting bases are a sampling of analyses from a library of 112 whole-rock analyses, 501 lithic fragment analyses (mostly DBAs), and 2364 glass particle analyses that we have accumulated from the literature (all missions). Not all are plotted; the library was randomly sampled in such a way as to plot about 50 each of the three categories of analyses. The three-axis plotting routine was developed to detect broad clusterings and trends among analyses of lunar materials.

The whole range of lunar materials was sampled for Figure III-24; "pins" at the far left (low Al_2O_3, variable TiO_2) are mare basalts. Only highland materials (according to criteria involving their Al_2O_3 and TiO_2 contents) are included in Figures III-25 through III-28. Entries in these plots range from noritic or gabbroic at the low-plagioclase end of the box, to anorthositic at the high-plagioclase end. Where mineral content or composition is plotted, this refers to normative mineralogy, computed from the chemical analysis.

The boulder materials plotted are entered as letters above dashed pinshafts, as follows:

- A: Pigeonite basalt (average of columns 1 to 5, Table III-5).
- B: 72275 gray matrix (column 2, Table III-6).
- C: 72255 matrix (column 3, Table III-6).
- D: Dark matrix breccia clasts (average of columns 5 to 9, Table III-6).
- E: Civet Cat clast (column 9, Table III-5).

Note that these boulder analyses are averages of DBAs from our laboratory, not the analyses of Haskin et al. (Section V). Analyses of similar materials by the two groups diverge considerably. This divergence is partly attributable to differences in accuracy and sampling coverage of atomic absorption analysis versus defocused-beam microprobe analysis, but it should also be borne in mind that we analyzed different splits and sampled them in different ways. For example, our defocused-beam analyses of breccia matrices (B, C, D) were limited to very fine-grained material; clasts as large as 50 μ in dimension were systematically avoided. Also, our analysis of the Civet Cat clast was corrected to allow for the macroscopically apparent proportions of plagioclase and pyroxene, as it seemed clear that our thin sections contained nonrepresentative proportions of these components.

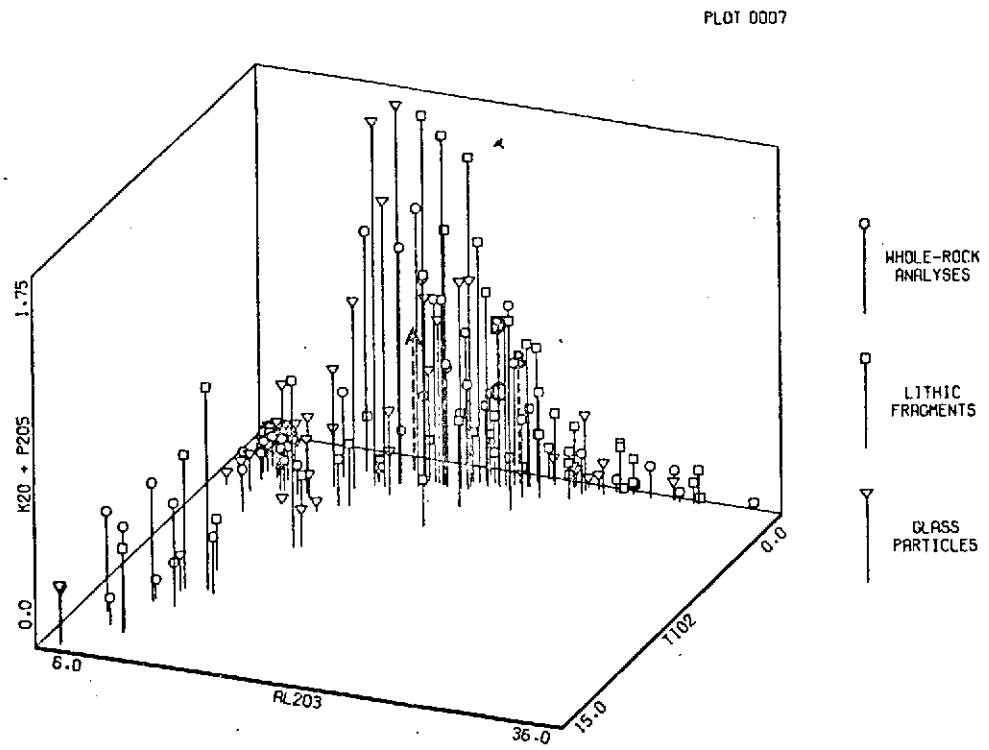

Figure III-24.

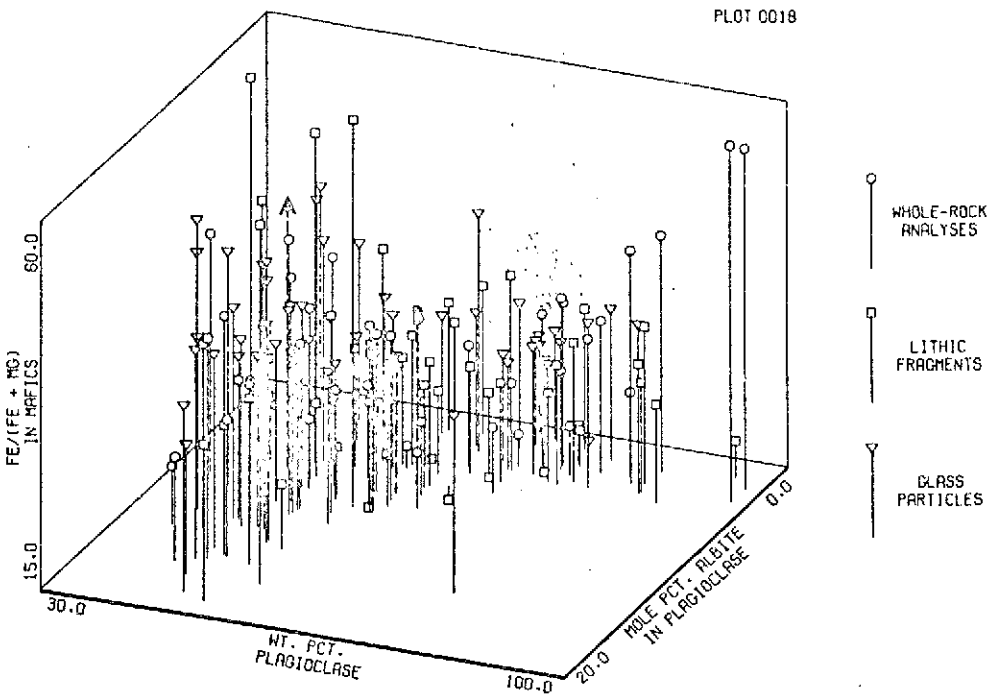

Figure III-25.

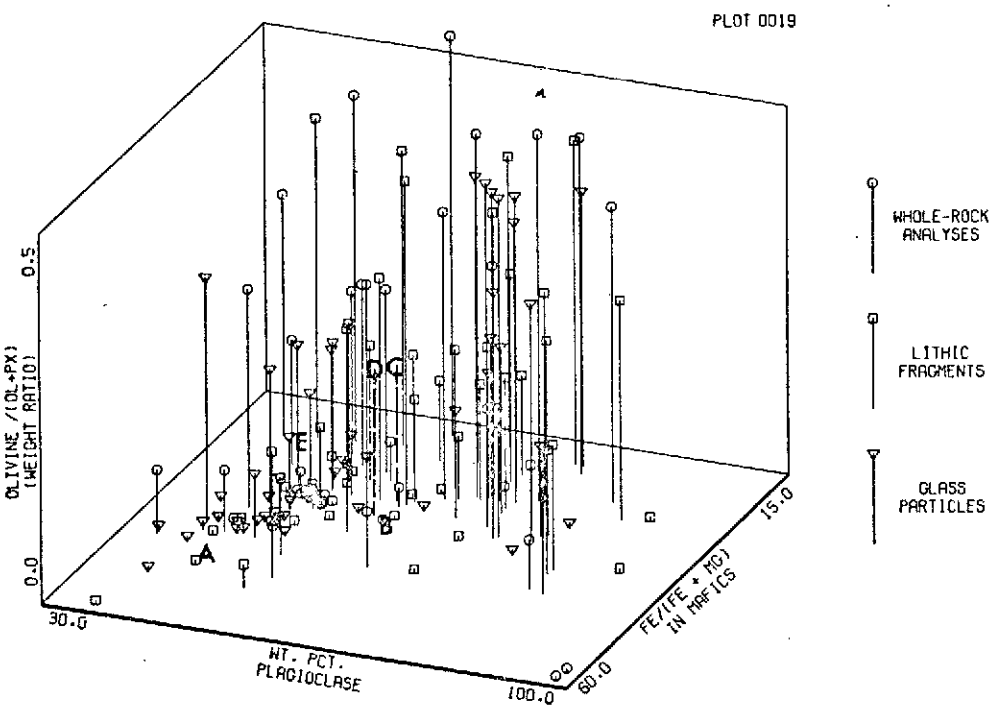

Figure III-26.

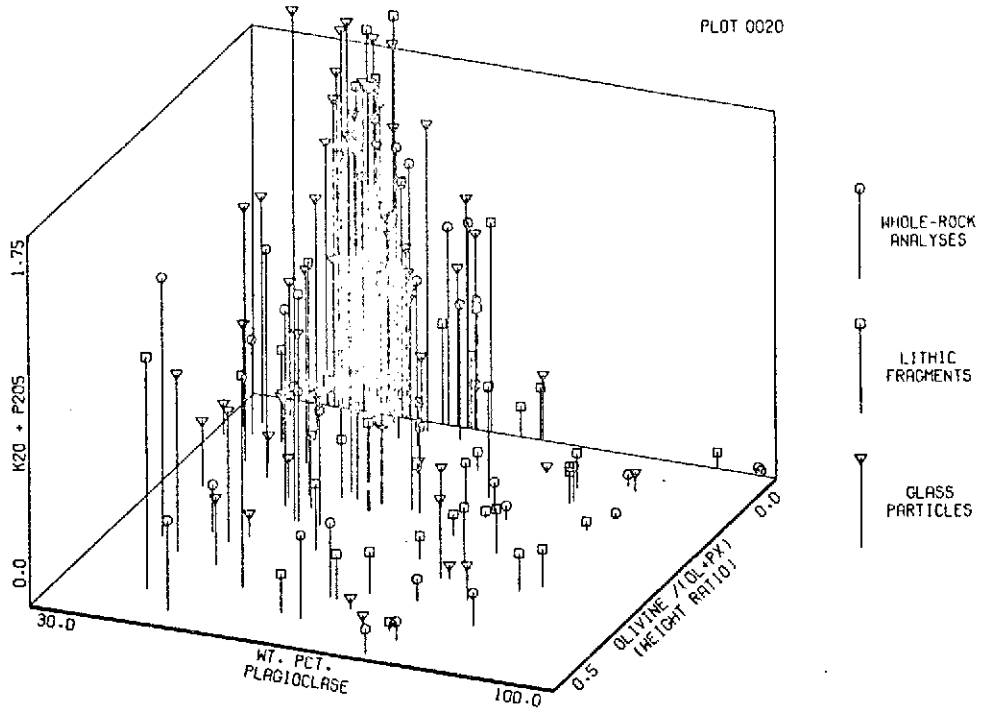

Figure III-27.

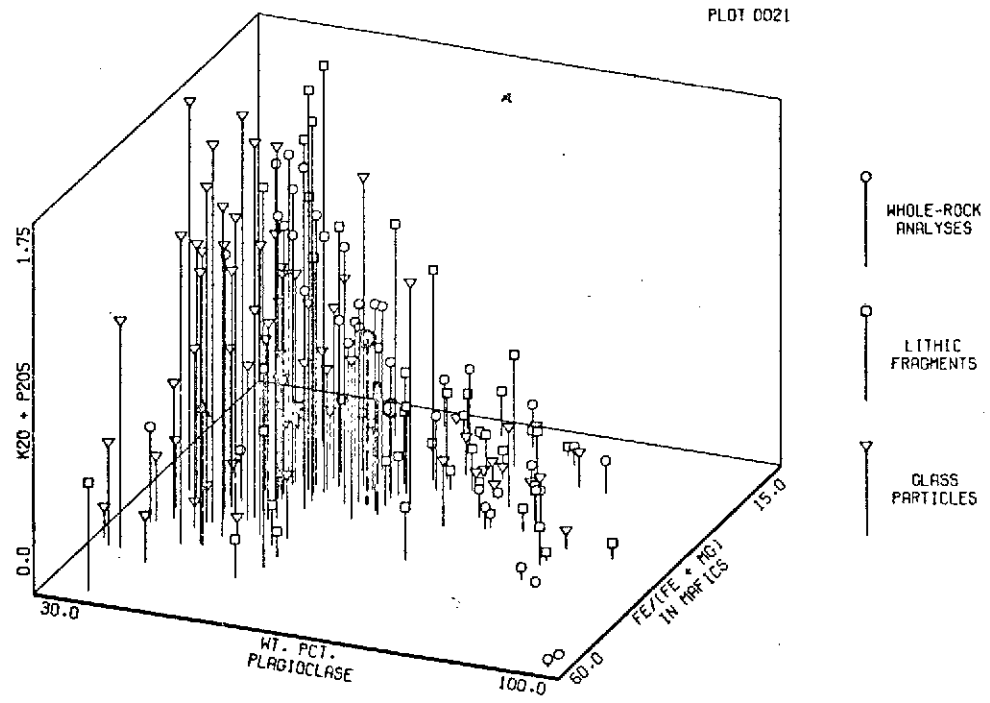

Figure III-28.

B. Which Mare Basin?

Debris from major cratering events are cast very great distances on the Moon and, in principle, many different mare basins are candidate sources for the debris that comprises Boulder 1. McGetchin et al. (1973) list seven mare basins that could have delivered to the Taurus-Littrow site mean thicknesses of debris sufficiently great to have formed the source of Boulder 1. However, Oberbeck et al. (1973) have argued that debris from a large crater is only laid down as a continuous deposit relatively close to the crater rim (in an annular region extending one to two crater radii); beyond this, the crater debris falls as discrete fragments and clumps of fragments, each of which excavates a secondary crater. During the secondary cratering process, debris from the primary crater is thoroughly mixed with and diluted by indigenous material, instead of forming a discrete blanket over the latter. From this point of view, only Mare Serenitatis is close enough to the Taurus-Littrow site to have deposited a discrete layer of basin debris. Mare Crisium, the only other possible source, is at least two crater radii away; the probability that Crisium could have deposited a thick mass of material at Taurus-Littrow (as a statistical fluctuation) is extremely small. Mare Imbrium appears to be completely out of the question.

Imbrium and Crisium debris were undoubtedly deposited at the Taurus-Littrow site, but our expectation is that all of it was mingled with indigenous (i.e., Serenitatis) material and is present now only as a minor component in complex breccias. The Boulder 1 breccias could contain such components, but we are inclined to doubt it; if small amounts of Imbrium or Crisium debris, however hot, were mixed with larger amounts of cold, indigenous material in relatively low-energy secondary cratering events, the heat content of the mixture would not be great enough to account for the metamorphic effects observed.

Other boulder and breccia samples from the Apollo 17 site are substantially different from Boulder 1 in composition and structure, but can with equal validity be understood as samples of the Serenitatis ejecta blanket. A basin-forming impact would have sampled many different lithologies, which would have mingled in various proportions and temperatures in the many jets and rays that were projected outward.

Resulting heterogeneities in the deposits can account for large-scale differences from one sample (or massif) to another, as well as for the small-scale differences within Boulder 1.

C. Pre-Basin Sources of Lithologies

A basin-forming impact on the Moon would sample from a great range of depths, from the surface to the lower crust, or even conceivably to the upper mantle (30 to 60 km deep). We tentatively assign the sources of the lithologies in Boulder 1 as follows:

A. The deep crust. Cataclastic anorthosites and Civet Cat norite must have been derived from the deep crust because of their relatively coarse grain size and simple mineralogy and, in the case of Civet Cat, because of its lack of meteoritic trace elements (see Section VI).

B. The upper crust – ancient highlands regolith (kilometers deep, brecciated, stirred, and thermally recrystallized many times). Granulitic anorthositic (ANT) rocks and troctolites are probably upper crustal materials chiefly because of their fine grain size and because of the ubiquity of the ANT lithologies everywhere the Moon has been sampled.

C. Surface of the Moon. From its texture, we interpret the pigeonite basalt in Boulder 1 as a volcanic rock, a KREEP-rich pre-mare-basalt lava that flowed onto the lunar surface before the Serenitatis(?) impact.

D. Undetermined source. The granite clasts remain a puzzle. Their fine textures make it unlikely that they were derived from granitic plutons. Since we have never observed fragments of earlier, more mafic minerals attached to the granitic clasts, the clasts must have been derived from other than merely oversized pockets of residual melt after the crystallization of some more mafic magma. Possibly they are fragments of granophyre veins, injections of residual melt into cracks in the country rock enclosing bodies of crystallizing magma.

D. Megascopic and Microscopic Structure in the Boulder

We recognize three structural entities in Boulder 1: 1) The dark, fine-grained, "globby" clasts (sometimes containing cores of anorthositic rock) that are abundant in Boulder 1 (Figures III-16 and III-17) but that have been observed in very few other lunar samples; 2) the friable breccia of 72275, similar to many highland samples returned from the Moon (and which encloses the dark clasts noted in 1 above); 3) the hard, competent breccia of 72255, which is intermediate in texture between 1 and 2 (materials of this sort are also common among previously studied lunar samples).

All three materials are, to a first order, similar in composition (see Table III-6 and Figures III-22 through III-28). They consist basically of minerals and lithic clasts from noritic (including Civet Cat) and troctolitic sources, but they also contain minor components of anorthositic and KREEPy materials. The chemical variations displayed by these materials can be understood in terms of differing levels of anorthositic and KREEP components. In the dark clasts, the KREEP component takes the form of smaller (sub)clasts of granite. In 72275, the KREEP level (and the higher degree of silica saturation) appears due to a substantial component of pigeonite basalt.

The modes of aggregation of the three classes of material are critically different. The dark, globby clasts are least readily understood. Although some of them are distinctly angular in form, it does not seem likely that the dark clasts in general were formed simply by the fragmentation of a preexisting breccia deposit, as is commonly postulated to explain the existence of breccias-within-breccias elsewhere on the Moon (e.g., the Apollo 14 samples). In the case of rebrecciation, the clasts are much more consistently angular in form than those in the boulder. The concentric core-and-rind arrangement in some boulder clasts militates against this simple origin. Rather, it seems that "globbiness" is the primary characteristic of the dark clasts in the boulder samples and that such angular clasts as exist were formed from globby clasts by secondary fragmentation.

One possibility is that the clasts were globs of molten rock, melted and thrown out by a major impact event. Comparisons have been drawn with inclusions in the Ries suevites, which were patently formed in such a way. However, the suevite inclusions

are typically quite vesicular and have been transformed almost entirely into glass. The boulder inclusions consist largely of mineral detritus and very rarely contain vesicles (Figure III-16A, B, and C shows the one prominent example we have found). One-shot melting and ejection could not produce such an aggregation, nor could it account for the concentric coating of dark clast material on anorthositic cores such as that shown in Figure III-16.

Some special place and stage in the impact process is required to form these clasts, where mineral debris was particularly finely comminuted; metallic iron was present in an extremely finely divided state, perhaps even vaporized (metallic iron is present in the clasts as 0.1 to 0.5 μ grains in a very even state of distribution); temperatures were high; and larger (anorthositic) clasts had an opportunity to accrete fine material onto their surfaces. We suggest that the clasts are aggregations of hot mineral and glass debris that collected in flight, either in ballistic trajectory or in a churning base-surge environment, in the aftermath of the hypothetical basin-forming impact that formed the boulder materials in general. Aggregation sometimes nucleated on anorthositic fragments, also in flight, that had been derived from deep in the basin. The aggregation included melt-spray droplets as well as solid debris; this liquid component both served to hold the mineral and glass debris together and lent a degree of mobility or plasticity to the mush-like accumulations, thus accounting for their globby forms.

The state of aggregation of 72275 appears easiest to account for. The 72275 breccia is a porous, friable conglomeration of mineral and lithic clasts (as well as the dark clasts discussed above), highly variable in dimension, that was deposited in a short time on the lunar surface. We suggest that the debris was hot enough when it was deposited to promote partial sintering of the grains to one another (Section IV), lending the aggregation its modest degree of coherency. Much of the debris from a Serenitatis-type event might have been deposited at temperatures too low to have given rise to any degree of sintering whatsoever, but such deposits are automatically excluded from our study (except as soil samples); a breccia even weaker than 72275 could not have survived the roll down the South Massif, nor the trip back in the Command Module.

One aspect of 72275 that is not so easy to explain is the integrity of the zone of pigeonite basalt. One can picture an isolated ray or jet from the impact delivering a rain of pure pigeonite basalt to the site of deposition; but as the particles impacted the depositional surface at ballistic velocities, we would expect secondary cratering and thorough mixing of the pigeonite basalt with lithologies deposited earlier.

One possibility is that the pigeonite basalt had accreted in flight (as discussed above for dark globby breccias) and was deposited as a coherent mass; under these circumstances, however, we would expect to observe pronounced interfaces between pigeonite basalt zones and enclosing matrix, as is the case with dark breccia clasts; these are lacking. Conceivably, the pigeonite basalt mass developed just enough coherency in flight to shatter but not mix when it impacted the lunar surface.

Another possibility is that the pigeonite basalt was deposited as a single large lithic clast, which was subsequently brecciated in situ by shock events accompanying the deposition of later units. However, it is puzzling that the dark breccia clasts still visible were not also disrupted by these hypothetical stresses.

The competent portions of 72255 can best be described as having properties intermediate between dark globby breccia clasts and 72275. The layer that 72255 was taken from may have been hotter when deposited than the 72275 layer, and therefore was more rigidly sintered. Or compositional differences might have made the 72255 layer more amenable to sintering than the 72275 layer. (This seems unlikely, however; Section V shows that 72275 contains a higher level of the KREEP component – which correlates with easily meltable material – than does 72255.)

Alternatively, the 72255 layer may actually be a very large "dark globby clast," rather than a discontinuously deposited layer of indefinite extent. In photographs of the boulder (Figure II-1), the unit that 72255 came from appears more like a pod than a continuous layer. The astronauts stated, at the time 72255 was taken, that they were sampling a clast.

At this point, we tend to think of the competent portions of 72255 as occupying a position intermediate between these two modes of aggregation. This may seem unrealistic; a mass of material was deposited either as a coherent whole or as independent particles. However, we found in trying to evaluate the various lithologies in the 72255 slab (Figures II-11 and III-21) that all gradations exist between obvious dark clast material and obvious friable enclosing matrix material; there is no sharp line of demarcation between the two. This has eroded our confidence in our ability to provide a pat explanation for all lithologies. A definitive explanation for the 72255 competent lithology will have to await our pronouncement in Volume 2 or Volume 3 of this series.

ACKNOWLEDGMENTS

We are indebted to Mss. Karen Motylewski and Judy Stoeser for preliminary editing and typing, to Mss. Arlene Walsh and Vicki Snow for compiling the analyses of lunar materials plotted in Figures III-24 to III-28, and to Mr. Elwood Adams for manning the CalComp plotter at the SAO Computer Center.

REFERENCES

Anderson, A. T., Brazunas, T. F., Jacoby, J., and Smith, J. V. (1972). Thermal and mechanical history of breccias 14306, 14270, and 14321. Proc. Third Lunar Sci. Conf., Geochim. Cosmochim. Acta, Suppl. 3, vol. 1, pp. 819-835.

Cameron, K. L., Delano, J. W., Bence, A. E., and Papike, J. J. (1973). Petrology of the 2-4 mm soil fraction from the Hadley-Apennine region of the moon. Earth Planet. Sci. Lett., vol. 19, pp. 9-21.

Delano, J. W., Bence, A. E., Papike, J. J., and Cameron, K. L. (1973). Petrology of the 2-4 mm soil fraction from the Descartes region of the moon and stratigraphic implications. Proc. Fourth Lunar Sci. Conf., Geochim. Cosmochim. Acta, Suppl. 4, vol. 1, pp. 537-551.

Drake, J. C., and Klein, C., Jr. (1973). Lithic fragments and glasses in microbreccia 15086: Their chemistry and occurrence. Proc. Fourth Lunar Sci. Conf., Geochim. Cosmochim Acta, Suppl. 4, vol. 1, pp. 467-479.

Engelhardt, W. von, Arndt, J., Stöffler, D., and Schneider, H. (1972). Apollo 14 regolith and fragmental rocks, their compositions and origin by impacts. Proc. Third Lunar Sci. Conf., Geochim. Cosmochim. Acta, Suppl. 3, vol. 1, pp. 753-770.

Hodges, F. N., and Kushiro, I. (1973). Petrology of Apollo 16 lunar highland rocks. Proc. Fourth Lunar Sci. Conf., Geochim. Cosmochim. Acta, Suppl. 4, vol. 1, pp. 1033-1048.

Keil, K., Kurat, G., Prinz, M., and Green, J. A. (1972). Lithic fragments, glasses and chondrules from Luna 16 fines. Earth Planet. Sci. Lett., vol. 13, pp. 243-256.

Levin, E. M., Robbins, C. R., and McMurdie, H. F. (1964). Phase Diagrams for Ceramists. Amer. Ceramic Soc., Columbus, Ohio, p. 158 (see Figure 412).

Longhi, J., Walker, D., and Hays, J. F. (1972). Petrology and crystallization history of basalts 14310 and 14072. Proc. Third Lunar Sci. Conf., Geochim. Cosmochim. Acta, Suppl. 3, vol. 1, pp. 131-139.

McGetchin, T. R., Settle, M., and Head, J. W. (1973). Radial thickness variation in impact crater ejecta: Implications for lunar basin deposits. Earth Planet. Sci. Lett., vol. 20, pp. 226-236.

Meyer, C., Jr., Brett, R., Hubbard, N. J., Morrison, D. A., McKay, D. S., Aitken, F. K., Takeda, H., and Schonfeld, E. (1971). Mineralogy, chemistry, and origin of the KREEP component in soil samples from the Ocean of Storms. Proc. Second Lunar Sci. Conf., MIT Press, Cambridge, Mass., vol. 1, pp. 393-411.

Oberbeck, V. R., Hörz, F., Morrison, R. H., and Quaide, W. L. (1973). Emplacement of the Cayley Formation. NASA Tech. Memorandum TM X-62, 302, 38 pp.

PET (Preliminary Examination Team) (1973a). Lunar Sample Information Catalog – Apollo 17. Lunar Receiving Laboratory, Lyndon B. Johnson Space Center, Houston, 447 pp.

PET (Preliminary Examination Team) (1973b). Apollo 17 lunar samples: Chemical and petrographic description. Science, vol. 182, pp. 659-690.

Phinney, W. C., Warner, J. L., Simonds, C. H., and Lofgren, G. E. (1972). Classification and distribution of rock types at Spur Crater. In The Apollo 15 Lunar Samples, Lunar Science Institute, Houston, pp. 149-153.

Prinz, M., Dowty, E., Keil, K., and Bunch, T. E. (1973a). Mineralogy, petrology and chemistry of lithic fragments from Luna 20 fines: Origin of the cumulate ANT suite and its relationship to high-alumina and mare basalts. Geochim. Cosmochim. Acta, vol. 37, pp. 979-1006.

Prinz, M., Dowty, E., Keil, K., and Bunch, T. E. (1973b). Spinel troctolite and anorthosite in Apollo 16 samples. Science, vol. 179, pp. 74-76.

Reid, A. M., Warner, J., Ridley, W. I., Johnson, D. A., Harmon, R. S., Jakes, P., and Brown, R. W. (1972). The major element compositions of lunar rocks as inferred from glass compositions in the lunar soils. Proc. Third Lunar Sci. Conf., Geochim. Cosmochim. Acta, Suppl. 3, vol. 1, pp. 363-378.

Reid, J. B., Jr. (1972). Olivine-rich, true spinel-bearing anorthosites from Apollo 15 and Luna 20 soils – Possible fragments of the earliest formed lunar crust. In The Apollo 15 Lunar Samples, Lunar Science Institute, Houston, pp. 154-157.

Taylor, G. J., Marvin, U. B., Reid, J. B., Jr., and Wood, J. A. (1972). Noritic fragments in the Apollo 14 and 12 soils and the origin of Oceanus Procellarum. Proc. Third Lunar Sci. Conf., Geochim. Cosmochim. Acta, Suppl. 3, vol. 1, pp. 995-1014.

Taylor, G. J., Drake, M. J., Hallam, M. E., Marvin, U. B., and Wood, J. A. (1973). Apollo 16 stratigraphy: The ANT hills, the Cayley Plains, and a pre-Imbrium regolith. Proc. Fourth Lunar Sci. Conf., Geochim. Cosmochim. Acta, Suppl. 4, vol. 1, pp. 553-568.

Walker, D., Longhi, J., Grove, T. L., Stolper, E., Hays, J. F. (1973). Experimental petrology and origin of rocks from the Descartes Highlands. Proc. Fourth Lunar Sci. Conf., Geochim. Cosmochim. Acta, Suppl. 4, vol. 1, pp. 1013-1032.

IV. PRELIMINARY RESULTS OF EXPERIMENTS TO DUPLICATE BOULDER TEXTURES BY THERMAL SINTERING OF POWDERS

Marie E. Hallam

Center for Astrophysics
Harvard College Observatory and Smithsonian Astrophysical Observatory
Cambridge, Massachusetts 02138

Petrography of Boulder 1 samples 72255 and 72275 reveals three distinct matrix textures (see Section III of this compendium, Figure III-18):

A. Compact, cohesive material with a visually estimated porosity of 5 to 10% and an average grain size much less than 1 μ. This material forms the matrix of the dark matrix breccias and the rims of cored anorthositic-noritic-troctolitic (ANT) clasts.

B. Compact, cohesive material with a visually estimated porosity of 5 to 10% and an average grain size of about 4 μ. This material forms the medium-to-dark gray matrix of 72255.

C. Very porous, very friable material with a visually estimated porosity of 30 to 40%. This material forms the light gray matrix of 72275.

All three matrix types have very nearly the same chemical composition (Table IV-1). The principal distinction to be made among them is textural.

One process capable of producing the varying degrees of porosity and cohesiveness observed in these matrix materials is sintering. Sintering is essentially the welding together of initially distinct grains at temperatures below or about the minimum melting temperature of the given system under consideration. The driving force for this process is surface free energy – in other words, sintering operates to reduce this particular property of the system. The chief effect observed is shrinkage, which becomes evident microscopically and macroscopically as an increase in density and a decrease in porosity.

Table IV-1. Average oxide compositions of three Boulder 1 matrix types, from defocused-beam microprobe analyses.

Oxide	72275, 128 gray polymict breccia	72255, 95 dark gray	72275, 134 dark matrix breccia
SiO_2	47.3	45.1	47.7
TiO_2	0.6	0.6	1.1
Cr_2O_3	0.1	0.2	0.2
Al_2O_3	21.3	20.0	20.3
FeO	8.8	7.7	10.6
MnO	0.1	0.1	0.2
MgO	8.3	9.1	10.0
CaO	12.4	12.7	11.5
Na_2O	0.4	0.5	0.5
K_2O	0.1	0.2	0.2
P_2O_5	0.5	0.2	0.4
Total	99.9	96.4	102.7
Number of analyses averaged	26	40	21

It has been suggested that lithification of Apollo 14 breccias took place by sintering of glassy material in an ejecta-blanket environment (Simonds, 1973). (The matrices of some of these breccias have a texture closely resembling the 72255 matrix described above.) To test the idea that sintering played an important role in the lithification of the boulder, we have begun a course of experiments to compare textures produced from Boulder 1 sawdust by sintering and devitrification of glass powder, sintering of crystalline powder, and devitrification of glass chunks.

EXPERIMENTAL METHODS

About 0.2 g of boulder sawdust was ground under acetone for 10 min with an agate mortar and pestle. In each run where sawdust was the starting material, approximately 2 to 4 mg of the resulting powder was utilized.

The experimental method employed is the same as one described in detail by Walker et al. (1972); we shall therefore only summarize it here. The experiments listed in Table IV-2 were performed in vacuo in sealed silica tubes. During the evacuation procedure, each sample was mildly heated to drive off volatiles. The silica tube was sealed under vacuum and lowered into the hot spot of a vertical Pt-wound furnace. Temperature was continuously monitored and automatically controlled. All runs were terminated by quenching into water. Quench times were not longer than a few seconds.

All samples were run in "hog" capsules of exceptionally high-purity iron. Use of these very high-quality iron containers places oxygen fugacity in our experiments below iron-wüstite buffer values; the actual value for an individual experiment can be much more accurately evaluated by determining the Fe/Mg ratio of the product (Walker et al., 1973).

PRELIMINARY EXPERIMENTAL RESULTS

The conditions and results of experiments performed to date are summarized in Table IV-2.

Table IV-2. Summary of runs using Boulder 1 sawdust.

Run number	Time (hr)	Temperature °C, ±1	Purpose of run	Starting material	Products; comments
275-1	20	1142	Sinter	Sawdust, uncompacted	Cohesive, low-porosity material; above solidus
275-2	5	1275	Establish liquidus	Sawdust, uncompacted	Glass, one fragment containing plagioclase; slightly below liquidus
275-3	5	1300	Establish liquidus	Sawdust, uncompacted	Glass; above liquidus
275-3*	3	1100	Sinter/devitrify	Glass powder, product of 275-3	Well-sintered and devitrified material; resembles 72255 matrix but grain size smaller
275-4	15.75	1000	Sinter/devitrify	Glass powder, made by fusing sawdust at 1300°C for 1.75 hr, then quenching	Sintered and partially devitrified; some glass remaining
275-5	18.25	898	Sinter/devitrify	Glass powder, made by fusing sawdust at 1300°C for 2 hr, then quenching	Sintered and partially devitrified; some glass remaining
275-6	18.25	898	Sinter	Sawdust, uncompacted	No change; no coherence other than electrostatic
275-7	100	1000	Sinter	Sawdust, uncompacted	No change; no coherence other than electrostatic
275-8	53	1075	Sinter	Sawdust, uncompacted	Slightly sintered; weak coherence
275-8*	88.25	1075	Sinter; continuation of 275-8	Product of 275-8	Slightly sintered; weak coherence; no change from 275-8

*Indicates continuation of previous run.

Attempts to dry-sinter uncompacted crystalline sawdust at temperatures of 1000° C and below for periods of 100 hr or less were unsuccessful, resulting in no change in porosity or cohesiveness of the starting material. In contrast, wet-sintering of uncompacted sawdust at about 1140°C (slightly above the estimated solidus of the system) for 20 hr produced a material having even lower porosity than the dark matrix breccia matrix and the dark gray matrix of 72255 (Figure IV-1A, see below).

Boulder sawdust begins to sinter at about 1075°C. Heating at this temperature for approximately one week produced a very weakly sintered material having even less coherence than the 72275 matrix.

Powdered glass (produced by fusion of sawdust at 1300°C) was also run at temperatures of 900, 1000, and 1100°C for times ranging from 3 to 19 hr. Figures IV-2A, B, and C show reflected-light photomicrographs of the products of these runs. After heating at 900 and 1000°C, the products had undergone appreciable sintering but still contained residual glass. At 1100°C, extensive sintering and complete devitrification had occurred. The dark matrix breccia matrix, shown in Figure IV-2D, looks texturally intermediate between the products of the runs at 900 and 1000°C.

In Figure IV-1, we compare the light gray matrix of 72255 to textures produced during experimental runs. Figure IV-1A shows sawdust wet-sintered at 1142°C for 20 hr. Extensive recrystallization and welding of the sawdust occurred in this run. The texture of the product is similar to that of the 72255 matrix (Figure IV-1B), but the average grain size is much larger. In Figure IV-2C, we see that glass powder of the same composition, run at 1100°C for 3 hr, has sintered and completely devitrified, forming a material that texturally resembles the 72255 matrix but has a grain size (~1 μ) much smaller than that of the 72255 matrix (~4 μ).

These experiments seem to indicate that at the low pressures characteristic of an ejecta blanket, sintering or sintering/devitrification could have lithified Boulder 1 matrix materials and produced the textural types observed in 72255 and 72275. If so, this very preliminary conclusion is consistent with Stoeser et al.'s observation (see Section III of this compendium, especially Figure III-13F) that granitic clasts have undergone a slight degree of partial melting (and have therefore experienced temperatures

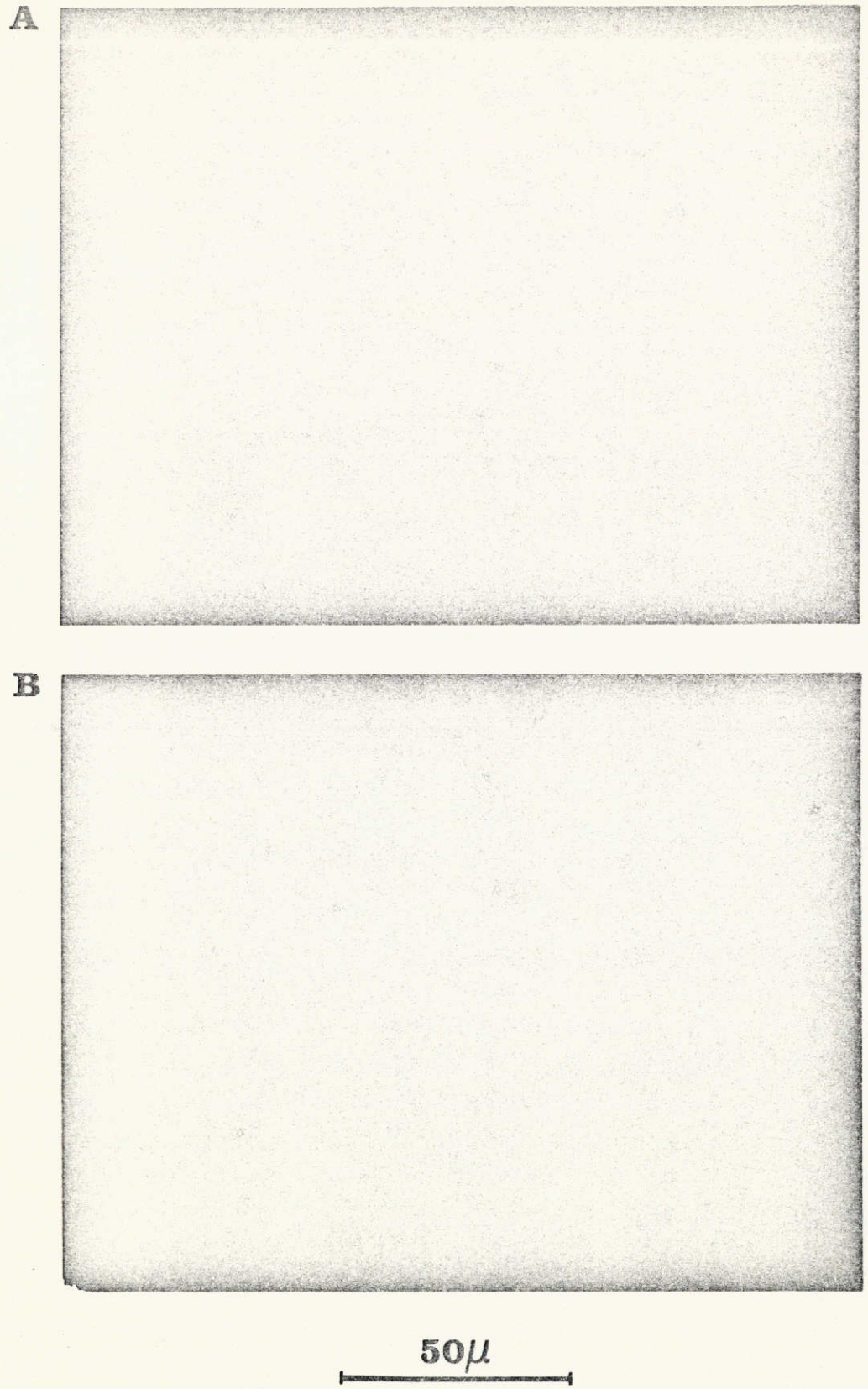

Figure IV-1. Reflected-light photomicrographs of A: Boulder sawdust, sintered and partially melted at 1142°C for 20 hr; B: Boulder sawdust, sintered at 1000°C for 100 hr.

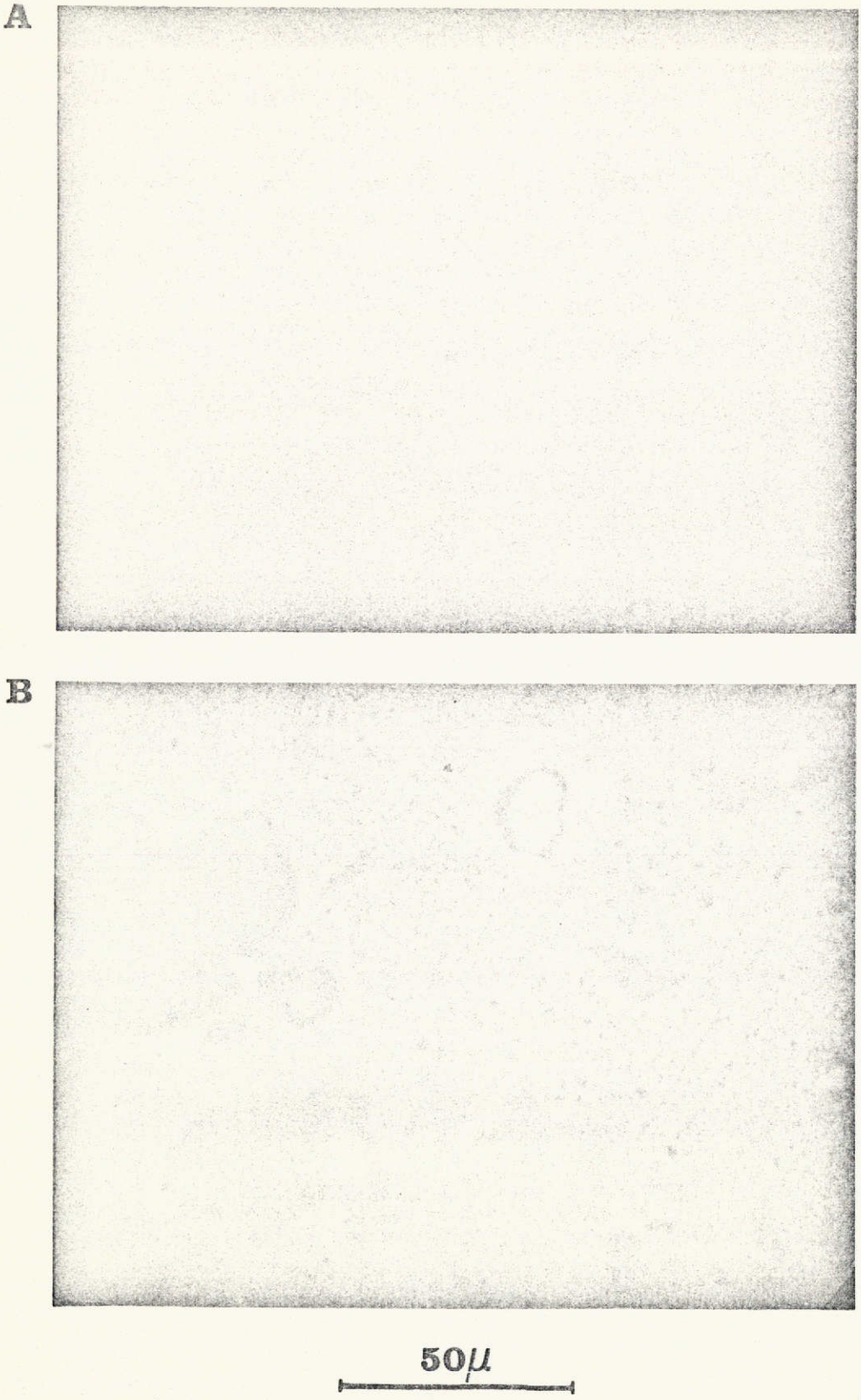

Figure IV-2. Reflected-light photomicrographs of A: Glass powder (made by fusing boulder sawdust at 1300°C), sintered and devitrified at 900°C for 18 hr; B: Same glass powder, sintered and devitrified at 1000°C for 16 hr.

C

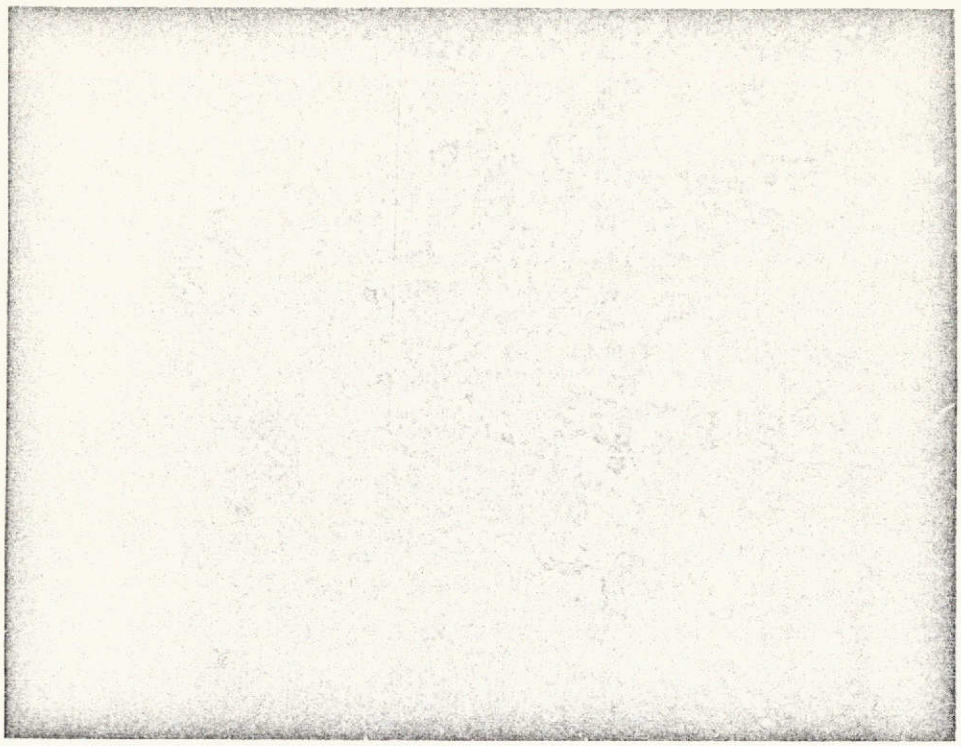

Figure IV-1 (cont.). C: Reflected-light photomicrograph of 72255 matrix.

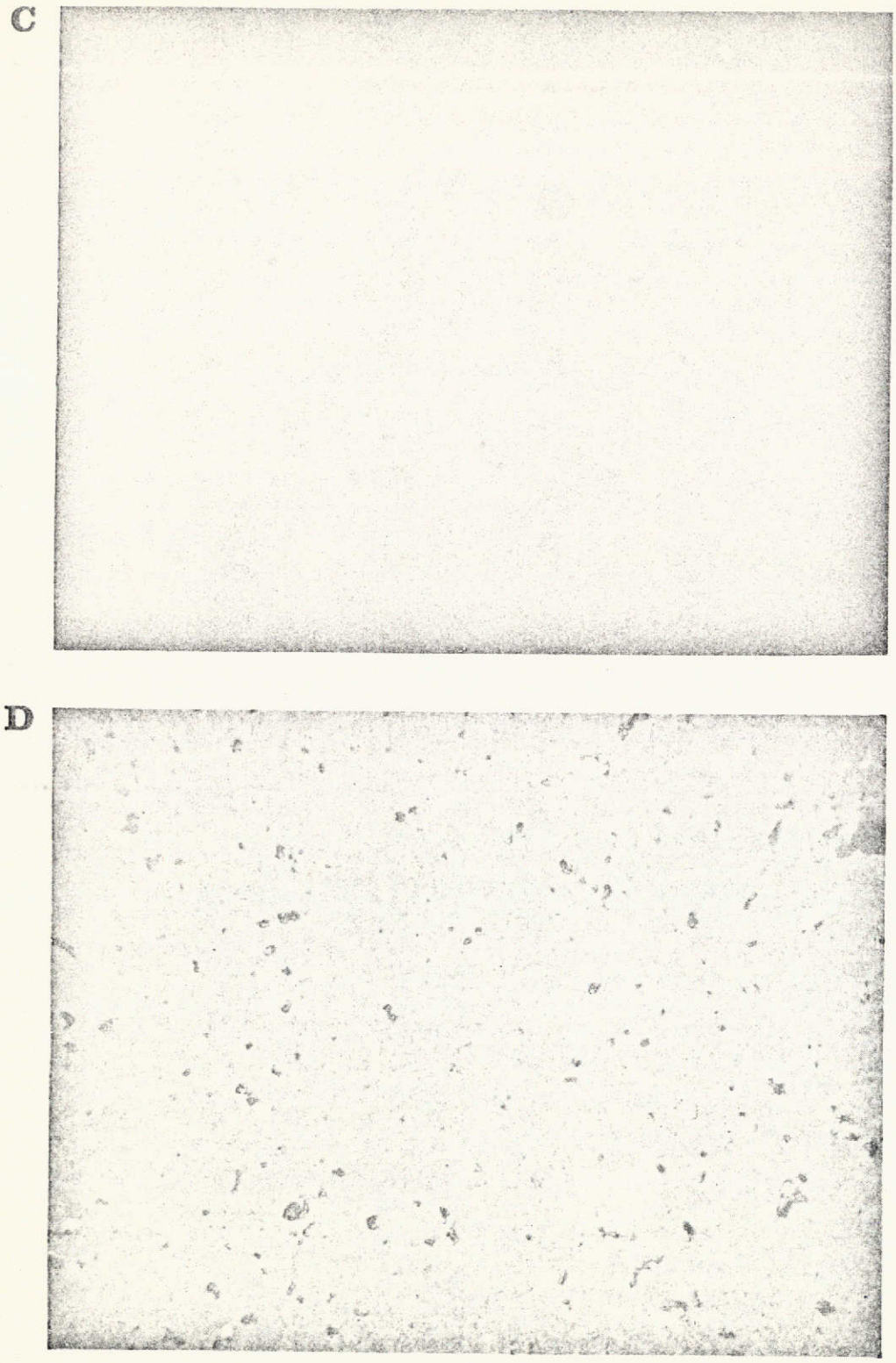

Figure IV-2 (cont.). Reflected-light photomicrographs of C: Same glass powder, sintered and devitrified at 1100°C for 3 hr; D: 72275 dark matrix breccia matrix.

on the order of 1000°C). This conclusion is also in agreement with Stoeser et al.'s report (Section III) that maskelynite in the boulder is completely devitrified; according to Bunch et al. (1969), maskelynite devitrifies almost completely above 900°C in 2 hr but shows little or no apparent change when heated at 800°C for 4 hr.

ACKNOWLEDGMENT

We wish to thank Dave Walker, without whose cooperation and assistance this work would not have been done.

REFERENCES

Bunch, T. E., Cohen, A. J., and Dence, M. R. (1969). Shock-induced structural disorder in plagioclase and quartz. In Shock Metamorphism of Natural Materials, ed. by B. M. French and N. M. Short, Mono Book Corp., Baltimore, pp. 509-519.

Simonds, C. H. (1973). Sintering and hot pressing of Fra Mauro composition glass and the lithification of lunar breccias. Amer. Journ. Sci., vol. 273, pp. 428-439.

Walker, D., Longhi, J., and Hays, J. F. (1972). Experimental petrology and origin of Fra Mauro rocks and soil. In Proc. Third Lunar Sci. Conf., Geochim. Cosmochim. Acta, Suppl. 3, vol. 1, pp. 799-817.

Walker, D., Longhi, J., Grove, T. L., Stolper, E., and Hays, J. F. (1973). Experimental petrology and origin of rocks from the Descartes Highlands. In Proc. Fourth Lunar Sci. Conf., Geochim. Cosmochim. Acta, Suppl. 4, vol. 1, pp. 1013-1032.

V. MAJOR- AND TRACE-ELEMENT CONCENTRATIONS IN SAMPLES FROM 72275 AND 72255

L. A. Haskin, D. P. Blanchard, R. Korotev, J. W. Jacobs, J. A. Brannon, R. S. Clark

NASA Lyndon B. Johnson Space Center
Houston, Texas 77058

and

A. G. Herrmann

Lunar Science Institute
Houston, Texas 77058

Analytical data have now been obtained for Co, Sc, Hf, Zn, Cr, Ga, Rb, Cs, Ni, major elements, and rare-earth elements (REE) in eight samples from Boulder 1 (see Tables V-1 and V-2). The data for trace elements were obtained by radiochemical neutron activation analysis. Major elements, except Na and Mn, were obtained by atomic absorption spectral photometry as in previous work (Helmke et al., 1973; Haskin et al., 1973) but with slightly poorer precision and no values for SiO_2 for the present, owing to a change in spectral photometers and associated problems. The uncertainty for FeO in Table V-2 is ±5% of the reported value. We expect to provide more precise values for Fe as well as the value for SiO_2 in the near future. The accuracy has been tested so far by the internal consistency of the results (i.e., SiO_2 values obtained by difference are reasonable) and by a single analysis of sample 65015. Values for Na and Mn were obtained by neutron activation analysis of the same powder that was later dissolved to provide the atomic absorption analyses. A single value for 72275 obtained by PET agrees well with the values for major elements reported here (PET, 1973).

The massif rocks, as PET indicated, are unexpectedly rich in refractory trace elements, somewhat reminiscent of the Fra Mauro material from Apollo 14. Concentrations of these elements in the massif rocks are not so extreme, however, as those in the Apollo 14 samples. Of the two rocks analyzed so far, 72275 has higher REE concentrations than does 72255, with only a slight overlap between the two. The slope

Table V-1. Trace-element concentrations for samples from 72275 and 72255.

	72275,91 Pigeonite basalt*	72275,83 Dark clast #2	72275,80 Dark rind, clast #1	72275,76 Light core, clast #1	72275,57 Matrix	72255,69 Dark matrix	72255,52 Light matrix	72255,42 Civet Cat clast
La	48 ± 1	41	78	48	47	43	31	16
Ce	131 ± 2	112	220	131	150	95	80	46
Nd	82 ± 4	67	130	76	100	69	57	26
Sm	23.0 ± 0.2	18.7	35.5	22.4	24.5	20	15.5	7.6
Eu	1.58 ± 0.05	1.50	2.18	1.81	1.67	1.76	1.49	1.75
Tb	4.5 ± 0.2	3.8	7.6	4.7	6.1	4.7	3.8	1.9
Dy	25.9 ± 0.4	22.4	43	28				
Ho	5.8 ± 0.6	5.2	9.7	6.4	6.8	6.0	4.7	2.7
Yb	11.9 ± 0.5	12.1	23	13.9	15.1	14.8	11.6	6.6
Lu	1.75 ± 0.03	1.82	3.5	2.04	2.21	2.25	1.69	1.01
Co	36.8 ± 0.8	30	28	18.7	27	21	28	29
Sc	60.6 ± 0.2	28	34	25	39	19.5	19.8	13.2
Hf	17.8 ± 0.5	13.7	19.8	14	14.0	13.1	9.8	5.5
Zn	4.0 ± 0.7	<16	<3.3	<6.7	<1.8	<1.8	<2.8	1.9
Cr	3140 ± 60	1610	3140	1390	1680	2110	1510	1100
Ga	3.14 ± 0.02	3.3	4.0	3.7	3.4	3.6	3.7	3.9
Rb	10 ± 1	5.7 ± 0.8	16 ± 2	11 ± 1	9 ± 2	8 ± 2	5 ± 1	3 ± 1
Cs	0.42 ± 0.04	0.29	0.60	0.40	0.41	0.33	0.31	0.11
Ni	<40	<15	32	<30				

*The uncertainties are ±1 standard deviation based on counting statistics. These uncertainties, converted to percentages, can be applied to the trace-element data for the other samples. (For a better assessment of accuracy and precision, see Kosiewicz et al., 1974.)

Table V-2. Major-element concentrations for samples from 72275 and 72255.

		72275,57 Matrix	72275,76 Light core, clast #1	72275,80 Dark rind, clast #1	72275,83 Dark clast #2	72275,91 Pigeonite basalt	72255,42 Civet Cat clast	72255,52 Light matrix	72255,69 Dark matrix
SiO_2*		48	47	47	46	46	52	49	48
TiO_2		0.8	1.8	1.8	1.5	0.7	0.3	1.4	0.9
Al_2O_3		17.9	23.5	17.9	13.9	19.8	15.0	14.5	18.9
FeO		9.9	7.4	10.3	15	9.8	7.4	14	9.8
MnO		0.12	0.077	0.104	0.156	0.111	0.122	0.163	0.108
MgO		11.0	5.24	9.43	9.38	10.4	15.9	9.71	10.3
CaO		11.0	14.2	11.7	10.9	12.3	9.1	10.7	11.2
Na_2O		0.40	0.36	0.39	0.29	0.38	0.33	0.32	0.40
K_2O		0.22	0.32	0.47	0.26	0.25	0.08	0.27	0.28
Cr_2O_3†		0.25	0.20	0.46	0.24	0.46	0.16	0.22	0.31
					Normative Mineralogies				
weight percentages	Fo	1.8	0.0	1.2	0.0	7.3	0.0	0.0	1.4
	Fa	1.2	0.0	0.9	0.0	5.2	0.0	0.0	1.0
	En	25.0	13.1	21.9	23.5	15.5	39.5	24.1	23.6
	Fs	15.3	10.6	14.6	25.2	9.9	13.1	23.4	15.1
	Wo	3.4	3.7	5.2	7.6	3.9	2.5	6.6	2.8
	Or	1.3	1.9	2.8	1.5	1.5	0.5	1.6	1.7
	Ab	3.4	3.0	3.3	2.5	3.2	2.8	2.7	3.4
	An	46.6	61.6	46.0	36.0	51.5	39.1	37.3	48.9
	Il	1.5	3.4	3.4	2.9	1.3	0.6	2.6	1.7
	Chr	0.4	0.3	0.7	0.4	0.7	0.2	0.3	0.5
	Qtz	0.0	2.5	0.0	0.4	0.0	1.8	1.3	0.0
mole percentages	Fo	68.1	–	66.3	–	67.2	–	–	67.2
	Fa	31.9	–	33.7	–	32.8	–	–	32.8
	En	63.0	53.7	58.4	47.6	58.6	76.5	50.7	63.0
	Fs	29.5	33.1	29.7	39.0	28.6	19.3	37.4	30.7
	Wo	7.5	13.2	11.9	13.4	12.8	4.1	11.9	6.3
	Or	2.5	2.8	5.3	3.8	2.6	1.1	3.8	3.0
	Ab	7.0	4.8	6.7	6.5	6.0	6.9	6.9	6.6
	An	90.5	92.3	87.9	89.7	91.4	92.0	89.3	90.3

*By difference.

†From radiochemical activation analysis.

Note:

Uncertainties for FeO and TiO_2 are ±5% of the reported value; those for other elements are ±1 to 2% of the reported values.

of the chondrite-normalized REE abundances and the magnitude of the Eu anomaly (Figure V-1) are like those reported by Hubbard et al. (1973) for Apollo 16 KREEP basalts. The chondrite-normalized REE abundances for the samples from 72255 (Figure V-2), while roughly similar to those found in KREEP basalts, are significantly different, as discussed below. All comments on the petrology and general character of the samples have been taken from Section III of this report.

72275, 57

This sample is a portion of the friable light gray polymict breccia, which has a porous, poorly sintered matrix, and is heterogeneous with light streaks that are plagioclase-rich. The analysis given in Table V-2 for this sample can be compared with the Apollo 17 PET report on 72275. The REE concentrations are intermediate between those of 72275, 80 (dark matrix breccia rind of clast #1), and those of 72275, 91 (pigeonite basalt clast) or 72275, 76 (light matrix "marble cake" interior of clast #1). The REE concentrations are toward the low edge of those reported by Hubbard et al. (1973) for Apollo 16 KREEP.

72275, 76

This "marble cake" material is a mixture of crushed gabbroic anorthosite and dark matrix breccia that is perhaps the same as the rind of clast #1 (sample 72275, 80). The texture is suggestive of two immiscible fluids poorly mixed by moderate amounts of stirring. The REE abundances in this material are the same, within uncertainty, as those found in the sample of pigeonite basalt breccia 72275, 91. This similarity extends to the elements Ga, Rb, and Cs as well, but is presumably fortuitous. The basalt material has lower concentrations of the constituents of plagioclase, higher concentrations of the constituents of mafic minerals, and higher concentrations of Co, Sc, Hf, and Cr.

72275, 80

This is a sample of dark matrix breccia that was present as the rind of clast #1. It contains stringers of the anorthositic core material. The highest REE concentrations

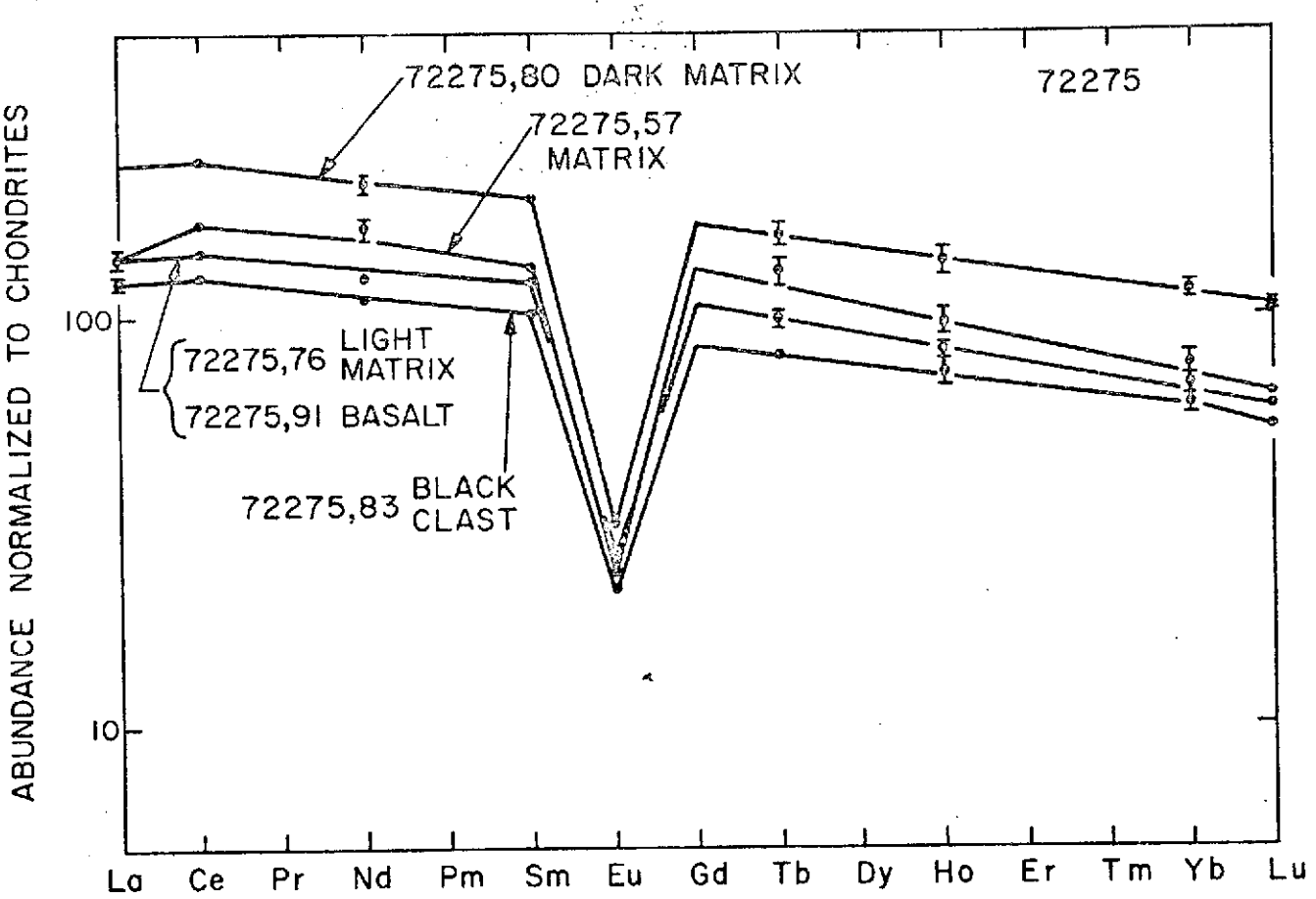

Figure V-1. Rare-earth abundance patterns in samples from 72275.

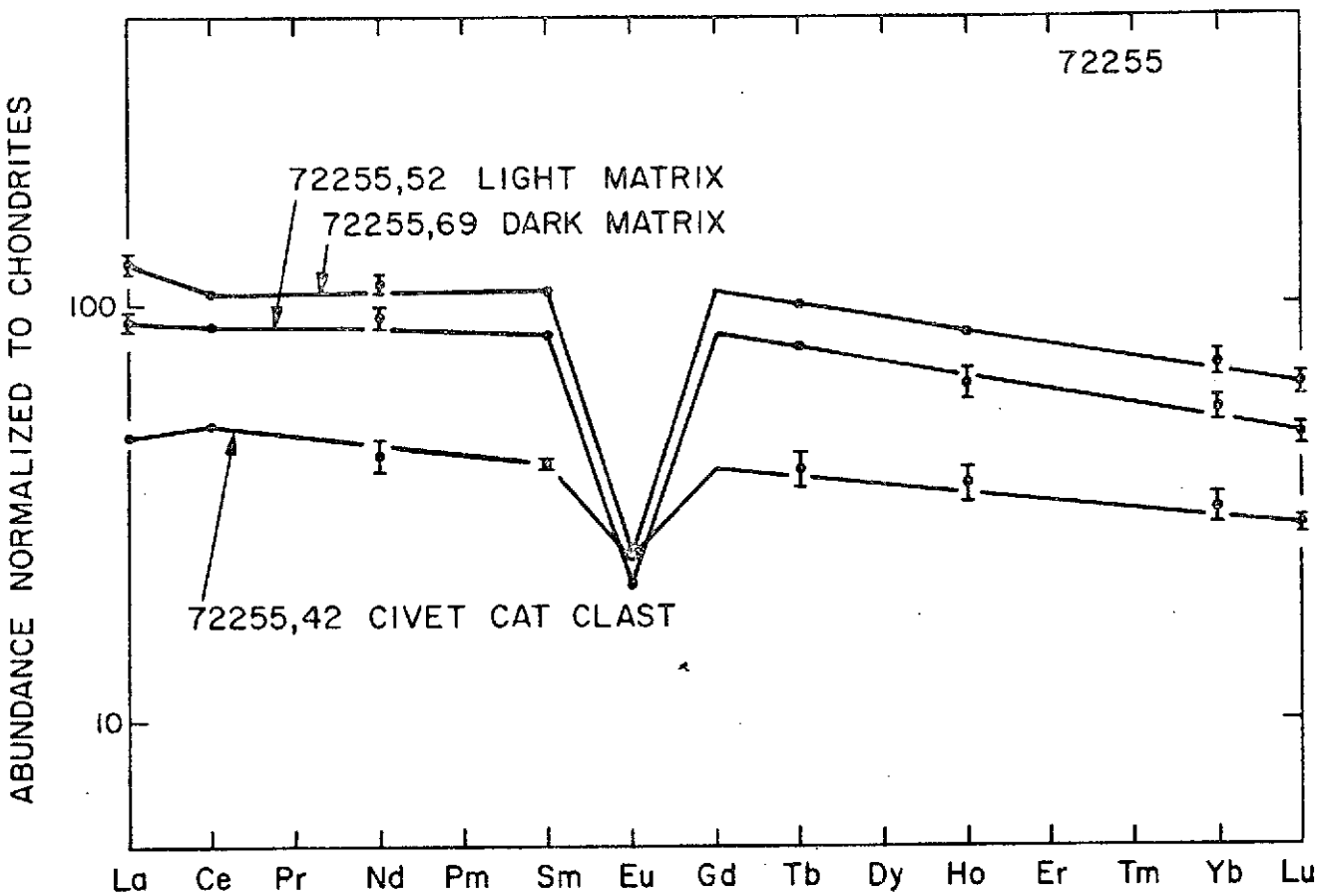

Figure V-2. Rare-earth abundance patterns in samples from 72255.

of any 72275 sample studied were found in this material. These concentrations are well within the range given by Hubbard et al. (1973) for Apollo 16 KREEP basalts.

72275, 83

Sample 72275, 83 is also dark matrix breccia, but taken from clast #2. It is interesting to note that this material contains the lowest concentrations of REE in any of our 72275 samples analyzed. The concentrations are still within the range for Apollo 16 KREEP. This sample is more mafic and contains less plagioclase than the other sample of dark matrix breccia (72275, 80). This may indicate that material with the highest concentrations of REE and of other KREEP-associated trace elements can be equally well diluted by plagioclase or by mafic minerals, which have low concentrations of these elements.

72275, 91

This sample comes from pigeonite basalt breccia clast #5. The REE concentrations are identical to those found for 72275, 76, and the reader is referred to the discussion of that sample. We note no obvious effects of the presence of basalt in this material as opposed to its absence in the other general types of 72275 material.

The major-element concentrations for the samples from 72275, in general, reflect the petrologic character, but the trace-element concentrations are, to a first approximation, independent of the major-element compositions and petrologic character. This suggests that the refractory trace elements may be present either in a noritic material that has been mixed with relatively small-to-equal amounts of mafic or plagioclase-rich materials or in extremely high concentrations in some identified material that has become mixed in unknown proportions with the trace-element-poor materials that would then comprise the bulk of the samples.

72255, 42

This sample is part of the so-called Civet Cat clast, which is mainly a mixture of plagioclase and orthopyroxene. From visual examination and photography, Stoeser

et al. (Section III) estimated that this clast consists of approximately 40% ± 10% plagioclase and 60% ∓ 10% orthopyroxene, suggesting that it is the shocked remains of a plutonic rock. From our major-element analysis (Table V-2), we calculate a norm of 55% orthopyroxene and 42% plagioclase in our sample. The relatively low REE concentrations and the much smaller Eu anomaly for the Civet Cat clast, when compared with the other samples from 72255 that we have analyzed so far, do argue in favor of a possible plutonic origin for this rock. If the clast is entirely of plutonic origin, it contains a significant component of the parent liquid from which the plagioclase and pyroxene crystallized. This liquid was somewhat higher in trace-element concentrations than is required for most liquids that were parents for other plutonic rocks (see, for example, Haskin et al., 1973, 1974). The parent liquid would also have had a significant negative Eu anomaly since the precipitation of plagioclase would enrich the resulting rocks in Eu relative to the other REE. The slope of the rare-earth pattern in 72255, 42 is not so great as that in the KREEP-like distributions found for all samples from 72275, but more nearly approaches that slope for the light REE than do the other two samples from 72255. Perhaps its altered slope reflects in some way the REE pattern found for the samples of matrices 72255, 69 and 72255, 52.

72255, 52

This material consists of interior chips of light gray matrix. The REE concentrations in this material are only 80% as high as those in the dark matrix material 72255, 69. The REE distribution relative to chondrites (Figure V-2) shows an interesting departure from the KREEP pattern found in 72275. The extent of enrichment of the elements La to Sm relative to chondrites in 72255, 52 is about the same, although the size of the Eu anomaly is about that expected, based on concentration levels and rare-earth distribution found in Apollo 16 KREEP. The slope of the chondrite-normalized REE distribution of 72255, 52 for Gd to Lu is the same as that found in the more KREEP-like samples from 72275. It is interesting to note that this light matrix sample, while slightly more mafic in major-element composition than its darker counterpart 72255, 69, has essentially the same concentrations of Co, Sc, and Hf as does 72255, 69, even though in many materials these elements associate principally with mafic minerals as rocks crystallize from silicate melts. These elements tend to remain in the liquid while crystals of plagioclase or orthopyroxene form but are enriched in later crystallizing minerals – Co in olivine and Co or Sc in clinopyroxene.

The samples from 72255 show lower trace-element concentrations and greater deviation from KREEP-like trace-element patterns than appears to be characteristic of noritic materials sampled from other boulders (unpublished results).

REFERENCES

Haskin, L. A., Helmke, P. A., Blanchard, D. P., Jacobs, J. W., and Telander, K. (1973). Major and trace element abundances in samples from the lunar highlands. Proc. Fourth Lunar Sci. Conf., Geochim. Cosmochim. Acta, Suppl. 4, vol. 2, pp. 1275-1296.

Haskin, L. A., Shih, C. Y., Bansul, B. M., Rhodes, J. M., Weismann, H., and Nyquist, L. E. (1974). Chemical evidence for the origin of 76535 as a cumulate. In Lunar Sci. V, pp. 313-315.

Helmke, P. A., Blanchard, D. P., Haskin, L. A., Telander, K., Weiss, C., and Jacobs, J. W. (1973). Major and trace elements in igneous rocks from Apollo 15. The Moon, vol. 8, pp. 129-148.

Hubbard, N. J., Rhodes, J. M., Gast, P. W., Bansul, B. M., Shih, C. Y., Weismann, H., and Nyquist, L. E. (1973). Lunar rock types: The role of plagioclase in non-mare and highland rock types. Proc. Fourth Lunar Sci. Conf., Geochim. Cosmochim. Acta, Suppl. 4, vol. 2, pp. 1297-1312.

Kosiewicz, S. T., Schomberg, P. J., and Haskin, L. A. (1974). Rare earth analysis of U.S.G.S. rocks SCo-1 and STM-1; Evaluation of standards for homogeneity and of the precision and accuracy of a procedure for neutron activation analysis. Journ. Radioanal. Chem. (in press).

PET (Apollo 17 Preliminary Examination Team) (1973). Apollo 17 lunar samples: Chemical and petrographic descriptions. Science, vol. 182, pp. 659-672.

VI. SIDEROPHILE AND VOLATILE TRACE ELEMENTS IN 72255 AND 72275

John W. Morgan, R. Ganapathy, Hideo Higuchi, and Edward Anders
Enrico Fermi Institute and Department of Chemistry
University of Chicago
Chicago, Illinois 60637

ABSTRACT

Of six samples from Boulder 1 at Station 2, four contain a unique meteoritic component, which we attribute to the Crisium projectile. The other two samples are meteorite-free, igneous rocks: an unusual, alkali- and Ge-rich pigeonitic basalt, and an alkali-poor norite of unexceptional trace-element chemistry.

INTRODUCTION

Six samples have been analyzed for 17 elements by radiochemical neutron-activation analysis (Table VI-1). Four of these have substantial meteoritic components, judging from the ~100-fold enrichment in siderophiles (Ir, Re, Au, Ni, etc.) over their indigenous levels in crystalline highland rocks.

METEORITIC COMPONENTS

Different types of lunar meteoritic components are best distinguished from each other on ternary plots of diagnostic elements, for example, IrAuGe (Figure VI-1, from Morgan et al., 1974a). All four Boulder 1 samples fall in Group 3, where no other Apollo 17 samples lie (Figure VI-2). Essentially, the same groupings are found on a ReAuSb plot.

It is possible to assign these lunar meteoritic components to specific basins, by comparing their abundances at different landing sites (Morgan et al., 1974a, b) with calculated ejecta thicknesses at those sites (McGetchin et al., 1973). By such arguments, we have assigned Group 3 to the Crisium projectile. This is consistent with

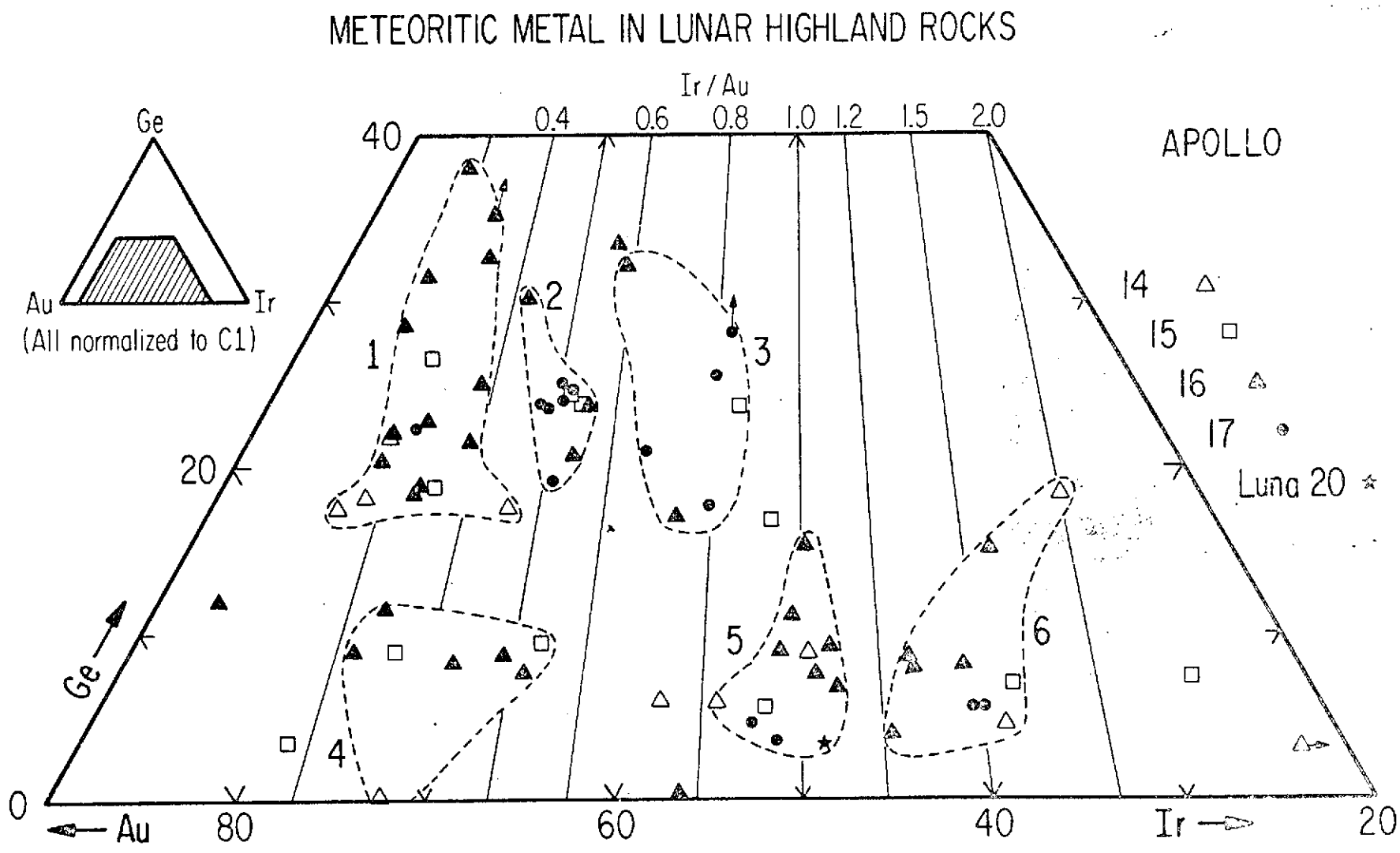

Figure VI-1. Six discrete ancient meteoritic components are present in highland rocks, as seen from the clustering of points on ternary diagrams such as IrAuGe or ReAuSb (Morgan et al., 1974a).

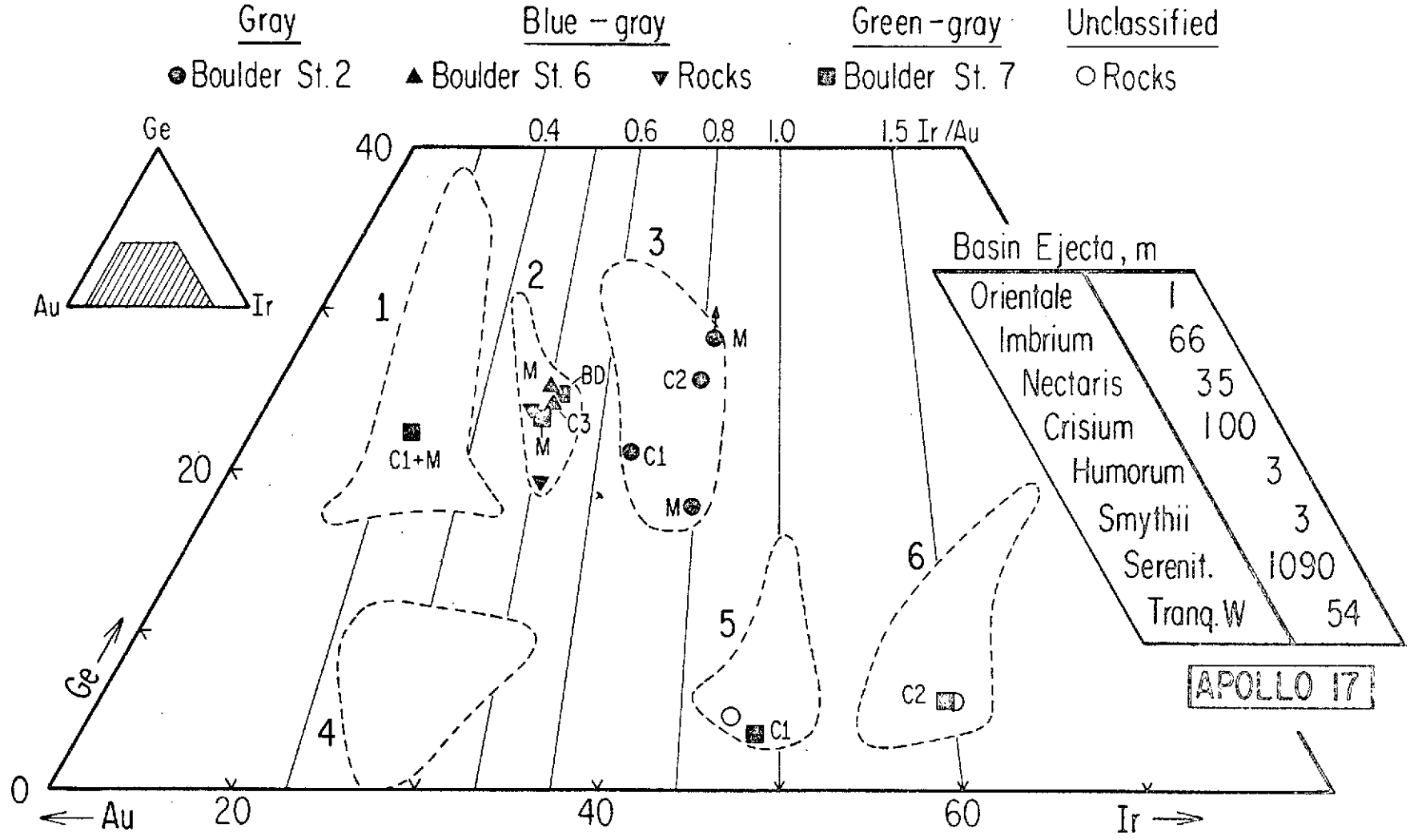

Figure VI-2. At the Apollo 17 site, samples from the gray, foliated Boulder 1 form a unique grouping. All fall into Group 3, in contrast to the blue-gray and green-gray breccias, which fall into Group 2 and Groups 1, 2, 5, and 6, respectively. From its geographic distribution and stratigraphic position, the Group 3 component is assigned to the Crisium projectile.

the high stratigraphic position of Boulder 1 (Schmitt, 1973) and the rarity of Group 3 at other landing sites (Figure VI-1). According to McGetchin et al. (1973), a 100-m layer of Crisium ejecta is expected at the Apollo 17 site (Figure VI-2). Other major contributors and their assignments according to Morgan et al. (1974a, b) are as follows:

Imbrium = 1,
Nectaris = 5,
Serenitatis = 2.

The rind of clast #1 contains essentially the same Group 3 meteoritic component as do the other samples, but it is enriched in Rb, Cs, and U (Table VI-1). Our data are quite consistent with the notion (Section III of this report) that the rind consists of ejecta welded on in flight. We have not yet analyzed the anorthositic core of this clast.

INDIGENOUS TRACE ELEMENTS

General

All samples except the Civet Cat clast are KREEP-rich, as determined from the Rb, Cs, and U contents. They lie near the top of the Apollo 15 or 16 range, though somewhat below Apollo 14.

Matrix

We see no significant difference between the matrices of 72255 and 72275, except for a twofold higher abundance of meteoritic elements in the former. Judging from the alkali and U contents, their major-element compositions ought to be fairly similar. There is no evidence for depletion of volatiles in 72255, in spite of its more metamorphosed nature. (The most labile volatiles under such conditions might be Se, Te, Br, Bi, Cd, and Tl.) This is not surprising, because we have never seen clear evidence of metamorphic losses in any lunar rock. Presumably the metamorphism took place under closed-system conditions, at least for our suite of volatiles.

Table VI-1. Abundances of 17 trace elements in 72255 and 72275.

Element	72255, 42, 9001 Black and white clast (Civet Cat)	72255, 52, 9004 Matrix*	72275, 57, 9002 Matrix†	72275, 80, 9004 Clast #1 black rim	72275, 83, 9005 Clast #2 gray aphanitic	72275, 91, 9006 Basalt clast
Ir	0.0040	5.28	2.26	2.54	3.44	0.023
Re	0.0068	0.498	0.225	0.233	0.334	0.0066
Au	0.008	2.00	0.82	1.16	1.30	0.045
Ni	4	227	97	122	147	43
Sb	0.26	0.77	1.17	0.94	1.06	2.87
Ge	61	174	406	137	178	1290
Se	280	77	34	63	52	230
Te	14.3	5.2	4.4	3.6	3.7	7.3
Ag	0.76	0.57	0.74	0.93	0.56	0.58
Br	15.3	101	48	290	95	44
Bi	0.30	0.21	0.11	0.14	0.12	0.14
Zn	4.5	2.8	2.7	2.8	2.4	2.7
Cd	5.8	8.1	13	15	26	8.3
Tl	0.30	1.18	0.71	0.71	0.62	0.58
Rb	1.27	5.8	5.9	11.3	5.4	8.0
Cs	67	240	260	480	260	360
U	240	1790	1500	3100	1840	1500

*Light-to-medium gray, with ~10% dark-gray material like 72255, 64.

†Possibly contaminated by pigeonite basalt.

72275, 91 (Basaltic Clast #5)

This interesting rock belongs to a small but growing family of nonmare basalts, possibly ancestral to KREEP-rich breccias. Like 14310, 62295, and 68415, it has an igneous texture and a fairly high content of KREEP-type elements (U, Rb, Cs). But unlike these rocks, it is 2 to 3 orders of magnitude lower in siderophile elements (Ir, Re, Au, Ni) than a typical KREEP-rich breccia is. A previous example is the mesostasis-rich basalt 15272, 9, 22 (Morgan et al., 1973).

Because of the high content of siderophiles, we have argued that 14310, 62295, and 68415 are not true igneous rocks, but impact melts. Conversely, siderophile-poor basalts such as 72275, 91 are either igneous progenitors of KREEP breccias, from a depth below the ancient highland regolith, or impact melts on a gigantic enough scale to permit segregation of siderophiles. A Rb/Sr age determination on this clast would be of very great interest.

In its overall trace-element pattern, basalt 72275, 91 is very similar to 15272, 9, 22, except for a 50-fold higher Ge abundance and lesser enrichments of Sb and Se. This is by far the highest Ge content seen in a meteorite-free lunar rock to this date. Igneous rocks usually contain only a few ppb to a few tens of ppb, while typical soils and breccias contain ~100 to ~2000 ppb Ge, largely of meteoritic origin. We suspect that the high Ge content of 72275 matrix (which causes it to plot off-scale in Figure VI-2) reflects admixture of Ge-rich, pigeonitic basalt. Some 20% would suffice. We note with some satisfaction that Stoeser et al. (1974) have found zones of crushed pigeonite basalt to be "fairly abundant in 72275."

72255, 42 (Civet Cat Clast)

This clast is relatively low in alkalis and U. Since it has essentially no meteoritic component, it presumably came from a depth below the ancient highland regolith.

72275, 83 (Clast #2)

Clast #2 looks very much like matrix 72255, 52.

REFERENCES

McGetchin, T. R., Settle, M., and Head, J. W. (1973). Radial thickness variation in impact crater ejecta: Implications for lunar basin deposits. Earth Planet. Sci. Lett., vol. 20, pp. 226-236.

Morgan, J. W., Ganapathy, R., Higuchi, H., and Anders, E. (1974a). Abstract submitted to Soviet-American Conference on Cosmochemistry of the Moon and Planets, Moscow, June 4-8.

Morgan, J. W., Ganapathy, R., Higuchi, H., Krähenbühl, U., and Anders, E. (1974b). Lunar basins: Tentative characterization of projectiles, from meteoritic elements in Apollo 17 boulders. In Lunar Sci. V, pp. 526-528.

Morgan, J. W., Krähenbühl, U., Ganapathy, R., Anders, E., and Marvin, U. B. (1973). Trace element abundances and petrology of separates from Apollo 15 soils. Proc. Fourth Lunar Sci. Conf., Geochim. Cosmochim. Acta, Suppl. 4, vol. 2, pp. 1379-1398.

Schmitt, H. H. (1973). Apollo 17 report on the valley of Taurus-Littrow. Science, vol. 182, pp. 681-690.

Stoeser, D. B., Wolfe, R. W., Marvin, U. B., Wood, J. A., and Bower, J. F. (1974). Petrographic studies of a boulder from the South Massif. In Lunar Sci. V, pp. 743-745.

VII. Rb-Sr AGE OF THE CIVET CAT CLAST, 72255,41

W. Compston and C. M. Gray

Department of Geophysics and Geochemistry
Research School of Earth Sciences
The Australian National University
Canberra, Australia

Plagioclase-rich clasts, orthopyroxene-rich matrix, purified pyroxene, and plagioclase from the Civet Cat clast define a Rb-Sr isochron age of $4.18 \pm 0.04 \times 10^9$ yr and an initial $^{87}Sr/^{86}Sr$ ratio of 0.69922 ± 0.00005 (Table VII-1 and Figure VII-1).

The fit of all data to the line is within error except for plagioclase 3, and blank corrections are essentially negligible. The decay constant used is 1.39×10^{-11}/yr. Possible bias in age due to spike calibration seems very low and can be compared with our published results of, for example, 3.93 ± 0.04 b.y. for 14310 and 3.83 ± 0.10 b.y. for 70035.

The plagioclase-rich "clasts" referred to in Table VII-1 are presumably deformed phenocrysts. The sample as received was coarsely crushed, and the white portions were picked out to make two (nonrepresentative) samples, or "clasts." Similarly, the coarse gray portions were selected for two "matrix" samples, and the finer, mixed white and gray remainder was used for two further samples. Following this, minerals were hand-picked from the combined +100-mesh size fraction.

The isochron probably measures the original igneous age of the Civet Cat norite, before its brecciation and incorporation in Boulder 1. Figure VII-1 shows our accumulated mean measurement for the initial $^{87}Sr/^{86}Sr$ ratio of the meteorite Angra dos Reis. Our measurements are higher than those of the Caltech group by about 0.00010, so that BABI on our scale is close to 0.69910. The reference line on the isochron marked "Model 4.5 b.y." is drawn through 0.69910. Relative to this line, the average total-rock clast shows at least a two-stage Rb/Sr evolution. (This assumes $^{87}Rb/^{86}Sr \sim 0.16$ for the whole clast, as determined from the modal estimates of

Table VII-1. Analytical data, 72255,41, Civet Cat clast.

Sample	Rb (ppm)	Sr (ppm)	$^{87}Rb/^{86}Sr$	$^{87}Sr/^{86}Sr$
Pyroxene	1.092	16.12	0.19560	0.71080 ± 0.00015
Pyroxene-rich matrix #1	5.68	79.8	0.20530	0.71148 ± 0.00003
Pyroxene-rich matrix #2	5.75	99.7	0.16620	0.70919 ± 0.000035
Plagioclase-rich clast #1	4.20	219.5	0.05520	0.70250 ± 0.000065
Plagioclase-rich clast #2	3.96	226.5	0.05037	0.70217 ± 0.00003
Mixed clast, matrix #1	2.562	101.4	0.07293	0.70355 ± 0.00002
Mixed clast, matrix #2	3.020	100.9	0.08640	0.70443 ± 0.00002
Plagioclase 1	3.591	224.6	0.04614	0.70203 ± 0.000025
Plagioclase 2	3.596	221.2	0.04692	0.70202 ± 0.000027
Plagioclase 3	3.290	209.5	0.04530	0.70168 ± 0.00008

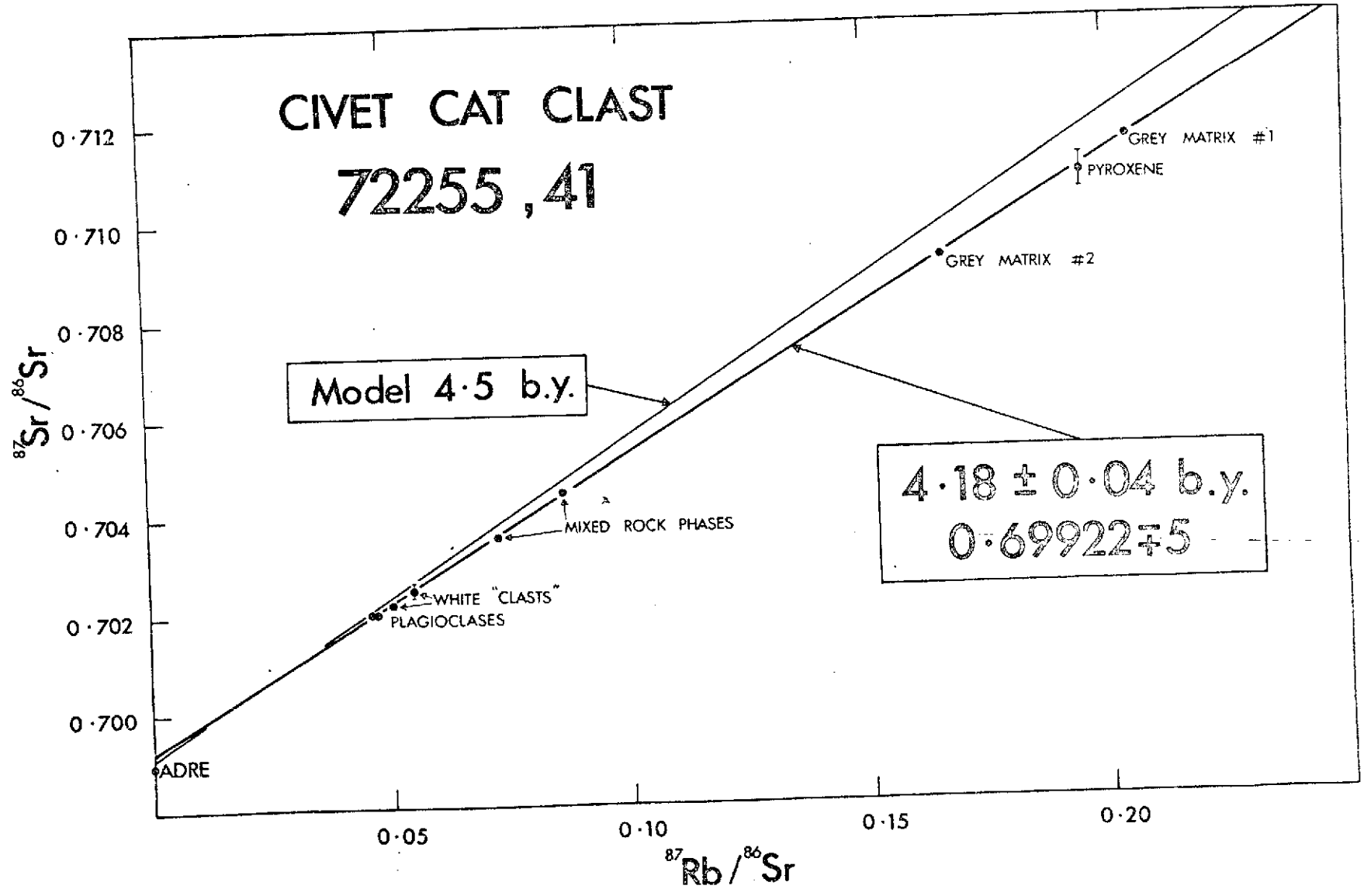

Figure VII-1. ^{87}Sr evolution diagram for mineral separates from the Civet Cat clast, 72255,41.

proportions of dark and light material in Section III of this report.) For example, if the norite was a direct melt of a 4.5×10^9 yr source, its Rb/Sr ratio was increased during melting relative to that of the source. Alternatively, and more probably, if it was an accumulate of pyroxene and plagioclase, then it also accumulated interstitial Rb-rich mesostasis, which increased its Rb/Sr ratio. The above is also true if some lower initial $^{87}Sr/^{86}Sr$ ratio is used, instead of BABI.

The above assumes that the norite was chemically closed during the major impact event that put it into Boulder 1. If this was not so and if Rb was added during boulder assembly, the isochron could be dominated by the new Rb and the age could refer to the major impact. We have not yet found the Rb-rich phase(s) in the rock – presumably they are lost in fine-grained shocked material. However, the purified pyroxene fits exactly on the isochron. If it was originally older, then there must also have been Sr-isotope equilibration when the (hypothetical) new Rb was added. This, in turn, implies high temperatures during assembly, for a period long enough for Sr diffusion. We have studied polished thin sections of tiny fragments of our sample, and agree with the assessment of Section III that the clast is a shocked igneous rock. There does not seem to be any evidence for the recrystallization that we think ought to accompany high temperatures, so we think it unlikely that Sr isotope re-equilibration occurred.

Even if this reading is wrong, metamorphic re-equilibration of the rock cannot have occurred long after the 4.18-b.y. age reported. The initial $^{87}Sr/^{86}Sr$ ratio of the clast is low compared with mare basalts, and the mean Rb/Sr ratio is moderately high at 0.055. This combination restricts closed-system Sr-isotope equilibration during any later heating to within about 100 m.y. of the original age, as the $^{87}Sr/^{86}Sr$ ratio of the clast increases by 0.00010 per 45 m.y.

The clast age is older than any samples from the Fra Mauro formation, but it is comparable with the $^{39}Ar/^{40}Ar$ ages of Schaeffer and Husain (1973) for fragments in Apollo 16 soils. The clast age puts a broad limit on the age of Boulder 1 and the (?)Crisium or Serenitatis impact event: The time of impact was equal to or less than 4.18×10^9 yr ago.

REFERENCE

Schaeffer, O. A., and Husain, L. (1973). Early lunar history: Ages of 2 to 4 mm soil fragments from the lunar highlands. Proc. Fourth Lunar Sci. Conf., Geochim. Cosmochim. Acta, Suppl. 4, vol. 2, pp. 1847-1864.

VIII. U-Th-Pb SYSTEMATICS

P. D. Nunes and M. Tatsumoto

U.S. Geological Survey
Denver, Colorado 80225

We have analyzed the following boulder samples for U, Th, and Pb concentrations and for Pb isotopic compositions (Table VIII-1):

72275, 53	Matrix
72275, 73	Matrix
72275, 81	Dark rind, clast #1
72275, 117	White interior, clast #1
72255, 49	Civet Cat clast
72255, 54	Light gray matrix
72255, 67	Dark gray matrix

CONCENTRATION DATA

The U, Th, and Pb concentrations of the dark rind of clast #1 are high (Table VIII-1) – similar to those of Apollo 12 and 14 KREEP-rich soils and breccias – indicating that this clast has a substantial KREEP component. This contrasts markedly with the Apollo 17 basalts 74275, 75035, and 75055, which have low U (0.132 to 0.151 ppm), Th (0.407 to 0.488 ppm), and Pb (0.265 to 0.326 ppm) contents, similar to Apollo 11 low-K basalts. The dark rind material was hand-picked to >95% purity. Unfortunately, the white interior material was mixed with black specks, and the small sample size allocated permitted white material only 70 to 90% pure to be concentrated. Thus, the relatively high U, Th, and Pb contents (Table VIII-1) of this "white clast" are probably due to a significant contribution of dark rind material (typically, pure lunar plagioclase contains <0.01 ppm U and ≤0.2 ppm Pb). Similarly, the rather high U, Th, and Pb contents of the 72275 matrix likely reflect a significant black (KREEP-like) component. These concentration data and associated high $^{238}U/^{204}Pb$ ratios indicate that these rocks were derived from U-rich source regions very different from the Apollo 17 mare basalts.

Table VIII-1. Analytical data for 72275 and 72255 samples.

Sample number	Type of run*	Weight (mg)	Concentration (ppm)†			Corrected for analytical blank						
			U	Th	Pb	$\frac{^{232}Th}{^{238}U}$	$\frac{^{238}U}{^{204}Pb}$	$\frac{206}{204}$	$\frac{207}{204}$	$\frac{208}{204}$	$\frac{207}{206}$	$\frac{208}{206}$
72275,73 Matrix #1	P	162.0‡					1,325	1,225	599.3	1,218	0.48925	0.9945
	C	131.8	1.561	5.962	3.096	3.945	4,284	3,961	1,905	–	0.48105	–
72275,73 Matrix #2	C only	150.0	1.672	6.285	3.451	3.885	4,712	4,556	2,183	–	0.47921	–
72275,81 Dark rind, clast #1	P	53.3					1,915	1,937	1,176	1,880	0.60724	0.9705
	C	31.7	3.500	13.21	7.878	3.899	2,493	2,521	1,492	–	0.59177	–
72275,117 White interior, clast #1	P	83.3					1,473	1,423	818.2	1,347	0.57522	0.9472
	C	50.7	0.670	lost	1.410	–	2,445	2,361	1,360	–	0.57606	–
72255,49 Civet Cat	P	66.2					177.4	198.2	128.9	173.3	0.6505	0.8743
	C	51.6	0.3874	1.216	0.9448	3.24	194.8	217.6	138.6	–	0.6369	–
72255,54 Light matrix	P	124.1					3,525	3,296	1,709	3,186	0.5187	0.9666
	C	98.4	1.536	5.724	3.080	3.85	2,998	2,803	1,449	–	0.5171	–
72255,67 Dark matrix	P	100.8					2,833	2,815	1,601	2,682	0.5685	0.9527
	C	132.5	1.145	4.222	2.478	3.81	1,414	1,405	802.5	–	0.5711	–

*P = Pb isotopic composition; C = concentration.

†Concentration runs were "total spiked" to ensure equilibration of spikes and samples.

‡Actually, only ~54 mg were analyzed since ~2/3 of the solution was spilled, which explains why the Pb isotopic composition ratios appear low.

AGE RELATIONSHIPS

The data are plotted on a concordia diagram in Figure VIII-1. The data points fall within the error of concordia at about 4.25 b.y. (matrices), 4.50 b.y. (clast #1), and 4.65 b.y. (Civet Cat). The spread in these must reflect at least two very old events, but no accurate time assessment can yet be made from this limited quantity of information, owing to the flatness of concordia in the 3.9- to 4.7-b.y. region; we emphasize, however, that one event distinctly older than the "Imbrian event" (~4.0 b.y. old) is reflected in these analyses. It may be worth noting that these data lie within the error of the 3.99- to 4.47-b.y. discordia line documented by Nunes et al. (1973) for Apollo 16 highland rock samples. We are optimistic that with other Apollo 17 boulder workers' Rb-Sr and $^{40}Ar/^{39}Ar$ analyses and our own Rb-Sr and U-Th-Pb work on the Chao consortium Station 7 boulder samples 77215 and 77135 (work in progress), we will be able to piece together a more definitive history of events for these materials.

REFERENCE

Nunes, P. D., Tatsumoto, M. T., Knight, R. J., Unruh, D. M., and Doe, B. R. (1973). U-Th-Pb systematics of some Apollo 16 lunar samples. Proc. Fourth Lunar Sci. Conf., Geochim. Cosmochim. Acta, Suppl. 4, vol. 2, pp. 1797-1822.

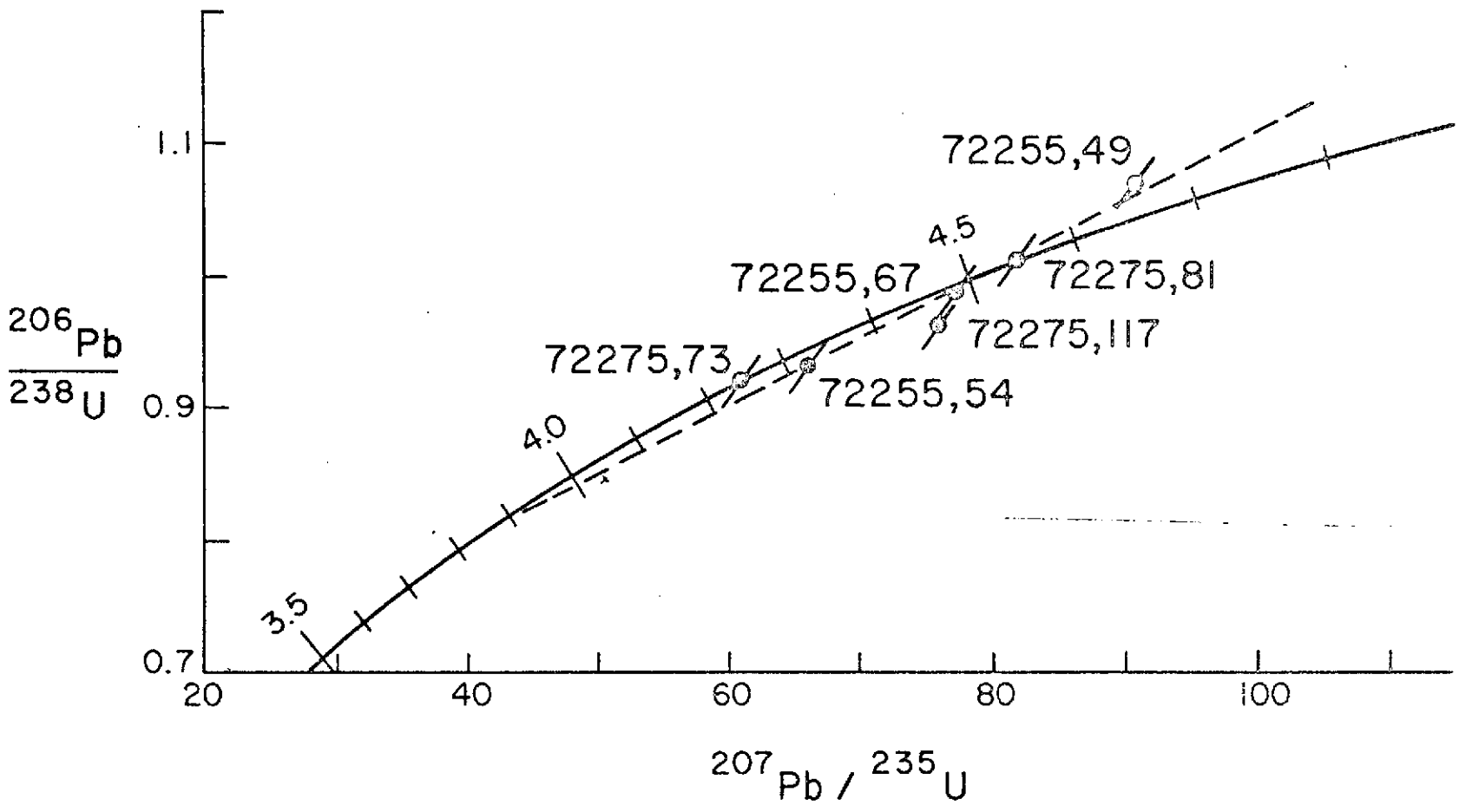

Figure VIII-1. Concordia diagram for samples from Boulder 1, Station 2. Data have been corrected for blank and primordial Pb.

IX. TRACK STUDIES OF SAMPLES 72255 AND 72275

I. D. Hutcheon

Department of Physics
University of California
Berkeley, California 94720

Optical microscopic studies of two intermediate pieces of 72255, located 1 to 3 cm below the surface, indicate an upper limit to the track exposure age of 15 to 20 m.y. Exposure ages determined by track methods, in the context of the large boulders, require some explanation. They do not necessarily bear any relation to the time at which the boulder rolled to its present location. Lunar surface photographs show considerable debris, including large fragments surrounding the boulders. Because of the steep depth dependence of the particle-track production rate, the surface under a spalled-off fragment of typical thickness 10 cm is essentially virgin. We thus expect that particle-track exposure ages determined at different locations on the same large boulder will reflect the local rate of large-scale discontinuous erosion and will not necessarily be the same.

A striking feature of the track studies of breccias 72255 and 72275 is the peculiar etching behavior of many of the feldspar and olivine crystals. After standard etching procedures, crystal surfaces are frequently irregular and bumpy, presumably owing to nonuniform dissolution of the surface, thus hindering track observations and perhaps introducing significant errors if the rate of track etching is as irregular as surface dissolution is. Figures IX-1 through IX-4 contrast the normal and peculiar etching behavior of feldspar grains in 72255. Although we have not observed this effect in feldspars or olivines in samples from other missions, it is apparently widespread among Apollo 17 samples. We have noticed similar behavior in numerous soil samples, in other boulder samples, in basalt 71055, and occasionally in Apollo 17 deep-core samples. Viewed in thin section, some affected areas are seen to contain larger than normal densities of dislocations and inclusions. Microprobe analysis on another Apollo 17 boulder chip similarly afflicted has revealed no apparent chemical differences between normal and peculiar areas. Fission-track dating of a whitlockite crystal in 72255 yields an uncorrected track retention age of 3.9 to 4.0 b.y.

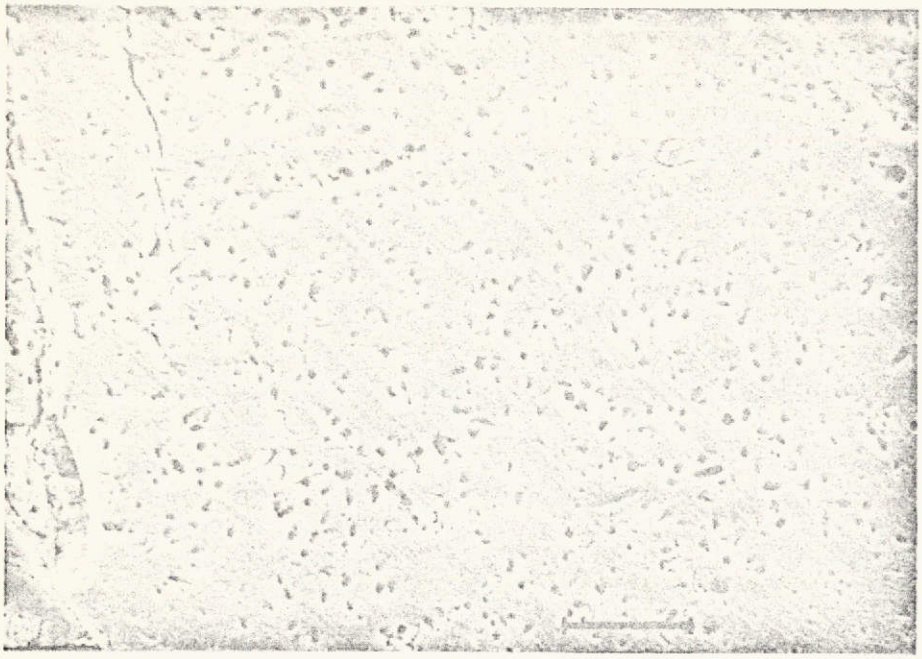

Figure IX-1. A "normal" feldspar crystal after etching in NaOH solution (1 g NaOH: 2 g H_2O) for 60 min. Tracks are visible as distinctly shaped pits and are easily countable with a track density $\simeq 8.5 \times 10^6/cm^2$. 72255, 30; scale bar, 20 μ.

Figure IX-2. Plastic replica of the same grain. Tracks are well-developed and exhibit no unusual features. 72255, 30; scale bar, 20 μ.

Figure IX-3. A typical "peculiar" area after an identical etching treatment. The surface has been attacked and eroded in a very nonuniform fashion, complicating the recognition of track etch pits. 72255, 30; scale bar, 20 μ.

Figure IX-4. Plastic replica of an etched "peculiar" area. Only a few well-developed tracks are visible. 72255, 30; scale bar, 20 μ.

X. A PRELIMINARY REPORT ON THE MAGNETIC MEASUREMENTS OF SAMPLES 72275 and 72255

S. K. Banerjee
Department of Geology and Geophysics
University of Minnesota
Minneapolis, Minnesota 55455

We have studied 1) the direction and magnitude of natural remanent magnetization (NRM) of five ~3-g subsamples of 72275 and 72255 and 2) the high-field saturation magnetization (σ_s), coercive force (H_c), and isothermal remanent magnetization (IRM_{SAT}) of a 100-mg chip from each of these samples. Given an understanding of the magnetization processes, group 1 experiments provide information about the absolute direction of the ancient magnetizing field and a qualitative estimate of its size (paleointensity). The group 2 experiments yield a quantitative estimate of the iron content and a qualitative idea of the grain sizes.

Figure X-1 shows an equatorial projection of the NRM vector directions from three matrix subsamples of 72275 (46, 47, and 56) and two matrix subsamples of 72255 (33 and 36). Mutual-orientation information was available from sample photographs and from Lunar Sample Information Catalog - Apollo 17 (p. 24). The average NRM directions of the two rocks (each representing a different layer from the same boulder) are seen to be ~100° to each other. It is estimated that orientation errors can be as large as ±20°; however, the data are significant enough in spite of them. In a terrestrial situation, we would ascribe such errors to a rotation of the magnetizing field due to secular variation or to the onset of a field reversal that happened to get recorded.

However, before we consider such speculation, it is necessary to conduct storage tests and partial alternating-field (AF) or thermal-demagnetization experiments to establish whether the different directions are indeed stable. We have thus far completed

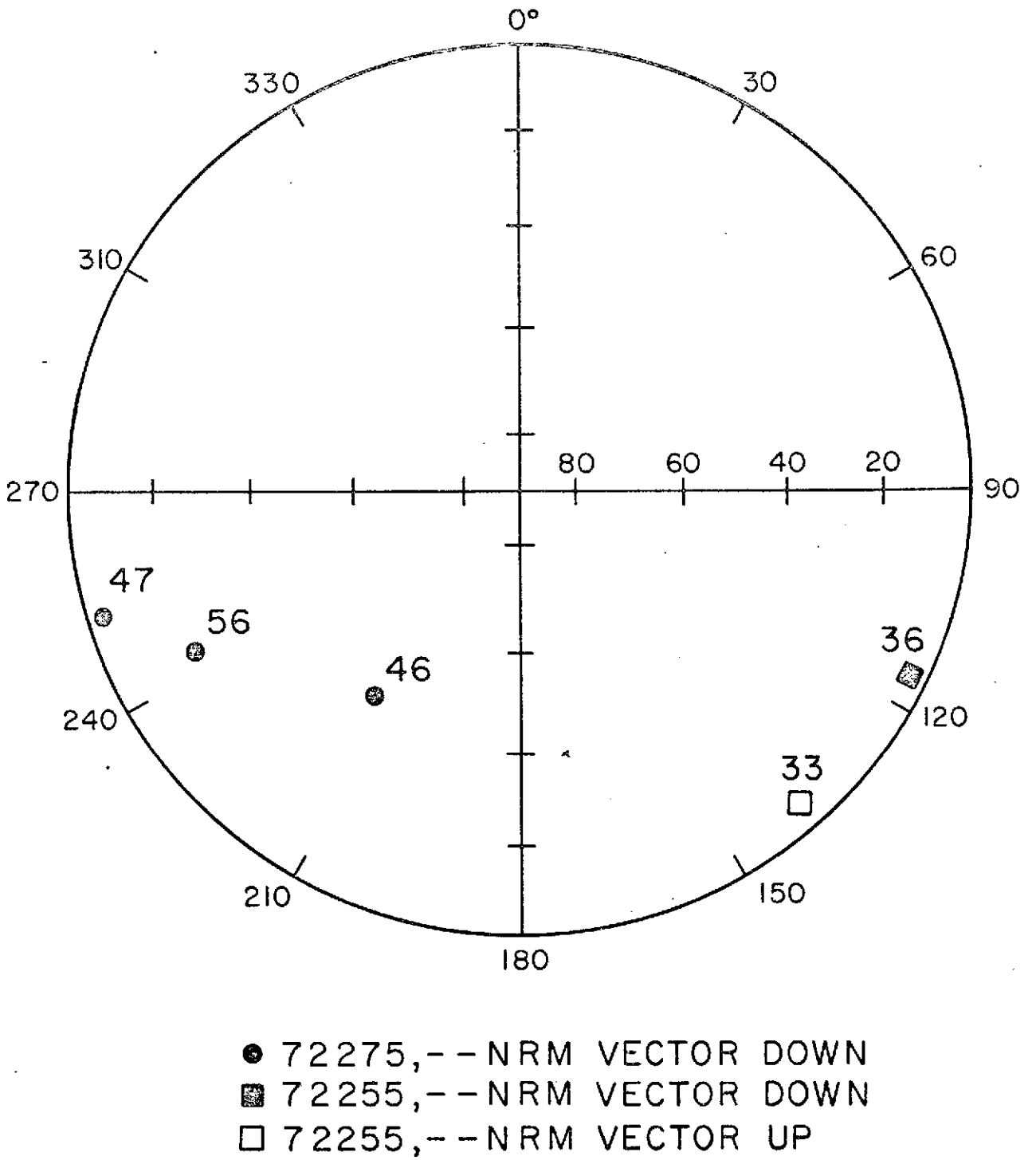

Figure X-1. NRM directions of samples from Boulder 1, Station 2; equal-area projection.

only a storage test (>80 days in zero field). Fortunately, unlike many lunar rocks, these samples do not show a decay of NRM with time; that is, there is no sign of an unstable viscous remanent magnetization. Since AF-demagnetization has been shown to impart irregular error signals to some lunar rocks, we are proceeding with thermal demagnetization in a H_2/CO_2 gas buffer system suitable for preventing the oxidation of iron grains while thermal demagnetization is in progress. Until that is completed, our tentative conclusion is that the two rocks, 72275 and 72255, are probably magnetized at an angle to each other. If we assume that the NRM is a thermoremanent magnetization and that these divergent directions are not due to physico-chemical reasons, then the two layers must have been magnetized (i.e., cooled from above 770°C) at different times. More specifically, for secular variation and field reversal, the terrestrial dynamo (size $\sim 10^3$ km) has a time constant of 2×10^3 to 5×10^3 yr. If we assume the ancient lunar magnetizing field also to be due to such a dynamo, then, purely by analogy, these two rocks could be that much different in age. Even without this conclusion, what we find remarkable about the NRM properties of these samples is that, compared to most lunar samples, the NRM intensities (Table X-1) and directions (Figure X-1) are very homogeneous among subsamples. Therefore, we can indeed state that the data in Figure X-1 are truly representative of the two rocks allocated to us from two layers of the same large boulder.

In Table X-I, we show the values of various magnetic properties for the 3-g and 100-mg subsamples of 72275 and 72255. Those for σ_s, H_c, and IRM_{SAT} were measured only for the 100-mg (chip) subsamples. NRM values of the larger samples of 72275 are an order to magnitude greater than 72255. Values of σ_s suggest that half this increase can be attributed to a greater iron content in 72275 (~0.8% by weight) than in 72255 (0.16%). This is corroborated by IRM_{SAT} data. The other half of the specific NRM increase in 72275 may be due to a larger number of more efficient carriers of NRM.

Table X-1. Magnetic parameters of 72275 and 72255 samples.

Sample number	NRM ($emug^{-1}$)	σ_s ($emug^{-1}$)	H_c (Oe)	IRM_{SAT} ($emug^{-1}$)
72275, 46	2.40×10^{-4}			
72275, 47	1.30×10^{-4}	1.72	~25	7×10^{-3}
72275, 56	1.09×10^{-4}			
72255, 33	1.23×10^{-5}			
72255, 36	1.17×10^{-5}	0.36	~18	2.3×10^{-3}

XI. SPECTRAL REFLECTANCE OF 72275 FROM BOULDER 1, STATION 2, APOLLO 17

John B. Adams

West Indies Laboratory
Fairleigh Dickinson University
St. Croix, Virgin Islands 00820

Planetary Astronomy Laboratory
Department of Earth and Planetary Sciences
Massachusetts Institute of Technology
Cambridge, Massachusetts 02139

and

Thomas B. McCord

Planetary Astronomy Laboratory
Department of Earth and Planetary Sciences
Massachusetts Institute of Technology
Cambridge, Massachusetts 02139

Spectral-reflectance measurements (0.35 to 2.5 μm) were made of samples 72275, 103 (chip) and 72275, 98 (saw cuttings). Both the chips and the cuttings consist mainly of friable feldspathic breccia. Sample 72275, 103, a chip taken from east-end piece 72275, 27, is rich in gray polymict breccia (see Section III). The saw cuttings were derived from the entire rock, but they are probably strongly biased toward the friable feldspathic matrix material that has been preferentially disaggregated.

The spectra of both samples (one of which is presented in Figure XI-1) are very similar. They show two prominent absorption bands, one at 0.91 μm and another at 1.93 μm, arising from Fe^{2+} in pyroxene. The depths of these bands (~15%) are large enough to preclude the presence of much glass or opaque material in the samples. From the spectral properties alone, it is clear that the samples are not soil breccias nor vitric breccias, as, of course, has been verified by petrography. The wavelengths of the principal absorption bands plot on the pyroxene trend (Figure XI-2), indicating that orthopyroxene is spectrally dominant. Although it is clear from petrographic examination that lesser amounts of other pyroxenes and olivine occur in the samples, we can expect that the orthopyroxene with its strong absorption would monopolize the

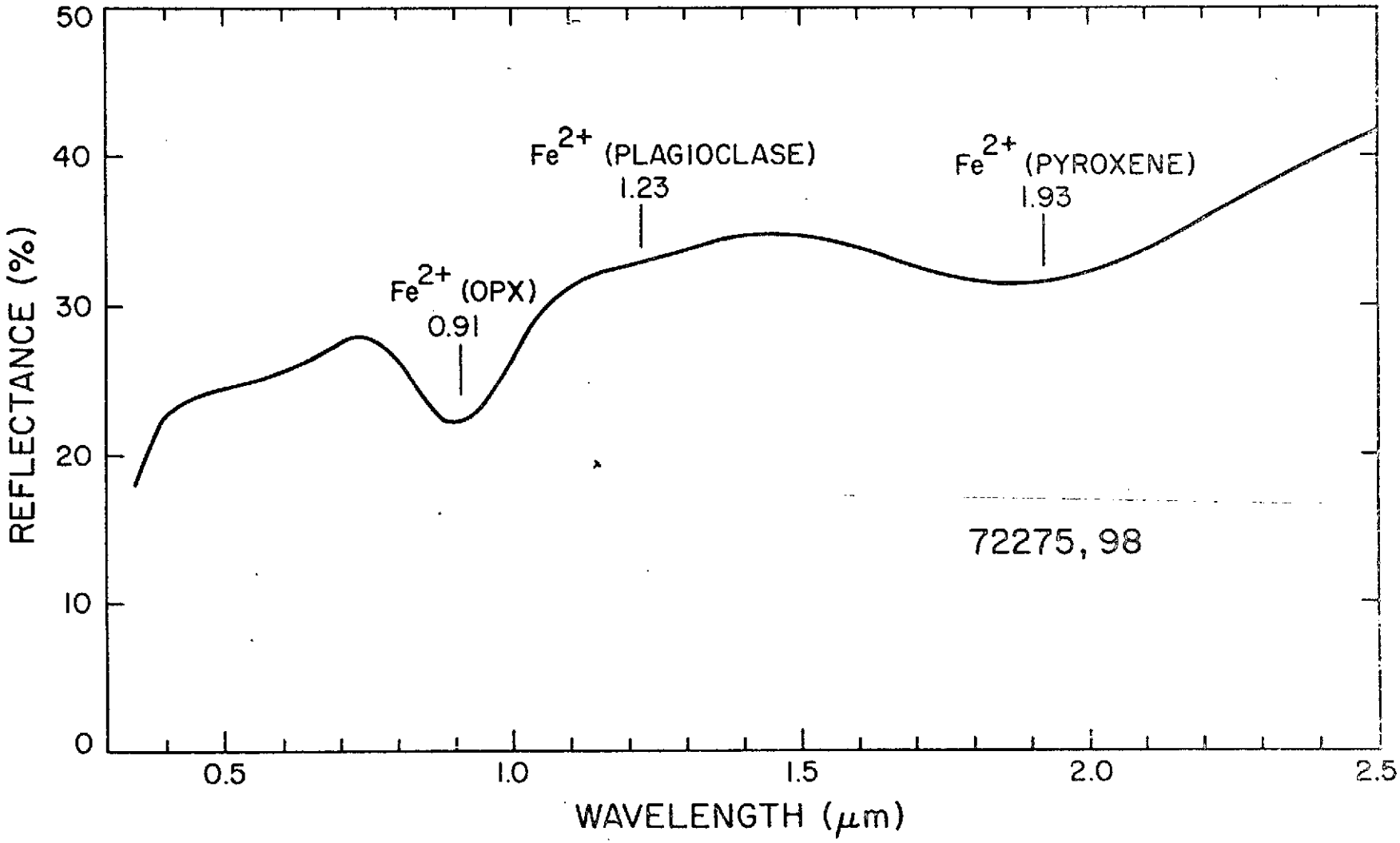

Figure XI-1. Reflectance spectrum of 72275, 98.

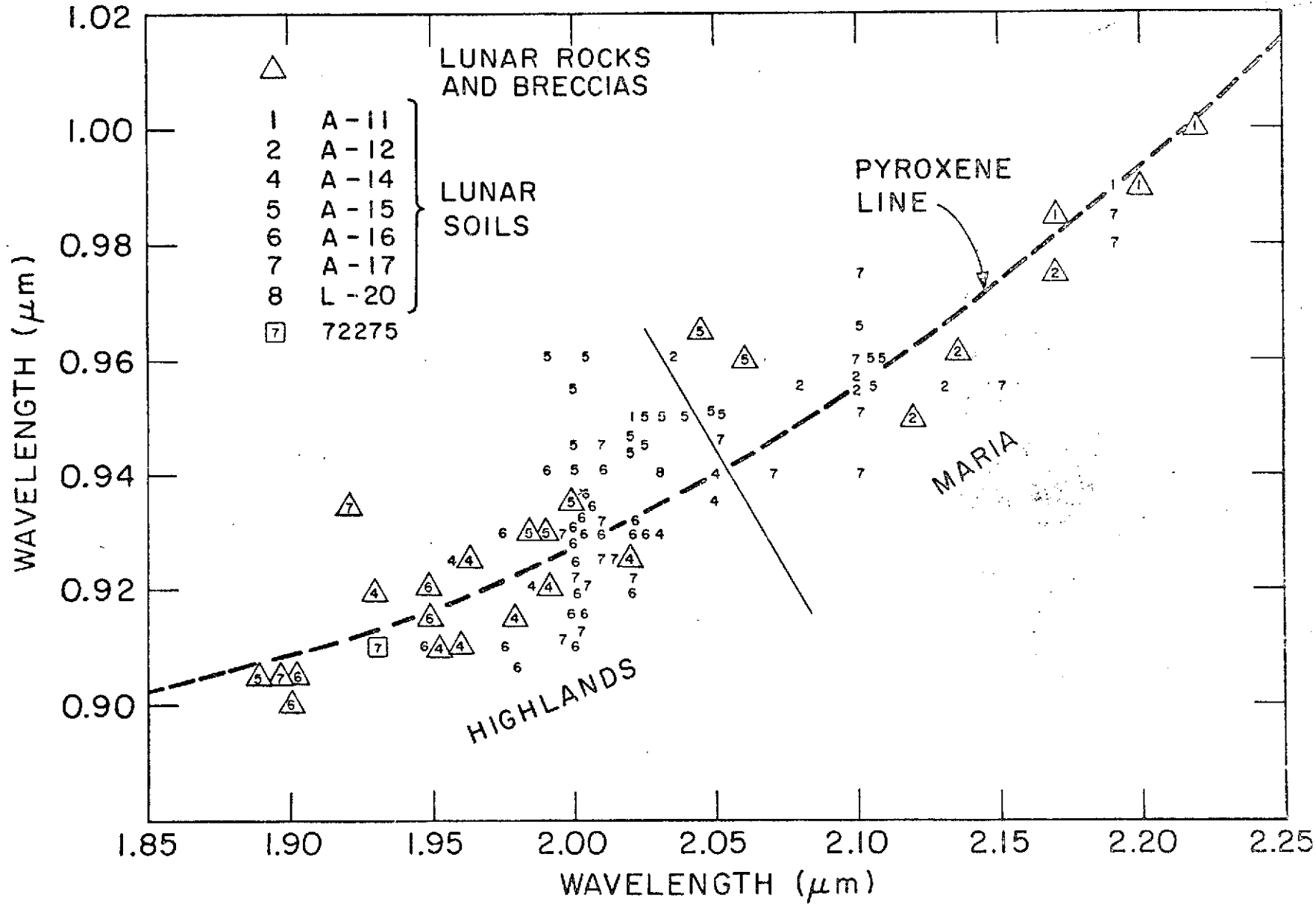

Figure XI-2. Plot of the absorption band near 1 μm versus that near 2 μm for lunar samples.

rock spectrum. From the data of Adams (1974), the composition of the dominant pyroxene, as determined from the reflectance spectra, is $En_{60-65}Fs_{35-40}Wo_{<}$. This composition agrees well with the orthopyroxene analyzed by Stoeser et al. (Sec. III) in the anorthositic gabbro bands in clast #1 (marble cake) and in the gray polymict breccia. The weak band near 0.6 μm probably involves a titanium and iron charge transfer and is typical of many lunar pyroxenes. The weak band near 1.23 μm is contributed by Fe^{2+} in calcic plagioclase.

A principal reason for studying the spectral reflectance properties of the boulder samples has been to gain a better understanding of the rock types from which the terra soils are made. The soils, in turn, can be measured from earth-based telescopes (McCord et al., 1972) down to areas about 1 km^2. If 72275 is representative of the South Massif, we would expect the soils in that area to show a weak band near 0.91 μm. Telescopic spectra are not yet available for the massifs at the Apollo 17 site; however, spectra taken of a terra region north of the crater Littrow show a weak band at 0.92 to 0.93 μm, and the bright crater Proclus to the southeast has a band at 0.91 μm. Only tentative conclusions can be drawn from these sparse data. It appears that the optical spectra of our samples of 72275 are dominated to a greater extent by orthopyroxene than are spectra of the regional terra in the Littrow area. It is likely, however, that orthopyroxene-rich feldspathic rocks may be locally abundant, as, for example, may be the case in the crater Proclus.

REFERENCES

Adams, J. B. (1974). Visible and near-infrared diffuse reflectance spectra of pyroxenes as applied to remote sensing of solid objects in the solar system. Submitted to Journ. Geophys. Res.

McCord, T. B., Charette, M. P., Johnson, T. V., Lebofsky, L. A., Pieters, C., and Adams, J. B. (1972). Lunar spectral types. Journ. Geophys. Res., vol. 77, pp. 1344-1359.

MITPAL #92

APPENDIX A

SPECIMEN 72275 DOCUMENTATION

Ursula B. Marvin

The friability of the matrix of specimen 72275 caused numerous fragments and an abundance of fines to break away from the main mass during transport from the Moon and handling in the Lunar Receiving Laboratory. Figure A-1 shows five pieces reassembled in their original positions plus an array of 20 undocumented chips.

Samples 72275, 1 to 72275, 14 were labeled during the PET examination in January 1973. Samples 72275, 1, 4, 6, 7, 8, and 9 were placed in storage, and the remainder were distributed as follows (see also Table A-1):

72275, 2	Nyquist
72275, 5	Strangway; subsequently returned to storage
72275, 11	Thin section of undocumented chip; in library
72275, 12	Thin section of undocumented chip; to Wood
72275, 13	Thin section of undocumented chip; in library
72275, 14	Probe mount of undocumented chip; in library.

On July 24, 1973, the following samples were pried or chipped from the surface of the specimen before sawing began:

72275, 15, 16, 17	Chips of the rippled material coating the E_1 surface (see Figure A-2); for Agrell and Wood
72275, 18 to 72275, 26	Chips of matrix from the southwest surface (see Figure A-3); for Agrell and Wood.

The sawing of 72275, 0 was done on July 26 and 27. The friability of the matrix and the hardness of some of the clasts combined to cause much breakage. When sawing was complete, the specimen consisted of four main subdivisions (see Figure A-4):

72275, 102	The west end, or main mass
72275, 27	The east end
72275, 28 to 72275, 31	Clast #1 and adjacent pieces of matrix
72275, 42	The slab.

The above pieces were sampled as follows:

72275, 102	From this specimen, fresh interior chips of matrix were pried loose from the fractured, protruding part of the west face at the location outlined in Figure A-5. The chips were numbered and distributed as follows:
72275, 66	Reed
72275, 67	Burns
72275, 68	Eglinton
72275, 69	Storage
72275, 70	Burlingame
72275, 71	Moore
72275, 27	From this east-end piece, the following chips were taken (see Figure A-6):
72275, 103	Adams
72275, 110	Reed
72275, 111, 112, 113	Storage
72275, 114	Agrell
72275, 42	The slab
72275, 28	Clast #1 and its adjacent pieces

These two specimens were subdivided and distributed as indicated in Figures A-7, A-8, and A-9.

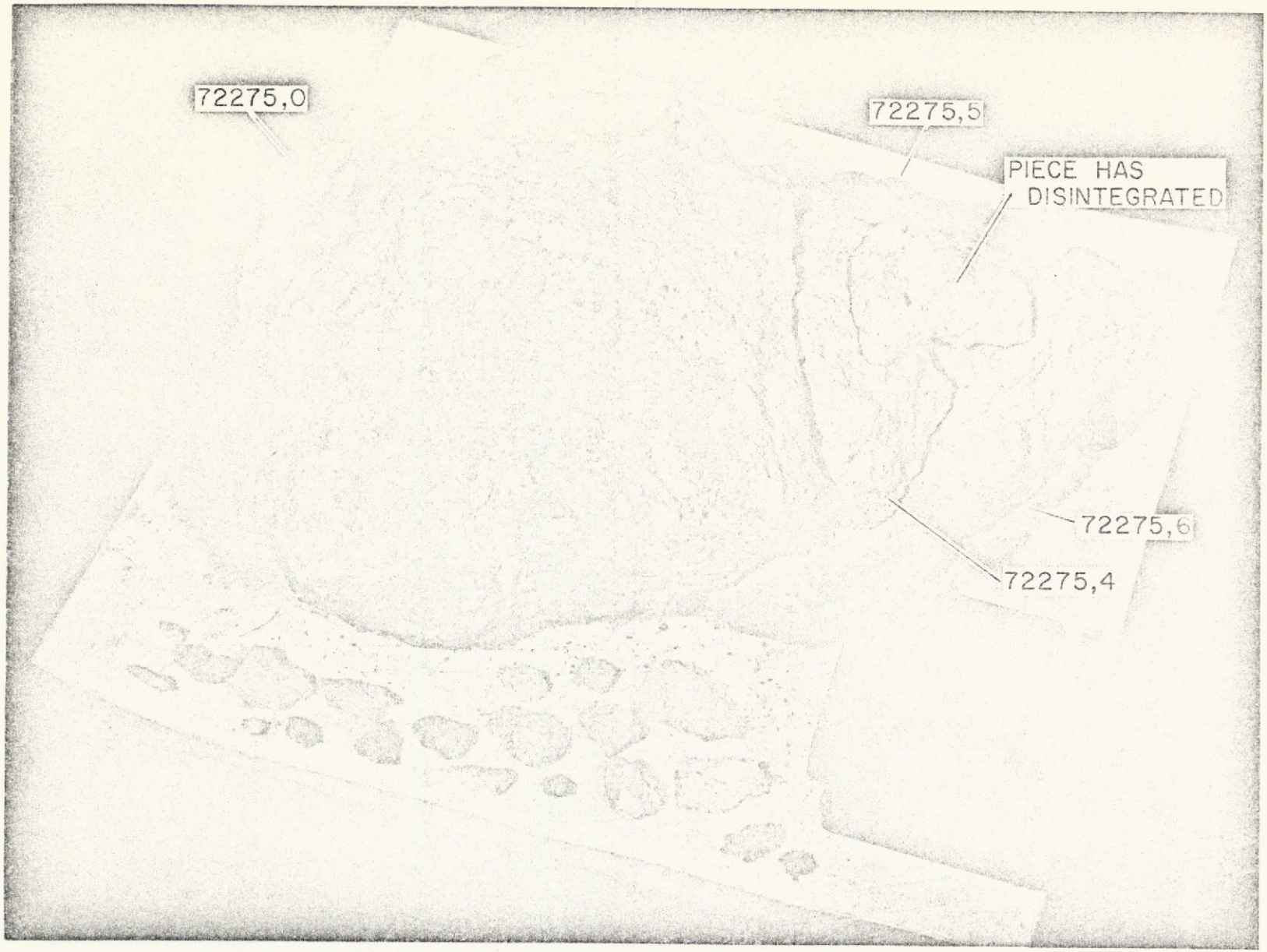

Figure A-1. A reassembly of the five documented pieces of 72275, photographed at the Lunar Receiving Laboratory in January 1973. Twenty undocumented chips are shown in the foreground (NASA photograph S-73-16077).

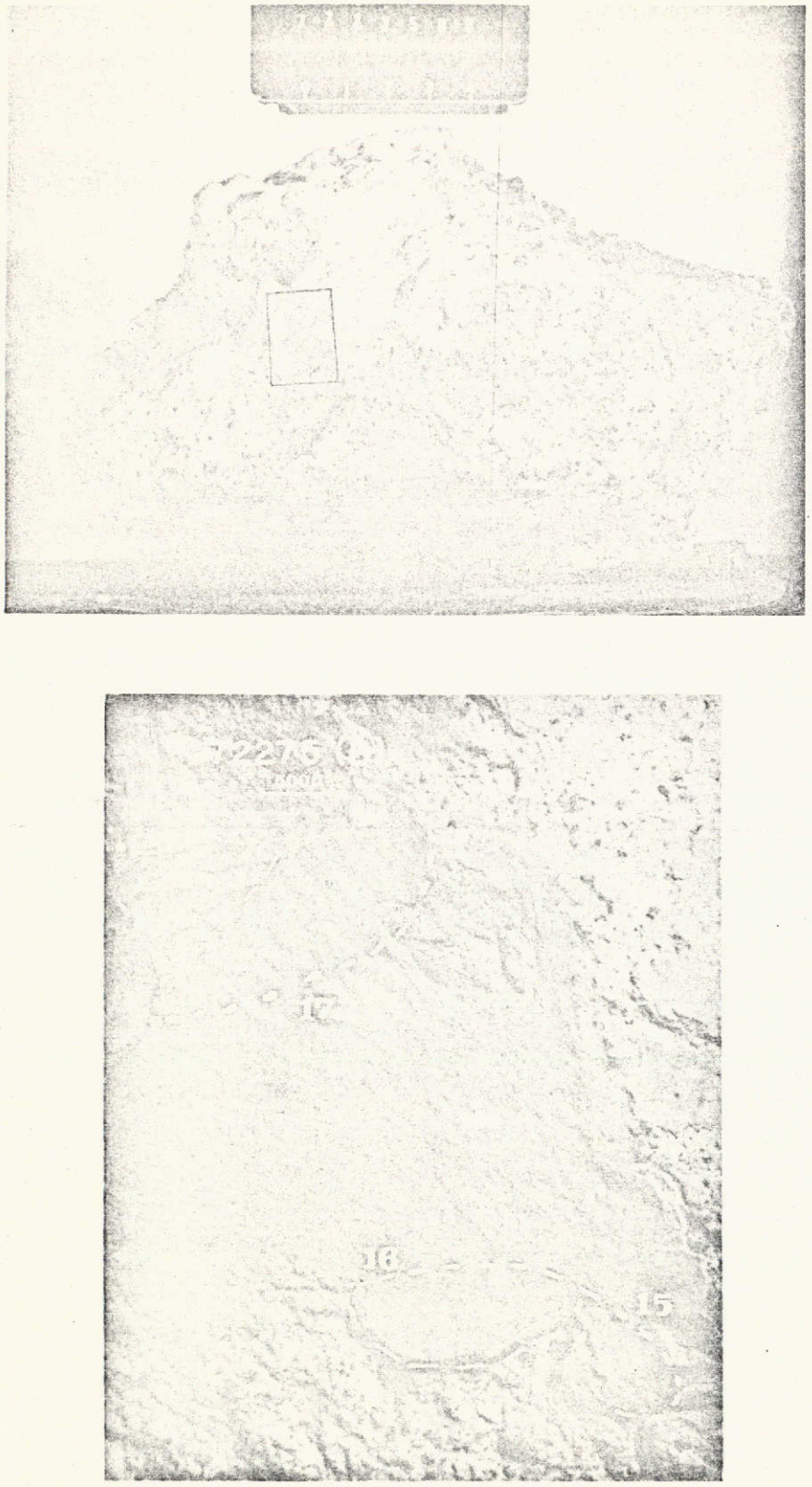

Figure A-2. Sampling sites of the ripple-marked layer on the east face. Upper photograph shows the region of pronounced rippling; lower photograph, the source of samples 72275, 15, 16, and 17.

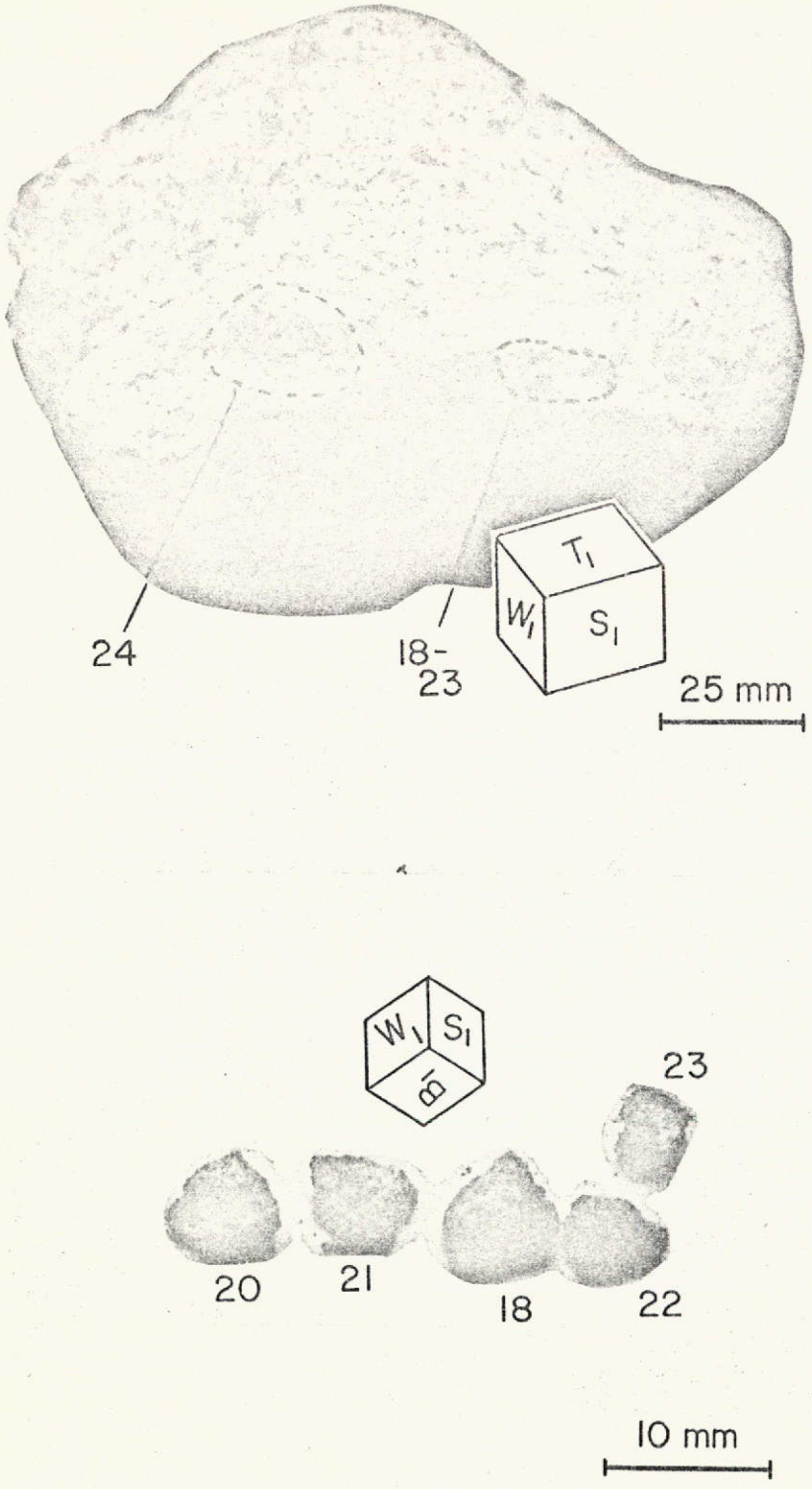

Figure A-3. Sampling sites and photographs of documented matrix chips from the southwest surface of 72275.

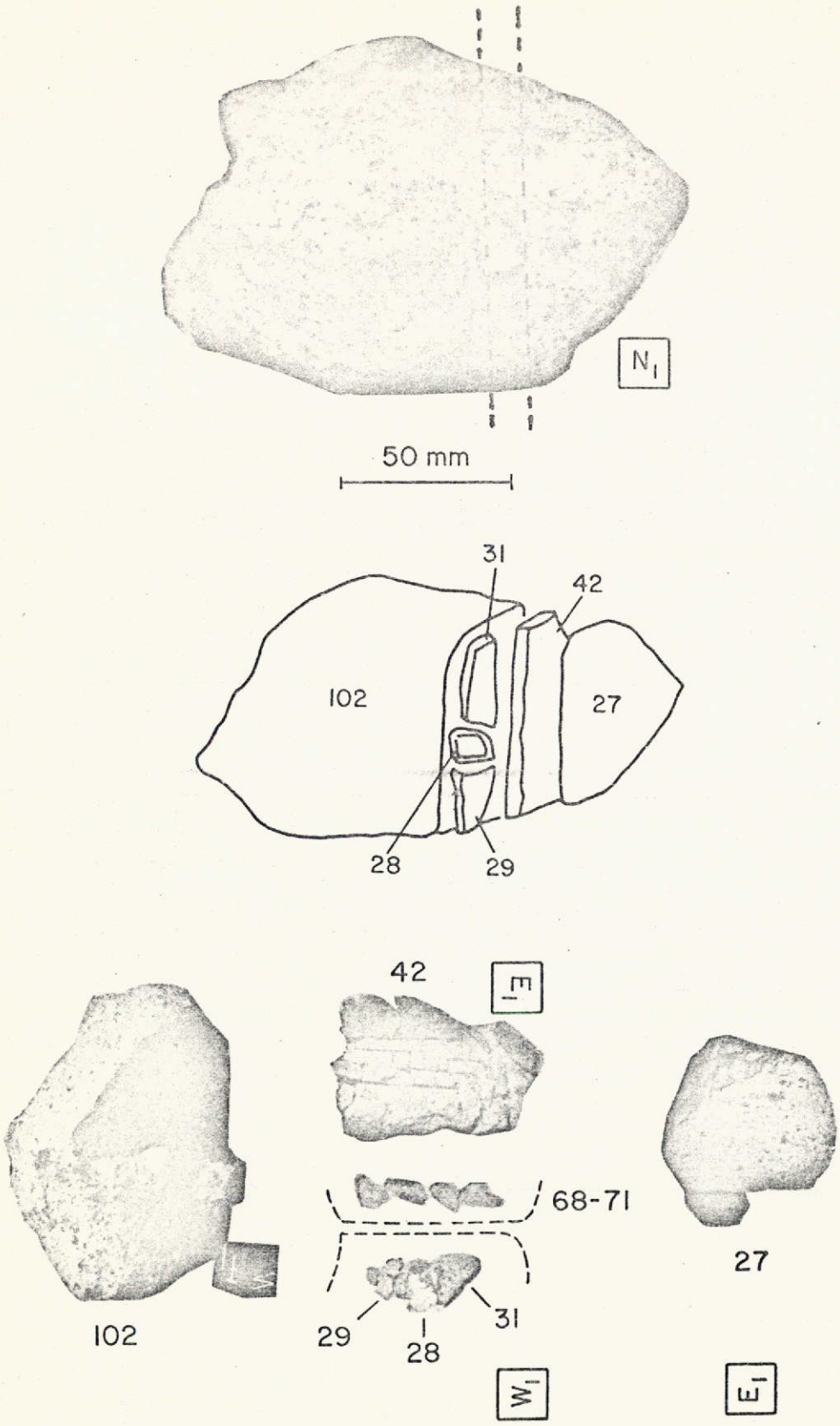

Figure A-4. Top: Specimen 72275, 0 with dashed lines indicating cutting plans. Bottom: The main subdivisions of 72275, 0 after removal of the slab and clast #1.

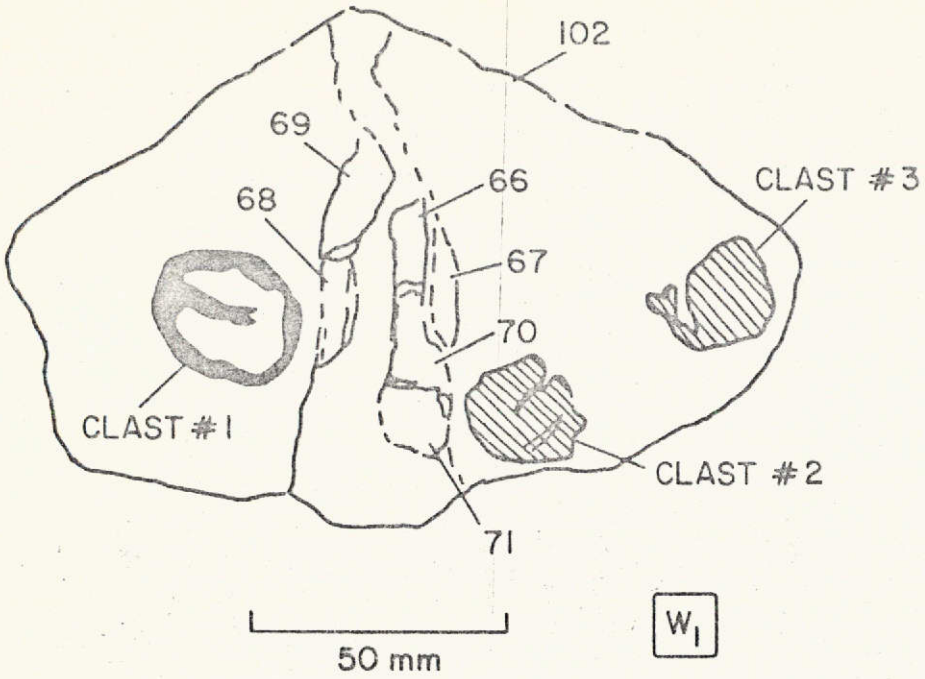

Figure A-5. Sketch showing source area of documented interior matrix chips from the west surface of 72275, 102.

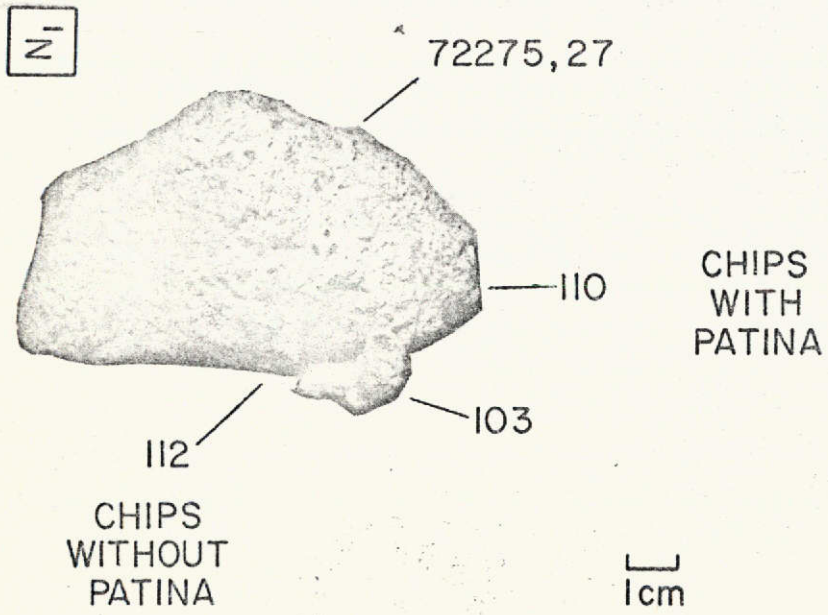

Figure A-6. The east-end piece, 72275,27, and the source area of some daughter chips.

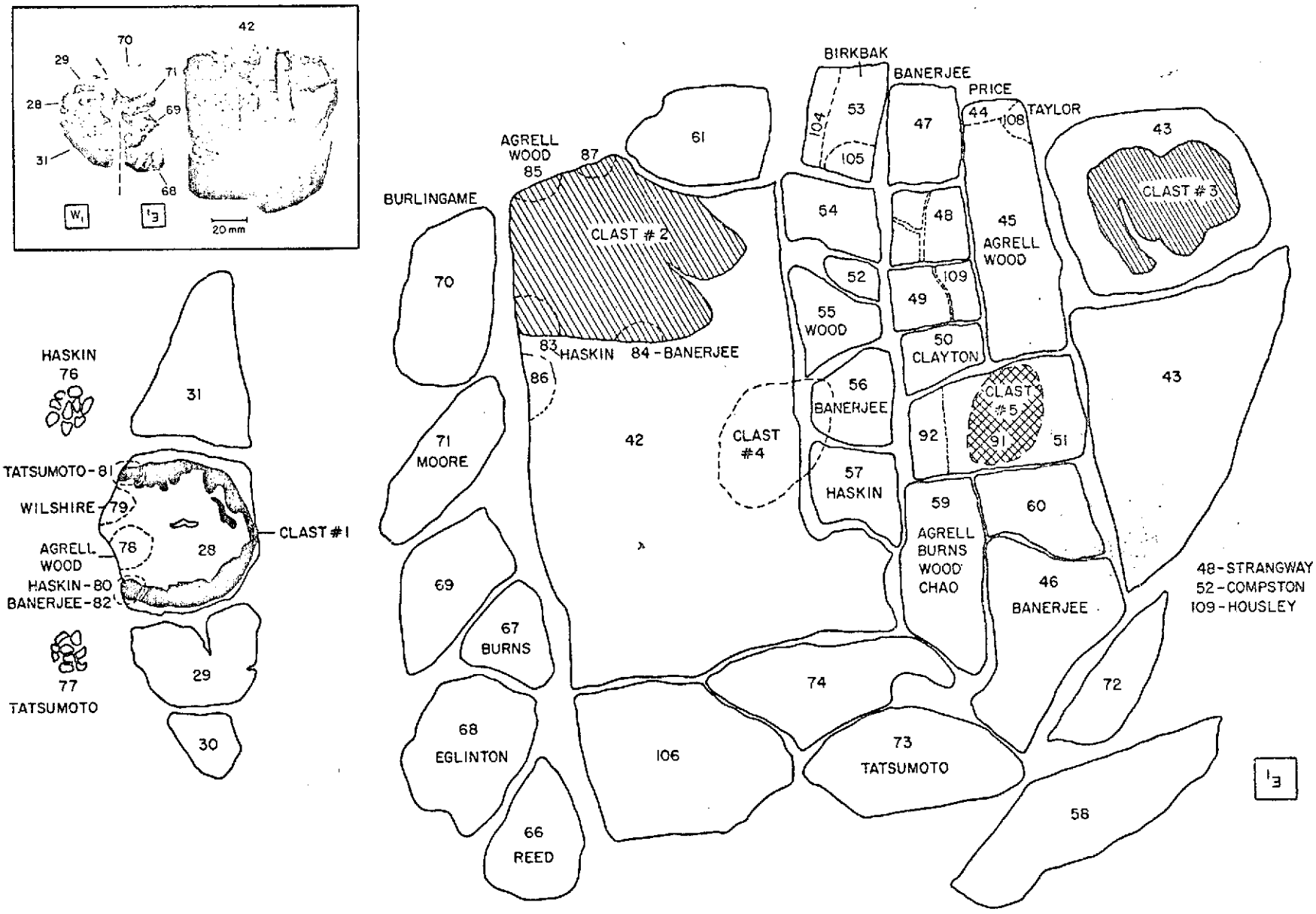

Figure A-7. Subdivisions of the slab, 72275,42, some matrix chips, and clast #1. Sketches of the subdivisions indicate the sources of samples sent to investigators. Unlabeled pieces were put in storage (see also Table A-1). Inset: Photograph of the reassembled pieces.

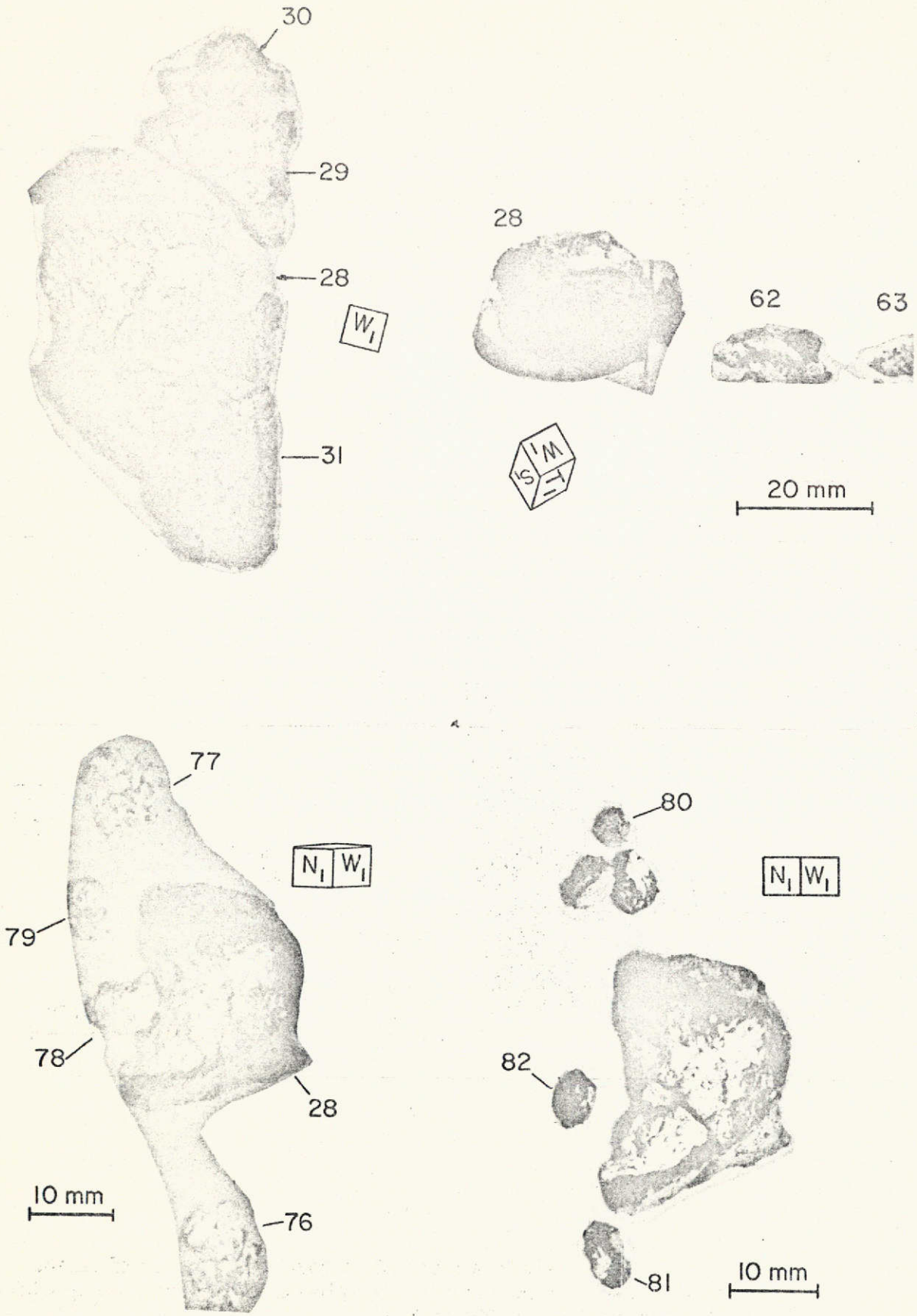

Figure A-8. Photographs of clast #1 and several daughter samples.

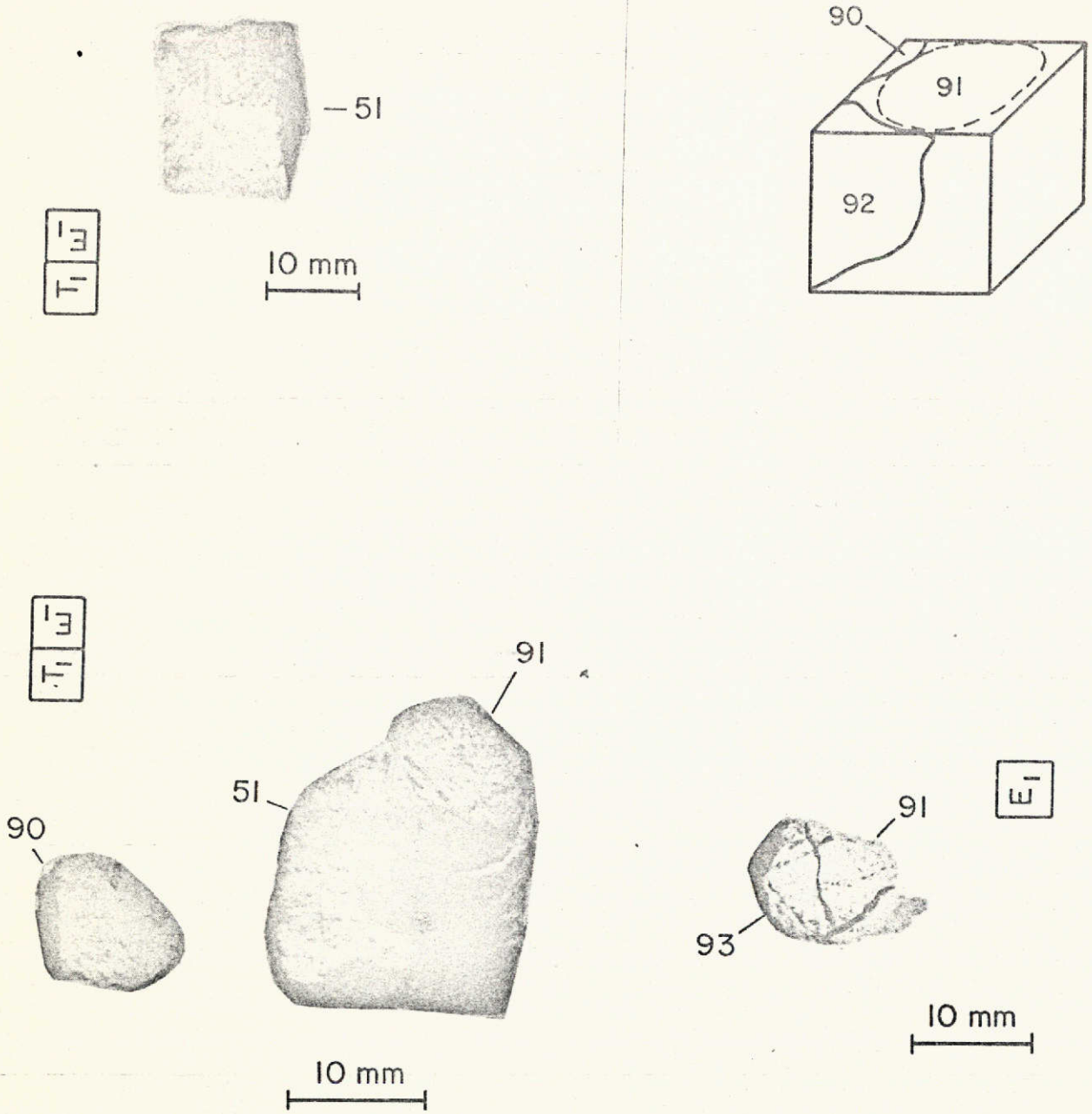

Figure A-9. Photographs and a sketch of clast #5, a rounded fragment of pigeonite basalt embedded in a matrix of crushed basalt of the same composition (see also Figure A-7 and Table A-1).

Table A-1. 72275: Inventory of daughter samples.

Number	Grams	Distribution	Description
	72275: Samples Taken before Cutting (see Figures A-1, A-2, and A-3)		
0	3640.00	Subdivided	Original specimen
1	0.01	Library	Thin section of undocumented chip
	0.67	Library	Potted butt
2	1.02	NYQUIST	Chip from pan
3	5.87		Attrition
4	547.10	Storage	Piece broken off in transit
5	105.10	STRANGWAY	Piece broken from main mass
6	132.10	Storage	Piece broken from main mass
7	50.29	Storage	Chip from pan
8	18.90	Storage	Chip from pan
9	4.80	Storage	Chip from pan
10	18.80		Attrition
11	0.01	Library	Thin section #11: undocumented chip
12	0.01	WOOD	Thin section #12: undocumented chip
13	0.01	Library	Thin section #13: undocumented chip
14	0.01	Library	Probe mount of undocumented chip
15	0.01	WOOD	Chip of rippled surface material
16	0.01	AGRELL	Chip of rippled surface material
17	0.02	WOOD	Chip of rippled surface material
18	0.02	WOOD	Thin sections #122, #123: matrix
	0.18	Library	Potted butt
19	0.32	Storage	Chip: clast plus matrix
20	0.13	WOOD	Documented matrix chip
21	0.09	Storage	Documented matrix chip
22	0.09	AGRELL	Documented matrix chip
23	0.09	Storage	Documented matrix chip
24	0.17	AGRELL	Gray clast chip
25	0.08	Storage	Undocumented chip
26	2.61	Storage	Undocumented chips plus fines
27	298.42	Storage	West-end piece after sawing (see Figure A-4)

Table A-1 (Cont.)

Number	Grams	Distribution	Description
72275: Black and White Clast (Clast #1) (see Figures A-7 and A-8)			
28	10.91	Storage	Remainder of clast #1
29	1.83	Storage	Matrix adjacent to clast
30	0.76	Storage	Matrix adjacent to clast
31	6.34	Storage	Matrix adjacent to clast
32	1.42	Storage	9 fragments of black and white clast
33–41			Undocumented chips (see pages 175 and 176)
42–61			Slab (see pages 173 and 174)
62	0.67	Storage	Black chips from rim of clast #1
63	0.35	Storage	9 white chips from clast #1
64–65			Fines from cleaning cabinet
66–71			Chips from west face of main mass (see page 174)
72–75			Slab (see pages 174 and 175)
76	0.46	HASKIN	White chips from center of clast #1
	0.07	ANDERS	White chips from center of clast #1 (see Table A-2)
	0.27	REYNOLDS	White chips from center of clast #1 (see Table A-2)
77	0.24	TATSUMOTO	White chips from center of clast #1
78	0.02	AGRELL	Thin sections #138, #139: black and white material
	0.02	WOOD	Thin sections #140, #141: black and white material
	0.39	Library	Potted butt
79	0.18	WILSHIRE	Thin section #142: black and white material
	0.02	Library	Thin sections #143, #144: black and white material
	0.15	Library	Potted butt
80	0.44	HASKIN	Chip of black rim
	0.10	ANDERS	Chip of black rim (see Table A-2)
	0.21	REYNOLDS	Chip of black rim (see Table A-2)
81	0.21	TATSUMOTO	Chip of black rim
82	0.17	BANERJEE	Chip of black rim
83–109			Slab (see page 175)
110–115			Surface chips and fines (see page 176)

Table A-1 (Cont.)

Number	Grams	Distribution	Description
116	1.12	Storage	Black and white chips
117	0.21	TATSUMOTO	White chips
118	0.57	Storage	5 matrix chips
119–121			Numbers not assigned to any sample
	72275: Slab, 72275,42; 1.5 cm Thick (see Figure A-7)		
42	53.29	Storage	Matrix and clast #2 of gray aphanitic material
43	37.80	Storage	Matrix and clast #3 of gray aphanitic material
44	0.64	PRICE	Surface chip with patina (broken from piece 72275,45)
45	0.03	AGRELL	Thin sections #124, #125, #126: matrix
	0.02	WOOD	Thin sections #128, #129: matrix
46	3.10	BANERJEE	Matrix (interior piece)
47	2.45	BANERJEE	Matrix (surface piece)
48	2.90	STRANGWAY	Matrix (interior piece)
107	1.41	STRANGWAY	Pieces broken from 72275,48
49	1.54	Storage	Matrix chip
109	1.06	HOUSLEY	Piece broken from 72275,49
50	2.38	CLAYTON	Matrix (interior piece)
51	5.07	Subdivided	Basalt clast #5 in matrix (see Figures A-7 and A-9)
90	0.50	ROSE	Matrix adjacent to basalt clast #5 in 72275,51
91	0.39	HASKIN	Portion of basalt clast #5
	0.07	ANDERS	Portion of basalt clast #5 (see Table A-2)
	0.19	REYNOLDS	Portion of basalt clast #5 (see Table A-2)
92	1.02	Storage	Matrix adjacent to basalt clast #5
93	0.01	WOOD	Thin section #147: clast #5
	0.01	AGRELL	Thin section #148: clast #5
	0.01	Library	Thin section #149: clast #5
	0.54	Library	Potted butt
52	2.34	COMPSTON	Matrix (interior piece)
53	1.84	BIRKEBAK	Piece with patina

Table A-1 (Cont.)

Number	Grams	Distribution	Description
104	1.11	Storage	Piece broken from 72275, 53
105	0.63	Storage	Piece broken from 72275, 53
54	3.93	Storage	Matrix slab: $1 \times 0.8 \times 1.5$ cm
55	1.95	WOOD	Matrix piece
56	3.83	BANERJEE	Matrix piece
57	2.04	HASKIN	Matrix piece
	0.12	ANDERS	Matrix piece (see Table A-2)
	0.52	REYNOLDS	Matrix piece (see Table A-2)
58	4.33	Storage	Clast plus matrix
59	0.03	AGRELL	Thin sections #130, #132, #133: matrix
	0.01	BURNS	Thin section #131: matrix
	0.03	WOOD	Thin sections #134, #135, #136: matrix
	0.01	CHAO	Thin section #137: matrix
60	2.54	Storage	Matrix (interior piece)
61	2.52	Storage	Matrix (surface piece)
62	0.67	Storage	Black chips from black and white clast #1 (see page 172)
63	0.35	Storage	9 white chips from black and white clast #1 (see page 172)
64	29.25	Storage	Fines from air cleaning
65	8.62	Storage	Fines from freon cleaning
		72275, 102: Chips from West Face Adjacent to Slab (Figures A-4 and A-5)	
66	0.95	REED	Interior chip of matrix
67	1.09	BURNS	Interior chip of matrix
68	1.01	EGLINTON	Interior chip of matrix
69	1.53	Storage	Interior chip of matrix
70	2.98	BURLINGAME	Interior chip of matrix
71	1.06	MOORE	Interior chip of matrix
		72275: Slab	
72	1.46	Storage	Matrix slab
73	2.04	TATSUMOTO	Matrix slab
74	1.87	Storage	Matrix slab

Table A-1 (Cont.)

Number	Grams	Distribution	Description
75	13.71	Storage	Band saw chips
76–82			Black and white clast (see page 172)
83	0.44	HASKIN	Chips from gray aphanitic clast #2
	1.00	ANDERS	Chips from gray aphanitic clast #2 (see Table A-2)
	0.16	REYNOLDS	Chips from gray aphanitic clast #2 (see Table A-2)
84	0.14	BANERJEE	1 chip from clast #2
85	0.01	AGRELL	Thin section #145: gray aphanitic clast #2
	0.01	WOOD	Thin section #146: gray aphanitic clast #2
	0.27	Library	Potted butt
86	1.44	Storage	Matrix chips
87	2.78	Storage	Chips of clast #2
88	0.37	Storage	Chips of clast #2 and fines
89	0.38	Storage	Matrix, chips and fines
90–93			Subdivisions of 72275, 51, basalt clast #5 (see page 173)
94–103			Chips and fines from sawing (see page 176)
104	1.11	Storage	Surface piece broken from 72275, 53
105	0.61	Storage	Matrix piece broken from 72275, 53
106	1.72	Storage	Matrix piece broken from 72275, 53
107	1.41	STRANGWAY	Matrix broken from 72275, 48
108	0.41	TAYLOR	Surface piece broken from 72275, 45
109	1.06	HOUSLEY	Matrix piece broken from 72275, 49
		72275: Mostly Undocumented Chips and Fines	
33	6.81	Storage	15 fragments of matrix
34	4.00	Storage	3 fragments with patina
35	2.26	Storage	5 fragments of gray aphanitic material
36	1.13	Storage	Breccia fragment including one gray aphanitic clast and one 3-mm basaltic clast
37	1.05	Storage	Fragment of sugary granulitic anorthosite

Table A-1 (Cont.)

Number	Grams	Distribution	Description
38	7.18	Storage	West-end surface, broken piece
39	1.27	Storage	Cabinet sweeping
40	0.28	Storage	Fines
41	0.09		Consumed
94	2.96	AHRENS	Undocumented chips
95	1.93	LOVERING	Undocumented chips
96	1.99	MORRISON	Undocumented chips
97	1.02	SIEVERS	Undocumented chips
98	1.00	ADAMS	Undocumented fines
99	2.00	WOOD	Undocumented fines
100	9.88	AGRELL	Undocumented fines
101	0.11	HASKIN	Undocumented fines
102	2093.6	Storage	Main mass; east-end piece
103	1.59	ADAMS	Surface chip from west-end piece 72275, 27
104–109			Slab (see page 175)
110	0.97	REED	Chips with patina from end piece 72275, 27
111	39.25	Storage	Undocumented fines
112	3.41	Storage	Chips
113	1.02	Storage	Surface chips
114	0.23	AGRELL	Chips with zap pits and patina
115	16.18		Attrition
116–118			See page 173
119–121			Numbers not assigned to any sample
122–149			Thin sections (see Table A-3)
150	3.46		Attrition
151	0.63	Storage	Recovered from crucible
152	0.55	Storage	Recovered from crucible
153	6.62		Attrition
154	0.02		Consumed

Table A-2. Subdivisions of Haskin samples.

Number	Grams	Distribution	Parent sample
9001		Entirely subdivided	2
9002	0.12	ANDERS	57
9003	0.07	ANDERS	76
9004	0.10	ANDERS	80
9005	1.00	ANDERS	83
9006	0.07	ANDERS	91
9007	0.52	REYNOLDS	57
9008	0.27	REYNOLDS	76
9009	0.21	REYNOLDS	80
9010	0.16	REYNOLDS	83
9011	0.19	REYNOLDS	91

Table A-3. 72275: Thin sections.

Number	Parent sample	Distribution	Area (mm^2)
11	1	Library (undocumented)	12
12	1	WOOD (undocumented)	12
13	1	Library (undocumented)	12
14	1	Library (undocumented)	12
122	18	WOOD	5
123	18	WOOD	5
124	45	AGRELL	50
125	45	AGRELL	50
126	45	AGRELL	50
127	45	USSR	48
128	45	WOOD	46
129	45	WOOD	40
130	59	AGRELL	6
131	59	BURNS	36
132	59	AGRELL	35
133	59	AGRELL	35
134	59	WOOD	35
135	59	WOOD	35
136	59	WOOD	35
137	59	CHAO	25
138	78	AGRELL	10
139	78	AGRELL	10
140	78	WOOD	10
141	78	WOOD	10
142	79	WILSHIRE	5
143	79	Library	5
144	79	Library	5
145	85	AGRELL	5
146	85	WOOD	5
147	93	WOOD	20
148	93	AGRELL	20
149	93	Library	20

APPENDIX B

SPECIMEN 72255 DOCUMENTATION

Ursula B. Marvin

Three documented pieces broke away from specimen 72255 during transport. A reconstruction is shown in Figure B-1. Samples 72255, 1 to 72255, 9 were assigned numbers during the PET examination in February 1973. Samples 72255, 3 to 72255, 6 and 72255, 9 were placed in storage, and the remainder were distributed as follows (see also Table B-1):

72255, 1	Thin section of undocumented chip; in library
72255, 2	Strangway; subsequently returned to storage
72255, 7	Thin section of undocumented chip; in library
72255, 8	Thin section of undocumented chip; to Agrell.

The sawing of a slab 1.5 cm thick was accomplished on July 26, 1973. The specimen is sufficiently coherent for sawing to proceed smoothly. The slab, 72255, 10, was removed as a single large piece, from which a small fragment, 72255, 11, broke off along a preexisting crack. The major subdivisions of 72255 are shown in Figure B-2.

After removal of the slab, a small piece of chalky white matrix material, 72255, 18, was sawed from the east tip of 72255, 23, and surface chips were taken at the sites indicated in Figure B-2. The remaining documented pieces were all derived from the slab, 72255, 10.

The main subdivisions of the slab are outlined in Figure B-3. The further subdivisions of the Civet Cat clast and a strip of adjacent matrix are documented in Figures B-4 and B-5. Subdivisions of the slab pieces 72255, 29 and 72255, 76 are outlined in Figures B-6 and B-7, respectively.

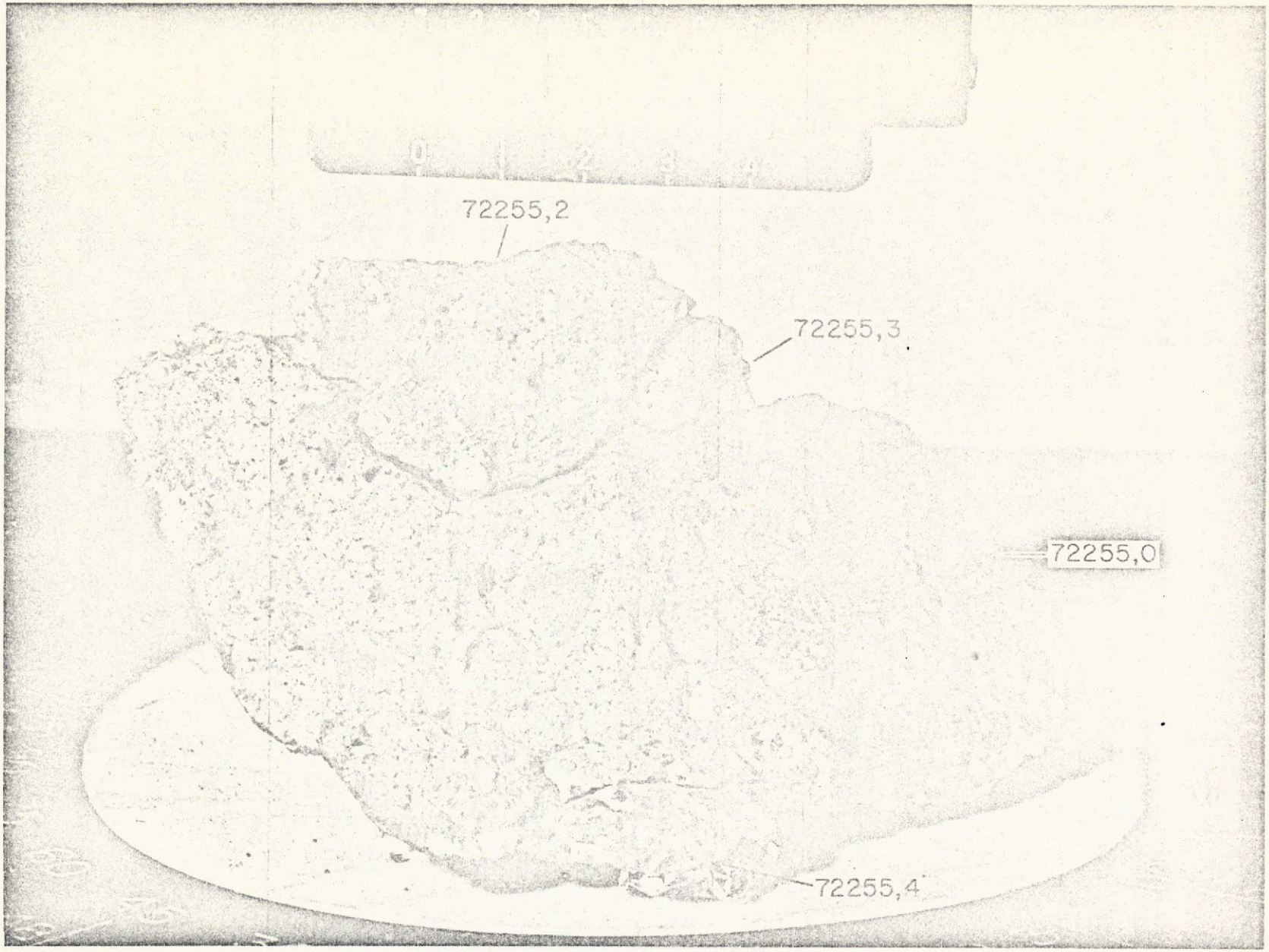

Figure B-1. A reassembly of the four documented pieces of 72255, photographed in the Lunar Receiving Laboratory in January 1973 (NASA photograph S-73-16003).

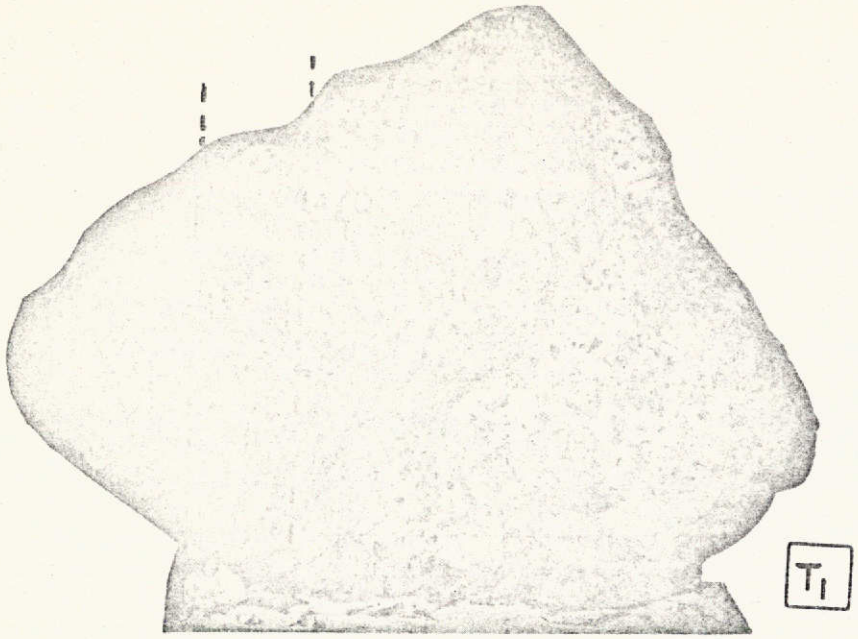

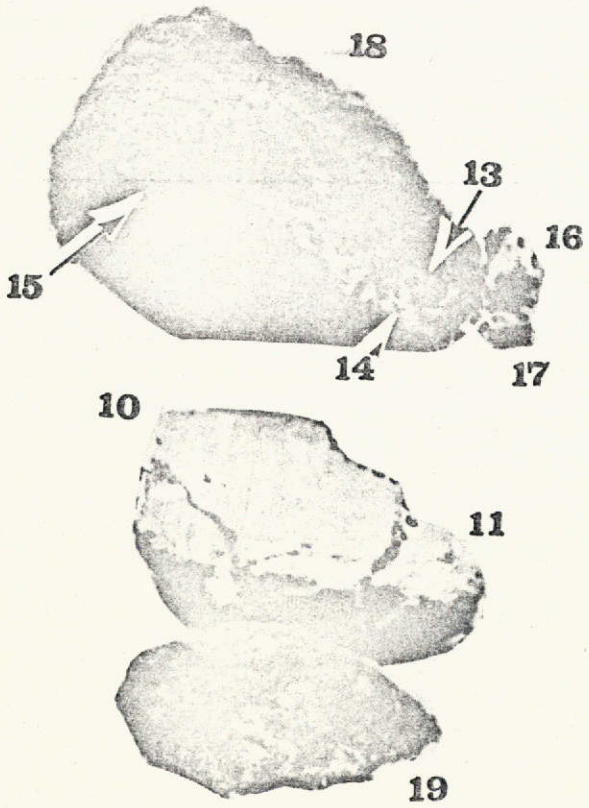

Figure B-2. Upper photograph: Specimen 72255, 0. Dashed lines indicate cutting plans. Lower photograph: The main subdivisions of 72255, 0 after removal of the slab.

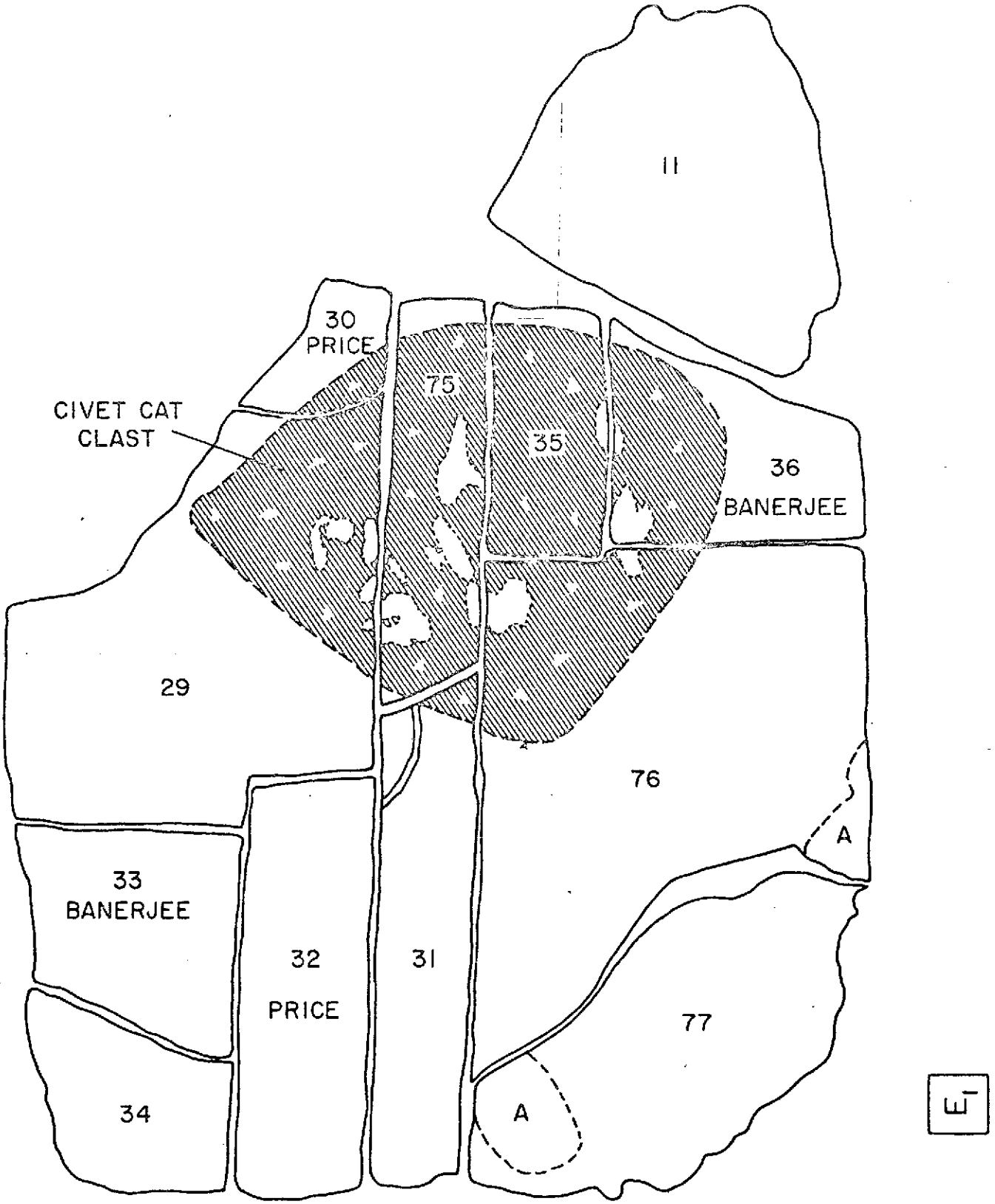

Figure B-3. Subdivisions of the slab, 72275, 10.

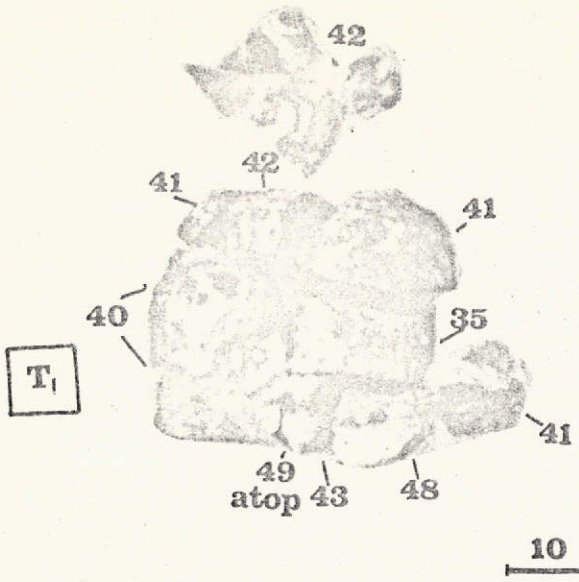

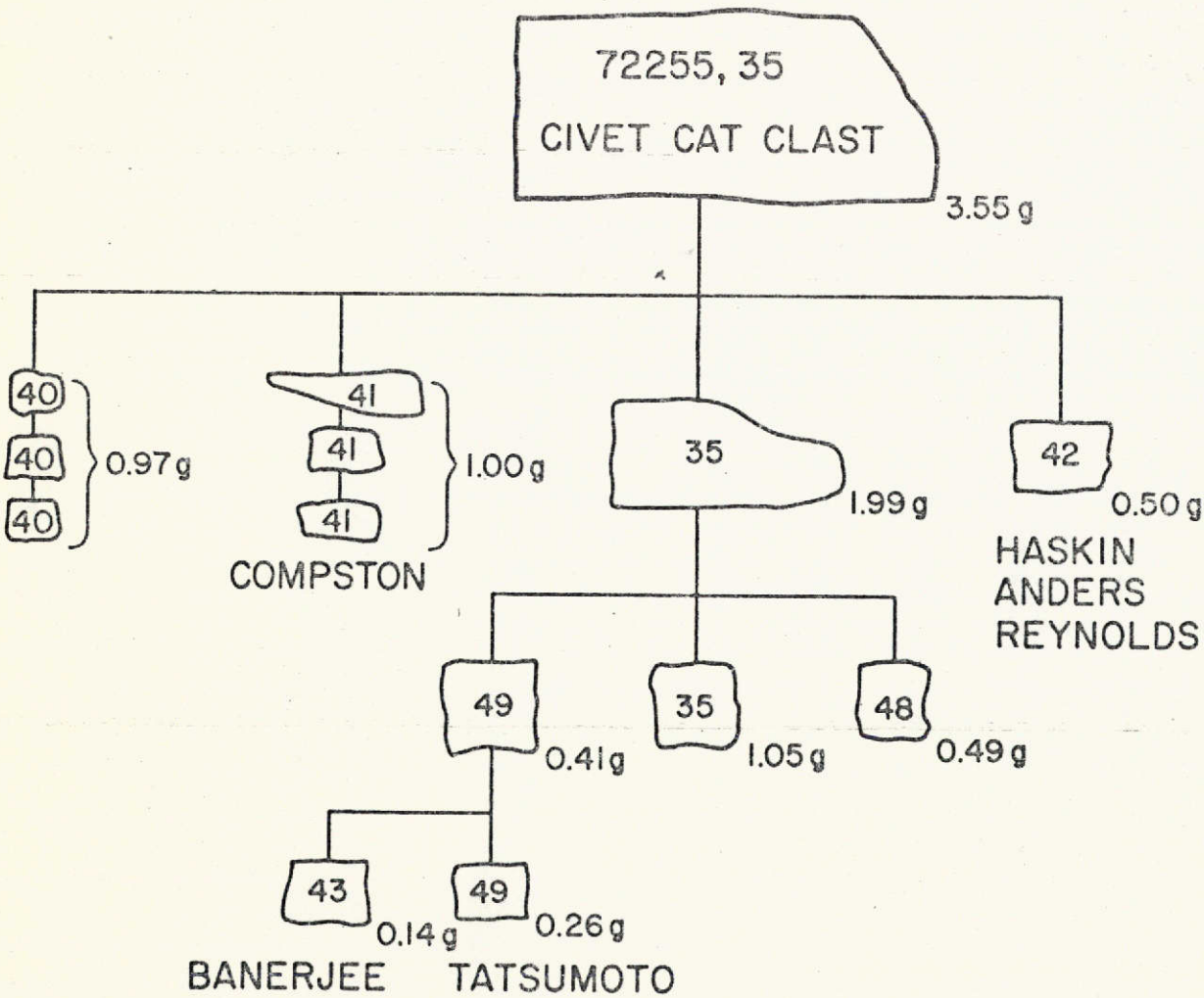

Figure B-4. Subdivisions of the Civet Cat clast and the distribution of the daughter samples of 72255, 35.

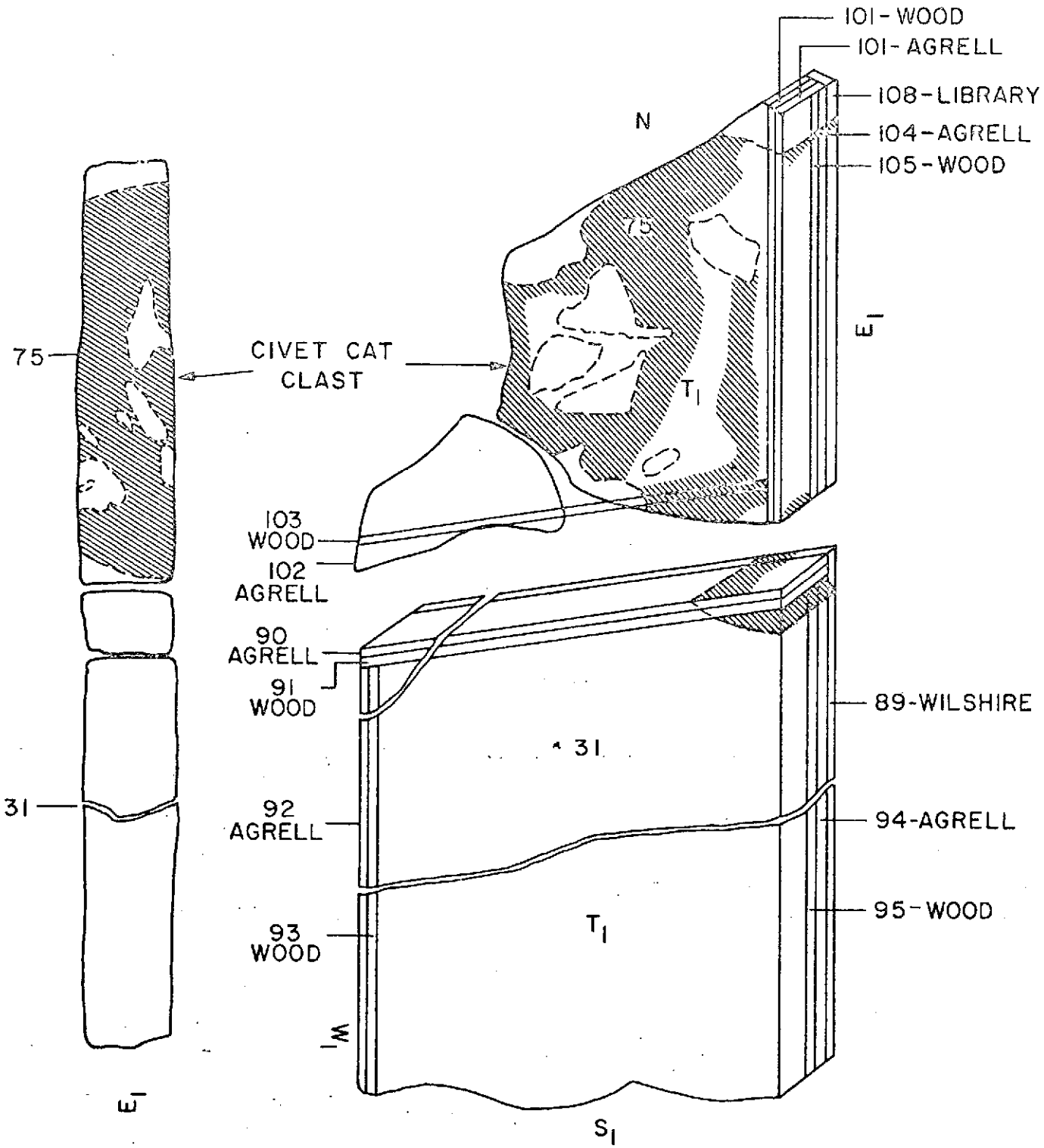

Figure B-5. Sketch of the locations from which orthogonal thin sections were taken from pieces 72255, 75 and 72255, 31, the Civet Cat clast and adjacent matrix.

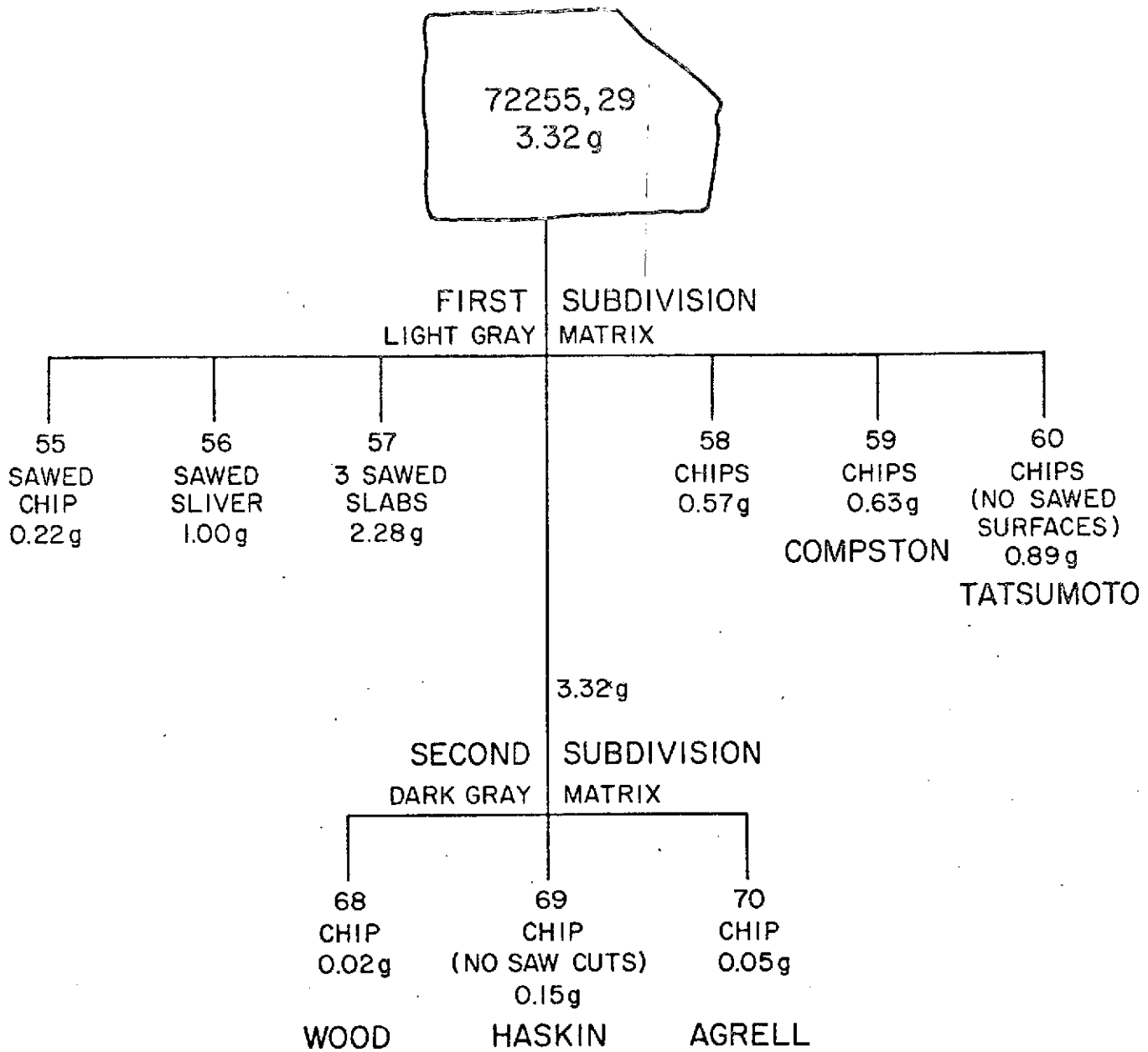

Figure B-6. Subdivisions of slab piece 72255, 29.

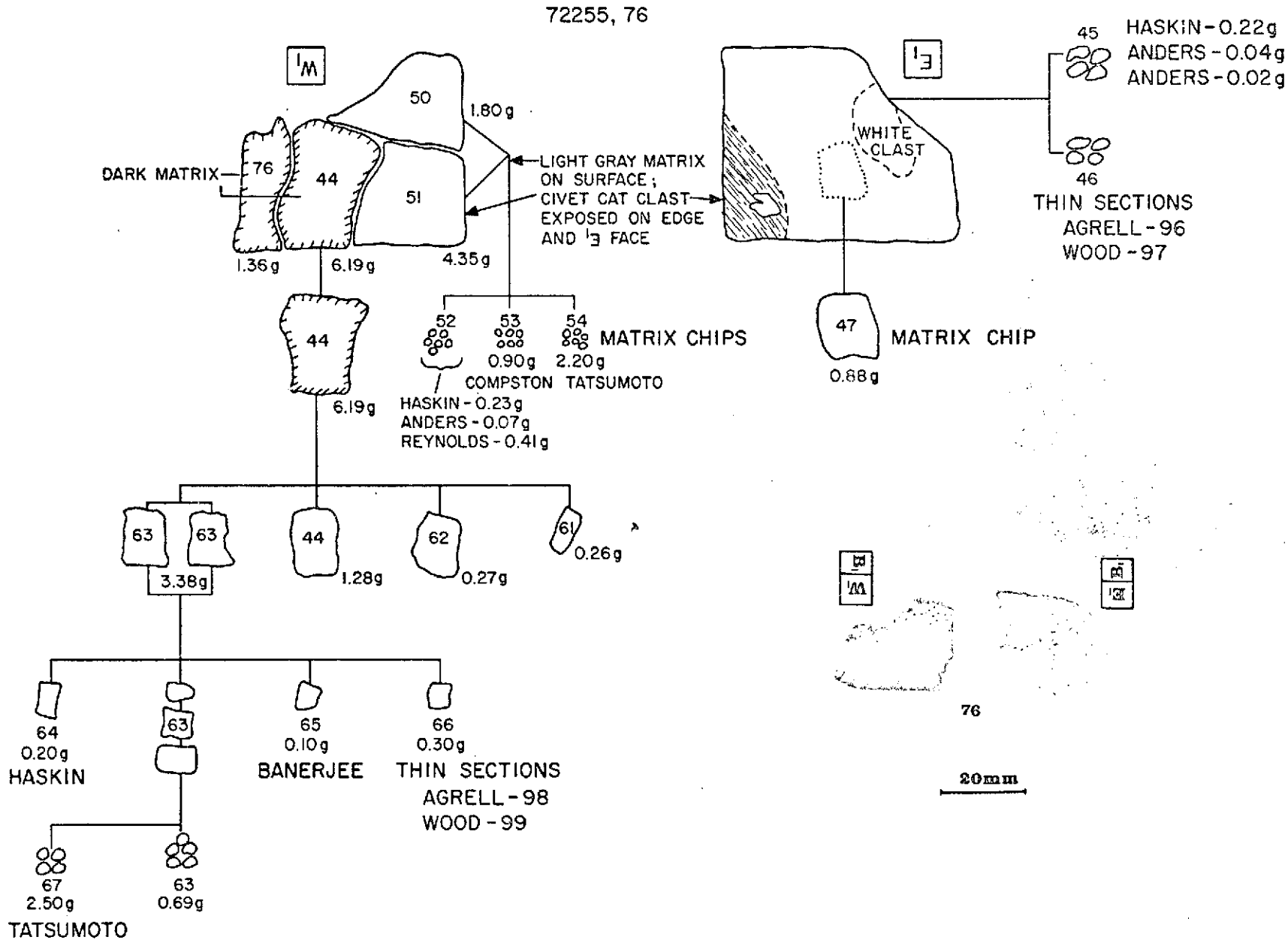

Figure B-7. Subdivisions of slab piece 72255, 76.

Table B-1. 72255: Inventory of daughter samples.

Number	Grams	Distribution	Description
0	461.20	Subdivided	Original specimen
1	0.01	Library	Thin section of undocumented chip from tray (see Table B-3)
	0.37	Library	Potted butt
2	45.66	STRANGWAY	Documented piece broken from specimen
3	7.88	Storage	Documented piece broken from specimen
4	3.30	Storage	Documented piece broken from specimen
5	1.40	Storage	Undocumented chips
6	0.30	Storage	Undocumented chip
7	0.01	Library	Thin section of undocumented chip
8	0.01	AGRELL	Thin section of undocumented chip
9	0.09	Storage	Documented chip
10	54.51	Subdivided	Slab 1.5 cm thick (see Figures B-2 and B-3)
11	5.50	Storage	Piece broken from north end of slab
12	2.04	Storage	Surface chip broken during sawing
13	0.25	Storage	Surface chip broken during sawing
14	0.60	Storage	Surface chip broken during sawing
15	1.62	Storage	Surface chip broken during sawing
16	0.80	Storage	Piece sawed from north end of specimen
17	0.30	Storage	Piece sawed from north end of specimen
18	1.18	Subdivided	2 sawed chips of grayish-white matrix from east end of specimen
	0.10	HASKIN	Piece of the grayish-white matrix
	0.01	AGRELL	Thin section #106: grayish-white matrix
	0.01	WOOD	Thin section #107: grayish-white matrix
	0.12	Library	Potted butt
	0.95	Storage	Grayish-white matrix
19	32.41	Storage	West end of specimen
20	2.79	Storage	Band saw chips
21	6.87	Storage	Band saw fines
22	0.63	Storage	Undocumented fines
23	287.30	Storage	Remnant of main mass

Table B-1 (Cont.)

Number	Grams	Distribution	Description
24	2.94	Storage	Fines from freon cleaning
25	2.41		Attrition
26–28			Numbers not assigned to samples
	72255, 10: Slab Subdivisions (see Figures B-2 to B-7)		
29	3.32	Storage	Matrix plus part of Civet Cat clast
30	0.60	PRICE	Matrix plus Civet Cat clast
31	4.93	Subdivided	Slice of matrix (see Figure B-5)
	0.01	WILSHIRE	Thin section #81
	0.03	AGRELL	Orthogonal thin sections #90, #92, #94
	0.03	WOOD	Orthogonal thin sections #91, #93, #95
	1.43	Library	Potted butt
32	1.76	PRICE	Track strip with patina
33	2.08	BANERJEE	Interior slab, $0.5 \times 0.5 \times 1.5$ cm
34	0.32	Storage	Surface slab
35	1.05	Storage	Remnant of Civet Cat clast and adhering matrix
36	3.49	BANERJEE	Slab with patina on one edge
37	1.47	Storage	Band saw chips
38	1.89	Storage	Band saw fines
39	0.27	Storage	Fines from cleaning cabinet
40	0.97	Storage	Fragment of Civet Cat clast plus matrix
41	1.00	COMPSTON	Fragment of Civet Cat clast
42	0.20	HASKIN	Fragments of Civet Cat clast
	0.06	ANDERS	Fragments of Civet Cat clast (see Table B-2)
	0.22	REYNOLDS	Fragments of Civet Cat clast (see Table B-2)
43	0.14	BANERJEE	Fragments of Civet Cat clast
44	1.28	Storage	Dark matrix material in piece 72255, 76
45	0.22	HASKIN	White clast plus light gray matrix
	0.04	ANDERS	White clast plus light gray matrix (see Table B-2)
	0.02	ANDERS	White clast plus light gray matrix (see Table B-2)

Table B-1 (Cont.)

Number	Grams	Distribution	Description
46	0.01	AGRELL	Thin section #96: white clast plus matrix
	0.01	WOOD	Thin section #97: white clast plus matrix
47	0.88	Storage	Chip of matrix of 72255,76
48	0.49	Storage	Fragment of Civet Cat clast
49	0.26	TATSUMOTO	Interior chip of Civet Cat clast
50	1.80	Storage	Matrix and Civet Cat clast
51	0.98	Storage	2 chips of matrix and Civet Cat clast
52	0.23	HASKIN	Interior chips of light gray matrix
	0.07	ANDERS	Interior chips of light gray matrix (see Table B-2)
	0.41	REYNOLDS	Interior chips of light gray matrix (see Table B-2)
53	0.90	COMPSTON	Interior chips of light gray matrix
54	2.20	TATSUMOTO	Interior chips of light gray matrix
55	0.22	Storage	Sawed chip from matrix of 72255,29 (see Figure B-6)
56	1.00	Storage	Sawed sliver from matrix of 72255,29
57	2.28	Storage	Sawed chip from matrix of 72255,29
58	0.57	Storage	Sawed chip from matrix of 72255,29
59	0.63	COMPSTON	Chips of light gray matrix from 72255,29
60	0.88	TATSUMOTO	Chip (no sawed surface) of light gray matrix from 72255,29
61	0.26	Storage	Chips of dark gray matrix from 72255,76 (see Figure B-7)
62	0.27	Storage	Chips of dark gray matrix from 72255,76
63	0.69	Storage	Chips of dark gray matrix from 72255,76
64	0.20	HASKIN	Chips of dark gray matrix from 72255,29
65	0.10	BANERJEE	Chips of dark gray matrix from 72255,29
66	0.01	WOOD	Thin section #99: dark gray matrix of 72255,76
	0.30	Library	Potted butt
67	2.50	TATSUMOTO	Chips of dark gray matrix of 72255,76
68	0.02	WOOD	Chip of dark gray matrix of 72255,29
69	0.15	HASKIN	Chip of dark gray matrix of 72255,29 (no sawed surfaces)

Table B-1 (Cont.)

Number	Grams	Distribution	Description
70	0.05	AGRELL	Chip of dark gray matrix of 72255, 29
71	2.05	Storage	Anvil chips and fines
72	0.45	Storage	Chips without patina
73	0.11	HASKIN	Band saw fines
74	1.00	ADAMS	Band saw fines
75	0.03	WOOD	Orthogonal thin sections #101, #103, #105: Civet Cat clast (see Figure B-5)
	0.03	AGRELL	Orthogonal thin sections #100, #102, #104: Civet Cat clast
	4.86	Library	Potted butt
76	1.36	Storage	Remnant of slab piece
77	4.05	Storage	Remnant of slab piece
78	1.81		Attrition
79	0.08	HASKIN	Interior chip of whitish material from 72255, 18
	0.01	AGRELL	Thin section #106: whitish material from 72255, 18
80	0.01	WOOD	Thin section #107: whitish material from 72255, 18
	0.12	Library	Potted butt
81	0.95	Storage	Remnant of 72255, 18
82–88			Numbers not assigned to samples

Table B-2. Subdivisions of Haskin's samples.

Number	Grams	Distribution	Parent sample
9001	0.06	ANDERS	42
9002	0.04	ANDERS	45
9003	0.02	ANDERS	45
9004	0.07	ANDERS	52
9005	0.23	REYNOLDS	42
9006	0.41	REYNOLDS	52

Table B-3. 72255: Thin sections.

Number	Parent sample	Distribution	Area (mm^2)
1	0	Library	
7	1	Library	4
8	1	AGRELL	5
89	31	WILSHIRE	40
90	31	AGRELL	15
91	31	WOOD	10
92	31	AGRELL	15
93	31	WOOD	15
94	31	AGRELL	35
95	31	WOOD	35
96	46	AGRELL	5
97	46	WOOD	4
98	66	AGRELL	6
99	66	WOOD	6
100	75	AGRELL	10
101	75	WOOD	10
102	75	AGRELL	12
103	75	WOOD	12
104	75	AGRELL	25
105	75	WOOD	25
106	80	AGRELL	5
107	80	WOOD	5
108	75	Library	30
109	46	Attrition	